Critical Transport Across a Finite Temperature Bosonic Josephson Junction: Resistive Superflow Dynamics, Vortex Ring Generation and Thermal Damping.

Klejdja Xhani

Thesis submitted for the degree of
Doctor of Philosophy

School of Mathematics, Statistics & Physics
Newcastle University
Newcastle upon Tyne
United Kingdom

2021

To my husband Alessio and my son Gabriel

Acknowledgements

First and foremost, I would like to thank my supervisor Nick Proukakis for his support, his guidance throughout my PhD towards interesting topics, his passion for research and for letting me continue my PhD from Florence. My gratitude goes to Giacomo Roati for his support during the second part of my PhD conducted in Florence and for believing in me. I am grateful to the School of Mathematics, Statistics and Physics for the financial support for this project and for their great support to women in science.

My gratitude goes also to my collaborators Luca Galantucci who teached me a lot on the vortex ring properties and to Carlo Barenghi for introducing the physics of vortex rings through inspiring discussions. I am grateful to Kean Loon Lee for teaching me his technical and scientific knowledge during the first year of my PhD. I am thankful to Matteo Zaccanti for his expertise and fruitful discussions, and to Francesco Scazza for interesting discussions and for his help on the long paper submission process. My gratitude extends to Andrea Trombettoni for his support and the interesting discussions. I am thankful to the experimental group for sharing their data with us, in particular to Elettra Neri.

I am thankful to Paolo Comaron and Tom Bland for proofreading part of this thesis. I am thankful to Nick Parker for his continuos support during my remote PhD studies. I am thankful to Thomas Billiam for his interesting questions and discussions. Further, I would like to thank the persons with whom I shared my experience in Newcastle and who supported me and make my experience enjoyable: Mariam, Julienne, Francesca, Sophie, Mae, Aida, Hayley, Paolo, Luca, Fabrizio, Tom, Amos, Omar, Matthew. I am thankful to the persons with whom I shared my experience in Florence: Alessio, Eugenio, Francesco, Santiago, Nicolas, Lorenzo V., Matteo, Giulia, Rita, Irene, Lorenzo B.. I am thankful to Michael Beaty and George Stagg for their technical support. I am grateful to the General Office with their help on resolving formal bureaucracy issues.

I am very thankful to my parents Vjollca and Xhimi for their love, advices and for supporting my wish on studing physics even when many people said physics is not for girls. I am thankful to my sisters Jona and Stela and for their help and love. I am very grateful to my mother-in-law Paola and my father-in-law Franco for their incredible help and their support, making so possible to finish my thesis in these hard times. I am very thankful to my grandparents Nena Gjylo, Gjysh Elez, Nena Salo and Gysh Habib for their love and for always being with me. My gratitude goes to all the people who has supported me in my life.

Finally, there is no word suitable for describing my infinite gratitude to my husband Alessio for his love, his patience, for always encouraging and supporting me and for making my life happier together with our amazing and lovely son Gabriel.

Abstract

A Josephson junction consists of two-weakly coupled quantum fluids through a barrier and is an ideal environment for studying coherent quantum transport and its breakdown due to dissipation, depending on whether or not the superfluid velocity exceeds a critical value. Motivated by a recent experiment with ^{6}Li (in the Bose-Einstein condensation limit) at LENS (Florence), in this thesis we firstly characterised the dynamical regimes observed experimentally for an elongated three-dimensional bosonic Josephson junction: the coherent dynamics Josephson 'plasma' oscillations regime and the dissipative one. Our analysis is based on both zero-temperature mean-field theory (Gross-Pitaevskii equation), and its finite temperature kinetic theory generalisation, in which the condensate is coupled to a dynamical thermal cloud, described by a quantum Boltzmann equation (Zaremba-Nikuni-Griffin method), and reveals excellent agreement with experimental findings.

Secondly, we showed a direct connection between resistive superfluid current and vortex ring (VR) nucleation, through the mechanism of phase slips, thus demonstrating a close analogy with the phase-slippage phenomenon in superfluid helium. Specifically, we identify the origin of dissipation as the transfer of the incompressible kinetic energy from the axial flow to the VR swirling flow, and the phonon emission during vortex propagation. Performing a detailed study of the VR dynamics in our three-dimensional inhomogeneous superfluid, we highlighted the role of trap asymmetry on the emergence of elliptical VRs exhibiting Kelvin wave excitations. The dissipation due to relative condensate-thermal motion (at fixed condensate number, well below the transition temperature) was found to have no effect at early times but it becomes relevant at longer timescales, affecting both the oscillatory relative population dynamics and the VR dynamics.

Exploring a wider range of barrier heights/widths beyond the experimental parameters, we constructed an extended phase diagram for the elongated trap, including –beyond Josephson 'plasma' and dissipative regimes discussed above – also the expected Macroscopic Quantum Self-Trapping regime. Confirmation of the emergence of an analogous phase diagram in a spherical trap, demonstrates unequivocally that all three regimes should be observable in carefully-tailored ultracold experiments.

Studying the role of finite temperature, we distinguished two regimes: at relatively low temperatures, where condensate mean field dynamics dominates, the relative population imbalance oscillates with two main frequencies: in this regime, the thermal cloud is driven by the condensate, with its presence damping the condensate motion and decreasing its frequency. However, when the temperature becomes such that the thermal cloud mean kinetic energy exceeds the barrier height, the thermal cloud oscillates with its own frequency, and begins to drive the condensate, significantly affecting its observable dynamics.

Contents

Part I

Introduction

Chapter 1

Introduction to superfluids, supercurrent and the superfluid instabilities

One of the most impressive phase transitions is Bose-Einstein condensation [1, 2] which manifests itself as a phase transition both in the momentum and in coordinate space. It was theoretically predicted by Bose and Einstein in 1925 [3, 4] for non-interacting dilute bosonic gases and its first experimental observation in weakly interacting ultracold gases was achieved in 1995 by [5–7]. Based on the studies of Bose and Einstein and after the discovery of superfluidity in ^{4}He by Allen, Misener and Kapitza [8, 9], London in 1938 [10] suggested the idea that superfluidity and Bose-Einstein condensation are related and that a superfluid has a non-zero condensate fraction, i.e. a macroscopically occupied quantum state. The first self-consistent theory on the superfluidity was achieved by Landau in 1941 [11]. Superfluids have the ability to flow without viscosity if their velocity with respect to an obstacle is smaller than a critical velocity. If such a condition is not fullfilled, elementary excitations are generated and the superflow becomes resistive.

One of the most incredible manifestations of the macroscopic phase coherence characterising a condensate state is the observation of the Josephson effect which consists of a supercurrent flowing across a thin barrier even in the absence of any external potential due to the tunneling of particles through the barrier. One of the main parts of this chapter and of this thesis will be the study of the Josephson-like quantum oscillations between two weakly coupled Bose-Einstein condensates (BEC) in a three-dimensional atomic Josephson junction.

Given the relation between BEC and superfluidity, the concept of the critical velocity for the onset of a resistive flow applies also for an ultradilute BEC. One of the dissipative phenomena is the generation of vortices which causes the condensate phase to slip by 2π. Initially studied in superfluid ^{4}He [12–15], phase-slippage induced resistive flows were also observed and studied in ultradilute atomic BEC [16–24]. The onset of such dissipative phenomena in three-dimensional atomic Josephson-junctions and the analogy with superfluid helium will be the second part of this chapter.

One of the most important stages in achieving the Bose-Einstein condensates in ultracold atom experiments is the evaporative cooling [25]. Essential for such cooling techniques is the thermalization due to collisions between condensate and thermal cloud. Moreover, even when the BEC is formed, the system is still partly condensed even at the lowest experimental temperature and the condensate cloud is surrended by the thermal particles. Thus it is important for a better understanding and comparison with experimental results to include the effect of the thermal cloud on the system statics and dynamics. In this thesis the modelling of finite temperature Bose-Einstein condensate is performed by using the 'Zaremba-Nikuni-Griffin' model [26–28] and the third part of this chapter consists on showing the success of such model in reproducing experimental results.

1.1 Quantum degenerate gases

In 1925 De Broglie [29] suggested the concept of wave-particle duality according to which particles behave like waves with an associated wavelength $\lambda_{dB} = h/p$, where h is Planck's constant and p is the momentum of the massive particle. For a thermal gas at temperature T the de-Broglie wavelength is defined as

$$\lambda_{dB} = \frac{h}{\sqrt{2\pi m k_B T}}, \tag{1.1}$$

with m the particle mass and k_B the Boltzman constant. At high temperature λ_{dB} assumes values which are small compared to the interparticle separation given by $n^{-1/3}$, with n the particle density. The particles are well-localized (pointlike) and they can be considered as distinguishable ones (classical regime). At low temperature instead, the spatial wavefunctions of individual particles start to overlap as λ_{dB} becomes larger. Consequently, the particles cannot be considered anymore as distinguishable ones and they enter the quantum degenerate regime $\lambda_{dB} \approx n^{-1/3}$.

In the quantum degenerate regime, N elementary particles of the same species, each characterized by a coordinate vector $\mathbf{r}_i$ and by a projection σ_i of their spin along a certain axis, for example the z axis, are described by the Schrödinger wavefunction $\Psi(\mathbf{r}_1\sigma_1, ..., \mathbf{r}_j\sigma_j, ..., \mathbf{r}_i\sigma_i, ..., \mathbf{r}_N\sigma_N)$. One of the fundamental principles of quantum mechanics is the indistinguishability of elementary particles of the same species. A direct consequence of this is that the probability, defined as the modulus squared of the many-body Schrödinger wave function $|\Psi|^2$, must be invariant under the simultaneous exchange of all the variables (position and spin projection) of two particles, i.e.

$$|\Psi(\mathbf{r}_1\sigma_1, ..., \mathbf{r}_j\sigma_j, ..., \mathbf{r}_i\sigma_i, ..., \mathbf{r}_N\sigma_N)|^2 = |\Psi(\mathbf{r}_1\sigma_1, ..., \mathbf{r}_i\sigma_i, ..., \mathbf{r}_j\sigma_j, ..., \mathbf{r}_N\sigma_N)|^2. \tag{1.2}$$

This condition is fulfilled if the many-body wave-function is antisymmetric or symmetric under the exchange of two particles

$$\begin{cases} \Psi(\mathbf{r}_1\sigma_1, ..., \mathbf{r}_j\sigma_j, ..., \mathbf{r}_i\sigma_i, ..., \mathbf{r}_N\sigma_N) = -\Psi(\mathbf{r}_1\sigma_1, ..., \mathbf{r}_i\sigma_i, ..., \mathbf{r}_j\sigma_j, ..., \mathbf{r}_N\sigma_N) & \text{Antisymmetric} \ , \\ \Psi(\mathbf{r}_1\sigma_1, ..., \mathbf{r}_j\sigma_j, ..., \mathbf{r}_i\sigma_i, ..., \mathbf{r}_N\sigma_N) = \Psi(\mathbf{r}_1\sigma_1, ..., \mathbf{r}_i\sigma_i, ..., \mathbf{r}_j\sigma_j, ..., \mathbf{r}_N\sigma_N) & \text{Symmetric} \ . \end{cases} \tag{1.3}$$

In the first case Ψ describes an ensemble of fermions, that have a half-integer spin in units of the reduced Planck's constant; in the second case instead, it describes an ensemble of bosons, which have an integer spin in the same units. Bosons obey the Bose-Einstein statistics; for example the photon has spin 1 and is a boson, while fermions obey the Fermi-Dirac statistics; for example an electron or a nucleon has spin 1/2 and is a fermion. For non-interacting bosons and fermions, the average occupation number of a single-particle state, i , with energy ϵ_i is given by

$$f(\epsilon_i) = \frac{1}{\mathrm{e}^{(\epsilon_\mathrm{i}-\mu)/(\mathrm{k_B T})} \pm 1}, \tag{1.4}$$

where μ is the chemical potential, with the sign '+' for fermions and the sign '$-$' for bosons. The first one gives the Fermi-Dirac distribution function while the second one gives the Bose-Einstein distribution function. The antisymmetry condition for the fermion's many-body wave-function implies that two identical fermions can not occupy the same quantum state because this would lead to $\Psi = 0$. This represents the Pauli exclusion principle [30].

For bosons instead the symmetry condition for Ψ implies that there is no constraint on the number of particles occupying the same quantum state. For temperature lower than a critical value the macroscopic occupation of the lowest energy level happens and the system exhibits a phase transition known as Bose-Einstein condensation [3, 4]. For a fermionic system, for temperature going towards $T = 0$ and in the absence of Cooper pairing each energy state is occupied by only one fermion (known as the Fermi sea [31]). The distinction between these two different classes is valid not only for elementary particles but also for composite ones, with the sum of spins of their costituents defining the quantum nature (bosons or fermions) of these particles. For instance, a ^{6}Li atom is composed of an odd number of fermions (3 neutrons, 3 protons and 3 electrons) and it is therefore a fermion.

The condition for the onset of Bose-Einstein condensation corresponds to the onset of the quantum degenerate regime where λ_{dB} becomes on the order of the interparticle distance. For an ideal gas of non-interacting particles in a three-dimensional box this condition is given by [1]

$$n\lambda_{dB}^3 = \zeta(3/2) \approx 2.612, \tag{1.5}$$

where $n\lambda_{dB}^3$, also known as the phase-space density, gives the number of particles within a volume $V = \lambda_{dB}^3$ (where $n = N/V$ is the density with N the particle number). This condition leads to a critical temperature

$$T_c = \frac{2\pi}{[\zeta(3/2)]^{2/3}} \frac{\hbar^2 n^{2/3}}{m k_B} \approx 3.31 \frac{\hbar^2 n^{2/3}}{m k_B}, \tag{1.6}$$

where $\zeta(3/2)$ is the Riemann zeta function evaluated at 3/2. The occupancy or the number of particles in the condensate state for an ideal non-interacting gas in a 3D box [1] can be found as

$$N_0 = N\left[1 - \left(\frac{T}{T_c}\right)^{3/2}\right]. \tag{1.7}$$

The condition (1.5) means that for Bose-Einstein condensation to happen, relatively high densities are required at relatively low temperature. On the other hand, a phase transition into a liquid or solid has to be avoided in order to achieve a BEC. Therefore the density must be high enough in order for the trapped particles to thermalize but also low enough in order to avoid three-body collisions and thus favouring the dominance of elastic two-body collisions. Due to such conditions a pure Bose-Einstein condensate was observed experimentally for the first time in weakly interacting gases in 1995 [5, 6, 32]. For the three dimensional weakly interacting BEC trapped in a harmonic potential, the critical temperature instead is found as [1, 2]:

$$T_c = \frac{\hbar\bar{\omega} N^{1/3}}{[\zeta(3)]^{1/3}} \approx 0.94 \frac{\hbar\bar{\omega}}{k_B} N^{1/3}, \tag{1.8}$$

where $\bar{\omega} = (\omega_x \omega_y \omega_z)^{1/3}$ is the geometric mean of the trap frequencies along the x, y and z directions and $\zeta(3) = 1.202$ is the Riemann function evaluated at 3. The condensate number is found as

$$N_0 = N\left[1 - \left(\frac{T}{T_c}\right)^{3}\right]. \tag{1.9}$$

1.1.1 The relation between Bose-Einstein Condensation and superfluidity

Bose-Einstein condensates are described by a wavefunction Ψ_0, which is not invariant under Galilean transformations [2] as it acquires a phase factor. For a uniform system, the field operator $\hat{\Psi}(\mathbf{r},t)$ satisfies the equation

$$i\hbar\frac{\partial\hat{\Psi}(\mathbf{r},t)}{\partial t} = \left[-\frac{\hbar^2\nabla^2}{2m} + \int \hat{\Psi}^\dagger(\mathbf{r}',t)V(\mathbf{r}'-\mathbf{r})\hat{\Psi}(\mathbf{r},t)d\mathbf{r}'\right]\hat{\Psi}(\mathbf{r},t) \tag{1.10}$$

in the Heisenberg representation with $V(\mathbf{r}'-\mathbf{r})$ the interaction potential. Also the field operator $\hat{\Psi}'(\mathbf{r},t)$ found under the Galilean transformation satisfies the equation

$$\hat{\Psi}'(\mathbf{r},t) = \hat{\Psi}(\mathbf{r}-\mathbf{v}t,t)\exp\left[\frac{\mathrm{i}}{\hbar}\left(\mathrm{m}\mathbf{v}\cdot\mathbf{r}-\frac{1}{2}\mathrm{m}\mathbf{v}^2\mathrm{t}\right)\right], \tag{1.11}$$

with $\mathbf{v}$ a constant vector. For a large particle number, at $T=0$ and for ultradilute weakly-interacting BEC, we could neglect the quantum and thermal fluctuations [2]. In this approximation, the condensate component is found from the expectation value of the field operator $\psi_0 = \langle\hat{\Psi}\rangle$ (which is also called the order parameter) and it also follows the same transformation law as the field operator (1.11). In the reference frame where the system is in equilibrium and for a uniform system, the condensate wavefunction can be written as $\psi_0 = \sqrt{n_0}\mathrm{e}^{-\mathrm{i}\mu\mathrm{t}/\hbar}$ with n_0 the position-independent condensate density and μ the chemical potential. In the frame where the fluid is not at rest and moves with a constant velocity $\mathbf{v}$, the order parameter becomes $\psi_0 = \sqrt{n_0}\mathrm{e}^{\mathrm{i}\phi}$ with ϕ expressed as

$$\phi(\mathbf{r},t) = \frac{1}{\hbar}\left[m\mathbf{v}\cdot\mathbf{r}-\left(\frac{1}{2}m\mathbf{v}^2+\mu\right)t\right]. \tag{1.12}$$

In this way the system velocity is proportional to the phase gradient

$$\mathbf{v}_s = \frac{\hbar}{m}\nabla\phi, \tag{1.13}$$

which can be identified as the superfluid velocity (it is also valid if the velocity is not constant in time and space but vary slowly). This equation guarantees the irrotationality of the superfluid motion, where the phase of the order parameter plays the role of a velocity potential. Equation (1.13) represents is a consequence of Bose-Einstein condensation, i.e. of the existence of a macroscopically populated state to which is associated a classical field ψ_0 [2]. We must note that Eq. (1.13) does not include the system density. This means that the condensate density does not map onto the superfluid density. Even at $T=0$ where the fluid is all superfluid, the condensate density is smaller than the superfluid one due to quantum depletion of the condensate [33]. However, in three-dimensional dilute ultracold atoms the quantum depletion is very small [34]. Moreover, a recent experiment perfomed by R. Lopes *et al.* in [35] has measured the quantum depletion for a 3D interacting homogeneous BEC, where they showed that in this case the quantum depletion is present but it is small. Thus for our three-dimensional geometry and in the case of $T=0$ we use the words 'superfluid' and 'condensate' interchangeably (disregarding the small difference between them due to quantum depletion).

1.2 Josephson current and Josephson-Anderson relation

One of the most fascinating manifestations of superfluidity is the presence of a non-zero stationary current between two weakly linked superfluids even in the absence of any external potential; this is known as the Josephson '*dc*' current. This is associated with the macroscopic quantum phase coherence related to the presence of a non-zero BEC fraction, allowing to describe each part of the superfluid in terms of an order parameter also called the superfluid order parameter. In this section we show the consequence of such coherence following the description in [12] by introducing the general equations which describe the Josephson effect. The superfluid order parameter can be found as the expectation value of the Bose-field operator $\langle\hat{\Psi}(\mathbf{r})\rangle = \sqrt{n(\mathbf{r})}e^{i\phi(\mathbf{r})}$ in the limit of large particle number and under the assumption that the phase and the amplitude are slowly varying functions of the position $\mathbf{r}$. Penrose and Onsager in 1956 [36] suggested the idea that the superfluids are characterized by non-zero values of the off-diagonal long range order (ODLRO) term, which is consistent with the superfluid exhibiting a macroscopic phase coherence. The total particle number operator is conjugated to the phase operator, satisfying the relations:

$$\begin{cases} \hbar\frac{d\langle\hat{N}\rangle}{dt} = \langle\frac{\partial\hat{H}}{\partial\hat{\phi}}\rangle = \frac{\partial E}{\partial\phi}, \\ \hbar\frac{d\langle\hat{\phi}\rangle}{dt} = -\langle\frac{\partial\hat{H}}{\partial\hat{N}}\rangle = \frac{\partial E}{\partial N}. \end{cases} \tag{1.14}$$

In a superfluid state the average value is to be taken over a coherent state, with definite phase. In Eq. (1.14) [right side], the energy change for adding or removing a particle from the system, i.e. $\partial E/\partial N$, gives the chemical potential μ. Let us suppose now that two parts of a superfluid are linked through a barrier, for example. Each part of the superfluid is coherent and has a definite phase $\phi_{1(2)}$. The coupling energy E_J between the two reservoirs must depend on the relative phase $\Delta\phi = \phi_1 - \phi_2$ and the flux through the barrier can be defined as:

$$J = \frac{dN_1}{dt} = -\frac{dN_2}{dt} = \frac{\partial E_J}{\hbar\partial\phi}. \tag{1.15}$$

This current, called also the Josephson current, is a supercurrent because it is different from zero even in the case where no external drive is applied. In the presence of a chemical potential difference $\Delta\mu$ between the two subsystems instead, the relative phase evolves in time with a rate:

$$\frac{d\Delta\phi}{dt} = -\frac{\Delta\mu}{\hbar} \tag{1.16}$$

and this is called the Josephson-Anderson relation. This '*ac*' effect was firstly discussed by Brian Josephson [37] in superconductors for the tunneling current between two superconductors separated by a thin insulator. The Josephson-Anderson relation means that in a steady state, where the superfluid state is constant in time and thus the chemical potential is also constant in time, there is no chemical potential difference $\Delta\mu = 0$. Moreover by taking the gradient of the Josephson-Anderson relation we obtain:

$$\mathbf{F} = \hbar \frac{d(\nabla\phi)}{dt}, \tag{1.17}$$

and by defining the superfluid momentum $\mathbf{p} = \hbar\nabla\phi = m\mathbf{v}$ we conclude that the superfluid accelerates under the effect of a chemical potential difference.

1.3 Experimental observation of the Josephson effect

As we discussed in the previous section, when two superfluids (of bosonic or fermionic nature) or two superconductors are weakly coupled together through a barrier or a thin insulator, a supercurrent flows across the barrier driven by the phase difference between the two reservoirs, which is called the Josephson current. It is named after the scientist Brian Josephson who first discovered the effect in 1962 [37] in superconductors. He found that even in the absence of an applied external potential difference $\Delta V = 0$, a current flow between two superconductors separated by a thin insulator due to the tunneling of Cooper pairs across the junction occurs. This current is called the '*dc*' Josephson current. In the presence of an applied external potential the quasiparticles tunnel through the insulator contributing to the Josephson current which is now an alternating current oscillating sinusoidally in time and it is called the '*ac*' Josephson current. For weak links, the Josephson junction is characterised by a sinusoidal current-phase relation

$$I = I_c \sin(\Delta\phi), \tag{1.18}$$

where $\Delta\phi$ is the relative phase between the two superconductors and I_c is the critical current, defined as the maximum current that can flow in the junction. In the '*dc*' Josephson effect if the external applied current is smaller that I_c then no chemical potential difference is present in the junction and the current has a constant value. For the '*ac*' Josephson effect and for an applied time-independent ΔV the relative phase increases linearly in time depending on the external ΔV according to the Josephson-Anderson relation Eq. (1.16) applied to the superconductors:

$$\frac{\partial \Delta\phi}{\partial t} = \frac{2e\Delta V}{\hbar} \tag{1.19}$$

and the Josephson current oscillates sinusoidally in time with a frequency set by the external ΔV. In this way a Josephson junction becomes also an efficient tool for precise measurement of frequencies acting like a voltage to frequency converter. The Josephson effect was then first observed in [38].

Since its discovery the Josephson effect is also observed between two neutral superfluids such as between two helium superfluids coupled by a small orifice [39, 40] or between two ultacold atoms superfluids coupled by a thin barrier. In this system the Josephson current consists of atomic mass current and not of a charge current as in superconductors. Moreover the analogue of the external voltage difference of superconductors is given by the chemical potential difference $\Delta\mu$ between the two superfluids. The Josephson effect in superfluid helium was initially observed in ^{4}He [39] and then in ^{3}He superfluids [40] where the superfluid dynamics was induced through the nanoscopic apertures (with a size on the order of the superfluid healing length [1]) due to the presence of a pressure and/or a temperature gradient that creates a chemical potential difference between the two superfluids.

Josephson effects have also been studied in dilute quantum gases, where the weak coupling between spatially separated parts can be tuned by controlling the height of the energy barrier between them both for ultracold bosons [41–48] and fermions [49, 20, 50, 51]. Josephson effects have also been studied for exciton-polariton condensates in semiconductors [52, 53]. Moreover, the dissipation of Josephson oscillations due to quantum, and/or thermal fluctuations and due to the generation of topological defects has been studied in different geometries and dimensionalities [18, 21, 54, 55, 22, 23, 56–58, 49, 20].

Unlike superconducting Josephson junctions, in their ultracold counterparts, even in the absence of any external chemical potential difference, a finite chemical potential difference can be present due to non-linear interactions and for a non-zero fractional population imbalance $z = \Delta N/N$, where ΔN is the difference between the number of atoms in the two wells and N is the total number. Such population imbalance is a typical parameter used to characterise ultracold Josephson junction dynamics [59–61]. In fact, when the initial fractional population imbalance z_0 is smaller than a critical value the system enters the Josephson 'plasma' oscillations regime, featuring periodic oscillations of both relative population imbalance and relative phase about zero. When z_0 instead becomes larger than a characteristic critical value, $z(t)$ is no longer able to reach the zero value, with a bias towards the initially more populated well. The sign of the relative population imbalance remains unchanged in time, despite the existence of low amplitude population transfer across the weak link. This regime is known as Macroscopic Quantum Self-Trapping (MQST) [59], and it is characterized by a 'running relative phase (i.e. a relative phase which grows with time similar to the profile of the relative phase in superconductor '*ac*' Josephson effect). The occurrence of the self-trapping regime and the estimation of the critical fractional imbalance [59] can be easily obtained for a Bose-Einstein condensate (BEC) in a double-well potential by writing a two-mode model starting from the mean

[1] More details will be given in the following sections.

field Gross-Pitaevskii description. Note that in general, for long times, the self-trapped regime is eventually destroyed by thermal or quantum fluctuations [61–64, 60, 46] and/or by higher order tunneling processes [65].

Both the Josephson 'plasma' and MQST regimes, discussed for ultracold bosons in double- and multi-well potentials [59–61, 66], have been clearly observed both in ultracold ^{87}Rb [42] and ^{39}K [47] bosonic atomic clouds trapped in a harmonic potential perturbed by a shallow optical lattice which creates a weak link across two well-separated minima, and in the presence of a deep optical lattice [41, 43]. Recently, the Josephson plasma regime has also been observed with fermionic superfluids [49, 20]. In ultracold atomic experiments the role of the weak link can be played by a blue-detuned laser beam in single [42, 46, 48, 49, 20, 50, 51] or multiple double-well potentials [41] or by Raman coupling between two condensates in different hyperfine levels [67]. In the context of ultracold atoms, one can also realize Josephson junctions coupling two internal states via a weak driving field [68–71] where the chemical potential difference comes from an external asymmetric potential, as happens in optical lattices [41].

The first experimental observation of the Josephson effect in bosonic ultracold atoms with ^{87}Rb and in a double-well potential was performed by Albiez *et al.* [42] in 2005. Their geometry was almost a spherical trap and they had $N = 1150$ atoms. The barrier separating the two condensates had a 1/e^2 width of $4.4\mu m$ (around 10 healing lengths). The chemical potential difference which triggered the condensate dynamics across the barrier was set by an initial population imbalance. They showed the observation of both the Josephson 'plasma' and MQST regimes with the first found for initial imbalance $z_0 < z_{cr}$ and the second one when $z_0 \geq z_{cr}$, where the critical imbalance was around 60%. Fig. 1.1(i) shows the experimental density image revealing the difference between Josephson 'plasma' and MQST regime where in the first one the density oscillates between the two wells symmetrically while in the MQST regime one well remains more populated than the other in time. The relative imbalance and relative phase (obtained experimentally from time of flight images) are then showed for the 'plasma' regime in (ii) and the MQST regime in (iii). While in the plasma regime both $z(t)$ and $\Delta\phi$ (in this experiment they called the relative phase ϕ) oscillate sinusoidally in time around a zero mean value, in the MQST regime the $z(t)$ perform small-amplitude oscillations around a non-zero mean value and the relative phase, shown for a shorter time evolution with respect to $z(t)$, increases in time as expected for the MQST regime.

Later in 2007, Levy *et al.* [46] performed the first experimental observation of the '*dc*' Josephson effect in bosonic ultracold atoms (see Fig. 1.2(ii)). A BEC of ^{87}Rb ($N = 10^4$ atoms) were trapped in harmonic potential with axial frequency of $\omega_z = 2\pi \times 26$Hz and radial frequency $\omega_z = 2\pi \times 224$Hz (an experimental image is shown in Fig. 1.2(i)). The double-well potential was created by imposing a blue-detuned laser barrier to the trapping

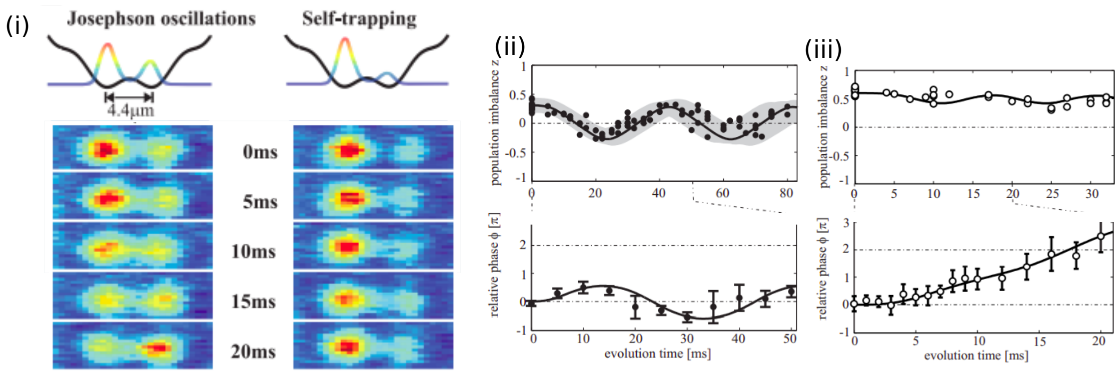

Figure 1.1: Albiez *et al.* [42]; the first implementation of a single bosonic Josephson junction: (i) the schematic image of the experimental double-well potential in the upper plot and the absorption image taken at different time evolutions and showing the density profile oscillations in the Josephson 'plasma' (left) and MQST regime (right). (ii) The population imbalance and relative phase time evolution in the Josephson 'plasma' and in the MQST regime (iii). [Copyright (2005) by the American Physical Society [42]].

potential which separates the condensate into two parts parallel to its long axis. The laser barrier can be approximated by a Gaussian profile which in their case had a $1/e^2$ width of 1.4μm along the tunneling axis. A superfluid current was induced by moving the harmonic trap center with respect to the barrier with a constant velocity. At the end of this process, the current and the chemical potential difference between the two wells was measured. They showed that as the condensate current is smaller than a critical value, the current flows in the atomic junction, without causing a chemical potential difference (see Fig. 1.2(iii)), performing so the first experimental observation of the '*dc*' Josephson effect in ultracold atoms. In this experiment the '*ac*' Josephson effect was also observed where, differently from the experimental procedure for observing '*dc*' Josephson effect, initially an asymmetric double-well potential was created and then the harmonic trap was shifted in order to form a symmetric double-well potential, creating so an initial relative imbalance between the two wells and thus an initial $\Delta\mu_0 \neq 0$. For different values of $\Delta\mu_0$, the population imbalance oscillation frequency was extracted and it was shown to depend linearly on the chemical potential difference as expected for the '*ac*' Josephson effect (see Fig. 1.2(ii)). In this regime, the population imbalance was shown to oscillate around a non-zero mean value [46] as expected for the MQST regime. Another important result of this paper was the demonstration of the fact that MQST regime is highly unstable against thermal fluctuations which destabilize it and make it decay gradually.

Recent experiments at LENS (Florence) with fermionic ^{6}Li have investigated the Josephson effect in an elongated fermionic superfluid across the BEC-BCS regime [49, 20]. The presence of a broad Feshbach resonance between the two lowest hyperfine states of ^{6}Li offers the possibility to finely tune the interatomic interaction, parameterized by the

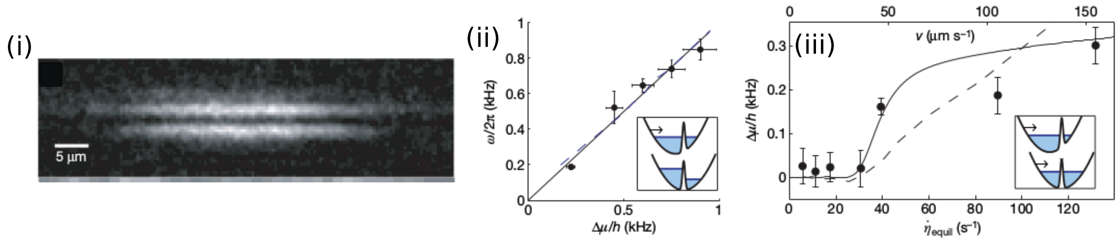

Figure 1.2: Levy *et al.* [46]: The first experimental observation of the '*dc*' Josephson effect with two-weakly coupled BECs of ^{87}Rb: (i) an in situ image of the experimental BEC Josephson junction , (ii) the '*ac*' Josephson effect demonstrated by the linear dependence of the oscillation frequency of the population imbalance $\eta(t)$ on the chemical potential difference. (iii) The $\Delta\mu - I$ relation where the current $I = \dot{\eta}$, and the '*dc*' Josephson effect. Adapted by permission from Springer Nature: Nature [46] [COPYRIGHT] (2007).

s-wave scattering length a [72], by changing the magnetic field value (as is described in Sect. 2.2). This is an efficient way used to create from a BEC of tightly-bound molecules to BCS-like fermionic superfluids within a single experimental set-up. The Josephson effect was studied by trapping around $N = 10^5$ atom pairs in an elongated three-dimensional trapping potential with frequencies $\omega_{\rm x} = 2\pi \times 15$ Hz, $\omega_{\rm y} = 2\pi \times 150$ Hz and $\omega_{\rm z} = 2\pi \times 170$ Hz, with an 'in-situ' experimental density image shown in Fig. 1.3(i). A repulsive laser barrier along the x axis (the long-axes) is then superimposed to the trapping potential separating so the fermionic superfluid in two parts which are weakly-coupled through the barrier. The $1/{\rm e}^2$ barrier width is on the order of the superfluid coherence length, $2.0(2)\mu$m and it is homogeneous along the transverse axes. Similar to the experiment of Ref. [42], the trap center was initially shifted with respect to the barrier along the x axis. At $t = 0$ the trap center was shifted back non-adiabatically to the barrier position. In this way an initial population imbalance and initial chemical potential difference were created, inducing superfluid flow across the barrier. For small enough initial imbalance, they observed coherent oscillations of both pair population imbalance and relative phase with the same frequency, demonstrating the conjugate nature of these two variables as they oscillate out of phase by $\pi/2$. This is the so-called Josephson 'plasma' regime and it was found throughout the whole BEC-BCS crossover (see Fig. 1.3), demonstrating the presence of macroscopic phase coherence in these superfluids.

Moreover they showed that the plasma frequency and the Josephson coupling energy exhibit a non-monotonic behaviour across the BEC-BCS crossover with a maximum near unitarity, revealing in this way the importance of the composite nature of the superfluid pairs. Another interesting finding of this experiment was the explicit observation (across the entire BEC-BCS regime) of a transition from Josephson 'plasma' oscillations to a dissipative regime with increasing initial population imbalance – with no evidence of the existence of MQST regime found in the probed parameter space. One of the main pur-

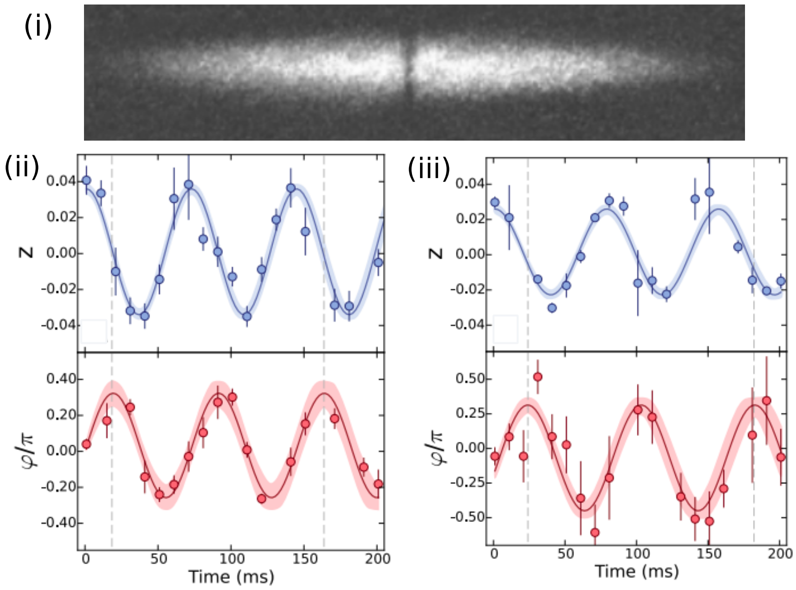

Figure 1.3: Valtolina *et al.* [49]: The first experimental observation of the Josephson 'plasma' oscillations regime with fermionic superfluid across the BEC-BCS crossover: (i) an in situ density image revealing the elongated trap geometry, (ii) the population imbalance and relative phase time evolution in the Josephson 'plasma' regime in the BEC limit, (iii) the corresponding plots in the unitarity limit. Reprinted with permission from AAAS.

poses of the studies presented in this thesis is to give further insight into the microscopic mechanism responsible for the onset of the dissipative regime observed in the experiment. Specifically, in this thesis we model the experimental set-up of ^{6}Li LENS experiment [49, 20] in the limit of the Feshbach resonance where BEC of molecules of lithium are created. Motivated by the theoretical studies in [59–61] and the observation of the MQST state by other ultracold atoms experiments in spherical traps [42] for example, in this thesis we explore values of barrier heights and widths beyond the experimental range of parameters, finding the onset of the MQST regime even in the elongated trap of the ^{6}Li experiment.

Most recently the '*dc*' Josephson effect was also observed with fermionic superfluids [50] and the Josephson effects were also investigated in two-dimensional geometry [51].

The Josephson effect is crucially used for high-precision measurements, a major example being the measurement of magnetic fields with superconducting quantum interference devices (SQUID) [73]. The control of ultracold atomic matter has given rise to the investigation towards analogous 'atomtronic' applications, such as the atomtronic analogue of SQUID, termed AQUID [74–76], leading to a plethora of studies of weak link dynamics across diverse geometries and dimensionalities (see e.g. [77, 78] and references therein).

1.4 Phase-slippage experiments

One of the most remarkable properties of a superfluid is its ability to flow without viscosity with respect to an obstacle or the walls of a container. This dissipationless flow is limited by a threshold velocity v_c, if the superfluid velocity with respect to an obstacle (or vice-versa the obstacle velocity with respect to the superfluid) exceeds v_c the superfluid flow ceases to be dissipationless and dissipative mechanisms are generated such as phonon modes or vortices [12, 13]. The presence of vortices causes the local superfluid phase to slip by 2π and, as part of the superfluid flow energy is now transfered from the flow to the vortex, the superflow becomes resistive. Such vortex (or phase-slippage) induced dissipative regime has been investigated in superfluid Helium [12, 14, 15], where they showed that if the superflow velocity through an orifice exceeded a critical value, the superfluid velocity jumped by a quantised quantity Δv once vortices were generated inside the orifice. In analogy to superfluid helium, phase slips in ultracold Josephson junctions have been analysed across different atomic geometries and dimensionalities [16–24]. In particular, in Refs. [16, 18] it was shown that the vortex-induced phase-slippage was responsible for the decay of the supercurrent in a ring-shaped trap in quantised steps, while in Refs. [20, 22, 23] instead an intial decay of the population imbalance between the two reservoirs was observed which was associated to the generation of vortices.

S. Eckel *et al.* in 2016 [22] studied experimentally the transport properties of a bosonic superfluid flowing through a mesoscopic channel, with length much larger than the superfluid coherence length but small with respect to the inelastic mean path, which connects two large reservoirs (in-situ image of the confined BEC shown in Fig. 1.4(A)). They considered a BEC of 495×10^3 ^{23}Na atoms. The system initial state consists of all the atoms being trapped in one of the reservoirs which they called 'source' by a 'gate' potential applied at the middle of the channel in order to 'trap' the atoms in the 'source'. When the 'gate' potential is removed, the BEC flows freely through the mesoscopic channel driven by the change in the interaction energy which makes the superfluid accelerate. Then, the BEC enters the other reservoir which they called 'drain'. Once the superfluid is in the 'drain' the supercurrent between the two reservoirs depends on the relative phase. If the supercurrent is larger than a critical value then vortices are generated at the interface between the channel and the 'drain'. Instead of measuring the current, they measured the normalized population imbalance between the 'source' and 'gate' defined as $n = \Delta N/2N_e$, such that $N_e + \Delta N$ and $N_e - \Delta N$ are the number of atoms in the 'source' and 'gate' reservoirs respectively. Fig. 1.4(B) shows their results for the time evolution of n for different one dimensional densities inside the channel. The imbalance decays initially fast in time followed by sinusoidal oscillations around a zero mean value with the plasma frequency. The initial decay of the imbalance was associated with the generation of vortices, whose

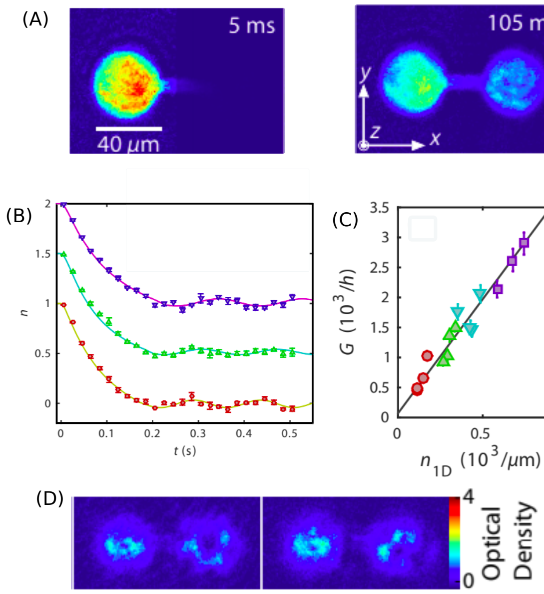

Figure 1.4: S. Eckel *et al.* [22]: (A) In-situ images of a BEC in a dumbbell-shaped potential with all the atoms in the left reservoir (left image) and at time t = 105ms where the BEC has flown freely in the right rerservoir. (B) The temporal evolution of the normalized population imbalance between the two reservoirs for different 1D density inside the channel. (C) The conductance versus the one-dimensional density profile. (D) The TOF images revealing the presence of vortices in the right reservoir (the initially empty reservoir). [Copyright (2016) by The American Physical Society [22]].

presence was revealed by time of flight images shown in Fig. 1.4(D). Following Feynman's argument [13], the generation of vortices leads to a finite conductance in the system even at $T = 0$ which is proportional to the density inside the channel. To fit the population imbalance, they modelled their system as a RSJ-like (resistively-shunted junction) circuit [79] composed of a Josephson weak link with sinusoidal current-phase relation, a shunt resistance R which takes into account the presence of dissipation and a series LC where L is the system inductance, related to the kinetic energy of the atoms, and C represents the energy stored in the chemical potential difference. In this way, they extracted the system conductance and they showed that it depends almost linearly on the 1D density inside the channel, as expected for the cases when dissipation was induced by the vortex generation (i.e. phase-slippage mechanism) [13].

A. Burchianti *et al.* in [20] studied the onset of dissipation in a 3D atomic Josephson junction (elongated trap) where two fermionic superfluids of ^{6}Li were separated by a thin barrier with width comparable to the superfluid coherence length, contrary to the mesoscopic channel presented above. An initial population imbalance between the two wells, or reservoirs, was created by shifting the trap center with respect to the barrier. Then they measured the time evolution of the normalized population imbalance (shown in Fig. 1.5 (a)-(c) [upper subplots]) defined as $z = \Delta N/N$ with ΔN the relative population between

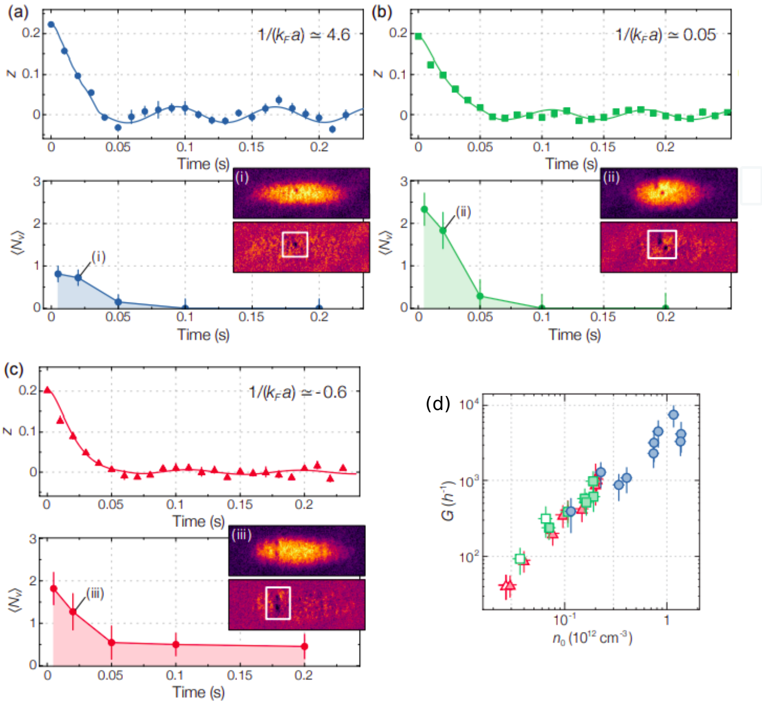

Figure 1.5: A. Burchianti *et al.* [20]: (a)-(c) Upper subplot: The temporal evolution of the population imbalance for a molecular BEC and for $V_0/\mu \simeq 1$ (a), for a unitary superfluid and $V_0/\mu \simeq 0.9$ (b), for a BCS superfluid and $V_0/\mu \simeq 0.9$ (c) with the solid line the results from the RSJ-like circuit model. (a)-(c) Lower subplots: Temporal evolution of the mean value of the vortex counts $\langle N_v \rangle$ with the insets TOF images after 20ms of system evolution (upper inset) and the residual images obtained after substracting the image without vortices (lower inset). (d) The conductance G as a function of the pair density inside the barrier for the molecular BEC (ble circles), unitary superfluid (green squares) and BCS superfluid (red triangles). [Copyright (2018) by The American Physical Society [20]].

the two-wells and N the total number of pairs. Similar to Ref. [22], even though the geometry is different and the link between the two superfluids is of different nature, they found an initial fast decay of the population imbalance followed by harmonic oscillations around a zero mean value. Such a profile was found throughout the entire crossover. From TOF images (after removing the barrier) they found the presence of vortices in the superfluid along the BEC-BCS crossover (TOF images shown in Fig. 1.5 insets). They also measured the mean value of the vortex counts, with the results shown in Fig. 1.5(a)-(c) lower subplots. Similar to [22], the profile of the normalized imbalance $z(t)$ were fitted with an RSJ-circuit model (following the formalism derived in [80–82]). The extracted conductance was then shown as a function of the density at the barrier center with their results shown in Fig. 1.5(d). Across all the crossover, the junction conductance depends almost linearly on the density at the barrier, demonstrating that the main reason for dissipation is the vortex generation.

The emergence of dissipation is also well-known in superconducting wires [80, 73] when vortex arrays proliferate in the system for magnetic fields larger than a critical value, causing a finite electrical resistance across superconductors.

Vortex-induced phase slippage has also been discussed in the context of macroscopic quantum self-trapping: specifically, Abad *et al.* [83] numerically related the self-trapping regime to phase slips created by emergent vortex rings which annihilate within the weak-link region (but outside the region of observable condensate density). Their studies were performed in a spherical trap (shown in Fig. 1.6(a)) with frequency $\omega = 2\pi \times 70$ Hz with $N = 1150$ number of ^{87}Rb atoms, finding a critical imbalance for the onset of MQST regime $z_c \simeq 0.33$. Apart for the population imbalance, they also described the BEC dynamics across the barrier through the x axis superfluid velocity v_x. Fig. 1.6(b) shows their results for the temporal evolution of the normalized population imbalance (upper subplot) and of the v_x (lower subplot) in the MQST regime. The population imbalance oscillates around a non-zero mean value (as expected from [59]) and the superfluid velocity has jumps in the correspondence of the population imbalance minimum. The presence of superfluid velocity jumps was related to the generation of vortex rings which causes the relative phase to jump by 2π. In their paper, two possible processes are described for the vortex ring dynamics at the barrier region: first is that a vortex ring, created at the surface, shrinks inside the weak link; the second process corresponds to a vortex ring generated at the center and expanding with a second vortex generated at the surface and shrinking, thus annihilating the first vortex ring. Fig. 1.6 (c)-(d) shows the 2D phase snapshots at the upper plane $y > 0$ (and for $z = 0$) and at two different times around the first minimum of imbalance, i.e. the first maximum of the velocity. The second vortex ring process is described by Fig. 1.6(c)-(d) where there is a phase-winding around the vortex core in (c) related to the first vortex ring that expands from the center, while in Fig. 1.6(d) a second phase-winding is revealed which corresponds to the second vortex ring which tends to shrink and annihilate the first one.

From these experimental/numerical results one can conclude that dissipative dynamics can thus be related to an emerging vortex propagating along the main axis of the junction while MQST regime can be related to the generation of vortices which annihilate within the weak-link. One of the main goals of this thesis is to investigate in detail the differences between the dissipative and MQST regimes, not only in terms of the population imbalance and relative phase evolution, but also in terms of the vortex dynamics and associated acoustic (sound) emission. This study will be the topic of Chapt. 5.

For completeness, we note that the fast initial decay of the population imbalance in the dissipative regime is a very distinct physical process to the thermal-induced decay of self-trapping state observed in [84] and qualitatively reproduced numerically in [63]. The transition from dissipationless to dissipative superflow is a fundamental topic in its own

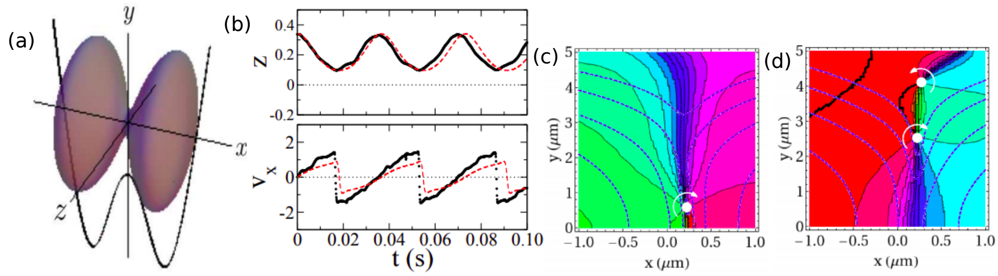

Figure 1.6: M. Abad *et al.* [83]: (a) The spherical Josephson junction geometry. (b) The time evolution of the population imbalance (upper subplot) and the BEC velocity (lower subplot) along x-axis from numerical Gross-Pitaevskii equation (the black lines) and the two mode model results (dashed red lines). (c)-(d) The 2D phase snapshots of the upper plane ($y > 0$) for $z = 0$ at $t = 16.6ms$ (c) and at $t = 17.6ms$ (d). Adapted by permission from EPL.

right, whose understanding and control are central to any potential Josephson junction application to atomtronics.

1.4.1 Analogy with superfluid Helium

In superfluid of ^{4}He, the first phase slippage experiments were performed by Avenel and Varoquaux in 1985 [14], confirming Feynmann and Anderson argument on the phase-slippage induced resistive superflow through an orifice. Subsequent experiments followed which gave further insight into the critical velocity for the onset of such vortex (phase-slippage) induced dissipative phenomena and its dependence on the temperature [85–88]. In this section we give some analogy between the physics of ultracold atoms flowing across a barrier in a Josephson-like junction (considering the experiment of ^{6}Li at LENS in the BEC limit of molecules) and the physics of superfluid helium flowing through an orifice referring to the experiment of Ref. [39], in which the temperature was smaller than superfluid helium transition temperature T_λ. While the experiment of LENS was already introduced previously, here we start by introducing the experiment of Hoskinson *et al.* [39] in ^{4}He. Fig. 1.7 shows their experimental set-up which consists of an inner cylindrical reservoir which is connected to a flexible diaphragm on which a layer of superconducting lead has been evaporated. There is an array of 4225 apertures at the bottom of the inner cell which connects the inner cell to the bath outside the cell. In order to induce a pressure gradient through the array, an electrostatic force is applied between the membrane and the electrode. The motion of the membrane is an indication of the superfluid flow acoss the array of apertures. The superfluid healing length ξ is a function of temperature and for fixed aperture width d the ratio ξ/d changes with temperature. They showed two cases of strong coupling $\xi/d = 0.4$ at low temperatures and $\xi/d = 1.8$ found at a higher temperature, where the two superfluids are weakly linked. In the first case the phase-slippage regime was found, while in the second case the analogue of the Joseph-

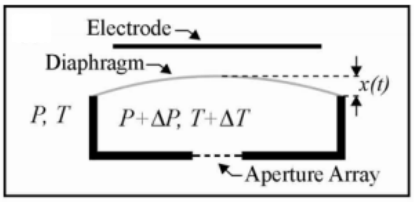

Figure 1.7: E. Hoskinson *et al.* [39]: Schematic figure of the experimental cell, where a pressure or/and a temperature gradient across the array lead to a chemical potential difference. Adapted by permission from Springer Nature: Nature [39] [COPYRIGHT] (2006).

son oscillations regime was observed. In our analogy we focus on the first case of low temperature. According to the Josephson-Anderson relation the relative phase between the two reservoirs depends on the chemical potential difference as $d(\Delta\phi)/dt = -\Delta\mu/\hbar$. In our case of a Josephson junction in a molecular BEC of lithium, the $\Delta\mu$ is induced by an initial population imbalance between the two wells, while in superfluid helium the chemical potential difference can be created by either the presence of a pressure gradient or by the presence of a temperature gradient across the arrays. The first analogy between such systems relates to the similarity of the time evolution of quantities such as the left well population in the case of molecular BEC of lithium and the membrane displacement $x(t)$ in the case of superfluid ^{4}He. Both such quantities are related to the supercurrent across the barrier (in the first case) or across the array of apertures (in the second case). The temporal evolution of $x(t)$ shown in Fig. 1.8(a) is induced by applying a step ΔP across the array which causes the superfluid to move along the positive axis. The time derivative of $x(t)$ is related to the superfluid current as $I = nAdx/dt$, where n, A are the density and the area of the array respectively. The $x(t)$ presents some 'kinks' during its initial short-time evolution (highlighted by a dashed black box) which happens when a vortex crosses the orifice, causing the phase to jump by 2π. Interestingly, similar 'kinks' related to the phase-slippage and vortex generation are also found in the time evolution of the BEC population in the left well $N_L(t)$ (shown in Fig. 1.8(b)), extracted by our numerical simulations, in the Josephson junction of BEC of molecules of lithium. In fact, in Fig. 1.8(b) such 'kinks' are present during the initial time evolution of $N_L(t)$ (shown within the black-dashed box) and thus of the population imbalance $z = 1 - 2N_L/N$ (not shown here), even though they are less pronounced with respect to the 'kinks' present in the $x(t)$ of the membrane in superfluid ^{4}He. Moreover, also the time derivative of the left (or right) well BEC population gives the superfluid current across the barrier. This means that in both cases of superfluid helium and molecular BEC, every time the supercurrent exceeds a critical value, vortices are nucleated, which cause the superfluid phase to slip by 2π and thus the superfluid current to jump sharply. During each phase slippage event the $\Delta\mu$ decreases towards its equilibrium value and, when $\Delta\mu = 0$, the phase-slippage

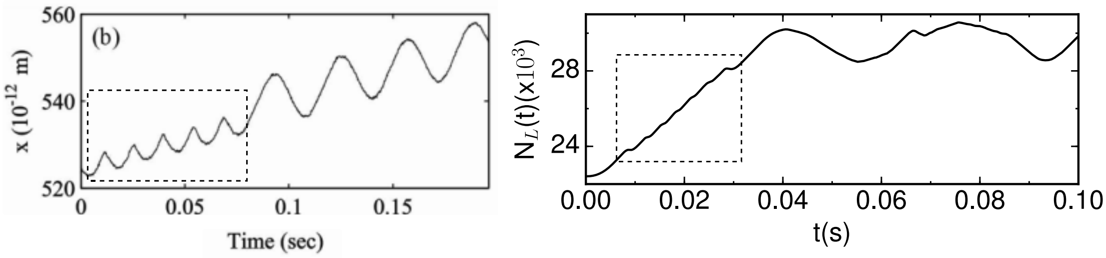

Figure 1.8: (a) Hoskinson *et al.* [39]: Diaphragm position $x(t)$ as a function of time for $T - T_\lambda =$ 7.4 mK, $\xi/d = 0.4$ [39] where ξ is the superfluid healing length and d the aperture diameter. For time evolution until $t \sim 0.07$ s, the oscillations of $x(t)$ are driven by phase-slippage and after that they represent Helmholtz resonator oscillations. Adapted by permission from Springer Nature: Nature [39] [COPYRIGHT] (2006). (b) The left well condensate particle number time evolution extracted from our numerical simulations for an atomic ultracold Josephson junction of ^{6}Li molecular BEC. The black dashed-rectangular highlights the presence of 'kinks' both on the $x(t)$ and $N_L(t)$ revealing the presence of phase-slippage both in superfluid helium and BEC of molecules of lithium.

process ceases. After that, for superfluid ^{4}He the $x(t)$ shows higher amplitude oscillations characteristic of Helmholtz resonance at lower frequency (at $t \simeq 0.07$ s) while for the case of BEC of lithium molecules the population in the left well exhibits harmonic oscillations around $N_L = N/2$ from which can be extracted the population imbalance z, this performs oscillations around a zero mean value with the Josephson 'plasma' frequency and higher frequency modes.

The second analogy is related to the profile of the superfluid velocity following its phase slippage event. Driven by the chemical potential difference, induced by a pressure gradient for superfluid ^{4}He or by a population imbalance for molecular BEC of lithium, the superfluid accelerates along the array or the barrier until its maximum velocity exceeds a critical value and a vortex is generated. The vortex induced phase-slippage causes the superfluid velocity to jump by a quantised quantity $\varDelta v$ as the superfluid velocity is obtained by the phase gradient as $\mathbf{v} = (\hbar/m)\nabla\phi$. This process is schematized in Fig. 1.9(a) for the case of superfluid ^{4}He but it was first observed experimentally in Ref. [14]. For the case of lithium, we calculated numerically the density-weighted superfluid velocity along the radial plane at the barrier center $\langle v_x \rangle$ as shown in Fig. 1.9(b). The velocity jump $\varDelta v$ is less abrupt in the case of lithium due to the initial persistence of the vortex within the barrier region and it will be analysed in detail in Chap 3.

If there is still a $\varDelta\mu$ present in the system, then superfluid velocity is accelerated again and another vortex is generated at the aperture or the barrier which causes the superfluid phase to slip and thus its velocity to jump again by $\varDelta v$. This gives rise to a 'sawtooth-like' profile of v. The rate of phase slippage is given by $\nu_{\mathrm{slip}} = \varDelta\mu/\hbar$ following the Josephson-Anderson relation. In the case of helium, Fig. 1.9(a) [right plot] shows that, as the critical velocity for vortex-generation becomes smaller at higher T and, following a phase-slippage event, the superfluid velocity can even reverse its sign, i.e. its direction, if the velocity jump Δv (which is independent of T) is larger than v_c. In the case of lithium, the results shown are at $T = 0$ (in Fig. 1.9(b)) but even in that case we observe that after the first phase slippage events the superfluid velocity becomes slightly negative leading to flow reversal (i.e. backflow). Apart from similarities, there are also differences such as the fact that Δv is the same for all the phase slippage event in helium but in the case of lithium the first Δv is larger with respect to the others (as will be described in Chapt. 3).

E. Hoskinson *et al.* [39] showed also the current-phase relation, where the current extracted by the time derivative of the membrane displacement was also corrected for the presence of a small normal flow component and the phase difference was extracted by the time integration of the chemical potential difference. They showed that in this low temperature phase-slippage regime the current-phase relation is multivalued differently from our three dimensional Josephson junction with a barrier width $w/\xi = 4$ (with ξ the superfluid healing length) when the current-phase relation in the vortex-induced phase-slippage regime (that we call the dissipative regime) is single-valued and has a sinusoidal profile. Similar multivalued current-phase relations were found by F. Piazza *et al.* [89], in the study of a Bose-Einstein condensate flowing through a repulsive square barrier in a one-dimensional geometry, for barrier widths much larger than the BEC healing length and barrier height much smaller than the chemical potential.

1.5 Role of the thermal cloud

Ultracold atom experiments with Bose gases are performed at a non-zero temperature below the critical temperature, where a condensate co-exists with a cloud of non-condensed particles. Such non-condensed particles are collectively termed as the thermal cloud. Experimentally, the total particle density is usually measured and typically the total number of particles N_{tot} is kept fixed (within the experimental uncertainities) in the study at different temperatures. For fixed N_{tot}, in three dimensional ultradilute systems where the quantum depletion effect is negligible, at $T = 0$ we can practically consider all the particles to be in the condensate state while at a finite temperature the system is partly condensed; the condensate density at the trap center is then reduced and due to the repulsive interactions between the condensate and thermal cloud (for positive scattering length), the non-condensed particles are concentrated at the edges of the condensate and the total density is characterised by broader tails with respect to the zero temperature. Moreover, in the geometry of double-well potential studied throughtout this thesis, the thermal cloud density has a local peak even at the barrier position where the condensate density has a local minima. In ultracold bosonic atom experiments it was shown that the presence of the thermal cloud plays an important role on the damping and the frequency shifts of the

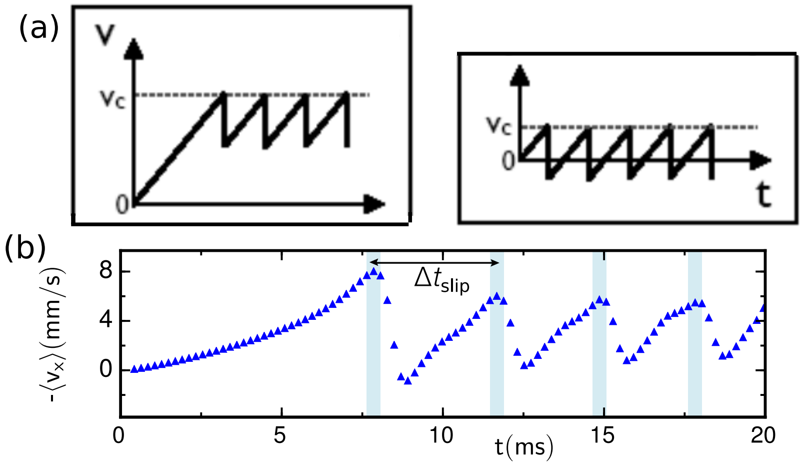

Figure 1.9: (a) Hoskinson *et al.* [39]: Schematic of the ^{4}He superfluid velocity v temporal profile which initially accelerates until it reaches a critical value v_c and a vortex is nucleated causing the superfluid velocity to drop adruptly by a quantised quantity Δv. The vortex generation is repeated with a rate given by the Josephson-Anderson relation and it gives rise to a sawtooth profile. In the right subplot, corresponding to higher temperature, the critical velocity is such that after the vortex generation the superfluid velocity reverses even its direction. Figure adapted by permission from Springer Nature: Nature [39] [COPYRIGHT] (2006). (b) Density-weighted x-component of the molecular BEC velocity at the barrier [90]. Vertical shaded blue areas denote the maxima of superfluid velocity when VRs are generated. In the figure is also shown the phase-slippage period $\Delta t_{\text{slip}} = 1/\nu_{\text{slip}} = h/\Delta\mu$.

condensate collective excitations in [91–95] or in the dissipative dynamics of topological defects such as solitons [96], vortex lines [97], vortex lattices [98] or vortex-pairs [99]. Many theoretical studies were perfomed on characterising the influence of the thermal cloud on the damping of collective modes [100–109], on the energy dissipation of topological defects [110–117] and on the defect formation, studied both experimentally and theoretically in [118–124]. Moreover the interaction between the thermal cloud and condensate is of fundamental role on the thermalization as shown both experimentally and theoretically in [125–135]. Modelling the dynamics of Bose gases at finite temperature requires the description not only of the dynamics of the condensate atoms but also the description of the dynamics of the non-condensate cloud. A full theoretical model would then include not only the mean-field coupling between the condensate and non-condensed atoms but also the collisions between the two clouds which result in particle exchange and also the collisions between thermal particles.

The theoretical model we are using in this thesis is the ‘Zaremba-Nikuni-Griffin’ model (known also as ZNG model), which was first implemented by Zaremba, Nikuni and Griffin [26–28] (based on the previous work by Kirkpatrick and Dorfman [136–138]). Such model fully takes into account both the dynamics of the condensate (described by a dissipative Gross-Pitaevskii equation) and of the thermal cloud (described by a Quantum

Boltzmann equation) in a self-consistent way. The ZNG model is valid for temperatures T far enough from the critical temperature T_c, both for temperature smaller (typically for temperatures up to $0.8 - 0.9T_c$ [139]) and larger than T_c (when it reduces to the kinetic Boltzmann equation). This also means that the ZNG model can not be used to describe spontaneous defect formation or the Kibble-Zurek mechanism ([118–123]) which happens near the critical temperature as it is a symmetry-breaking model. It has been successfully implemented to describe three-dimensional homogeneous and inhomogeneous Bose gas experiments, being in very good agreeement with experimental data on predicting the collective excitations frequency and damping and explaining the dynamics of topological defects.

One of the advantageous of using the ZNG model is the fact that it takes into account the full dynamics of the thermal cloud, which are only approximately included in other methods such as the 'classical field method' [140, 141, 139, 142–144]. In Ref. [135] a comprehensive description of finite temperature theoretical models, such as classical field methods and stochastic methods, is given. We must note that the ZNG model is not valid in two-dimensional systems where the stochastic methods can be used instead [145, 146, 143, 144, 139]. While a more detailed description of the ZNG model will be given in Chapt. 2, here we briefly describe the collisionless and collisional regime and its successful description of experimental results.

Depending on the collision rate or collision mean free path, two different regimes can be obtained: the collisionless regime where the mean-field effects dominate, and the collisional (or hydrodynamic) regime where collisional effects dominate instead. In the collisionless regime the collision time is much larger than the period of collective modes. In such a regime, the collisions can be treated perturbatively. In fact, to lowest approximation, the effect of collisions could be ignored. Moreover, the Landau damping mechanism (that originates from the interaction of a thermal excitation with the collective condensate excitations , with the thermal excitation being transfered to higher energy modes) and Beliaev damping (that is due to the creation of two thermal excitations by the absorption of a quantum of condensate collective oscillation) terms are already included within the collisionless ZNG. Moreover, it also includes the mutual 'dragging' between the condensate and thermal cloud. However, a complete description of the system would require the explicit treatment of collisions, which for example enhance the damping of collective modes or take into account the particle exchange between the two subsystems.

Many ultracold atoms experiments are in the collisionless limit due to their low density (differently from helium) and the ZNG collisionless limit gives results that are in quantitative agreement with the observed temperature-dependent frequency and damping of the many kinds of collective modes that can be excited in ultracold Bose gases. In the collisional, or hydrodynamic, regime instead the collisions between thermal particles are very frequent; the system enters into a state of local hydrodynamic equilibrium [28] and it can be thus described in terms of few local (dependent on position and time) hydrodynamic variables such as the chemical potential, the local density, the temperature, the velocity and the pressure. The presence of collisions is essential when describing the condensate growth [134] from a partially condensed initial state and the ZNG model can even give an accurate description of the condensate growth once a small condensate seed is present, but the Stochastic Gross-Pitaevskii equation SGPE is much better suited to this. Furthermore, it can be demonstrated [28] that the collisional ZNG model leads to the two-fluid model which was fistly derived for superfluid ^{4}He (characterised by high density and thus very frequent collisions). Few experiments have been performed in the collisional limit or crossover [96, 147].

An important test of the validity of a theoretical model describing finite temperature Bose gases is its ability to reproduce the dipole modes, that are also known as Kohn modes [148]. In order to excite the dipole mode, the condensate and the thermal cloud are initially shifted in opposite direction with respect to each other (by e.g. one harmonic oscillator length) and then the two subsystems start an oscillation out of phase, damping each other's oscillation. However the total center of mass, which is decoupled from the internal degrees of freedom, exhibits undamped oscillations at the trap frequency independent of the temperature of the system. The success of the ZNG model stands in its ability to describe both collisionless experiments and to reduce to the two-fluid model of ^{4}He in the collisional limit [27, 26, 149–152]. In describing ultracold atoms experiments, the collisionless ZNG model found excellent agreement with experimental data in the prediction of the collective mode frequencies and damping values [153, 105]; in describing theoretically the dissipative dynamics of macroscopic excitations where in the study of dark solitons in [110] the authors numerically reproduced the stages of the decay of dark solitons observed experimentally in Ref. [96] and in the study of the dynamics of vortex lines at finite temperature in [112, 115], the papers reproduce experimental findings [97, 98, 154, 155]. In the context of vortices, the thermal cloud becomes 'trapped' at the vortex core; some examples of the condensate and thermal cloud density in the presence of a vortex ring are shown in Fig. 1.10 for our case of a three-dimensional Josephson junction. The condensate density is minimum at the vortex core while the thermal density achieves its local maxima and it surrounds the condensate density. Recently the ZNG model was generalized to two component Bose gases in [156–158].

Given the success of the collisionless ZNG model in predicting condensate collective mode frequencies and damping rates, our study in Chapt. 6 on the oscillation frequencies of the condensate population imbalance, characterising the dynamics of the condensate flowing through a barrier in a three-dimensional elongated Josephson junction, is performed mostly in the collisionless limit. For completeness the effect of collisions is also

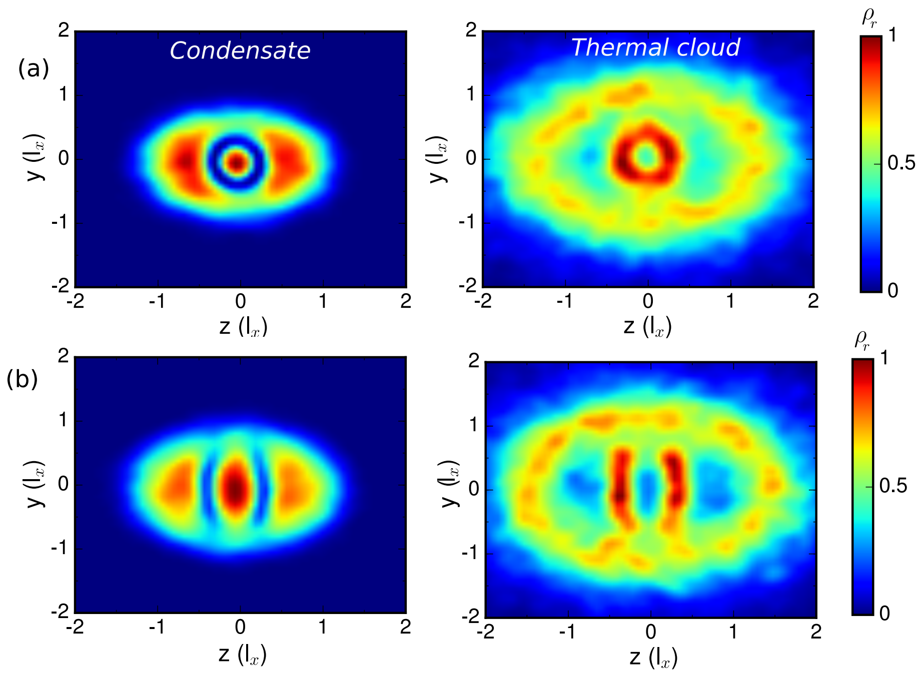

Figure 1.10: Density profile along the transverse yz plane at the x axis vortex position of the condensate (left subplot) and thermal cloud (right subplot) in an elongated three-dimensional Josephson junction (with x axis the long axes) for barrier height $V_0 = 67.2\hbar\omega_x \simeq 0.6\mu$ (a) and for $V_0 = 46\hbar\omega_x \simeq 0.4\mu$ (b). The numerical data are for initial imbalance larger than a critical value for the onset of the dissipative regime and at temperature T$\simeq 0.53T_c$. The axis values are scaled to the harmonic oscillator length along x axis, $l_x = 7.5\mu$m. The density in each plot is rescaled to the maximum density.

considered, but not to such extent as the collisionless study. Our numerical simulations in the collisionless limit found very good agreeement with the experimental data (for the experimental low temperature $T \simeq 0.3T_c$) as shown in Chap. 4 and in Ref. [90]. By using the ZNG model in the collisionless limit, we also qualitatively explained the experimental observation of off-center vortices showing that the presence of the thermal cloud, even though a small fraction of the total atom number, drifts the vortex ring off-center making it decay into single long off-center vortex line when the vortex ring approaches the boundary. The study of the effect of the thermal cloud on the BEC dynamics in a 3D Josephson-like junction, in particular on the decay of the Macroscopic Quantum Self-trapping, was also performed in Ref. [63] where they used the stochastic Gross-Pitaevskii equation where the system wavefunction is split into low energy and highly occupied modes and much less occupied high energy modes.

1.6 Thesis overview and collaborations

Here, we briefly describe the main topics in the rest of this thesis and highlight the contribution of our collaborators.

Chapt. 2: Theoretical model describing ultracold bosonic Josephson junction

In Chapt. 2 we introduce the theoretical models at zero and finite temperature we use to study the transport properties of a Bose-Einstein condensate across a barrier in a three-dimensional Josephson junction. This chapter starts with the introduction of the the Gross-Pitaevskii equation which models the dynamics of BEC at zero temperature. Then we introduce the concept of critical velocity in a superfluid by following the Landau and Feynman argument. This is followed by a brief description of some of the properties of topological defects in general and of vortex rings in particular. Subsequently, we focus on the two-mode model [59, 61] and on a microscopic description based on the tunneling Hamiltonian [65] of the dynamics of two-weakly coupled BECs. In order to describe the BEC at finite temperature we use the 'Zaremba-Nikuni-Griffin' model which solves the dissipative Gross-Pitaevskii (describing the condensate) and the quantum Boltzmann equation (describing the thermal cloud) self-consistently [28, 26, 27].

Part II : Dynamical regimes and vortex dynamics in an atomic Josephson-Junction

In Chapt. 3 we show our numerical results on the study of the dynamical regimes for the experimental parameters of ^{6}Li experiment at LENS in Florence [49, 20], which we model in the limit of Bose-Einstein condensates of molecules of lithium. For the experimental range of parameters the Josephson 'plasma' and dissipative regime are found. We extract the critical parameters such as critical imbalance and critical current defining the transition from dissipationless to dissipative regime. Our study is done mainly in the dissipative regime where vortex rings are generated. We show that the vortex ring nucleation causes the condensate relative phase to jump locally by 2π and that the condensate velocity exhibits 'sawtooth-like profile' similar to the mechanism of phase-slippage found in superfluid helium. We then give a detailed description of the vortex ring dynamics and its connection to macroscopic quantities such as population imbalance and superfluid current. Further insight into the dissipation mechanism is also given by the study of two of the components of the kinetic energy; the incompressible kinetic energy E_k^i, and the compressible kinetic energy E_k^c. We show that the dissipation originates not only from the kinetic energy transfer from the superfluid flow to the swirling velocity of the nucleated vortex rings but also from the phonon emission arising during vortex ring early stage dynamics.

In Chapt. 4 we show the direct comparison between our numerical simulations and experimental results from ^{6}Li experiments in the BEC limit. We find very good agreement with the experimental data not only on the value of the critical imbalance and current, but also in the dynamics of the population imbalance both in the Josephson 'plasma' and dissipative regime at small temperature by using the ZNG model in the collisionless limit. Moreover, we show that the experimental protocol of barrier removal is an efficient method for producing vortices with longer lifetime and larger radius than the case when the barrier is kept on, such that they can be experimentally observed. The thermal fraction in the experiment is small and it does not have any significant effect on the population imbalance dynamics but we show that it strongly influences the post-generation vortex ring dynamics.

The main results of Chapt. 3 and Chapt. 4 are included in the paper:
'Critical Transport and Vortex Dynamics in a Thin Atomic Josephson Junction'
K. Xhani, E. Neri, L. Galantucci, F. Scazza, A. Burchianti, K.-L. Lee, C.F. Barenghi, A. Trombettoni, M. Inguscio, M. Zaccanti, G. Roati, and N.P. Proukakis
Phys. Rev. Lett. 124, 045301 (2020)

and in the review *'State of the art and perspective on Atomtronics'* submitted to AVS, in the section:
'Phase Slips Dynamics Across Josephson Junctions'
A. Minguzzi, A. Perez-Obiol, J. Polo, N. Proukakis, **K. Xhani**
arXiv:2008.04439

Part III : Beyond the experiment

In Chapt. 5 we give the full phase-diagram for a three dimensional Josephson junction exploring barrier heights and widths beyond the experimental parameters. We show that even in the elongated trap geometry, where only the Josephson 'plasma' and dissipative regimes were observed experimentally [49, 20], the Macroscopic Quantum Self-Trapping regime (predicted by Smerzi *et al.* [59]) can be achieved for larger barrier widths, or larger barrier heights with respect to the parameters explored in the experiments [49, 20]. We then show the full phase diagram by characterising the three regimes; Josephson 'plasma', dissipative and MQST regimes. The role of the vortex ring dynamics and phonon modes on the transition from the dissipative to MQST regime is also shown. We also consider the case of the spherical trap where only the MQST regime was found [83] and show that a dissipative regime can be found where there are generated vortex rings which can eventually propagate into the superfluid. Our work shows that all the three dynamical regimes can be found for general three-dimensional geometry.

Part of this chapter results are included in the paper :
'Dynamical Phase Diagram of Ultracold Josephson Junctions'
K. Xhani, L. Galantucci, C. F. Barenghi, G. Roati, A. Trombettoni, N. P. Proukakis
New J. Phys. 22, 123006 (2020)

Part IV : Finite temperature effects

In Chapt. 6 we analyse the oscillation frequencies and damping rates of the condensate, thermal and total population imbalance as a function of the temperature with our analysis focused mainly on the collisionless regime. In the Josephson 'plasma' and in the dissipative regimes we show that at low temperature the thermal cloud follows the condensate while at high temperature the thermal cloud has its own motion over the barrier (for $k_B T \gtrsim V_0$) and thus 'drives' the condensate. Moreover in the limit of high temperature, where the thermal cloud has a significant contribution to the total imbalance, the latter exhibits beating and damping. The MQST regime is also studied (to lesser extent) and is found to be highly unstable against the thermal cloud, with the results even somewhat dependent on each individual stochastic realization. The effect of collisions on the main component of the condensate and the total imbalance is also shown. We also discuss the effect of the thermal cloud on the vortex ring nucleation and dynamics both in the collisionless and collisional limit.

Results presented in this chapter are included in the draft manuscript:
'Dissipation in a Finite Temperature Atomic Josephson Junction'
K. Xhani and N. P. Proukakis (in preparation).
intended for submission on Phys. Rev. A.

Studies in Chapt. 3 and 4 –already published in Phys. Rev. Lett. 124, 045301 (2020)– have been achieved in collaboration with my supervisor N. P. Proukakis and with contribution from theorists L. Galantucci, K. -L. Lee and C. F. Barenghi (Newcastle) and A. Trombettoni (SISSA, Trieste) and the experimental group at LENS: G. Roati, F. Scazza, M. Zaccanti, E. Neri, A. Burchianti and M. Inguscio. In particular, tracking of the vortex ring dynamics and the decomposition of the kinetic energy components are obtained by using the codes written by L. Galantucci and the results at finite temperature are achieved by using the code written by Kean Loon Lee. Both codes were adapted for our geometry and parameters. Moreover L. Galantucci and C. F. Barenghi have significantly contributed to the undertanding of the vortex ring dynamics in such an inhomogeous 3D constricted superfluids and on the investigation of the origin of dissipation of Josephson oscillations; M. Zaccanti provided his calculation of the second order term in the current-phase relation for our trap [159] based on the paper of Ref. [65] and contributed on its interpretation; A. Trombettoni contributed to the interpretation of the validity of two-mode model. The experimental group lead by G. Roati contributed by sharing their experimental results and helping with interpretations through fruitful discussions. In particular, we are thankful to G. Roati for his support during the second part of my PhD in Florence, being so in close contact with his group and to F. Scazza for his help on the editing of the main figures of our paper Phys. Rev. Lett. 124, 045301.

Chapt. 5 includes studies in collaboration with L. Galantucci, C. F. Barenghi, G. Roati, A. Trombettoni and with my supervisor N. P. Proukakis and these studies have been recently published in the paper 'Dynamical Phase Diagram of Ultracold Josephson Junctions', New J. Phys. 22 123006 (2020). In particular, L. Galantucci provided us his calculations on the vortex ring kinetic energy; A. Trombettoni contributed to the analogy with type II superconductors; G. Roati and C. F. Barenghi contributed to the physics interpretations.

The final part of this thesis is Chapt. 6, with results that are being included in the paper in preparation 'Dissipation in a Finite Temperature Atomic Josephson Junction'; this was done in collaboration with my supervisor. An important contribution to achieving the finite temperature results was done by Kean Loon Lee by sharing his code.

Chapter 2

Modeling an ultracold bosonic Josephson junction

2.1 Theoretical description of finite temperature Bose-Einstein condensates

Experiments are performed at finite temperature where the condensate cloud co-exists with a non-condensate part. A complete theory must take into account not only the mean-field interaction between the condensate and thermal cloud but also the coupling deriving from collisions between the condensate and thermal atoms and also between thermal particles which gives rise to a redistribution of particles within the thermal cloud. In the limit of dilute weakly interacting Bose-gases, such that the 'diluteness parameter' $na^3 \ll 1$, where n is the gas density and a the atomic s-wave scattering length, the binary collisions between two atoms dominate and thus a system composed of N bosons can be described by the Hamiltonian ([28, 135]):

$$\hat{H} = \sum_{i=1}^{N} \hat{H}_0(\mathbf{r}_i) + \frac{1}{2} \sum_{i,j=1}^{N} \hat{V}(\mathbf{r}_i, \mathbf{r}_j). \tag{2.1}$$

Here $\hat{H}_0(\mathbf{r}_i)$ is the single-particle Hamiltonian while $\hat{V}$ is the two-body interaction potential and the factor 1/2 is added in order for the interactions between a pair of atoms to be counted once. The Bose gas evolution is described by the N-body wavefunction $\psi(\mathbf{r}_1...\mathbf{r}_N, t)$ which satisfies the Schrödinger equation:

$$i\hbar \frac{\partial}{\partial t} \psi(\mathbf{r}_1...\mathbf{r}_N, t) = \hat{H} \psi(\mathbf{r}_1...\mathbf{r}_N, t). \tag{2.2}$$

This equation is difficult to be solved directly for a large number of particles as it requires to track each particle at each individual position and each energy level. Thus, instead of using the 'first-quantized' coordinate representation Eq. (2.2) a different approach is used, which consists of expanding the system wavefunction in the 'occupation number' basis $|n_1 ... n_\infty\rangle$ and it is called 'second quantization' approach. This new representation consists of writing the wavefunction as the sum $\sum_{n_1..n_\infty} c(n_1...n_\infty)|n_1...n_\infty\rangle$, where $c(n_1...n_\infty)$ are the expansion coefficients with n_j the number of particles in each state with energy ϵ_j. The expansion coefficients are normalized such that the probability to find the particle somewhere is one, and they are symmetric under the exchange of two quantum numbers. Even though this basis is infinite, for a bosonic system of fixed total particle number N there are a maximum of N-states populated while the others are not occupied. The expansion coefficients describe the process of particles moving within the accessible energetic states. Such processes can be described in terms of the single-particle annihilation, $\hat{a}_i$ and creation $\hat{a}_j^\dagger$ quantum operators, which describe the destruction of a particle in state $|i\rangle$ and the creation of a particle in state $|j\rangle$. The single-particle annihilation and creation operators satisfy the bosonic commutation rules. However, in the occupation number representation a linear combination of single-particle operators is used instead, defined as

$$\begin{aligned} \hat{\Psi}(\mathbf{r},t) &= \sum_i \hat{a}_i(t)\phi_i(\mathbf{r},t), \\ \hat{\Psi}^\dagger(\mathbf{r},t) &= \sum_i \hat{a}_i^\dagger(t)\phi_i^*(\mathbf{r},t), \end{aligned} \tag{2.3}$$

where the sum is over all single-particle states. The operators $\hat{\Psi}(\mathbf{r},t)$ and $\hat{\Psi}^\dagger(\mathbf{r},t)$ are termed 'field' operators and they are the annihilation and creation operators respectively for a particle at the position $\mathbf{r}$ at time t. These operators satisfy the commutation relations for bosons

$$\left[\hat{\Psi}(\mathbf{r},t), \hat{\Psi}^\dagger(\mathbf{r}',t)\right] = \delta(\mathbf{r}-\mathbf{r}'), \tag{2.4}$$

$$\left[\hat{\Psi}(\mathbf{r},t), \hat{\Psi}(\mathbf{r}',t)\right] = 0, \tag{2.5}$$

$$\left[\hat{\Psi}^\dagger(\mathbf{r},t), \hat{\Psi}^\dagger(\mathbf{r}',t)\right] = 0. \tag{2.6}$$

The transition from the coordinate to the occupation number representation is obtained by the following transformation of Eq. (2.1):

$$\sum_{i=1}^{N} \hat{H}_0(\mathbf{r}_i) \rightarrow \int d\mathbf{r} \hat{\Psi}^\dagger(\mathbf{r},t)\hat{H}_0\hat{\Psi}(\mathbf{r},t), \tag{2.7}$$

and

$$\sum_{i,j=1}^{N} \hat{V}(\mathbf{r}_i, \mathbf{r}_j) \to \int\int d\mathbf{r} d\mathbf{r}' \hat{\Psi}^\dagger(\mathbf{r}, t)\hat{\Psi}^\dagger(\mathbf{r}', t) V(\mathbf{r} - \mathbf{r}')\hat{\Psi}(\mathbf{r}', t)\hat{\Psi}(\mathbf{r}, t). \tag{2.8}$$

The single-particle operator $\hat{H}_0$ is the sum of the kinetic operator $-\hbar^2\nabla^2/2m$, with m being the particle mass, and the external trapping potential $V_{\text{ext}}(\mathbf{r})$: the latter is an harmonic potential in many ultracold atoms experiments. Thus the system total Hamiltonian can be written as

$$\begin{aligned} \hat{H} = &\int d\mathbf{r} \hat{\Psi}^\dagger(\mathbf{r}, t) \left[-\frac{\hbar^2}{2m}\nabla^2 + V_{\text{ext}}(\mathbf{r}) \right] \hat{\Psi}(\mathbf{r}, t) \\ &+ \frac{1}{2} \int\int d\mathbf{r} d\mathbf{r}' \hat{\Psi}^\dagger(\mathbf{r}, t)\hat{\Psi}^\dagger(\mathbf{r}', t) V(\mathbf{r} - \mathbf{r}')\hat{\Psi}(\mathbf{r}', t)\hat{\Psi}(\mathbf{r}, t), \end{aligned} \tag{2.9}$$

which takes into account both thermal and quantum fluctuations.

The interaction term 2.8 involves two particle states which after colliding are redistributed between two new particle states. In the limit of dilute Bose gases, and for low temperatures such that only elastic s-wave scattering between atoms is considered, the interaction potential has a contact-like form $V(\mathbf{r} - \mathbf{r}') = g\delta(\mathbf{r} - \mathbf{r}')$ where $g = 4\pi\hbar^2 a/m$ is the effective interaction strength. In Eq. 2.1 describing the time evolution of the system, the time dependence comes in the state vector, while the operators are time-independent: this is called the 'Schrödinger picture'. However here we follow the Heisenberg picture, in which the time dependence appears in the operators while the state vectors are time-independent.

The system dynamics is then described by the Heisenberg equation of motion for the field operator $\hat{\Psi}(\mathbf{r}, t)$:

$$i\hbar \frac{\partial}{\partial t} \hat{\Psi}(\mathbf{r}, t) = \left[\hat{\Psi}(\mathbf{r}, t), \hat{H} \right]. \tag{2.10}$$

After substituting the second-quantizated Hamiltonian in the above Heisenberg equation of motion we obtain:

$$i\hbar \frac{\partial \hat{\Psi}(\mathbf{r}, t)}{\partial t} = \left[-\frac{\hbar^2}{2m}\nabla^2 + V_{\text{ext}}(\mathbf{r}) + g\hat{\Psi}^\dagger(\mathbf{r}, t)\hat{\Psi}(\mathbf{r}, t) \right] \hat{\Psi}(\mathbf{r}, t). \tag{2.11}$$

In a Bose-Einstein condensate the lowest energy state ϕ_0 becomes macroscopically occupied with its occupation number $n_0 \equiv N_0 \gg 1$ and the Bose-field operator can be written as the sum of two terms

$$\hat{\Psi}(\mathbf{r}, t) = \hat{\psi}(\mathbf{r}, t) + \hat{\delta}(\mathbf{r}, t), \tag{2.12}$$

with the first one being the field operator for the condensate (corresponding to the annihilation operator for atoms in the condensate state) and the second one is the fluctuation operator. This separation is equivalent to the separation of zero-momentum modes for

BEC in a homogeneous system [28]. The operator $\hat{\delta}$ can include thermal atoms or quantum fluctuations or atoms in higher energy states due to interactions. The two operators can be expressed in a basis $\{\phi_0, \phi_i\}$ as $\hat{\psi}(\mathbf{r}, t) = \hat{a}_0(t)\phi_0(\mathbf{r}, t)$ and $\hat{\delta}(\mathbf{r}, t) = \sum_{j\neq 0} \hat{a}_j(t)\phi_j(\mathbf{r}, t)$. The number of particles in the condensate state is found by the action of the operator number $\hat{N}_0 = \hat{a}_0^\dagger \hat{a}_0$ on the condensate state with N_0 particles, i.e. $\hat{N}_0|N_0\rangle = N_0|N_0\rangle$. Knowing that $(1/N_0)(\hat{a}_0\hat{a}_0^\dagger - \hat{a}_0^\dagger\hat{a}_0)|N_0\rangle = (1/N_0)|N_0\rangle$ in the limit of large condensate number the $1/N_0 \longrightarrow 0$ and thus the annihilation and creation single-particle operator can be considered approximately as commuting. Thus one can make the Bogoliubov approximation [160] and substitute $\hat{a}_0$ with $\sqrt{N_0}$. The condensate operator in Eq. (2.12) is then replaced by $\sqrt{N_0}\phi_0(\mathbf{r}, t)$ which we call $\psi(\mathbf{r}, t)$ and thus

$$\hat{\Psi}(\mathbf{r}, t) = \psi(\mathbf{r}, t) + \hat{\delta}(\mathbf{r}, t). \tag{2.13}$$

Here, $\psi(\mathbf{r}, t)$ is termed the condensate wavefunction. By making this decomposition the condensate wavefunction has a fixed phase, which 'breaks' the symmetry of the Hamiltonian, which itself is invariant under a gauge trasformation in the phase of the Bose-field operator as it depends on equal number of annihilation and creation operators 2.9. As the phase and the total particle number are canonically conjugated variables, the symmetry breaking leads to the non-conservation of the total number of particles. However, this approach is good in the limit of large particle number. The condensate state is thus described by a classical field whose value is given by the ensemble average of the Bose-field operator, i.e. $\psi(\mathbf{r}, t) = \langle\hat{\Psi}(\mathbf{r}, t)\rangle$. We must note that even though we identify $\psi(\mathbf{r}, t)$ as the condensate state this can include also system excitations as long as their occupation number is large, i.e. $n_j \gg 1$. The fluctuation operator, also called the non-condensate operator, is instead taken to have a zero average value $\langle\hat{\delta}(\mathbf{r}, t)\rangle = 0$. It arises in general due to both quantum and thermal fluctuations. In 3D systems and even at $T = 0$ the quantum depletion is proportional to the square root of the 'diluteness parameter' $\sqrt{na^3}$ [34] which in ultracold atom experiments takes a small value and thus in 3D systems (which is the case we study in all this thesis) the fluctuation operator can be identified with the thermal cloud operator. We also note that in lower dimension geometries the quantum fluctuations can become important and new physics is found [161].

2.1.1 The limit of zero temperature: Gross-Pitaevskii equation

In the limit of zero temperature, all the particles occupied the condensate state which becomes macroscopic. Ignoring the fluctuation operators and altogether taking the ensemble average of Eq. 2.11, we obtain the well-known Gross-Pitaevskii equation (GPE) [162–164]:

$$i\hbar\frac{\partial\psi(\mathbf{r}, t)}{\partial t} = \left[-\frac{\hbar^2}{2m}\nabla^2 + V_{\text{ext}}(\mathbf{r}) + g|\psi(\mathbf{r}, t)|^2\right]\psi(\mathbf{r}, t). \tag{2.14}$$

Due to the presence of the nonlinear interaction term $g|\psi(\mathbf{r},t)|^2$ this equation is also called the non-linear Schrödinger equation. In ultracold atomic experiments with fermions, thanks to the presence of the Feshbach resonance (described in Sect. 2.2), at certain values of the magnetic field (called BEC limit of the Feshbach resonance) atom pairs tightly bind together and form molecules; for temperatures lower than a critical one these molecules exhibits Bose-Einstein condensation (see Sect. 2.2 for more details). The dynamics of molecular BEC is still described by the GPE with the only difference that the molecular scattering length is $a_M \simeq 0.6a$ [165] and the atomic mass m is substituted by the molecular mass $M = 2m$.

The equilibrium solution and the Thomas-Fermi approximation

The equilibrium state is found by the substitution of $\psi(\mathbf{r},t) = \mathrm{e}^{-i\mu t}\psi(\mathbf{r})$ in the GPE, where μ is the chemical potential, related to the energy cost for adding or removing a particle from the condensate. For temperature smaller than the critical temperature for condensation, the chemical potential is equal to the ground-state energy to within terms of order $k_B T/N$ that are small for large N [1]. The ground state wavefunction $\psi(\mathbf{r})$ then satisfies the so-called time-independent GPE:

$$\left[-\frac{\hbar^2}{2m}\nabla^2 + V_{\mathrm{ext}}(\mathbf{r}) + g|\psi(\mathbf{r})|^2\right]\psi(\mathbf{r}) = \mu\psi(\mathbf{r}). \tag{2.15}$$

In the limit of a large number of particles and for repulsive interaction, the nonlinear term dominates over the kinetic energy term [166]. In this limit and in the regime $\mu \geq V_{\mathrm{ext}}(\mathbf{r})$, the equilibrium condensate density is given by:

$$n_{\mathrm{BEC}}(\mathbf{r}) = |\psi(\mathbf{r})|^2 = \max\left\{\frac{\mu - \mathrm{V}_{\mathrm{ext}}(\mathbf{r})}{\mathrm{g}}, 0\right\}. \tag{2.16}$$

This is called the Thomas-Fermi approximation. Ultracold atoms are often confined in a harmonic trap potential

$$V_{\mathrm{ext}}(\mathbf{r}) = \frac{1}{2}m(\omega_x^2 x^2 + \omega_y^2 y^2 + \omega_z^2 z^2). \tag{2.17}$$

In that case, the ground state density has the shape of an inverted parabola and the half-condensate size along the x direction, i.e. the characteristic length over which the condensate density reaches zero is given by the Thomas-Fermi radius, $R_{\mathrm{TF}} = \sqrt{2\mu/(m\omega_x^2)}$.

For a molecular BEC the atom mass in the external potential and Eq. (2.15) must be replaced by the molecule mass $M = 2m$ and, in the Thomas-Fermi approximation, the molecular chemical potential is expressed by the formula:

$$\mu = \frac{1}{2}\hbar\bar{\omega}\left(\frac{15Na_M}{\bar{d}}\right)^{2/5}, \tag{2.18}$$

where $\bar{\omega}$ is the geometric mean of the trap frequencies, N is the total molecule number and $\bar{d} = \sqrt{\hbar/M\bar{\omega}}$ is the geometric mean harmonic oscillator length.

The hydrodynamic equations

The condensate wavefunction, which is a complex quantity, can be expressed as $\psi(\mathbf{r}, t) = \sqrt{n_{\mathrm{BEC}}(\mathbf{r}, t)}\mathrm{e}^{i\phi(\mathbf{r},t)}$ (the Madelung Transformation), with ϕ being the condensate phase. After substituting the wavefunction in the GPE equation (Eq. (2.14)) and taking into account that the superfluid velocity is $\mathbf{v}_{\mathrm{BEC}}(\mathbf{r}, t) = \frac{\hbar}{m}\nabla\phi(\mathbf{r}, t)$, the continuity equation and the Euler equation for a classical inviscid flow are obtained:

$$\frac{\partial n_{\mathrm{BEC}}}{\partial t} + \nabla \cdot (n_{\mathrm{BEC}}\mathbf{v}_{\mathrm{BEC}}) = 0 \tag{2.19}$$

and

$$m\frac{d\mathbf{v}_{\mathrm{BEC}}}{dt} = m\left(\frac{\partial}{\partial t} + \mathbf{v}\cdot\nabla\right)\mathbf{v} = -\nabla\mu_0(\mathbf{r}, t), \tag{2.20}$$

with μ_0 being the time-dependent chemical potential at $T = 0$ defined as:

$$\mu_0 = -\frac{\hbar^2}{2m\sqrt{n_{\mathrm{BEC}}(\mathbf{r}, t)}}\nabla^2\sqrt{n_{\mathrm{BEC}}(\mathbf{r}, t)} + V_{\mathrm{ext}}(\mathbf{r}) + gn_{\mathrm{BEC}}. \tag{2.21}$$

The first term in Eq. 2.21, also known as the quantum pressure term [1, 2], that is derived by the kinetic energy, takes into account the spatial wavefunction variations within a small length scale $\xi = \hbar/\sqrt{2mgn_{\mathrm{BEC}}}$ called the healing length. The healing length will play a crucial role in analysing our results as it relates both to the vortex size and the overlap of the superfluids across a weak link.

Collective Excitations in a Bose-Einstein condensate

The collective excitations of a Bose-Einstein condensate can be found following the Bogoliubov-de Gennes formalism [160], writing the wavefunction

$$\psi(\mathbf{r}, t) = \mathrm{e}^{-i\frac{\mu}{\hbar}t}[\psi_0(\mathbf{r}) + \delta\psi(\mathbf{r}, t)], \tag{2.22}$$

for a small perturbation $\delta\psi(\mathbf{r}, t)$ above the stationary ground state $\psi_0(\mathbf{r})$. The expression (2.22) for the wavefunction is then substituted into the time-dependent GPE and, as $\delta\psi \ll \psi_0$, only the linear term in $\delta\psi$ can be considered; this procedure is known as linearization. The solutions of the resulting equation are the collective modes of the condensate which are found by decomposing the perturbation $\delta\psi(\mathbf{r},t)$ into the sum of modes oscillating with frequency ω_k as

$$\delta\psi(\mathbf{r},t) = \sum_k a_k[\mathrm{e}^{-i\omega_k t}u_k(\mathbf{r}) + \mathrm{e}^{i\omega_k t}v_k^*(\mathbf{r})], \tag{2.23}$$

with $u_k(\mathbf{r})$ and $v_k^*(\mathbf{r})$ the complex amplitude of the k-mode. The substitution of this expression in the linearized equation leads to two coupled Bogoliubov equations:

$$\begin{bmatrix} \hat{L}(\mathbf{r}) & \hat{M}(\mathbf{r}) \\ -\hat{M}^*(\mathbf{r}) & -\hat{L}^*(\mathbf{r}) \end{bmatrix} \begin{bmatrix} u_k(\mathbf{r}) \\ v_k(\mathbf{r}) \end{bmatrix} = \epsilon_k \begin{bmatrix} u_k(\mathbf{r}) \\ v_k(\mathbf{r}) \end{bmatrix}, \tag{2.24}$$

with

$$\begin{aligned} \hat{L}(\mathbf{r}) &= -\frac{\hbar^2}{2m}\nabla^2 + V_{ext}(\mathbf{r}) + 2g|\psi_0|^2 - \mu, \\ \hat{M}(\mathbf{r}) &= g|\psi_0|^2, \end{aligned} \tag{2.25}$$

and $\epsilon_k = \hbar\omega_k$ the quasiparticle energy of level k. The excitations above the ground state, which can be considered as dressed particles or quasiparticles. The solutions of the Bogoliubov equations give the dispersion relation for low energy collective excitations $\omega(k)$. In the case of an homogeneous BEC, the external potential $V_{ext} = 0$ and the condensate density $n = |\psi_0|$ is independent of the position, one finds $\mu = g|\psi_0| = gn$ from the time-independent GPE equation Eq. 2.15. In this case, the Bogoliubov solutions are plane waves $u_k(\mathbf{r}) = u\mathrm{e}^{\mathbf{ik}\cdot\mathbf{r}}$ and $v_k(\mathbf{r}) = v\mathrm{e}^{\mathbf{ik}\cdot\mathbf{r}}$ and their substitution in Eq. (2.24) yields

$$\hbar\omega(\mathbf{k}) = \sqrt{\frac{\hbar^2k^2}{2M}\left(\frac{\hbar^2k^2}{2M} + 2gn\right)}, \tag{2.26}$$

where $\mathbf{k}$ is the wavevector of the collective excitations. In the limit of low momenta, the dispersion relation (2.26) becomes linear in k, i.e. $\omega = ck$ and it describes the phonon excitations, which propagate with the velocity $c = \sqrt{gn/M} = \sqrt{\mu/M}$ known as the speed of sound. In the opposite limit of high momenta, the dispersion relation reduces to that of a free particle $\hbar\omega = \hbar^2k^2/2M$.

2.1.2 Critical velocities

One of the most fascinating properties of a superfluid is that it is inviscid due to the absence of any dissipative interaction of the superfluid with its surroundings. However, according to Landau [167], there exists a critical velocity such that if the superfluid velocity with respect to an obstacle exceeds a critical value, then the superfluidity is broken, and elementary excitations are generated. This critical value is defined as $v_c^L = \min(E(p)/p)$ where $E(p)$ is the dispersion relation for elementary excitations with momentum p. Later, Feynman [13] realized that not only the vorticity is quantised in superfluids but also that generation of vortices, coming out from an orifice, causes dissipation. Therefore Feynman proposed that in the presence of an obstacle, the critical velocity for the superfluidity to break down is set by the nucleation of vortices or solitons which causes phase jumps of 2π, known as phase-slippage, and that it is smaller than v_c^L. Following Anderson's argument that treated vortices as Landau quasiparticles [14], we could apply the Landau criteria for the critical velocity defined as the minimum of the ratio $E(p)/p$. In the case of a circular vortex ring with radius R, the smallest value of the ratio $E_{\mathrm{VR}}/P_{\mathrm{VR}}$, where E_{VR} and P_{VR} are the vortex ring kinetic energy and impulse (Ref. [14]), is obtained for the largest possible vortex ring radius. The size of such a vortex ring is set by the transverse size of the orifice d where it is nucleated. Thus the Feynman critical velocity for vortex ring nucleation is:

$$v_F \simeq \frac{\kappa}{2\pi d} \ln\left(\frac{d}{a_0}\right), \tag{2.27}$$

where κ is the quantum of circulation and a_0 the vortex core size.

2.1.3 Topological defects

Vortices are interesting phenomena existing in nature, from classical to quantum fluid. In quantum fluids the vortices are characterised by having quantized circulation in a closed path C around the vortex core and inside the superfluid, which is defined as:

$$\Gamma = \oint_C \mathbf{v} \cdot d\mathbf{l} = n\frac{h}{m} = n\kappa. \tag{2.28}$$

This is a multiple of the quantum of circulation $\kappa = h/m$, with the integer n called the vortex 'charge'. Here, $\mathbf{v}$ is the superfluid velocity, and $d\mathbf{l}$ is the line element of the vortex. There is a phase winding of 2π around the vortex core (for single-charged vortices $n = 1$) and in order for the superfluid wavefunction to be single-valued its density must go to zero at the vortex core. In other words, the superfluidity is locally destroyed at the vortex core. The size of the vortex core for a trapped condensate is on the order of the local value of the healing length $\xi(\mathbf{r}) = \hbar/\sqrt{2mgn(\mathbf{r})}$. In particular, vortex rings are closed vortex lines.

In classical fluids, vortex rings can be created when the fluid is driven through an 'orifice' such as the smoke vortex rings or the vortex rings generated by dolphins. In quantum fluids, specifically in superfluid helium, Rayfield and Reif in 1964 [168] showed that ions or electrons during their motion, in the presence of an applied potential, could generate vortex rings (this was first demonstrated for a Bose gas by Pomeau *et al.* [169] in 1992). The vortex ring then grows and the electron becomes trapped inside it. Subsequent important studies have been performed since then on the dynamics of vortex rings [170–172].

One way of generating single or multiple vortices in condensates instead is by rotating the condensate around a symmetry axis with an angular velocity larger than a critical value, with vortices forming in order for the system to minimize its free energy. Vortices could be generated also in stirred condensates for rotation frequencies exceeding a critical value [173] or moving an obstacle, such as a laser, in a condensate with constant velocity exceeding the critical value, where one or multiple vortex clusters are generated [174]. In analogy with superfluid Helium, where vortices are generated by accelerating the superfluid flow through an orifice, vortices in condensates can also be generated by the flowing of uni-directional accelerated atomic superfluids across a barrier [49, 20, 90]. In the case of ultracold atoms, the acceleration of the superfluid can be induced by a relative population imbalance between two reservoirs across a Josephson junction. In the three-dimensional geometry, which is the case we study in this thesis, vortex rings are generated when the superfluid velocity maxima exceeds a critical value. This mechanism of vortex ring generation, whose analogy in the classical world is a smoke vortex gun, represents an efficient way of producing vortex rings with a nucleation frequency controlled by the initial relative imbalance.

An example of 2D density profile in the presence of a vortex ring is shown in Fig. 2.1(a), after substracting the condensate equilibrium density ($\varDelta\rho$). The superfluid density goes to zero at the vortex core. Moreover, in such 2D plots, the vortex ring appears as a vortex-antivortex pair and around each vortex core there is a phase-winding of 2π. A three-dimensional density plot reveals the presence of the vortex ring shown in Fig. 2.1(b).

2.1.4 Vortex ring velocity and energy

An implicit consequence of the quantization of circulation is that the vortex induced flow velocity, for a straight vortex line, can be expressed by

$$\oint_C \mathbf{v} \cdot d\mathbf{l} = \kappa \longrightarrow v_\omega = \frac{\kappa}{2\pi}\hat{\mathbf{z}} \times \frac{\hat{\mathbf{r}}}{r}, \tag{2.29}$$

where $\hat{\mathbf{z}}$ is the unit vector, r is the distance from the vortex with $r > a_0$, where a_0 is the size of the vortex core size. This means that the velocity around a vortex, as we approach the vortex core, goes faster and faster until it diverges as $r \longrightarrow 0$. Moreover as the distance from the vortex is increased, in the limit $r \longrightarrow \infty$, the $v_\omega \longrightarrow 0$. We consider single-charged vortices but if the vortex was multiply-charged then n would additionally appear in Eq. (2.29) with its sign defining the direction of the flow around the topological defect (i.e. , whether it is clockwise or anti-clockwise). In the presence of a vortex, the

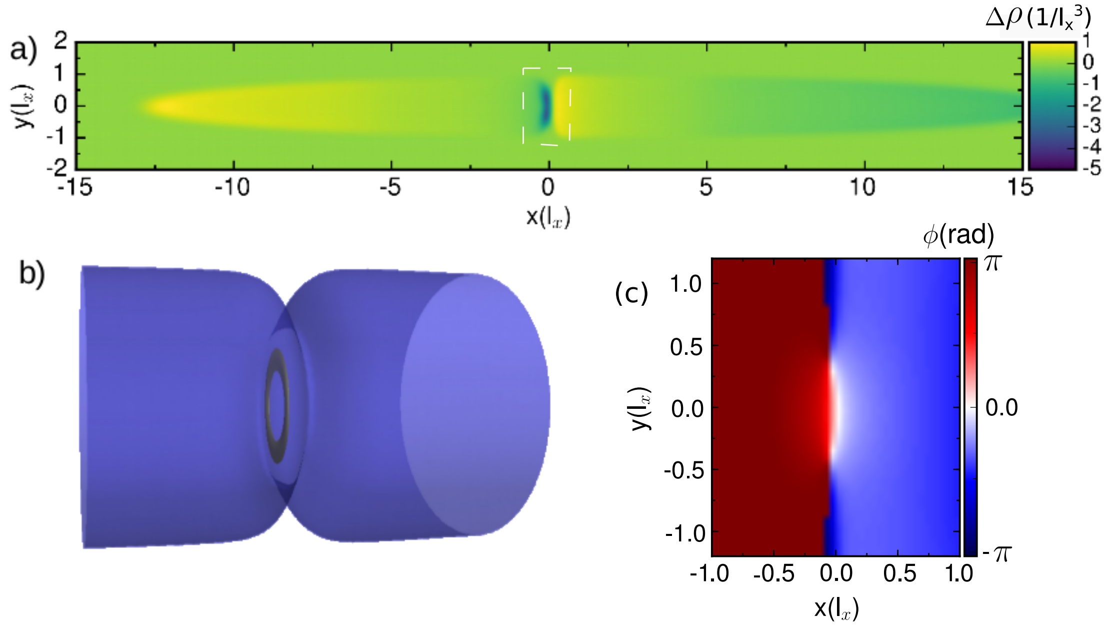

Figure 2.1: (a) The profile of the condensate density along xy-plane (for $z = 0$) after substracting the equilibrium density ($\Delta\rho$) , (b) the three dimensional isocontour density plot showing the vortex ring and (c) the two-dimensional phase profile along xy-plane (for $z = 0$) around the vortex ring position (for the corresponding density inside the selected white rectangular in (a)). The lengths are in units of l_x and the densities in units of $1/{l_x}^3$, where l_x is the harmonic oscillator length along the x axis equal to 7.5μm.

superfluid velocity $\mathbf{v}$ is then the sum of the external applied flow velocity $\mathbf{v}_f$ and the vortex-induced velocity: in the context of Eq. (2.29) it leaves the expression unchanged, as there is an exactly zero contribution of $\mathbf{v}_f$ to it.

This derivation of the vortex induced velocity (called also swirling velocity or vortical velocity or vortex self-induced velocity) can be generalized to vortex rings (VR) if the VR radius is much larger than the VR core. An interesting analogy is that the expression of Eq. (2.29) reminds us of the expression of the magnetic field generated by a straight wire (Ampere's law), where the vortical velocity v_ω is the analogue of the magnetic field and κ is the analogue of the current flowing in the wire. Based on this analogy, we can use the analogue of electrodynamics' Biot-Savart law for calculating the flow velocity induced by a vortex ring at a distance $\mathbf{r}$ from the vortex core [175], yielding:

$$\mathbf{v}_\omega(\mathbf{r}) = \frac{\kappa}{4\pi} \oint_C d\mathbf{l} \times \frac{\mathbf{r} - \mathbf{s}(l)}{|\mathbf{r} - \mathbf{s}(l)|^3}. \tag{2.30}$$

Here $\mathbf{s}$ is the vortex loop, such that the expression inside the integral gives the contribution of each infinitesimal vortex element to the total vortex self-induced velocity, and $d\mathbf{l} = d\mathbf{s}$ is a vector element along the tangent to the loop that has an infinitesimal length dl, where l is the arc length of the loop. For a vortex ring in a BEC, the vortical velocity is then given by [172]

$$v_\omega = \frac{\kappa}{4\pi R}\left[\ln\left(\frac{8R}{a_0}\right) - 0.615\right]. \tag{2.31}$$

The vortex ring kinetic energy for $R \gg a_0$ is given by the kinetic energy of the superfluid flow around the vortex core and is written as

$$E_{\mathrm{VR}} = \frac{1}{2}\int mn(\mathbf{r})v_\omega^2(\mathbf{r})d\mathbf{r}, \tag{2.32}$$

where m is the mass of the particles and $n(\mathbf{r})$ is the superfluid density. After substituting for a BEC the expression (2.31) and for $R \gg a_0$ the vortex ring kinetic energy is given by [171]

$$E_{\mathrm{VR}} = \frac{1}{2}n\kappa^2 R\left[\left(\frac{8R}{a_0}\right) - 1.615\right]. \tag{2.33}$$

For a multiply-charged VR with 'charge' n, the vortex ring kinetic energy would have been proportional to n^2, which suggests that the generation of multiple-charged VRs 'costs' more energy to the system and they are unstable, decaying into several single-charged VR. The expression (2.33) suggests that a VR with larger kinetic energy has a larger radius R and viceversa. Going back to the expression of the vortex self-induced velocity (2.31) a larger radius means a smaller velocity. Unlike a classical particle, the more energetic vortex ring has a smaller velocity. The vortex ring velocity and impulse satisfies the Hamilton's equation

$$P_{\mathrm{VR}} = \frac{\partial E_{\mathrm{VR}}}{\partial v_\omega}, \tag{2.34}$$

which gives

$$P_{\mathrm{VR}} = n\kappa\pi R^2. \tag{2.35}$$

For superfluid Helium the expressions for E_{VR} and v_ω are similar to the ones for an atomic BEC but they have a different numerical value for the right term inside the parenthesis.

2.1.5 Kelvin-waves excitation

If the vortex ring profiles differ from being circular, due to the presence of the thermal cloud or trapping potential anisotropy, bending waves are superimposed to the vortex core [176–178]. These bending waves are described by a dispersion relation $\omega(k)$ where ω is their angular frequency and k is the wavenumber. If R_{VR} is the vortex ring radius, the mode number m satisfies the relation $\lambda m = 2\pi R_{\mathrm{VR}}$ where $\lambda = 2\pi/k$ is the wavelength of the bending wave. For a Kelvin wave $m = 2$. In the thin core approximation the dispersion relation has the expression:

$$\omega_\pm(k) = \frac{\kappa}{2\pi {a_0}^2}\left(1 \pm \sqrt{1 + ka_0\frac{Y_0(ka_0)}{Y_1(ka_0)}}\right), \tag{2.36}$$

where a_0 is the vortex core size and Y_n are the Bessel functions of second order in imaginary argument. This means that there are two solutions of the dispersion relation, one fast (positive) ω_+ and one slow (negative) ω_- corresponding respectively to '+' and '−' signs in Eq. (2.36). The solution ω_- defines the Kelvin wave angular frequency, which in the approximation of $ka_0 \ll 1$ [178] becomes

$$\omega_-(k) \sim \kappa k^2/(4\pi)[\ln(2/(ka_0) - 0.5772]. \tag{2.37}$$

Thus the Kelvin wave period can be found as $T = 2\pi/\omega_-$. The presence of Kelvin wave modes makes the vortex ring move slower with respect to a circular vortex ring [179, 180].

2.2 Feshbach resonances

An extraordinary property of ultracold atomic gases is the possibility to tune their interaction, i.e. the scattering length, by just varying an external magnetic field, thanks to the Feshbach resonances they present [181]. Consequently, one can study different physical regimes: BEC and BCS superfluidity, offering the unique possibility to study the crossover between these two regimes that otherwise is not possible in condensed matter physics.

2.2.1 Basic theory concepts

The simplest model to describe the Feshbach resonance is the two-channel model shown in Fig. 2.2. In such a model, the Feshbach resonance occurs when the energy E of two colliding ultracold atoms (which is near zero) becomes equal to the energy of a bound molecular state, E_c, supported by a closed channel, i.e. a resonant coupling happens between the entrance channel (known also as open channel) and the closed one. In fact in Fig. 2.2 two molecular potentials $V_{bg}(R)$ and $V_c(R)$ are considered, with R being the interparticle distance, defining the open and the closed channel respectively. For large R the first potential which is also called the background potential tends to the energy of the two free colliding particles (ultracold atoms). The second potential instead, V_c, supports a molecular bound state with energy E_c near the energy of the two colliding particles. These two channels are characterised by different magnetic moments.

This means that by sweeping a static magnetic field, the open and closed channel potentials move with respect to each other varying so the energy difference

$$\Delta E = E_c - E = \Delta\epsilon(B - B_0), \tag{2.38}$$

where $\Delta\epsilon$ is the difference between the open and closed channel magnetic moments. At a certain value of the magnetic field B_0, the energy of the closed channel bound state becomes resonant with the energy of the scattering state ($E_c - E = 0$) and this is called

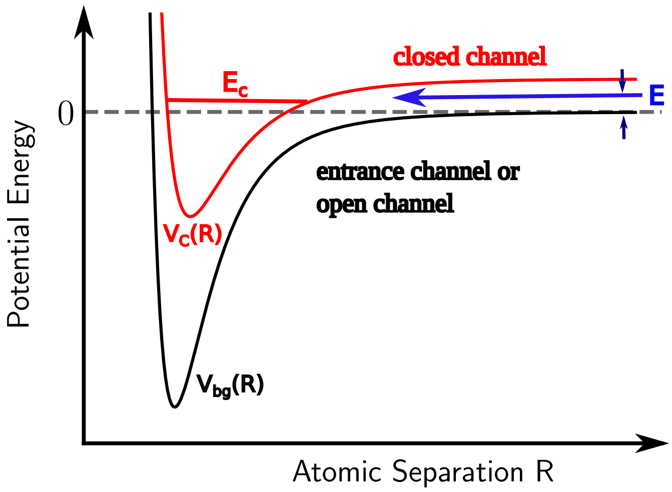

Figure 2.2: Two-channel model for a Feshbach resonance [181]: if two atoms colliding at energy E near zero, representing the entrance or the open channel, couple to a molecular bound state E_c of the closed channel potential, the Feshbach resonance happens. This figure is made by using the parameters of Ref. [182].

the Feshbach resonance [181]. At the Feshbach resonance the scattering length diverges and its expression around the Feshbach resonance is given by [181]:

$$a(B) = a_{BG}\left(1 - \frac{\varDelta}{B - B_0}\right), \tag{2.39}$$

with $\varDelta$ the width of the resonance and a_{BG} the scattering length corresponding to the situation where the atoms enter and exit in the open channel (no resonance scattering), which is associated to the potential $V_{bg}(R)$. The resonance width $\varDelta$ is such that at $B = B_0 + \varDelta$, the zero crossing of the scattering length ($a = 0$) is achieved. In our case we model the experiment of ^{6}Li which presents a broad Feshbach resonance between its two lowest hyperfine states at the magnetic field of 834G (Fig. 2.3).

Around the Feshbach resonance, if the magnetic field is such that the energy difference $\varDelta E$ is slightly negative then the energy of the colliding atoms is slightly larger than the molecular bound state and thus tightly bound fermionic pairs (or dimers) are formed. This case is characterised by weak repulsive interaction [184, 185, 72], i.e. positive interatomic scattering length, such that the ratio of the interparticle spacing to scattering length $1/(k_F a) \to +\infty$, with k_F the Fermi wave vector. Such tightly bound molecules can form a Bose-Einstein condensate if cooled to temperatures lower than the critical temperature for their condensation. This limit is also called the BEC limit of the Feshbach resonance and it is characterised by a critical temperature much smaller than the temperature corresponding to pair breaking [184, 185, 72]. Thus for weakly repulsive interaction, for which $n_M a_M^3 \approx (k_F a/6.5)^3 \ll 1$ [72], where a_M is the dimer-dimer (or molecule-molecule)

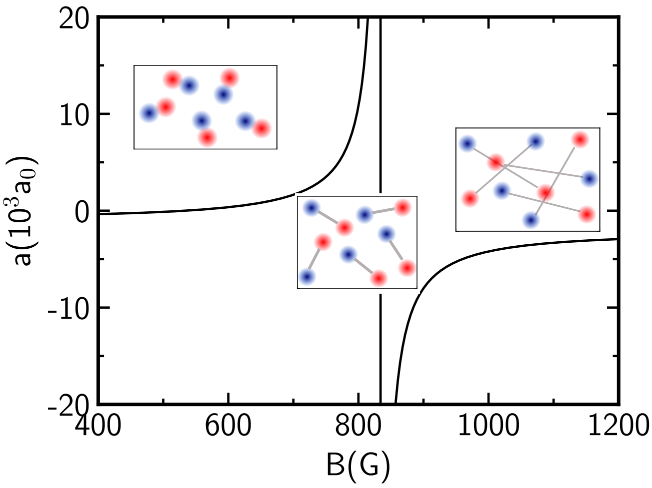

Figure 2.3: The scattering length in units of Bohr radius a_0 between the two lowest hyperfine states of ^{6}Li as a function of the magnetic field [72]. The Feshbach resonance happens for a magnetic field value $B_0 = 834$G. The data for building such plot are taken by Ref. [183]. In the inset is shown a schematic of pairs of fermion size, going from the regime of tightly bound molecules to the unitarity limit, where the pair size is on the order of interparticle distance, to the BCS limit, where the size of Cooper pairs-like is much larger than the interparticle distance.

scattering length, and for low temperature near zero, the molecular BEC dynamics can be described by the time-dependent GPE Eq. (2.14) with the main differences that the atomic mass m must be substituted by the molecular mass $M = 2m$ and the interparticle scattering length a must be substituted by the dimer-dimer scattering length $a_M \simeq 0.6a$ [165]. Usually by molecular BEC regime one refers to the region where $1/(k_F a) > 1$, while the region $1/(k_F|a|) < 1$ is called the crossover. At the Feshbach resonance where $1/(k_F a) \to 0$ the superfluid is called a unitary superfluid and it is composed of fermionic pairs which have a size on the order of the interparticle distance. If the energy difference ΔE instead is positive, the regime of weakly attractive interaction is obtained characterised by $1/(k_F a) \to -\infty$ where long-range Cooper-like pairs are formed and the ground state is the BCS superfluid.

2.3 Modelling the dynamics of a BEC in a double-well potential

A double-well potential is created by superimposing a laser barrier on the harmonic trapping potential. This barrier can be approximated with a Gaussian profile as $V_b = V_0 \mathrm{e}^{-2x^2/w^2}$ where V_0 is the barrier height and w is the barrier $1/\mathrm{e}^2$ width. Therefore the external trapping potential becomes

$$V_{\text{ext}}(\mathbf{r}) = \frac{1}{2}m(\omega_x^2 x^2 + \omega_y^2 y^2 + \omega_z^2 z^2) + V_0 \mathrm{e}^{-2x^2/w^2}. \tag{2.40}$$

Depending on the value of the barrier height with respect to the system chemical potential the superfluid can flow hydrodynamically through the barrier (if $V_0 < \mu$) or it can exhibit tunneling dynamics across the barrier (if $V_0 > \mu$). We note that even in the case of $V_0 < \mu$ and in a three-dimensional inhomogeneous system, we could have locally that $V_0 > \mu(\mathbf{r})$, where $\mu(\mathbf{r})$ is the local chemical potential in the local density approximation and $\mathbf{r}$ is the distance from the origin $O(0,0,0)$, and thus the dynamics across the barrier of such particles distant $\mathbf{r}$ from the trap center occurs via tunneling.

2.3.1 Hydrodynamic regime

In Ref. [186], the motion of a BEC in a quasi 1D cigar-shaped harmonic trap was studied in the presence a single localized Gaussian defect. The BEC motion was induced by a sudden displacement of the harmonic potential, thus exciting dipole oscillations. In the absence of the defect the BEC center of mass oscillates with the x axis trapping frequency ω_x. In the limit of small amplitude oscillations, the presence of the defect with $V_0 \ll \mu$ perturbs slightly the center of mass motion leading to a frequency shift:

$$\delta\omega_x = -\frac{3V_0\xi}{8\mu^{3/2}}\sqrt{m\pi}\,\omega_x^2, \tag{2.41}$$

with ξ the healing length at the trap center. For larger amplitude oscillations, when the BEC maximum velocity exceeds the local speed of sound, gray solitons detach from the defect, as well as some phonon-like excitations.

2.3.2 Tunneling regime and the Two-mode model

For barrier heights larger than the system chemical potential, the superfluid dynamics across the barrier can happen only due to tunneling and no hydrodynamic flow is possible. In this case the system can be visualized as two separate condensates, which have a small overlap of their respective wavefunctions in the barrier region.

Linear two-mode model

The simplest model to describe such a system is the linear two-mode model [59, 61], in which the system wave function is written as a linear superposition of the left and right condensate wavefunctions, i.e.

$$\psi(\vec{r},t) = \psi_{\mathrm{L}}(t)\cdot\eta_{\mathrm{L}}(\mathbf{r}) + \psi_{\mathrm{R}}(t)\cdot\eta_{\mathrm{R}}(\mathbf{r}), \tag{2.42}$$

where $\psi_L(t) = \sqrt{N_\mathrm{L}}e^{i\phi_\mathrm{L}}$ and $\psi_\mathrm{R}(t) = \sqrt{N_\mathrm{R}}e^{i\phi_\mathrm{R}}$ and $\int \eta_i \cdot \eta_j d\vec{r} = \delta_{i,j}$ with i, j = left,right. The $N_{\mathrm{R(L)}}$ and $\phi_{\mathrm{R(L)}}$ are the particle numbers and the condensate phases in the right and left well, respectively. The approximation (2.42) is valid if the overlap between the two condensates in the barrier region is small enough for the nonlinear interaction term to have negligible effect on mixing the left and right condensate wavefunctions. Moreover by writing the system wavefunction as Eq. (2.42) we are making the additional approximation of separating the spatial dependence of the wavefunction from its time dependence. The expression 2.42 of the wavefunction is then substituted in the time-dependent GPE Eq. (2.14) and the following equations are obtained:

$$i\hbar\frac{d\psi_L}{dt} = (E_L^0 + U_L N_L)\psi_L - K\psi_R, \tag{2.43}$$
$$i\hbar\frac{d\psi_R}{dt} = (E_R^0 + U_R N_R)\psi_R - K\psi_L, \tag{2.44}$$

where $E^0_{\mathrm{L(R)}}$ are the zero-point energy in each well, $U_{\mathrm{L(R)}}$ are the onsite interaction energy and K is the tunneling energy. The relevant energies are defined as

$$E^0_{\mathrm{L(R)}} = \int \left[\frac{\hbar^2}{2m}|\nabla\eta_{\mathrm{L(R)}}|^2 + |\eta_{\mathrm{L(R)}}|^2 V_\mathrm{ext}\right] d\mathbf{r}, \tag{2.45}$$
$$U_{\mathrm{L(R)}} = g\int |\eta_{\mathrm{L(R)}}|^4 d\mathbf{r}, \tag{2.46}$$
$$K = -\int \left[\frac{\hbar^2}{2m}(\nabla\eta_\mathrm{L}\nabla\eta_\mathrm{R}) + \eta_\mathrm{L} V_\mathrm{ext}\eta_\mathrm{R}\right] d\mathbf{r}. \tag{2.47}$$

If we now define the population imbalance between the two wells as

$$z(t) = \frac{N_\mathrm{L} - N_\mathrm{R}}{N} = \frac{|\psi_\mathrm{L}|^2 - |\psi_\mathrm{R}|^2}{|\psi_\mathrm{L}|^2 + |\psi_\mathrm{R}|^2}, \tag{2.48}$$

the relative phase $\Delta\phi = \phi_\mathrm{R} - \phi_\mathrm{L}$, and if we rescale the time to a dimensionless quantity by substituting $(2K/\hbar)t \longrightarrow t$, the system of equations Eq. (2.43)-(2.44) becomes:

$$\frac{dz}{dt} = \sqrt{1 - z^2(t)}\sin(\Delta\phi(t)), \tag{2.49}$$
$$\frac{d\Delta\phi}{dt} = \Delta E + \Lambda z(t) + \frac{z(t)}{\sqrt{1 - z^2(t)}}\cos(\Delta\phi(t)). \tag{2.50}$$

The new quantities ΔE and Λ appearing in the above equation are defined as follows:

$$\Delta E = \frac{E^0_\mathrm{L} - E^0_\mathrm{R}}{2K} + \frac{U_\mathrm{L} - U_\mathrm{R}}{2K}, \tag{2.51}$$
$$\Lambda = \frac{UN}{2K};\ U = (U_\mathrm{L} + U_\mathrm{R})/2. \tag{2.52}$$

We note that the first equation, Eq. (2.49), defines the Josephson current if Eq. (1.15) is used, i.e.

$$\mathrm{I} = \frac{dN_R}{dt} = -\frac{dN_L}{dt} = -\frac{N}{2}\frac{dz}{dt}, \tag{2.53}$$

the system of equations Eq. (2.49)-(2.50) corresponds to the Josephson equations for bosonic ultracold atoms in dimensionless time. We thus refer to them as Josephson equations. The Hamiltonian describing the system is given by

$$\mathrm{H} = \frac{\Lambda z^2}{2} + \varDelta E z - \sqrt{1-z^2}\cos(\varDelta\phi). \tag{2.54}$$

The population imbalance and the relative phase are canonically conjugate variables as they fullfil the condition

$$\dot{z} = -\frac{\partial \mathrm{H}}{\partial \varDelta\phi};\ \ \dot{\varDelta\phi} = \frac{\partial \mathrm{H}}{\partial z}. \tag{2.55}$$

For a symmetric double-well potential, there is no energy offset, and thus $\varDelta E = 0$. We will show that the scaled quantity $\varLambda$ defines the dynamics of the system. For an initial population imbalance z_0 and an initial phase difference $\varDelta\phi_0$ the total system energy is $\mathrm{H}(z_0, \varDelta\phi_0) = \Lambda z_0^2/2 - \sqrt{1-z_0^2}\cos(\varDelta\phi_0)$.

We consider here the case of zero initial relative phase and the solutions of Eq. (2.49)-(2.50) are called 'zero-phase modes'. In the case of small imbalance and phase difference $z, \varDelta\phi \ll 1$, the Josephson equations (2.49)-(2.50) can be linearized and the solution consists of small amplitude sinuosoidal oscillations of both the population imbalance and the relative phase around a zero mean value with a frequency:

$$\omega_p = \frac{1}{\hbar}\sqrt{2UNK + (2K)^2}. \tag{2.56}$$

Such a frequency is called 'plasma' frequency in analogy with superconductors where NK is the analogue of tunneling energy E_J and $2U$ is the analogue of the superconductor charging energy E_c. If the $(2K)^2$ term is much smaller than the first term then the 'plasma' frequency is given by

$$\omega_p \simeq \frac{1}{\hbar}\sqrt{2UNK}, \tag{2.57}$$

and in analogy with superconductors can be written as

$$\omega_p \simeq \frac{1}{\hbar}\sqrt{E_c E_J}. \tag{2.58}$$

The Josephson equations Eq. (2.49)-(2.50) remind us of the equations of a classical pendulum with a variable length $\sqrt{1-z^2}$ where z is the analogue of the pendulum angular momentum [59]. In this last analogy the Josephson 'plasma' regime would correspond to the oscillations of the non-rigid pendulum around the equilibrium position, which corresponds to a pendulum angle equal to zero. As the initial imbalance z_0 increases for a fixed Λ (or alternatively as Λ increases at fixed z_0) the population imbalance shows large amplitude anharmonic oscillations around a zero mean value. For initial imbalance equal to a critical value $z_0 = z_{\text{cr}}$ for a fixed Λ or for a value of $\Lambda = \Lambda_c$ for fixed z_0, the population imbalance remains 'self-locked' at a non-zero mean value $\langle z(t) \rangle \neq 0$, exhibiting small amplitude oscillations. This regime is called Macroscopic Quantum Self-Trapping (MQST). Such condition, expressed as $E(z_0, \Delta\phi = 0) = E(z = 0, \Delta\phi = \pi)$ gives the critical value of Λ for fixed z_0

$$\Lambda_c = \frac{1 + \sqrt{1 - z_0^2}\cos(\Delta\phi_0)}{z_0^2/2}. \tag{2.59}$$

In the case of a fixed Λ but variable initial imbalance, the critical value of the population imbalance can still be found by Eq. (2.59). For $\Lambda \geq \Lambda_c$ where the system is in the MQST regime the self-interaction energy (the first term in the Hamiltonian) exceeds the tunneling energy (second term in the Hamiltonian). Thus, for $z_0 < z_{\text{cr}}$ the mean value of the population imbalance is zero, while at the onset of MQST regime for $z_0 = z_{\text{cr}}$, the mean value of the population imbalance becomes 'suddenly' different from zero. If $\Lambda \gg 1$, Eq. (2.50) for the symmetric double-well potential can be written approximately as

$$\frac{d\Delta\phi}{dt} \approx \Lambda z(t). \tag{2.60}$$

Returning now to the dimensional time leads to

$$\frac{d\Delta\phi}{dt} \approx UNz(t) = \frac{1}{2}E_c N z(t). \tag{2.61}$$

By comparing with the Josephson-Anderson relation Eq. (1.16) the right hand side of Eq. (2.61) gives the chemical potential difference $\Delta\mu \approx UNz(t)$. In the MQST regime the population imbalance mean value is almost fixed at the initial imbalance (apart from small amplitude oscillations around this mean value) so we can write $\langle z(t) \rangle \simeq z_0$ and the expression (2.61) becomes $d\Delta\phi/dt \approx UNz_0$. This equation leads to a solution for the relative phase:

$$\Delta\phi \simeq UNz_0 t, \tag{2.62}$$

which increases linearly in time; for this reason the MQST regime is also called the 'running-phase mode'. The time-dependence of the relative phase in the MQST regime is similar to the superconductor '*ac*' Josephson effect with the main difference that there is no population imbalance between the two superconductors, in contrast to the BEC Josephson junction we considered. Moreover the presence of the nonlinear interaction term in the GPE is the reason for the presence of the MQST regime in ultracold atoms. After substituting the expression (2.62) in Eq. (2.50) and returning to the dimensional time we obtain:

$$I = -\frac{N}{2}\frac{dz}{dt} \simeq \frac{2K}{\hbar}\frac{N}{2}\sqrt{1-z_0^2}\sin(UNz_0t), \tag{2.63}$$

where the Josephson current depends on the initial population imbalance. However for $z_0 \ll 1$ the expression (2.63) becomes

$$I \simeq \frac{2K}{\hbar}\frac{N}{2}\sin(UNz_0t) = I_c\sin(UNz_0t), \tag{2.64}$$

(upon defining the critical current $I_c = KN/\hbar$) thus having a sinusoidal current profile, characterising the '*ac*' Josephson effect in superconductors. We also note that Eq. (2.50) for $d\Delta\phi/dt$ for the symmetric double-well potential and for zero population imbalance gives a constant relative phase, which when substituted into Eq. (2.49) and taking into account Eq. (2.53), gives a non-zero constant Josephson current $I = I_c \sin\Delta\phi$; this is the analogue of the so-called '*dc*' Josephson current in superconductors.

Nonlinear two-mode model

In the linear two-mode model, upon separating the spatial dependence of the wavefunction from its time dependence (expression (2.42)), we assume that the density profile of each condensate does not depend on the number of particles present at the same well at a given time. However, due to the presence of the nonlinear term in the GPE Eq. (2.14), this is not generally true [187, 188]. In order to write the two-mode model wavefunction in a more general form we must thus introduce the dependence of the spatial part on the particle number, as

$$\psi(\vec{r},t) = \psi_L(t)\cdot\eta_L(\mathbf{r};N_L(t)) + \psi_R(t)\cdot\eta_R(\mathbf{r};N_R(t)). \tag{2.65}$$

The left and right condensate wavefunctions can be obtained as a superposition of the wavefunction of the system ground state (spatially symmetric state) and the wavefunction of the first excited state, which is a spatially antisymmetric state: $\eta_{\mathrm{R,L}} = (\eta_{\mathrm{symm}} \pm \eta_{\mathrm{anti}})/\sqrt{2}$. By substituting the expression (2.42) in the time-dependent GPE (2.14) the following nonlinear two-mode expressions are obtained [187, 188]:

$$\hbar\frac{dz}{dt} = \Delta E_{\mp}\ \sqrt{1-z^2(t)}\ \sin(\Delta\phi(t)), \tag{2.66}$$

$$\hbar\frac{d\Delta\phi}{dt} = \Delta\mu - \Delta E_{\mp}\ \frac{z(t)}{\sqrt{1-z^2(t)}}\ \cos(\Delta\phi(t)), \tag{2.67}$$

where $\Delta\mu = \mu_{\mathrm{R}} - \mu_{\mathrm{L}}$ is the chemical potential difference between the two condensates, $\Delta E_{\mp}$ is the difference between the energy of the antisymmetric and symmetric states

$\Delta E_{\mp} = E_{-} - E_{+}$. The full expressions for these energies is given by

$$E_{\pm} = \int \left[\frac{\hbar^2}{2m}(\nabla\eta_{\pm})^2 + V_{\rm ext}\eta_{\pm}^2 + \frac{1}{2}gN\eta_{\pm}^4\right] d\mathbf{r}, \tag{2.68}$$

$$\mu_{\rm R,L} = \int \left[\frac{\hbar^2}{2m}(\nabla\eta_{\rm R,L})^2 + V_{\rm ext}\eta_{\rm R,L}^2 + gN_{\rm R,L}\eta_{\rm R,L}^4\right] d\mathbf{r}. \tag{2.69}$$

The energy difference $\Delta E_{\mp}$ can also be written as $\Delta E_{\mp} = 2N(K + N\beta)$ where K is the so-called tunneling energy in the linear two-mode model defined in Eq. (2.47) while β is defined as

$$\beta = -\frac{g}{4}\int \eta_{\rm R}^3\eta_{\rm L} d\mathbf{r}. \tag{2.70}$$

In the limit of small population imbalance and relative phase $z, \Delta\phi \ll 1$ the chemical potential can be expressed to first approximation as

$$\begin{aligned} \mu_{\rm R} \simeq & \int d\mathbf{r} \left\{ \frac{\hbar^2}{2m}\left(\nabla\eta_{\rm R}^2\Big|_{N_R=N/2}\right) + V_{\rm ext}\eta_{\rm R}^2\Big|_{N_R=N/2} + gN_{\rm R}\eta_{\rm R}^4\Big|_{N_R=N/2}\right\} \\ & + \frac{\partial\mu_R}{\partial N_R}\Big|_{N/2}\left(N_R - \frac{N}{2}\right) \\ & = \mu_{\rm R}^0 + 2\frac{\partial\mu_R}{\partial N_R}\Big|_{N/2} Nz. \end{aligned} \tag{2.71}$$

For a symmetric double-well potential, $\mu_{\rm R}^0 = \mu_{\rm L}^0$ and the solution of the linearized equations Eq. (2.66)-(2.67) consists of sinusoidal oscillations of the population imbalance and relative phase around a zero-mean value with the 'plasma' frequency:

$$\omega_p = \frac{1}{\hbar}\sqrt{\Delta E\frac{\partial\mu_{R,L}}{\partial N_{R,L}} + \Delta E^2}. \tag{2.72}$$

The linear two-mode model 'plasma' frequency is obtained from the expression (2.72) if the term $N\beta$ is much smaller than K so that $\Delta E_{\mp} \approx 2KN$ and the onsite interaction energy is substituted as $\partial\mu_{R,L}/\partial N_{R,L} \to U$. In analogy with superconductors the ΔE plays the role of $E_J/2$. The nonlinear two-mode model gives more accurate values of the tunneling and onsite interaction energy with respect to the linear case for barrier heights that are not much larger than the chemical potential, as we will show in Chapt. 3.

2.4 Current-Phase relation, beyond two-mode model (microscopic description)

The study we presented in Sect. 2.3.2, based on the papers of [59, 61, 187], considered the condensate-condensate tunneling process. Although Ref. [60] estimated the effect of normal current that comes from the thermal cloud, their study was based on the mean-field GPE equation which does not consider the presence of non-condensate states. In this section we reproduce the key results from the paper of Meier and Zwerger [65] where they considered higher order terms in the tunneling Hamiltonian, which take into account also the condensate to non-condensate tunneling processes.

If the two condensates in the left and right wells are weakly coupled, the system Hamiltonian can be written as the sum of each condensate Hamiltonian ($\hat{H}_L$ and $\hat{H}_R$ respectively) and a tunneling Hamiltonian $\hat{H}_T$; the latter considered as a small perturbation

$$\hat{H} = \hat{H}_L + \hat{H}_R + \hat{H}_T. \tag{2.73}$$

The tunneling Hamiltonian describes the particle transfer between left and right reservoirs and it can be written as $\hat{H}_T = \hat{\Lambda} + \hat{\Lambda}^{\dagger}$, where $\Lambda = -\sum_{l,r} t_{l,r}\hat{a}^{\dagger}_L\hat{a}_R$ and $t_{l,r}$ is the tunneling amplitude. This is based on the introduction of a set of orthonormal eigenstates $|l\rangle$ and $|r\rangle$ for left and right well, which decay exponentially in the barrier region.

If the condensate size is much larger than the condensate healing length, then a good candidate for the $|l\rangle$ and $|r\rangle$ states are the condensate ground state in each well $\psi_{L/R}$, found by solving the GPE equation, and a set of excited states, found by solving the Bogoliubov equations, with wavenumbers k and q for the condensate in the left and right wells respectively. The set of excited states are orthogonal to the condensate ground states. In this new basis the transfer Hamiltonian will in general have contributions from condensate-condensate, condensate to non-condensate and non-condensate to non-condensate tunneling. Thus, it can be expressed as:

$$\begin{aligned}\hat{\Lambda} = -t_{cc}\hat{a}^{\dagger}_{c,L}\hat{a}_{c,R} - \sum_{k} t_{kc}\hat{a}^{\dagger}_{k}\hat{a}_{c,R}\\ - \sum_{q} t_{cq}\hat{a}^{\dagger}_{c,L}\hat{a}_{q} - \sum_{kq} t_{kq}\hat{a}^{\dagger}_{k}\hat{a}_{q}.\end{aligned} \tag{2.74}$$

The tunneling Hamiltonian first term describes the condensate to condensate transfer (c-c term) and its expectation value is $\langle\phi|\hat{H}_T|\phi\rangle = -E_J\cos(\phi)$, where $\phi = \phi_L - \phi_R$ is the relative phase between the two-condensates, and E_J the Josephson coupling energy. The latter, defined as $E_J = 2t_{cc}(\bar{\mathrm{N}}_L\bar{\mathrm{N}}_R)^{1/2}$ ($\bar{\mathrm{N}}_{L/R}$ is the mean particle number in the left/right well) is positive; it gives rise to an energy gain and favours a relative phase $\phi = 0$ in the system ground state. The non-dissipative current can be found as

$$\mathrm{I}(\phi) = -\frac{1}{\hbar}\frac{\partial E(\phi)}{\partial \phi}, \tag{2.75}$$

and its lowest non-zero term is $\mathrm{I} = \mathrm{I}_c\sin(\phi)$ with I_c the critical Josephson current defined from the Josephson coupling energy as $\mathrm{I}_c = E_J/\hbar$. The Josephson current does not depend on the number of particles transfered between the two wells because we assume that it is much smaller than $\bar{\mathrm{N}}_{L/R}$.

The second order energy shift can be calculated by

$$\Delta E^{(2)} = -\sum_{e} \frac{|\langle \mathrm{e}|\hat{H}_T|\mathrm{O}\rangle|^2}{E_e - E_0}, \tag{2.76}$$

which includes all the possible excited states $|\mathrm{e}\rangle$ with $|\mathrm{O}\rangle$ being the ground state. In order to calculate this second order effect, Ref. [65] follows the derivation in [189] for the Josephson effect between two BCS superconductors. The condensate to non-condensate terms (c-nc) involve two possible processes; one is the transfer of a particle from the condensate state in the right well to a noncondensate (excited) state in the left well and the second one consists of transferring two bosons from the condensate states in the left well to two noncondensate states in the left well $(k, \bar{k})$ and then transferring one of the particles in non-condensate state in the left well to a condensate state in the right well. It can be shown [65] that the total c-nc contribution coming from Eq. (2.76) is

$$\Delta E^{(2)}_{\mathrm{c-nc}} = \left(\bar{N}_L \mu_R \sum_q \frac{|t_{cq}|^2}{E_q^2} + \bar{N}_R \mu_L \sum_k \frac{|t_{kc}|^2}{E_k^2} \right) \cos(2\phi). \tag{2.77}$$

Due to its dependence on $\cos(2\phi)$, the second order term favours a relative phase of $\pi/2$ of the coupled condensates. However this term is small compared to the first order term in the case of weakly-coupled condensates and thus the system ground state has a zero relative phase.

The non-condensate to non-condensate tunneling Hamiltonian (nc-nc term) phase dependence is given by the expression:

$$\Delta E^{(2)}_{\mathrm{nc-nc}}(\phi) = -2 \sum_{k,q} |t_{k,q}|^2 \frac{u_k v_k u_q v_q}{E_k + E_q} \cos(2\phi), \tag{2.78}$$

where $u_{k/q}$ and $v_{k/q}$ are the particle and hole amplitude appearing in the Bogoliubov transformation $\hat{a}_k^\dagger = u_k \hat{\alpha}_k^\dagger - v_k \hat{\alpha}_k$, with $\hat{\alpha}_k^\dagger$ and $\hat{\alpha}_k$ being the quasiparticle creation and annihilation operators respectively. This expression is similar to the analogous one obtained for superconductors [189] at second order which relates the Josephson coupling energy to the superconductor gap and normal state conductance if the average transfer amplitude $|t_{k,q}|$ at the Fermi energy is expressed in terms of the normal state conductance. In weakly interacting gaseous BEC, the nc-nc term is smaller by a factor proportional to $\sqrt{na^3}$ than the c-nc term, thus it is negligible.

Combining the equations (2.75) and (2.77) leads for the non-dissipative Josephson current to second order perturbation theory

$$\mathrm{I} = -\mathrm{I}_c \sin(\phi) - \mathrm{J}_1 \sin(2\phi), \tag{2.79}$$

where the first term comes from the condensate to condensate tunneling term (i.e. from the first term in Eq. 2.74) with $I_c > 0$, while the second term originates from condensate to non-condensate tunneling term and $J_1 < 0$. Specifically, J_1 is given by $-2/\hbar$ times the expression in parenthesis in Eq. (2.77). The presence of the second-order term means that the relative phase value at which the current achieves its maximum value is no longer exactly $\pi/2$, as predicted from 1^{st} order perturbation theory, but it is actually shifted to $\pi/2 + 2|J_1|/\mathrm{I}_c$.

The expression for the current (2.79) is obtained by assuming that the relative phase is time-independent. In the presence of a non-zero chemical potential difference between the two condensates, the relative phase is expected to change in time following the Josephson-Anderson relation $d\phi/dt = -\Delta\mu/\hbar$. If the chemical potential difference is kept fixed at a non-zero value and it is set externally, the Hamiltonian of the system contains an additional term $\Delta\mu\hat{\nu}$, where $\hat{\nu}$ gives the number of particles transferred between the two wells. By performing time dependent gauge transformation the $\Delta\mu\hat{\nu}$ term is eliminated in the Hamiltonian, such that the expression for the transfer amplitude contains instead the term $\mathrm{e}^{i\phi(t)}$, where $\phi(t)$ is determined by the Josephson-Anderson relation. The Josephson current becomes then

$$\hat{\mathrm{I}} = -\frac{d\hat{N}_L}{dt} = i\frac{(\hat{\Lambda} - \hat{\Lambda}^\dagger)}{\hbar}. \tag{2.80}$$

In the limit where the barrier height is much larger than the chemical potential, the ground state found by the GPE equation and the excited states given by the Bogoliubov equations in the local density approximation are a good basis for the diagonalization of the system Hamiltonian. In this limit, and for a small number of particles transferred, the Josephson current up to second order takes the form:

$$\mathrm{I} = -I_c \sin\phi(t) + J_n(\Delta\mu) - J_1(\Delta\mu)\sin(2\phi(t)) + J_2(\Delta\mu)\cos(2\phi(t)). \tag{2.81}$$

The first term in Eq. (2.81) is in agreement with the first-order non-dissipative current found in the case for constant relative phase. The second term instead is called the normal current because it describes a dissipative flow which tends to lower the system chemical potential and it is independent of the relative phase. The third term depends on $\sin(2\phi(t))$ and was also found in the case of zero $\Delta\mu$. Interestingly, there is a fourth term which depends on $\cos(2\phi(t))$ and it has a relative phase of $\pi/2$ (out of phase) with respect to the non-dissipative Josephson contributions. This $\cos(2\phi(t))$ is a dissipative current which tends to vanish for zero $\Delta\mu$. Differently from the BCS superconductors where the

J_n and J_2 terms vanish at $T = 0$ due the presence of an energy gap, the corresponding terms remain different from zero in Bose gases even at $T = 0$. All the terms J_n, J_1 and J_2 come from the condensate to non-condensate tunneling Hamiltonian. The dissipative second order terms (J_n and J_2) are related to dissipative phenomena even at $T = 0$, which tends to lower the chemical potential difference. Note that for $\Delta\mu > 0$, the sum $J_n(\Delta\mu) + J_2(\Delta\mu)\cos 2\phi(t)$ is positive.

We note that the chemical potential in each well depends on the particle number in each well. In order to take into account such dependence, the 'charging' Hamiltonian $U(\hat{N}_L - \hat{N}_R)^2/8$ is added to Eq. (2.73) (note that such contribution is the first term in the Hamiltonian of the two-mode model Eq. (2.54)). This means that the relative phase will evolve as $d\phi/dt = \Delta\mu_{\text{ext}} + U\nu$ where $\nu = (N_L - N_R)/2$. Ref. [65] obtained the expressions for each component of the current for a homogeneous system with a rectangular barrier, which does not vary much over lengths comparable to the healing length. The derivation of the expressions of the Josephson non-dissipative current for a Gaussian barrier was obtained in Ref. [159], whose model is used in this thesis in Chapt. 3 and Chapt. 4 to describe the critical current dependence on the barrier height, which is extracted both from numerical simulations and from the experimental data of ^{6}Li experiment [49, 20] in the BEC limit.

Ref. [65] also showed that if the chemical potential difference is much smaller than the mean value of the chemical potential $\bar{\mu} = (\mu_L + \mu_R)/2$, then only low energy phonon modes contribute to J_n and J_2. They also demonstrated that the second order non-dissipative term J_1 is small with respect to I_c and that the dissipative current J_n and J_2 depends linearly on $\Delta\mu$ for $\Delta\mu \ll \bar{\mu}$, i.e. $J_2(\Delta\mu \to 0) = J_n(\Delta\mu \to 0) = \mathrm{G}_n\Delta\mu$ where G_n is the normal conductance. The normal conductance is finite even at $T = 0$ in Bose gases. The nc-nc terms instead vanish as T^4 making them negligible in the $T \to 0$ limit. Moreover, the dissipative current could destroy the MQST regime predicted by Smerzi *et al.* [59]. We also note that the term t_{cc} is the same as the tunneling energy K defined in [59, 61].

2.5 Finite temperature theoretical model: The Zaremba-Nikuni-Griffin (ZNG) model

In order to study a bosonic system at finite temperature the fluctuation operator in the Heisenberg equation of motion Eq. (2.10) should not be neglected and so by taking the equation average the general expression is obtained:

$$i\hbar\frac{\partial\psi(\mathbf{r},t)}{\partial t} = \left[-\frac{\hbar^2}{2m}\nabla^2 + V_{\text{ext}}(\mathbf{r})\right]\psi(\mathbf{r},t) + g\langle\hat{\Psi}^\dagger\hat{\Psi}\hat{\Psi}\rangle. \tag{2.82}$$

The cubic term $\langle\hat{\Psi}^\dagger\hat{\Psi}\hat{\Psi}\rangle$ (arising due to binary interactions) can be written as:

$$\langle\hat{\Psi}^\dagger\hat{\Psi}\hat{\Psi}\rangle = n_{\mathrm{BEC}}\psi + 2n_{\mathrm{th}}\psi + m\psi^* + \langle\hat{\delta}^\dagger\hat{\delta}\hat{\delta}\rangle, \tag{2.83}$$

where $n_{\mathrm{th}} = \langle\hat{\delta}^\dagger\hat{\delta}\rangle$ is the non-condensate (thermal cloud in our case) density, and $m = \langle\hat{\delta}\hat{\delta}\rangle$ is the pair anomalous density.

The time evolution of the condensate wavefunction is then described by the following equation:

$$\begin{aligned} i\hbar\frac{\partial\psi(\mathbf{r},t)}{\partial t} &= \left[-\frac{\hbar^2}{2m}\nabla^2 + V_{\mathrm{ext}}(\mathbf{r}) + g(n_{\mathrm{BEC}}(\mathbf{r},t) + 2n_{\mathrm{th}}(\mathbf{r},t))\right]\psi(\mathbf{r},t) \\ &+ gm\psi^*(\mathbf{r},t) + g\langle\hat{\delta}^\dagger(\mathbf{r},t)\hat{\delta}(\mathbf{r},t)\hat{\delta}(\mathbf{r},t)\rangle. \end{aligned} \tag{2.84}$$

In other words, the condensate dynamics is coupled to the thermal cloud dynamics via the presence of the terms $2gn_{\mathrm{th}}$, $gm\psi^*$ and $g\langle\hat{\delta}^\dagger\hat{\delta}\hat{\delta}\rangle$. This equation reduces to the GPE equation Eq. (2.14) in the limit of zero temperature, where all the particles populate the condensate state (without considering the quantum depletion), and thus the non-condensate operator, the non-condensate density and the pair anomalous density tend to zero. At $T > 0$, the thermal cloud has its own dynamics being described by the Heisenberg equation of motion for the non-condensate:

$$i\hbar\frac{\partial}{\partial t}\hat{\delta}(\mathbf{r},t) = \left[\hat{\delta}(\mathbf{r},t), \hat{H}\right], \tag{2.85}$$

where $\hat{\delta}(\mathbf{r},t) = \hat{\Psi}(\mathbf{r},t) - \psi(\mathbf{r},t)$. This can be expressed as:

$$\begin{aligned} i\hbar\frac{\partial\hat{\delta}(\mathbf{r},t)}{\partial t} &= \left[-\frac{\hbar^2}{2m}\nabla^2 + V_{\mathrm{ext}}(\mathbf{r}) + 2g(n_{\mathrm{BEC}}(\mathbf{r},t) + n_{\mathrm{th}}(\mathbf{r},t))\right]\hat{\delta}(\mathbf{r},t) \\ &- 2gn_{\mathrm{th}}(\mathbf{r},t)\hat{\delta}(\mathbf{r},t) + g\psi^2(\mathbf{r},t)\hat{\delta}^\dagger(\mathbf{r},t) \\ &+ g\psi^*(\mathbf{r},t)(\hat{\delta}(\mathbf{r},t)\hat{\delta}(\mathbf{r},t) - m(\mathbf{r},t)) \\ &+ 2g\psi(\mathbf{r},t)(\hat{\delta}^\dagger(\mathbf{r},t)\hat{\delta}(\mathbf{r},t) - n_{\mathrm{th}}(\mathbf{r},t)) \\ &+ g(\hat{\delta}^\dagger(\mathbf{r},t)\hat{\delta}(\mathbf{r},t)\hat{\delta}(\mathbf{r},t) - \langle\hat{\delta}^\dagger(\mathbf{r},t)\hat{\delta}(\mathbf{r},t)\hat{\delta}(\mathbf{r},t)\rangle). \end{aligned} \tag{2.86}$$

The appearance of the condensate density and wavefunction in the thermal cloud equation of motion couples the condensate to the thermal cloud motion, and so the equations Eq. (2.84)-(2.86) have to be solved self-consistently.

2.5.1 Mean-field coupling: The Hartee-Fock limit

In the first approximation, in Eq. (2.84), only the terms including one annihilation and one creation non-condensate operator are considered (first order effects): this is known as the Hartee-Fock limit. In the semiclassical approximation (which approximates the

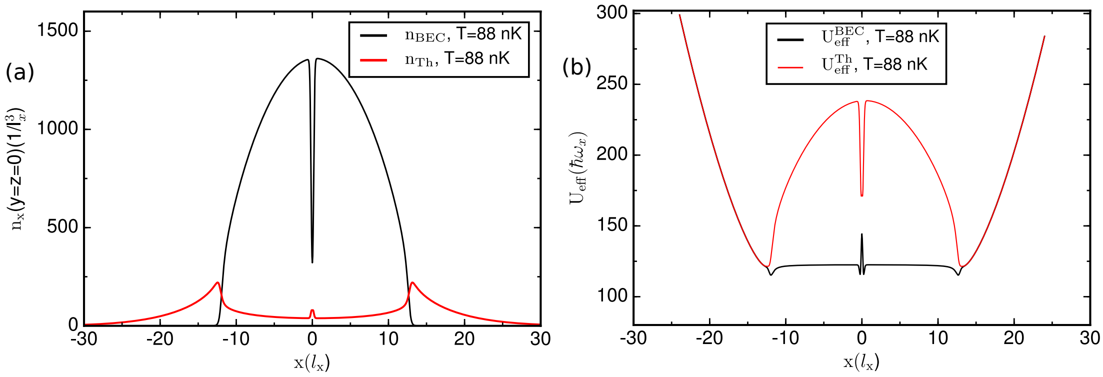

Figure 2.4: (a) The profile of the condensate and thermal cloud density along x direction (for $y = z = 0$), in units of the harmonic oscillator length $l_x = 7.5\mu$m, at T=88nK $\simeq 0.58T_c$. (b) The equilibrium effective potential felt by the condensate (black curve) and by the thermal cloud (red curve). Both subplots are for the double-well trap with a barrier height $V_0/\mu \sim 1$.

system with a homogeneous gas locally), the kinetic operator $-\hbar^2\nabla^2/2m$ is replaced by $\mathbf{p}^2/2m$, where $\mathbf{p}$ is the particle momentum, and it represents the kinetic energy of a free particle. In a trapping potential and in the Hartee-Fock limit, due to the presence of the condensate and thermal mean-field terms, the energy of a particle becomes (also called Hartee-Fock 'dressed' energies):

$$\epsilon(\mathbf{r}, t) = \frac{\mathbf{p}^2}{2m} + V_{\text{ext}}(\mathbf{r}) + 2g(n_{\text{BEC}}(\mathbf{r}, t) + n_{\text{th}}(\mathbf{r}, t)). \tag{2.87}$$

Thus the thermal particles feel an effective potential:

$$U_{\text{eff}}^{\text{th}}(\mathbf{r}, t) = V_{\text{ext}}(\mathbf{r}) + 2g(n_{\text{BEC}}(\mathbf{r}, t) + n_{\text{th}}(\mathbf{r}, t)) \tag{2.88}$$

while the condensate atoms feel an effective potential given by :

$$U_{\text{eff}}^{\text{BEC}}(\mathbf{r}, t) = V_{\text{ext}} + g(n_{\text{BEC}}(\mathbf{r}, t) + 2n_{\text{th}}(\mathbf{r}, t)). \tag{2.89}$$

Fig. 2.4(a) shows an example of the condensate and the thermal cloud density at finite temperature in the case of a three-dimensional elongated atomic Josephson-junction (which is the geometry we mainly consider in this thesis). The densities are along the x axis (long axis) and are extracted for $y = z = 0$ (i.e. sliced densities). Fig. 2.4(b) instead shows the effective potential profile felt by the condensate and the thermal particles for such double-well potential. Due to repulsive interactions between particles (i.e. g >0) the thermal cloud feels a larger potential where the condensate density is larger, i.e. is repelled by the condensate, which means that the thermal particles would have lower density. This explains why the thermal cloud density has local maxima at the barrier position (where the condensate density is minimized) and at the edges of the condensate.

In second approximation, also the quadratic terms containing pairs of non-condensate annihilation or creation operator, such as the anomalous pair density, are considered in the equation of motion of the condensate (also called the Hartee-Fock-Bogoliubov approximation), which can be solved via the diagonalization of its Hamiltonian via the Bogoliubov trasformation into a quasiparticle basis. Even though considering these quadratic terms gives a better approximation of the system ground state, it has the problem that the homogeneous energy spectrum in the limit of zero momentum has a gap, i.e. it does not go to zero as it should by the Goldstone theorem for a symmetry-breaking theory [190]. Such inconsistency can be avoided by neglecting the anomalous average, as described in [191, 100, 192, 193]. Moreover by neglecting the terms such as $\langle\hat{\delta}^\dagger(\mathbf{r},t)\hat{\delta}(\mathbf{r},t)\hat{\delta}(\mathbf{r},t)\rangle$ the Hartee-Fock-Bogoliubov limit is missing information about the collisions with the thermal cloud and particle exchange between condensate and thermal cloud.

2.5.2 Beyond Mean-Field theory: The Zaremba-Nikuni-Griffin model

In the Zaremba-Nikuni-Griffin formalism the triplet term $\langle\hat{\delta}^\dagger(\mathbf{r},t)\hat{\delta}(\mathbf{r},t)\hat{\delta}(\mathbf{r},t)\rangle$ which counts for particle exchange is considered but the pair anomalous average contribution is neglected (called also 'Popov' approximation) [28, 27]. However, the role of the pair anomalous average is partly taken into account in the implicit manner in the particle-exchanging collisions terms. By substituting the Madelung trasformation of the condensate wavefunction in Eq. (2.84) the hydrodynamic equations are obtained:

$$\begin{cases} \frac{\partial n_{\mathrm{BEC}}}{\partial t} + \nabla(n_{\mathrm{BEC}}\mathbf{v}_{\mathrm{BEC}}) = \frac{2g}{\hbar}\mathrm{Im}[\psi^*\langle\hat{\delta}^\dagger\hat{\delta}\hat{\delta}\rangle] \equiv -\mathit{\Gamma}_{12}(\mathbf{r},t), \\ m\frac{d\mathbf{v}_{\mathrm{BEC}}}{dt} = -\nabla\mu_{\mathrm{BEC}}(\mathbf{r},t) = -\nabla(\mu_0(\mathbf{r},t) + 2gn_{\mathrm{th}}(\mathbf{r},t)), \end{cases} \tag{2.90}$$

where $\mathit{\Gamma}_{12}(\mathbf{r},t)$ is the particle-exchange term (which will be described in the following section), $\mu_{\mathrm{BEC}}(\mathbf{r},t)$ is the time-dependent chemical potential at finite temperature, while $\mu_0(\mathbf{r},t)$ is the chemical potential at $T=0$ when only the condensate is present, and it is defined in Eq. (2.21), and thus:

$$\mu_{\mathrm{BEC}}(\mathbf{r},t) = -\frac{\hbar^2\nabla^2\sqrt{n_{\mathrm{BEC}}(\mathbf{r},t)}}{2m\sqrt{n_{\mathrm{BEC}}(\mathbf{r},t)}} + V_{\mathrm{ext}}(\mathbf{r}) + gn_{\mathrm{BEC}}(\mathbf{r},t) + 2gn_{\mathrm{th}}(\mathbf{r},t). \tag{2.91}$$

Equivalently to the hydrodynamic equations Eq. (2.90) and Eq. (2.91) we solve the time-dependent dissipative Gross-Pitaevskii equation on the condensate wavefunction:

$$i\hbar\frac{\partial\psi(\mathbf{r},t)}{\partial t} = \left[-\frac{\hbar^2}{2m}\nabla^2 + V_{\mathrm{ext}}(\mathbf{r}) + g(n_{\mathrm{BEC}}(\mathbf{r},t) + 2n_{\mathrm{th}}(\mathbf{r},t)) - iR(\mathbf{r},t)\right]\psi(\mathbf{r},t), \tag{2.92}$$

where $R(\mathbf{r},t) \equiv \hbar\Gamma_{12}/(2n_{\mathrm{BEC}})$ is the dissipative or source (or 'growth') term which is of second-order in the interaction strength, i.e. depends on g^2. Such a term facilitates the condensate number to change in time due to particle exhange with the thermal cloud. The corresponding equation for the thermal cloud is:

$$\begin{aligned}
i\hbar\frac{\partial\hat{\delta}(\mathbf{r},t)}{\partial t} &= \left[-\frac{\hbar^2}{2m}\nabla^2 + V_{\mathrm{ext}}(\mathbf{r}) + 2gn_{\mathrm{tot}}(\mathbf{r},t)\right]\hat{\delta}(\mathbf{r},t) \\
&- 2gn_{\mathrm{th}}(\mathbf{r},t)\hat{\delta}(\mathbf{r},t) + g\psi^2(\mathbf{r},t)\hat{\delta}^\dagger(\mathbf{r},t) \\
&+ g\psi^*(\mathbf{r},t)(\hat{\delta}(\mathbf{r},t)\hat{\delta}(\mathbf{r},t) - m(\mathbf{r},t)) \\
&+ 2g\psi(\mathbf{r},t)(\hat{\delta}^\dagger(\mathbf{r},t)\hat{\delta}(\mathbf{r},t) - n_{\mathrm{th}}(\mathbf{r},t)) \\
&+ g(\hat{\delta}^\dagger(\mathbf{r},t)\hat{\delta}(\mathbf{r},t)\hat{\delta}(\mathbf{r},t) - \langle\hat{\delta}^\dagger(\mathbf{r},t)\hat{\delta}(\mathbf{r},t)\hat{\delta}(\mathbf{r},t)\rangle),
\end{aligned} \tag{2.93}$$

where $n_{\mathrm{tot}} = n_{\mathrm{BEC}} + n_{\mathrm{th}}$ is the total density. Such kinetic formalism, originally developed by Kirkpatrick and Dorfman [136–138] in the 1980s, was subsequently extented to an inhomogeneous partly-condensed bosonic gas by Zaremba-Nikuni-Griffin [26, 28, 27].

The Zaremba-Nikuni-Griffin model is based on describing the system in terms of the Wigner distribution function $f(\mathbf{p},\mathbf{r},t)$ [194] which for an atom at position $\mathbf{r}$ with momentum $\mathbf{p}$ at time t is defined as the expectation value of the Wigner operator, i.e. $f(\mathbf{p},\mathbf{r},t) = \langle\hat{f}(\mathbf{p},\mathbf{r},t)\rangle$. The Wigner operator is related to the non-condensate operator as:

$$\hat{f}(\mathbf{p},\mathbf{r},t) = \int d\mathbf{r}' e^{i\mathbf{p}\cdot\mathbf{r}/\hbar}\hat{\delta}^\dagger\left(\mathbf{r}+\frac{\mathbf{r}'}{2},t_0\right)\hat{\delta}\left(\mathbf{r}-\frac{\mathbf{r}'}{2},t_0\right). \tag{2.94}$$

Thus the thermal density is obtained as:

$$n_{\mathrm{th}}(\mathbf{r},t) = \int \frac{d\mathbf{p}}{(2\pi\hbar)^3} f(\mathbf{p},\mathbf{r},t). \tag{2.95}$$

The expectation value of the Wigner operator can be found from the trace of $\langle\hat{f}(\mathbf{p},\mathbf{r},t)\rangle = \mathrm{Tr}\rho(t,t_0)\hat{f}(\mathbf{p},\mathbf{r},t)$ where $\rho(t,t_0)$ is the density matrix that satisfies the equation:

$$i\hbar\frac{d\rho(t,t_0)}{dt} = [\hat{H}_{\mathrm{eff}}(t), \rho(t,t_0)]. \tag{2.96}$$

The effective potential $\hat{H}_{\mathrm{eff}}$ is the sum of the unperturbed Hartee-Fock hamiltonian $\hat{H}^0_{\mathrm{HF}}$ and the perturbative hamiltonian $\hat{H}'(t)$ where:

$$\hat{H}^0_{\mathrm{HF}}(t) = \int d\mathbf{r}\hat{\delta}^\dagger\left(-\frac{\hbar^2\nabla^2}{2m} + U^{\mathrm{th}}_{\mathrm{eff}}(\mathbf{r},t)\right)\hat{\delta}, \tag{2.97}$$

and $\hat{H}'$ takes into account the multiple non-condensate operator terms described in [195, 28, 27]. From the kinetic theory of gases, the time evolution of the distribution function

$f(\mathbf{p},\mathbf{r},t)$ in an external field $U_{\text{eff}}(\mathbf{r},t)$ is described by:

$$\frac{df}{dt} = \frac{\partial f}{\partial t} + \mathbf{v}\cdot\nabla_{\mathbf{r}} f - (\nabla_{\mathbf{r}} U^{\text{th}}_{\text{eff}})\cdot(\nabla_{\mathbf{p}} f), \tag{2.98}$$

where $\nabla_{\mathbf{r}}$ and $\nabla_{\mathbf{p}}$ indicate the spatial and momentum gradients. In the case of no collisions $df/dt = 0$, and this is the Liouville equation. In the presence of collisions instead, the rate of temporal change df/dt is given by the collisional integral $\mathrm{C}[f]$. Taking into account that

$$\frac{df(\mathbf{p},\mathbf{r},t)}{dt} = \frac{1}{i\hbar}\mathrm{Tr}\rho(t,t_0)\left[\hat{f}(\mathbf{p},\mathbf{r},t),\hat{H}'(t)\right], \tag{2.99}$$

the ‘Quantum Boltzmann equation’ [126, 196] is obtained for the Wigner distribution function:

$$\frac{\partial f}{\partial t} + \mathbf{v}\cdot\nabla_{\mathbf{r}} f - (\nabla_{\mathbf{r}} U^{\text{th}}_{\text{eff}})\cdot(\nabla_{\mathbf{p}} f) = \mathrm{C}_{12}[f,\psi] + \mathrm{C}_{22}[f]. \tag{2.100}$$

Here, the first collisional term includes the collisions between the thermal and condensate particles which cause particle transfer between the two subsystems, while the second term includes collisions between the thermal particles which re-distributed the thermal atoms between the single-particle states. The destruction of a particle in the state i is given by the single-particle distribution function $f_i \equiv f(\mathbf{p}_i,\mathbf{r},t)$ while the inverse process of the creation of a particle in the state i is described by a statistical factor of $(1+f_i)$. In the semiclassical approximation, the thermal excitation spectrum is given by $\varepsilon_i = \mathbf{p}^2/2m + U^{\text{th}}_{\text{eff}}(\mathbf{r},t)$. By considering only binary collisions, the collisional terms can be expressed as:

$$\begin{aligned}\mathrm{C}_{12}[f,\psi] = {}& \frac{4\pi}{\hbar} g^2|\psi|^2 \int \frac{d\mathbf{p}_2}{(2\pi\hbar)^3}\int \frac{d\mathbf{p}_3}{(2\pi\hbar)^3}\int \frac{d\mathbf{p}_4}{(2\pi\hbar)^3} \\ & \times (2\pi\hbar)^3\delta(m\mathbf{v}_{\text{BEC}} + \mathbf{p}_2 - \mathbf{p}_3 - \mathbf{p}_4)\times\delta(\varepsilon_{\text{BEC}} + \varepsilon_2 - \varepsilon_3 - \varepsilon_4) \\ & \times (2\pi\hbar)^3[\delta(\mathbf{p}-\mathbf{p}_2) - \delta(\mathbf{p}-\mathbf{p}_3) - \delta(\mathbf{p}-\mathbf{p}_4)]\times[(f_2+1)f_3f_4 - f_2(f_3+1)(f_4+1)],\end{aligned} \tag{2.101}$$

where the δ function expresses the conservation of the energy and momentum. The terms ε_{BEC} and $m\mathbf{v}_{\text{BEC}}$ are the condensate energy and momentum respectively, such that $\varepsilon_{\text{BEC}} = (1/2)m\mathbf{v}^2_{\text{BEC}} + \mu_{\text{BEC}}$. The $\mathrm{C}_{12}[f,\psi]$ term is related to the source term $R(\mathbf{r},t)$ (conserving so the total particle number) in the dissipative GPE Eq. (2.92) as:

$$R(\mathbf{r},t) = \frac{\hbar}{|\psi(\mathbf{r},t)|^2}\int \frac{d\mathbf{p}}{(2\pi\hbar)^2}\mathrm{C}_{12}[f(\mathbf{p},\mathbf{r},t)]. \tag{2.102}$$

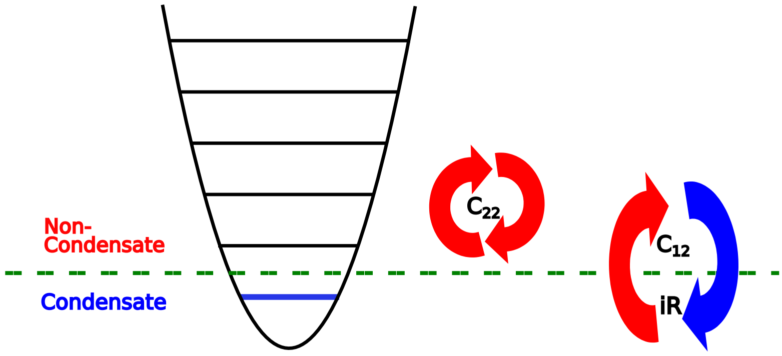

Figure 2.5: The collisional mechanisms included in the ZNG model. The red arrows show the collision process that includes the non-condensate particles and that are described in the Quantum Boltzmann equation (QBE) while the blue arrows indicate the collisions including condensate particles and that are described in the dissipative GPE.

The collisional integral within the thermal cloud is given by:

$$\begin{aligned} \mathrm{C}_{22}[f] = \frac{4\pi}{\hbar} g^2 \int \frac{d\mathbf{p}_2}{(2\pi\hbar)^3} \int \frac{d\mathbf{p}_3}{(2\pi\hbar)^3} \int \frac{d\mathbf{p}_4}{(2\pi\hbar)^3} \\ \times (2\pi\hbar)^3 \delta(\mathbf{p} + \mathbf{p}_2 - \mathbf{p}_3 - \mathbf{p}_4) \times \delta(\varepsilon + \varepsilon_2 - \varepsilon_3 - \varepsilon_4) \\ \times [(f+1)(f_2+1) f_3 f_4 - f f_2 (f_3+1)(f_4+1)]. \end{aligned} \tag{2.103}$$

The scattering amplitude $(f+1)(f_2+1)f_3f_4$ describes the collision process between two incoming thermal particles that are in states 3 and 4 (i.e f_3f_4) but the outgoing particles are distributed between state 1 and 2 after the collision (i.e. $(f+1)(f_2+1)$). The inverse process is describing by the scattering amplitude $ff_2(f_3+1)(f_4+1)$. The collisional integral $\mathrm{C}_{12}[f,\psi]$ can be expressed as the sum of the two terms:

- the 'in' collision $\mathrm{C}_{12}^{\mathrm{in}}$ in which two incoming thermal particles in the states 3 and 4 collide together and one particle is transfered to the condensate and the other to the state 2 (described by the statistical factor $(f_2+1)f_3f_4$).

- the 'out' collision $\mathrm{C}_{12}^{\mathrm{out}}$ in which a thermal particle in the state 2 collides with a condensate particle and both are then transfered to the states 3 and 4 of the thermal cloud $(f_2(f_3+1)(f_4+1))$.

If the condensed and non-condensed clouds are out of equilibrium there is a particle exchange between the two subsystems which ends once the two clouds are in 'diffusive' equilibrium leading to $\mathrm{C}_{12} = 0$. Equations (2.92) and (2.100) are the main equations of the ZNG model. The presence of the thermal cloud density in the equation of motion of the condensate wavefunction (the dissipative GPE) and the presence of the condensate density in the Quantum Boltzmann Equation indicate that these two equations should be solved self-consistently. Given the different nature of these two equations, they are solved from very different approaches, using a quantum-mechanical approach for the condensate wavefunction and a semiclassical approximation for the thermal atoms.

2.5.3 Numerical solution

A self-consistent kinetic model with collisions was first derived for a homogeneous bosonic ultracold gas in Refs. [136–138]. Then, the model was revisited for the specific case of an inhomogeneous single-component BEC [28, 26, 27], an inhomogeneous spinor BEC [197, 198], and Bose-Bose mixtures [158, 157, 148, 156]. The first numerical implementation of the ZNG code was achieved by Jackson and Zaremba [199] and this code has been used and adapted for different studies such as the study of topological defect dynamics in finite temperature BEC [112, 110, 110, 115–117], the study of first and second sound in a highly elongated trap [200], the study of evaporative cooling [134] and collective modes [201, 202, 148, 105]. The ZNG model has found very good agreement with the experimental data on the study of collective modes such as quadrupole [202] and scissors modes [105]; for the study of topological defect dynamics [110]; surface evaporative cooling [134] and multi-component BECs [156]. The results shown in this thesis are achieved by adapting for our geometry (double-well harmonic potential) the version of ZNG code written by Dr. Kean Loon Lee [148] for a single-component BEC. In this section we briefly describe the numerical procedure used to solve the generalized GPE equation and the Quantum Boltzmann equation [28, 199, 203].

As a first step we obtain the equilibrium distribution for both the condensate and thermal cloud. At equilibrium the collisional integrals and the source term vanish. Therefore, the condensate equilibrium state is found by solving the generalized GPE equation (2.92) for $R = 0$ in imaginary time propagation, which after substituting $\psi(\mathbf{r}, t) = \mathrm{e}^{-\mathrm{i}\mu_0 \mathrm{t}/\hbar}\psi_0(\mathbf{r})$ becomes:

$$\left(-\frac{\hbar^2}{2m}\nabla^2 + V_{\mathrm{ext}}(\mathbf{r}) + g|\psi_0(\mathbf{r})|^2 + 2gn^0_{\mathrm{th}}(\mathbf{r})\right)\psi_0(\mathbf{r}) = \mu_0\psi_0(\mathbf{r}), \tag{2.104}$$

with $n^0_{\mathrm{th}}(\mathbf{r})$ the equilibrium thermal cloud density. An initial guess of the condensate wavefunction is given by the Thomas-Fermi wavefunction Eq. (2.16) and then it is propagated in imaginary time. For the equilibrium thermal cloud density instead the Hartee-Fock semiclassical approximation is used and it is calculated by the integration in momentum space of the equilibrium phase-space distribution function $f_0(\mathbf{p}, \mathbf{r})$:

$$n^0_{\mathrm{th}}(\mathbf{r}) = \int \frac{d\mathbf{p}}{2\pi\hbar^3} f_0(\mathbf{p}, \mathbf{r}), \tag{2.105}$$

with $f_0(\mathbf{p},\mathbf{r})$ defined as

$$f_0(\mathbf{p},\mathbf{r}) = \frac{1}{\mathrm{e}^{\beta(\mathrm{p}^2/2\mathrm{m}+\mathrm{U}_{\mathrm{eff}}^{\mathrm{th},0}-\mu_0)}}, \tag{2.106}$$

with $\beta = 1/(k_B T)$ and $U_{\mathrm{eff}}^{th,0}$ is the effective potential felt by the thermal cloud in equilibrium whose expression is given by the Eq. (2.88) with the substitution of the equilibrium densities. The initial guess for the thermal cloud density is thus obtained by

$$n_{\mathrm{th}}^0 = g_{3/2}(z_0(\mathbf{r}))/\lambda_{\mathrm{dB}}, \tag{2.107}$$

where $g_{3/2}$ is the Bose function, λ_{dB} is the thermal or de Broglie wavelength also defined in Eq. (1.1) as

$$\lambda_{dB} = \frac{h}{\sqrt{2\pi m k_B T}}, \tag{2.108}$$

and the z_0 here is the equilibrium local fugacity:

$$z_0 = \mathrm{e}^{\beta(\mu_0 - U_{\mathrm{eff}}^{\mathrm{th},0})}. \tag{2.109}$$

The time-independent generalized GPE equation (due to the presence of the thermal cloud mean-field potential) is solved self-consistently with the QBE equation (2.100) (for $C_{12} = C_{22} = 0$). This is done for each time-step and this iteration process continues until the condensate chemical potential and the thermal cloud particle number are within the tolerance limit specified by us. The condensate and thermal cloud equilibrium states are then used in order to study the dynamics.

The condensate dynamics is described by solving the time-dependent dissipative or generalized GPE equation (2.92) with the Fourier split-step method while the QBE is solved with Monte-Carlo method [204, 205]. In order to construct the thermal cloud distribution function, a large number of test particles (typically in our case we have 7x10^6 test particles) are generated. As an initial guess of the test particle distribution function in phase-space we use

$$f(\mathbf{p},\mathbf{r},t) \simeq \gamma(2\pi\hbar)^3 \sum_{j}^{N_{\mathrm{t.p.}}} \delta(\mathbf{r}-\mathbf{r}_j(t))\delta(\mathbf{p}-\mathbf{p}_j(t)) \tag{2.110}$$

with $\mathbf{r}$ and $\mathbf{p}$ the particle position and momentum and with γ a scale factor which gives the number of thermal particles that are represented by $N_{\mathrm{t.p.}}$ test particles. Such test particles evolve in time (in an effective potential $U_{\mathrm{eff}}^{\mathrm{th}}$) according to Newton's equations of motion

$$\begin{aligned}\frac{d\mathbf{r}_j(t)}{dt} &= \frac{\mathbf{p}_j}{m},\\ \frac{d\mathbf{p}_j(t)}{dt} &= -\nabla U_{\mathrm{eff}}^{\mathrm{th}},\end{aligned} \tag{2.111}$$

which is solved by using Symplectic Integration [28, 203]. In this way the left-part of Eq. (2.100) is solved. In order to calculate the collisional integral the test particles are divided into spatial cells [206, 207]. The shape of these bins is chosen based on the trapping geometry and for our three-dimensional anisotropic geometry we use cubic bins. In order to calculate the collision probabilities, the test particles are re-binned in secondary smaller cells. Pairs of particles belonging to the same cell are randomly selected and then the probability for such particle to undergo a collisional process is calculated, using the acceptance-rejection method [28, 199]. Then such probabilities are used to calculate the source term R appearing in the dissipative GPE equation. Moreover some smoothing of the condensate and noncondensate densities (which present spatial fluctuations) is performed by convolving the effective potential with a Gaussian [28, 199, 203]. In particular, such smoothing is necessary when studying the dynamics because the presence of large spatial fluctuations could lead to non-smooth thermal cloud density.

Part II

Dynamical regimes and vortex dynamics in an atomic Josephson-Junction

Chapter 3

Modeling the LENS experiment: From dissipationless to the dissipative regime

In the presence of a chemical potential difference between two parts of a superfluid coupled by a barrier, the superflow is accelerated through the barrier (or through an orifice as in superfluid helium). This makes the relative phase change in time according to the Josephson-Anderson relation Eq. (1.16). In an atomic Josephson junction the initial chemical potential difference can be imposed by an initial non-zero population imbalance $z_0 = z(t = 0)$ between the two reservoirs. Here, the population imbalance is defined as

$$z(t) = \frac{N_R(t) - N_L(t)}{N}, \tag{3.1}$$

with N_L (N_R) the BEC particle number in the left (right) reservoir, and $N = N_L + N_R$ the total condensate particle number. In fact, as shown in Eq. (2.61), the initial relative population corresponds to a chemical potential difference $\mathit{\Delta}\mu = \mu_L - \mu_R = E_c z_0 N/2$ where E_c is the onsite interaction energy, also known as 'charging' energy in analogy with superconductors. For barrier heights larger than the chemical potential μ, the superfluid dynamics through the barrier happens only via tunneling where the coherent dynamics of atomic Josephson junctions (JJs) [59, 60, 208, 61, 41, 187, 42, 46–48, 65, 50, 51] is governed by the competition between the onsite interaction energy E_c and the Josephson tunneling energy E_J [59–61] (more details can be found in Sect. 2.3.2). The tunneling energy E_J promotes the delocalization of the superfluid across the two reservoirs and sets the maximum coherent flow through the weak link. When E_J dominates, superfluid current and relative phase oscillate in quadrature at the Josephson plasma frequency. In the opposite regime, and in the absence of dissipation [60, 208], the system may enter the

Macroscopic Quantum Self-Trapping (MQST) regime. This is characterized by coherent oscillations of the population imbalance around a non-zero value, driven by a monotonically increasing relative phase [59, 61, 187, 42, 46, 47] (see also Chapt. 5). Even without thermally induced decay of the population imbalance [46, 208, 63], the stability of MQST depends on whether vortices nucleated inside the barrier annihilate therein [209, 83], or penetrate into the superfluid reservoirs. Recent experiments with inhomogeneous three-dimensional Fermi superfluids [49, 20] revealed the intimate connection between phase slippage and dissipation arising from vortices created within the barrier and shed into the superfluid. Similar effects have been studied in ring-shaped bosonic condensates [18, 21, 54, 55], mesoscopic structures [22, 23] (some of the experimental results of [22] are also brought in Sect. 1.4) and lower-dimensional geometries [56–58].

Motivated by the experiment of Refs. [49, 20] which consists of two weakly coupled ^{6}Li fermionic superfluids through a Gaussian barrier in an elongated three dimensional trap, we model such experiment in the limit of BEC of molecules of ^{6}Li (the main experimental results are also reported in Sect. 1.4). In this chapter we present a theoretical study at $T = 0$, for the particular experimental geometry and parameters. We characterise the dynamical regimes emerging and give a detailed microscopic description of the mechanisms leading to dissipation such as the nucleation and early-stage dynamics of topological defects (which we show that in our three dimensional geometry consist of vortex rings) and associated sound waves [90]. The comparison with the experiment at small finite temperature is shown in the Chapt. 4.

For the experimental range of barrier heights $[0.6, 1.22]\mu$ and a fixed $1/e^2$ barrier width of $w/\xi = 4$ (where ξ is the mean healing length) two dynamical regimes are found depending on the initial value of the population imbalance: the Josephson 'plasma' oscillations regime and the dissipative regime.

3.1 Numerical simulations

One of the most fascinating properties of ^{6}Li is the presence of the Feshbach resonance (described in Sect. 2.2) between its two lowest spin states $|F = 1/2, m_F = \pm 1/2\rangle$ [49, 20] making possible the change of the interaction strength through a change in the magnetic field. In this way, it is possible to go from the limit of condensates of molecules of lithium to the limit of BCS superfluids. However, the focus of this work is on the regime of superfluidity of the molecular BEC, and we restrict our modelling to the case of $1/(k_F a) \simeq 4.6$ where $k_F = \sqrt{2mE_F}/\hbar$ is the Fermi wave-vector, m is the ^{6}Li atomic mass, E_F the Fermi energy and a is the interatomic tunable s-wave scattering length. Thus, the quantum transport properties of the molecular BEC through the thin barrier at $T = 0$ are studied by solving the time-dependent Gross-Pitaevskii equation (GPE) defined in Eq. (2.15)

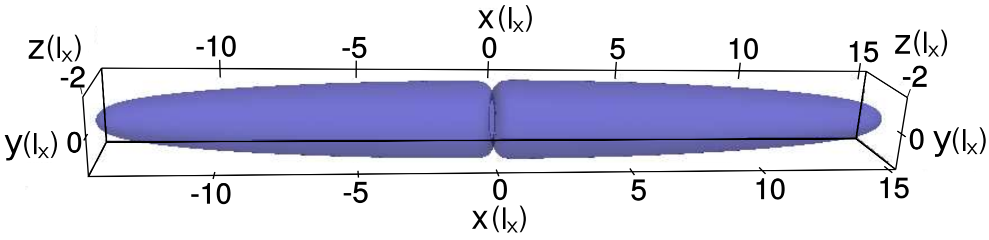

Figure 3.1: The three dimensional isocontour density profile (taken at 0.002 of maximum density) of the elongated atomic Josephson junction, with a barrier height of $V_0/\mu = 0.8$, barrier width of $w/\xi = 4$ and an initial relative imbalance of $z_0 = 0.17$.

[185, 184, 72]

$$i\hbar\frac{\partial\psi(\mathbf{r},t)}{\partial t} = \left(-\frac{\hbar^2}{2M}\nabla^2 + V_{\text{ext}}(\mathbf{r}) + g|\psi(\mathbf{r},t)|^2\right)\psi(\mathbf{r},t), \tag{3.2}$$

where $\psi(\mathbf{r},t)$ is the molecular condensate wavefunction, $g = 4\pi\hbar^2 a_M/M$ is the interaction strength with $a_{\text{M}} \simeq 0.6\,a$ [165] the molecular scattering length, $M = 2m$ the molecule mass and V_{ext} is the external potential.

In this thesis we study atomic Josephson junctions, which are realized experimentally by focusing into the atomic cloud a Gaussian-shaped repulsive sheet of light (blue-detuned with respect to the atomic main transition) which separates the superfluid into two reservoirs yielding a double-well trapping potential

$$V_{\text{trap}}(x,y,z) = \tfrac{1}{2}M({\omega_x}^2x^2 + {\omega_y}^2y^2 + {\omega_z}^2z^2) + V_0\cdot e^{-2x^2/w^2}, \tag{3.3}$$

where $\omega_{x,y,z}$ are the trapping frequencies along x, y and z directions, V_0 is the height of the Gaussian barrier and w is the barrier $1/e^2$ width. In order for the two-reservoirs to be coupled to each other, the barrier width w must be comparable to the superfluid mean healing length ξ and in our case it is set to $w = 4\xi$, which is $w \approx 2.0\mu$m. Moreover the Gaussian barrier in Eq. (3.3) depends only on the x axis, as the experimental barrier has a $1/e^2$ width of around 840 μm along the y and z direction which is much larger than the superfluid transverse extension. In this way the barrier can be considered as homogeneous along the transverse direction. We solve the Eq. (3.2) in dimensionless form where the lengths are expressed in units of harmonic oscillator length along the x axis $l_x = \sqrt{\hbar/M\omega_x}$, i.e. $\tilde{\mathbf{r}} = \mathbf{r}/l_x$, the energies are expressed in units of $\hbar\omega_x = h\nu_x$, i.e. $\tilde{E} = E/\hbar\omega_x$, the time in units of $1/\omega_x$, i.e. $\tilde{t} = \omega_x t$, the wavefunction $\tilde{\psi} = l_x^{3/2}\psi$ and interaction strength $\tilde{g} = g/(l_x^3\hbar\omega_x)$. In these units Eq. (3.2) becomes:

$$i\frac{\partial\psi(\mathbf{r},t)}{\partial t} = \left(-\frac{1}{2}\nabla^2 + V_{\text{ext}}(\mathbf{r}) + g|\psi(\mathbf{r},t)|^2\right)\psi(\mathbf{r},t), \tag{3.4}$$

where tildes have been dropped from this equation onwards for simplicity of notation. In these scaled units the trapping potential is expressed as

$$V_{\text{trap}}(x,y,z) = \frac{1}{2}\left(x^2 + \left(\frac{\omega_y}{\omega_x}\right)^2 y^2 + \left(\frac{\omega_z}{\omega_x}\right)^2 z^2\right) + V_0 \cdot e^{-2x^2/w^2}, \tag{3.5}$$

where V_0 is the barrier height in units of $\hbar\omega_x$. The experimental trap frequencies are $\omega_x = 2\pi \times 15$ Hz, $\omega_y = 2\pi \times 187$ Hz $= 12.47\ \omega_x$ and $\omega_z = 2\pi \times 148$ Hz $= 9.87\ \omega_x$, corresponding to a cigar-shaped trap (as shown in the Fig. 3.1). The harmonic oscillator length along x axis is $l_x = 7.5\mu$m. Fig. 3.1 shows the isocontour three-dimensional condensate density profile for 6×10^4 molecules, where the Thomas-Fermi radii along three directions are respectively $R_{\text{TF,x}} = 14.5l_x = 109\mu$m, $R_{\text{TF,y}} = 1.2l_x = 9\mu$m and $R_{\text{TF,z}} = 1.5l_x = 11.2\mu$m. The superfluid dynamics through the barrier is triggered by the creation of an initial population imbalance, z_0, between the two wells. Numerically it is achieved by adding a linear potential, $-\epsilon x$, along the x direction to the trapping potential (3.5), i.e. $V_{\text{ext}} = V_{\text{trap}} - \epsilon x$, which shifts the x axis harmonic trap center with respect to the barrier center. In our case ϵ is positive, meaning that the initial population is larger in the right well. Therefore, the initial flow is induced from right to left in the negative x direction. In order to find the equilibrium state in this configuration, the GPE equation is solved in imaginary time propagation, after substituting $\psi(\mathbf{r},t) = \psi_0(\mathbf{r})\exp(-i\mu t)$ in Eq. (3.4):

$$\mu\psi(\mathbf{r}) = \left(-\frac{1}{2}\nabla^2 + V_{\text{ext}} + g|\psi(\mathbf{r})|^2\right)\psi_0(\mathbf{r}), \tag{3.6}$$

with μ the system chemical potential.

The BEC dynamics instead is initiated by the instantaneous linear potential removal at time $t = 0$, i.e. by solving Eq. (3.4) with trapping potential V_{trap} as defined in Eq. (3.5). In our numerical simulations we use grid sizes $[-24, 24]\, l_x, [-4, 4]\, l_x, [-4, 4]\, l_x$ along the x, y and z directions, and $1024 \times 128 \times 128$ grid points respectively, i.e. with grid spacing $\Delta x = 0.0469 l_x$, $\Delta y = \Delta z = 0.0625 l_x$, and a time step of $\Delta t = 10^{-4}\omega_x^{-1}$. In this chapter the molecule number is set to $N = 6 \times 10^4$. The numerically-extracted equilibrium μ is well approximated by the analytical formula in the Thomas-Fermi approximation Eq. (2.18) which gives $\mu = 114\hbar\omega_x$ for our system parameters. Throughout this chapter, the barrier width is set to be equal to the experimental value of $w = 4\xi$, where $\xi = \hbar/(\sqrt{2\mu M}) \simeq 0.5\,\mu\text{m} \simeq\ 0.067\, l_{\text{x}}$. In analyzing our results, we express the barrier height V_0 in units of the system chemical potential μ.

3.2 The superfluid instability

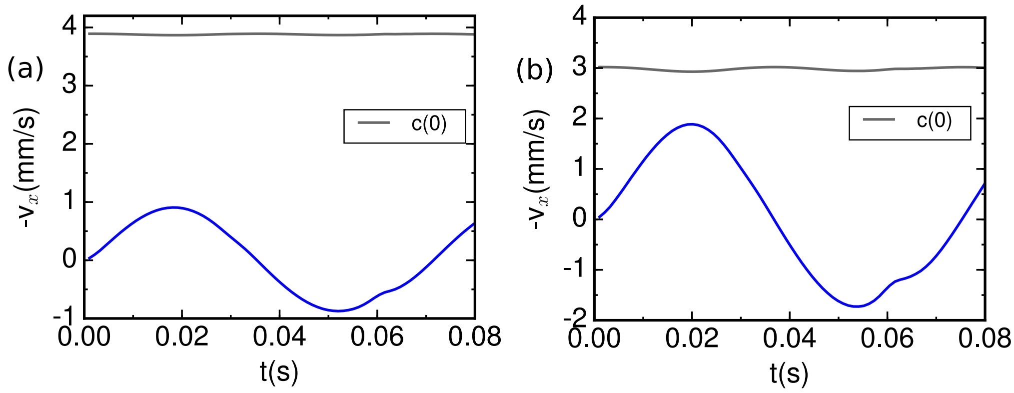

Figure 3.2: The temporal evolution of the x component of the superfluid velocity (blue line) at the trap center for $V_0/\mu = 0.9$ (a) and $V_0/\mu = 1.1$ (b) for $z_0 = 0.03$ which is smaller than the critical imbalance for both cases. The grey curve represents the speed of sound at the trap center.

The superfluid dynamics across a barrier is governed by the Josephson-Anderson relation Eq. (1.16), from which Eq. (1.17) for the superfluid acceleration can be derived and it can be written as [12, 14, 15]

$$M\dot{\mathbf{v}} = -\nabla\mu. \tag{3.7}$$

Such an equation states that the presence of a chemical potential gradient $\nabla\mu$ between the two sides of the barrier drives a unidirectional, accelerated superfluid flow across the junction, which in our case happens along the negative x axis. The superfluid velocity $\mathbf{v}$ can be found from the expression

$$\mathbf{v}(\mathbf{r}, t) = \frac{\mathbf{j}(\mathbf{r}, t)}{n(\mathbf{r}, t)}, \tag{3.8}$$

where $n(\mathbf{r}, t)$ is the condensate density and $\mathbf{j}(\mathbf{r}, t)$ is the condensate current density of probability:

$$\mathbf{j} = \frac{\hbar}{2iM}(\psi^*\nabla\psi - \psi\nabla\psi^*). \tag{3.9}$$

Given the symmetry of our junction, we consider the x-component of the superfluid velocity v_x and we calculate it at the trap center, i.e. at $x = y = z = 0$. As the superfluid flows along the negative x axis, we show $-v_x$ value for simplicity in Fig. 3.2. Driven by the initial imbalance, i.e. by the initial chemical potential difference $\Delta\mu_0$ across the barrier, the superfluid velocity $-v_x$ increases, starting from an initial value equal to zero. For small enough initial imbalance values, i.e. $z_0 < z_{\rm cr}$ with $z_{\rm cr}$ being the critical imbalance, $-v_x$ is found to oscillate harmonically around the zero value, as shown in Fig. 3.2. This regime is characterized by coherent oscillations of the imbalance and of the relative phase (shown in Sect. 3.3.1) and is henceforth labelled as Josephson 'plasma' oscillations regime.

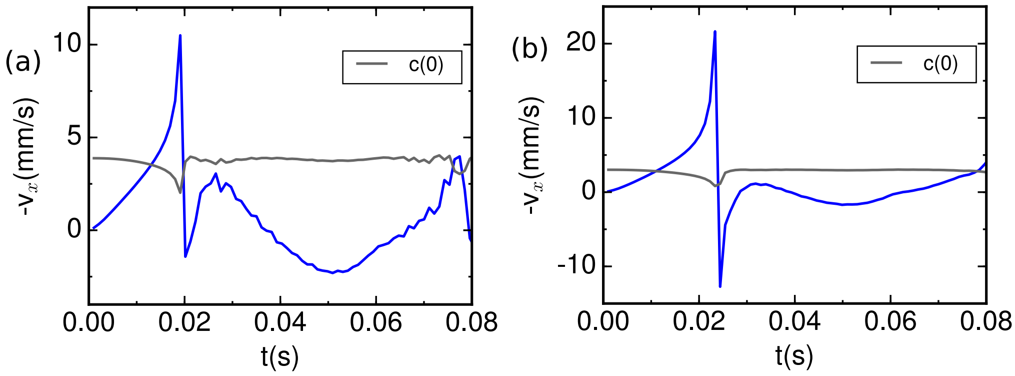

Figure 3.3: The temporal evolution of the x-component of the superfluid velocity (blue line) and the speed of sound (grey line) at the trap center for $V_0/\mu = 0.9$ (a) and $V_0/\mu = 1.1$ (b) for $z_0 \simeq z_{\rm cr}(V_0)$.

Following Landau [11] and Feynman [13] arguments on the critical velocity v_c (described in Sect. 2.1.2) it must exist a critical velocity such that if the maximum superfluid velocity exceeds such value excitations are generated in the system. In our case we find that the local speed of sound at the trap center $c(0) = \sqrt{gn(0)/M}$ gives an estimation of the critical velocity. A more detailed study perfomed in Chapt. 4 that takes into account also the condensate transverse extension at $x = 0$ shows that a better estimation for the critical velocity in our system is given by the mean speed of sound $\langle c \rangle = \sqrt{\mu/2M}$. Fig. 3.2 shows that in the coherent Josephson 'plasma' regime the maximum superfluid velocity is smaller than the local speed of sound. The numerical data in such figure are for $V_0/\mu = 0.9$ (a), $V_0/\mu = 1.1$(b) and for the same $z_0 = 0.03$, which is smaller than the critical value for both barrier heights. In both cases, as the initial imbalance increases, the superfluid initial acceleration becomes larger and for $z_0 \simeq z_{\rm cr}(V_0)$ the superfluid local maximum velocity temporally exceeds the local speed of sound (as shown in Fig. 3.3). Thus, the superfluid becomes unstable and it becomes energetically favourable for a topological defect to be generated at the barrier at $x = 0$. In our three dimensional geometry the topological defect nucleated is a vortex ring (VR) as revealed by the three-dimensional density isosurface shown in Fig. 3.4.

The critical imbalance at which the vortex rings are generated depends on the barrier height and it is smaller for higher barrier heights (as described in Sect. 3.3). In fact, in Fig. 3.2 we observe that for $V_0/\mu = 1.1$ the local speed of sound is smaller than the corresponding value at $V_0/\mu = 0.9$ as the condensate density at the trap center becomes smaller. Moreover, for the same initial imbalance, the superfluid local maximum velocity achieves larger values at higher $V_0/\mu = 1.1$ as the junction is thinner. Therefore at higher

V_0, the superfluid velocity reaches the local speed of sound for smaller critical imbalance.

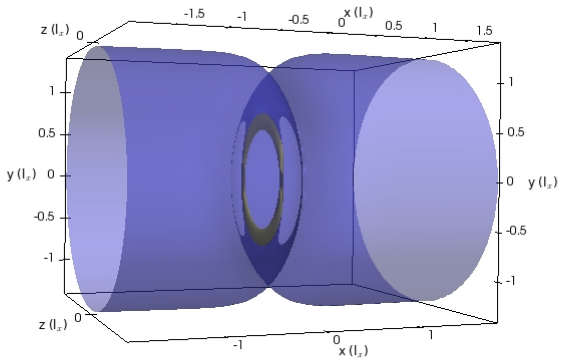

Figure 3.4: The three dimensional density profile with the density isosurface taken at 0.002 of the maximum density, shown in the x range $[-2, 2]$ l_x and at time $t = 12.30$ms when the vortex ring enters the local TF surface. The data are for barrier height of $V_0/\mu = 0.8$, the barrier width $w/\xi = 4$ and an initial relative imbalance $z_0 = 0.17 > z_{\rm cr} = 0.11$. The vortex ring is colored in yellow.

3.3 Dynamical regimes

We study the temporal evolution of the population imbalance $z(t)$, varying both the initial population imbalance z_0 and the barrier height V_0. At each value of V_0 we observe two distinct dynamical regimes. For z_0 smaller than a critical value $z_{\rm cr}$, $z(t)$ exhibits sinusoidal 'plasma' oscillations (Josephson regime) as shown in Fig. 3.5 (left inset).

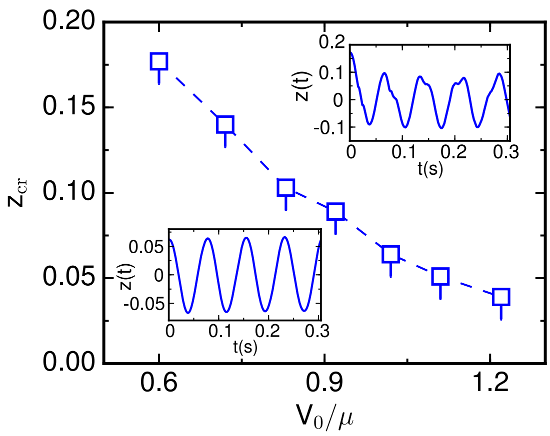

Figure 3.5: The critical imbalance as a function of the barrier height and for fixed barrier width $w/\xi = 4$ for the elongated trap at $T = 0$ and particle number $N = 6 \times 10^4$. In the inset is shown an example of the temporal evolution of the population imbalance in the Josephson 'plasma' oscillations regime (left subplot) and in the dissipative regime (right subplot) for $V_0/\mu = 0.8$.

For $z_0 \geqslant z_{\rm cr}$, we instead observe an initial rapid decay of $z(t)$ (dissipative regime) as shown in Fig. 3.5 [right inset]. Increasing V_0/μ, the onset of dissipation appears at smaller $z_{\rm cr}$ (see Fig. 3.5) which is consistent with our discussion in the previous section on how the barrier height affects v_x and c, and it has a similar profile to the superfluid maximum current shown in Sect. 3.6.1.

3.3.1 Josephson 'plasma' oscillations regime

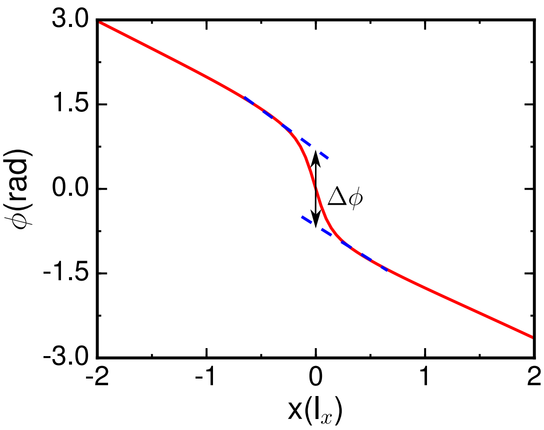

Figure 3.6: Phase profile along the x axis (for $y = z = 0$) (red line) plotted in the range $[-2, 2]l_x$ where the barrier center is at $x = 0$. The blue dashed lines are the linear fits of ϕ on the left and right sides of the barrier. The arrows indicate the relative phase $\Delta\phi$ calculated from the difference between the constants of the fits. These numerical data are for $V_0/\mu = 0.8$ and $z_0 = 0.17$ taken at $t = 10.6$ ms.

As the wavefunction is a complex quantity we extract its phase as

$$\phi(\mathbf{r}, t) = \arctan \frac{\mathrm{Im}\psi(\mathbf{r}, t)}{\mathrm{Re}\psi(\mathbf{r}, t)}. \tag{3.10}$$

The phase changes along x axis as shown in Fig. 3.6 characterised by a linear profile on the left and the right wells with its inclination defined by the superfluid velocity

$$v_x = \frac{\hbar}{m} \frac{\partial \phi}{\partial x}, \tag{3.11}$$

which is in agreement with the value of v_x found from Eq. 3.8. At the trap center, the phase has a step-like change due to the presence of the barrier. Thus in order to extract the relative phase between the two wells, we fit the phase in each side with a linear function, i.e. $\phi_{L(R)} = a_{L(R)}x + b_{L(R)}$, and the relative phase is then given by the difference between the two fitted constant values, i.e. $\Delta\phi = \phi_L - \phi_R = b_L - b_R$; this is indicated by the arrow in Fig. 3.6. It can be shown that the fit parameters $a_{L(R)}$ oscillate in time with the oscillation frequency of the population imbalance which is around 14.4Hz for these parameters. The results from the linear fit are shown in Fig. 3.6 as dashed blue lines with the fit performed in a narrow range around the barrier center.

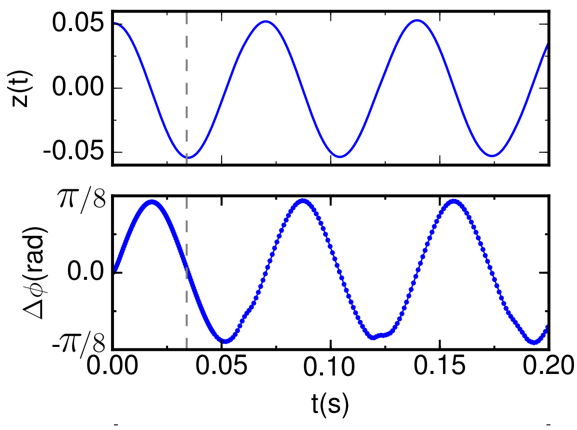

Figure 3.7: The temporal evolution of the population imbalance (a) and the relative phase (b) for $V_0/\mu = 0.8$ and $z_0 < z_{\mathrm{cr}}$.

The relative phase and the population imbalance are two canonically conjugate variables and in the Josephson 'plasma' regime ($z_0 < z_{\mathrm{cr}}$) they exhibit sinusoidal oscillations around a zero mean value with the same frequency, as observed from Fig. 3.7. In fact, the equilibrium state (i.e. at $t = 0$) has an initial imbalance between the two-wells but no phase difference and the relative phase is built in time due to the presence of z_0, i.e. $\Delta\mu_0$. Thus the $z(t)$ and $\Delta\phi(t)$ oscillations have an initial phase shift of $\pi/2$. For the value of the barrier height shown here selected as $V_0/\mu = 0.8$ the oscillation frequency cannot be estimated by the two-mode model expression for the Josephson 'plasma' frequency $\omega_J \simeq \sqrt{E_J E_C}/\hbar$ (the two-mode model is described in Sect. 2.3.2). This is due to the fact that the barrier separating the two superfluids is not sufficiently deep, i.e. for such combination of the barrier height and the barrier width value $w/\xi = 4$ the coupling between the two condensates is not weak and the two condensates wavefunctions are not well localized in each well as supposed in the two-mode model. Moreover we must note that for $V_0/\mu < 1$ the dynamics of the condensate across the barrier does not happen only due to tunneling. Part of the particles exhibits tunneling as locally $V_0/\mu(\mathbf{r})$ quantity can become larger than one but the rest of the condensate, that has enough energy to overcome the barrier, flow hydrodynamically without tunneling. The validity of the two-mode model in the range of the experimental parameters is discussed further in Sect. 3.4.

3.3.2 The dissipative regime

The onset of the dissipative regime happens when the initial imbalance becomes equal to a critical value z_{cr}. This value was identified as the value of z_0 at which $z(t)$ firstly exhibits fast decay of the population imbalance to zero, followed by sinusoidal oscillations with several modes with amplitude smaller than $z_{\rm cr}$. The temporal evolution of the relative imbalance and relative phase $\Delta\phi$ is shown in Fig. 3.8 for two values of the barrier height $V_0/\mu = 0.8$ and $V_0/\mu = 1.2$ and for initial imbalance larger or equal to the critical imbalance in the former and the latter case respectively.

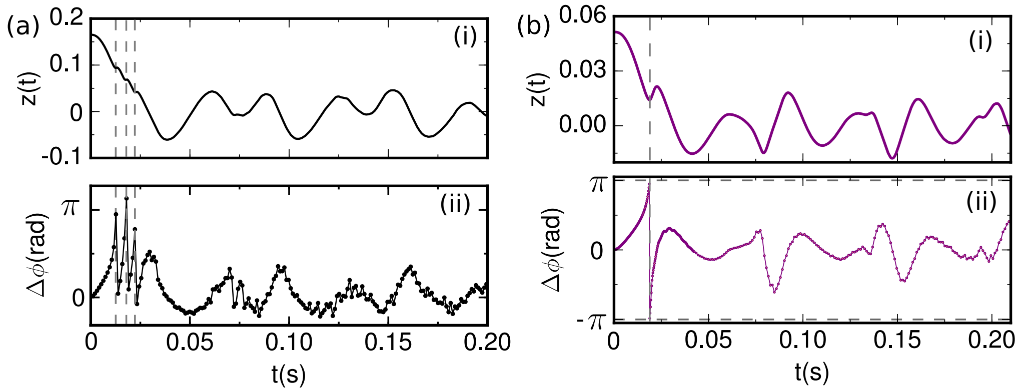

Figure 3.8: The temporal evolution of (i) the population imbalance and (ii) the relative phase for (a) $V_0/\mu = 0.8$ and $z_0 = 0.17 > z_{\rm cr} = 0.11$ and (b) $V_0/\mu = 1.2$ and $z_0 \simeq z_{\rm cr} = 0.05$. The vertical grey dashed lines are in correspondence of the time the imbalance has local minima (dips) (three in total for (a) and one for (b)).

During the initial decay of $z(t)$, which happens in a relatively short time evolution ($t < 0.05$s), the relative phase shows jumps [Fig. 3.8(ii)] by less than 2π for $V_0/\mu = 0.8$ and by around 2π for $V_0/\mu = 1.2$. This is the so-called phase-slippage mechanism associated to the vortex rings generation, as will be shown in Sect. 3.5.1. The vortex rings (VRs) are nucleated outside of the local Thomas-Fermi surface and subsequently can enter such surface and can even propagate into the left condensate as it is the case for $V_0/\mu = 0.8$ (shown in Sect. 3.7.1). Thus, for $V_0/\mu = 0.8$ the VR does not disappear (i.e. its radius does not become zero) within the barrier. As the $\Delta\phi$ is extracted for $y = z = 0$, this explains the reason why the phase-slippage is not exactly 2π. In fact, re-calculating the relative phase at the vortex core position for $V_0/\mu = 0.8$, leads to a phase slips of around 2π, as shown in the Fig. 3.9 (the relative phase at such position is called $\Delta\phi_1$). For $V_0/\mu = 1.2$ instead the VR disappears within the barrier and moreover the vortex core which is given by $\xi(0) = 1/\sqrt{8\pi a_M n(0)}$ becomes large enough (due to the vanishing density at $x = y = z = 0$) such that it causes the $\Delta\phi$ at $y = z = 0$ to jump by 2π. A closer inspection of the short time evolution of $z(t)$ shows the presence of dips in the otherwise rapid (and monotonic) decay of $z(t)$, that are indicated by the vertical dashed lines in Fig. 3.8(i). Interestingly such dips happen in the correspondence of the relative phase slippage and are thus related to the vortex rings emission. In fact, the vortex ring generation instantaneously opposes the population transfer, leading to the flattening of $z(t)$ visible in Fig. 3.9(a) or to a reverse of $z(t)$ direction as observed from Fig. 3.8(b)-

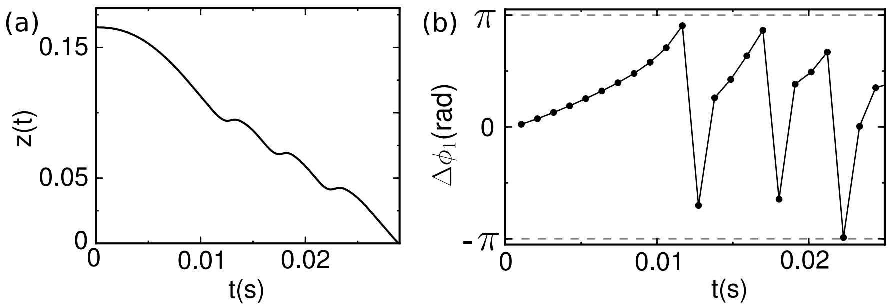

Figure 3.9: (a) The short-time evolution of the population imbalance shown in Fig. 3.8 and of the relative phase across the barrier calculated at $z = 0$ and $y = 0.44l_x$. The numerical data are for $V_0/\mu = 0.8$ and $z_0 = 0.17$.

(i), and can even lead to a reversal of the background superflow due to the additional 'swirling' velocity of the induced vortex ring (as will be shown in Sect. 3.5.2). Thus the number of such dips corresponds to the number of vortex rings generated, which is three for $V_0/\mu = 0.8$ and $z_0 = 0.17$ and one for $V_0/\mu = 1.2$ and $z_0 = 0.05 \simeq z_{\rm cr}$. The longer time evolution of $\Delta\phi$ is characterized by harmonic oscillations around a zero value with amplitude smaller than π and with the same frequencies as the population imbalance $z(t)$.

3.4 The two-mode model validity

In this section we discuss the validity of the commonly-used two-mode model [59, 61] for the specific geometry and parameter regime of our system. As described also in Sect. 2.3.2, in the two-mode model the two condensates are considered as well-localized in each well and there is a small overlapping of their wavefunction in the barrier region. The system wavefunction can then be expressed as a linear superposition of the left and right condensate wavefunctions

$$\psi(\mathbf{r}, t) = \psi_L(t) \cdot \eta_L(\mathbf{r}) + \psi_R(t) \cdot \eta_R(\mathbf{r}), \tag{3.12}$$

where $\psi_{L(R)}(t) = \sqrt{N_{L(R)}}e^{i\phi_{L(R)}}$, $\int \eta_i \cdot \eta_j d\mathbf{r} = \delta_{i,j}$ with i, j = left,right and $N_{L(R)}$, $\phi_{L(R)}$ being the condensate number and phase in the left (right) well respectively. By writing the wavefunction as in Eq. (3.12) the time dependence of the system wavefunction is separated by its spatial dependence and this model is known as linear two-model model. In a more general form the spatial part of the system wavefunction depends on the the particle number on the left or right condensate, i.e. on the time, and thus the system wavefunction can be written as

$$\psi(\mathbf{r}, t) = \psi_L(t) \cdot \eta_L(\mathbf{r}; N_L(t)) + \psi_R(t) \cdot \eta_R(\mathbf{r}; N_R(t)), \tag{3.13}$$

known as non-linear two-mode model.

Both the linear and non-linear two-mode models cannot capture the transition to the dissipative regime, since – with increasing population imbalance – it always predicts a transition from the Josephson 'plasma' oscillation regime to the Macroscopic Quantum Self-Trapping (MQST) regime. In the latter regime, the population imbalance oscillates around a non-zero mean value for a long enough time, which is much larger than the time the $z(t)$ decays to zero in our dissipative regime. Moreover the two-mode model is expected to be valid in the deep tunneling regime where $V_0/\mu > 1$ and the two condensates are weakly-coupled across the barrier [59, 61]. However, it is interesting to examine the extent to which such a model can predict *either* the location of the transition region where Josephson 'plasma' oscillations no longer occur, *and/or* the actual frequency of the Josephson oscillations within the Josephson regime.

For a symmetric double-well potential, the left and right wavefunction can be found from the symmetric and the first antisymmetric state wavefunction as $\eta_{R,L} = (\eta_S \pm \eta_A)/\sqrt{2}$. The symmetric state which is the ground state corresponds to having zero initial imbalance and zero initial relative phase, while for the antisymmetric state the correponding relative phase is π. The two important quantities characterising an atomic Josephson junction are the on-site interaction energy U and the tunneling energy K. In particular, their ratio or more specifically $UN/(2K)$, known as Λ, defines the critical imbalance for the onset of the MQST regime as expressed by Eq. (2.59)

$$\Lambda_c = \frac{1 + \sqrt{1 - z_0^2}\cos(\Delta\phi_0)}{z_0^2/2}. \tag{3.14}$$

Such equation finds the critical Λ for a given initial imbalance but in our case we are interested in finding the critical imbalance for given Λ, i.e. we are not varying Λ but z_0. From Eq. (3.14) and for $z_0^2 \ll 1$ (which is valid in our case) imposing $\Delta\phi_0 = 0$, the critical imbalance is given by

$$z_{cr} \simeq \sqrt{\frac{8K}{UN}}. \tag{3.15}$$

In the two-mode model the tunneling energy in first approximation is expressed as

$$K = -\int \left[\frac{\hbar^2}{2m}(\nabla\eta_{\rm L}\nabla\eta_{\rm R}) + \eta_{\rm L}V_{\rm ext}\eta_{\rm R}\right] d\mathbf{r}, \tag{3.16}$$

but this approximation is valid in the limit of small overlapping between the two condensate wavefunctions, which is not always valid in our case. For this reason in our simulations the tunneling energy is extracted from the difference ΔE between the antisymmetic-state energy and the symmetric-state energy (which reduces to $2KN$ in the limit of large barrier height $V_0/\mu \gg 1$) so the term $2K$ in Eq. (3.14) is substituted by $\Delta E/N$. The symmetric

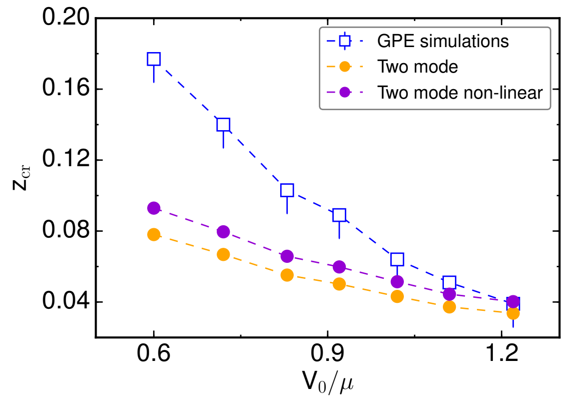

Figure 3.10: Critical initial population imbalance for different barrier height V_0/μ for 6×10^4 particles extracted from GPE simulations, from linear (orange circles) and nonlinear (violet circles) two-mode model. Note that while all models agree on the *existence* of a Josephson regime below their corresponding predictions for $z_{\rm cr}$, the two-mode models predict a transition to a different regime (namely MQST) than that found in the GPE simulations (dissipative regime).

and antisymmetric states are numerically found by solving the GPE equation for a linear shift $\epsilon = 0$, i.e. a symmetric double-well potential. The Josephson coupling energy $E_{\rm J}$ is defined as $E_{\rm J} = \Delta E/2$.

The onsite interaction energy U can be calculated *either* from the linear two-mode model [59], via $U_{\rm lin} = g\int \eta_L^4 d\mathbf{r}$ *or* from the nonlinear two-mode model [187] as $U_{NL} = 2(\partial\mu/\partial N)$. To evaluate the two-mode model prediction for the location of the crossover between Josephson and MQST, we calculate $z_{\rm cr}$ both from the linear and from the nonlinear two-mode model for each V_0/μ, and plot it against V_0/μ in the experimentally relevant range $[0.6, 1.22]$ in Fig. 3.10. We also plot on this figure the corresponding extracted values of $z_{\rm cr}$ from the GPE simulations [noting that in the latter case, the transition is to a different, dissipative, regime, rathen than to MQST]. The GPE prediction of $z_{\rm cr}$ is found by solving again the GPE simulation but this time with an initial shift ϵ different from zero, and thus $z_0 \neq 0$. The critical imbalance is defined then by looking at the time evolution of $z(t)$, if it decays initially fast and it has only one dip, the value of $z_0 = z(t=0)$ is the $z_{\rm cr}$. We find that both linear and nonlinear two-mode model clearly significantly underestimate the numerically predicted critical value of z_{cr} for all $V_0/\mu \leq 1.1$, yielding a correct value for the transition only at the highest probed point $V_0/\mu = 1.22$ (see Fig. 3.10).

Next, we examine the extent to which the oscillation frequency of the Josephson oscillation is correctly predicted by such two-mode model. In the regime of the Josephson 'plasma' oscillation, where $z_0 < z_{\rm cr}$, and for $2K \ll UN$ the plasma frequency, defined in Eq. 2.56, can be written as

$$\omega_J \simeq \frac{\sqrt{2U_{\rm lin(NL)}NK}}{\hbar} = \frac{\sqrt{\Delta E U_{\rm lin(NL)}}}{\hbar} \,. \tag{3.17}$$

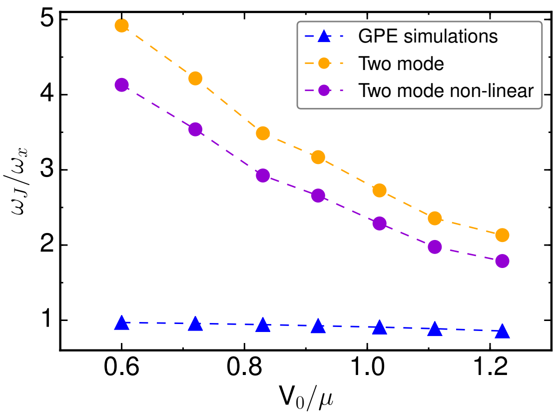

Figure 3.11: The oscillation frequency of the population imbalance for $z_0 < z_{\rm cr}$, i.e. Josephson plasma frequency, from linear (orange circles) and nonlinear (violet circles) two-mode model and GPE simulations (blue triangles).

In analogy with the expression of the plasma frequency in superconductors, $\omega_p = \sqrt{E_J E_c}/\hbar$, the term $2U$ is the analogue of the 'charging' energy E_c [59]. Plotting ω_J against V_0/μ in the considered range (Fig. 3.11), we find the predictions of both linear and nonlinear two-mode model to be incorrect by at least a factor of 2 (for $V_0/\mu = 1.22$), with the disagreement rapidly increasing for lower values of V_0/μ.

The above analysis thus proves that – for the parameter regimes of the experiment under study – the two-mode model is out of its validity range, due to the considered values of the ratio V_0/μ and the narrow width of the junction. The validity of the two-mode model beyond the experimental parameters is shown in the Chapt. 5.

3.5 Vortex ring tracking and early stage dynamics

We track the vortex ring via an algorithm based on the pseudo-vorticity vector [210, 211] defined as $\omega_{\rm ps} = (1/2)\nabla \times \mathbf{j}$, where $\mathbf{j}$ is defined in Eq. 3.9. The vortex ring is found by initially identifying grid points around which the circulation is equal to 2π and then looking for density minima via a Newton-Raphson method. Once the initial point is determined, the vortex is reconstructed employing the pseudo-vorticity vector whose direction is tangent to the vortexlines.

The VR is initially generated (as a 'ghost' vortex) in the low density region outside the local transversal spatial extent of the BEC on the central radial plane at $x = 0$ (shown in Fig. 3.12) where, the superfluid velocity is maximum, due to the flow constriction, and the local speed of sound is minimum, since density vanishes. Due to the trap anisotropy in the transverse directions, i.e. $\omega_z \neq \omega_y$ the nucleated VR has an elliptic two-dimensional shape (near circular as $\omega_y = 1.26\omega_z$). Thus we extract the y, z direction semiaxes by fitting the

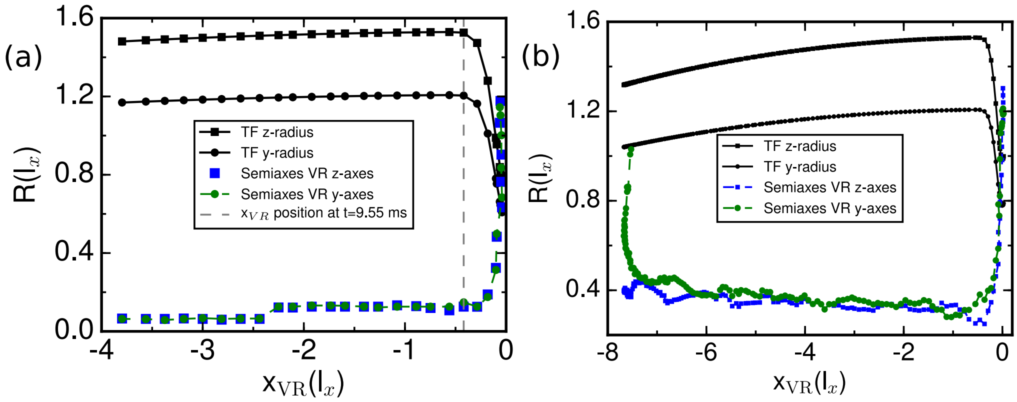

Figure 3.12: The vortex ring semiaxes along the two transverse direction y, z axis versus the vortex ring position along x axis (x_{VR}) and the transverse Thomas-Fermi radius calculated at x_{VR}. Shown are the semiaxes and position of the first VR generated for $V_0/\mu = 0.8$ and $z_0 = 0.25 > z_{\rm cr}$ (a) and of the only VR generated for $V_0/\mu = 0.6$ and $z_0 = 0.19 = z_{\rm cr}$ (b).

2D VR profile with an ellipse function centered at $y = z = 0$. Then the values of the VR semiaxes as a function of the VR position along x axis, $x_{\rm VR}$, are shown in Fig. 3.12 together with the values of the Thomas-Fermi radius $R_{\rm TF,y(z)}$ calculated at $x_{\rm VR}$. In this figure we show the analysis of the first generated VR for $V_0/\mu = 0.8$ and $z_0 = 0.25$ in the subplot (a) and for $V_0/\mu = 0.6$ and $z_0 = 0.19$ in (b) where in the first case there are in total seven VRs generated ($z_0 > z_{\rm cr}$) while in the second case only one VR is generated ($z_0 \simeq z_{\rm cr}$). Nevertheless the early-stage dynamics has the same features for all the z_0 and values of V_0/μ explored by us, as long as $V_0/\mu < 1$ (see Chapt. 5 for higher V_0/μ). The $R_{{\rm TF},y(z)}$ is estimated in the Thomas-Fermi approximation where the kinetic term is neglected ($gn \ll \hbar\omega_{\rm x,y,z}$) and thus the Thomas-Fermi radius along y axis (for $z = 0$) or along z axis (for $y = 0$) in the presence of a Gaussian barrier is given by

$$R^2_{{\rm TF},y(z)} = \frac{2\mu}{M\omega^2_{y(z)}} - \frac{2V_0}{M\omega^2_{y(z)}}{\rm e}^{-2x^2/w^2} - \left(\frac{\omega_x}{\omega_{y(z)}}\right)^2 x^2. \tag{3.18}$$

Both the $R_{{\rm TF},y(z)}$ have a minimum value at the barrier position and then increase as the $|x|_{\rm VR}$ increases until they achieve a maximum value at the edges of the barrier (i.e. at $|x|_{\rm VR} \simeq 2{\rm w}$) equal to $R_{{\rm TF},y(z)} = 1.2(1.5)l_x$. As observed from Fig. 3.12, after its generation, the VR shrinks initially fast its semiaxes values due to the presence of transversal density inhomogeneity at the barrier position. At a certain time, the VR enters the local TF surface near $x = 0$ and after that it continues reducing its radius, due to the density gradient (represented by the profile of the TF radius), until the moment the VR comes to the x axis position when the TF radius achieves its maximum value (i.e. the density is maxima), indicated by a grey vertical dashed line in Fig. 3.12(a). For a while the TF radius has a plateau-like profile and in correspondence the VR has almost a constant size, while propagating along the negative x axis (left condensate) with almost constant velocity (as we will show in Sect. 3.7.1. Depending on the value of the barrier height, i.e. , on the density at the barrier position, and thus on the value of the condensate incompressible kinetic energy (described in detail in Chapt. 5), two different scenarios can happen after the VR leaves the barrier: the vortex ring can shrink further its size, disappearing in the end of its dynamics and giving rise to rarefaction pulses (as happened in Fig. 3.12 (a)) or it can expand and then breaks in two vortex lines (as happened in Fig. 3.12 (b)). Moreover, as it will be described in Chapt. 4, the VR survival during its propagation in the superfluid bulk is determined by two effects: by the presence of a density gradient [212] and by the presence of $m = 2$ Kelvin wave excitation [178, 213, 214](due to the VR elliptic profile).

However in this section we focus in the early stage dynamics of the VR that happens within the barrier region $|x|_{\mathrm{VR}} \leq 2w$ and its effect on the condensate phase, population imbalance, superfluid velocity, superfluid current and condensate kinetic energy components. In our plots sometimes instead of showing the VR semiaxes we just show their mean value defined as $R_{\mathrm{VR}} = (a + b)/2$ (referred to as VR radius) where $a(b)$ is the VR semiaxis value along the y and z direction. The vortex ring has a core with a size defined by the local condensate healing length which depends on the local condensate density. This means that the VR core changes as the VR moves in an inhomogeneous density, being larger where the density is smaller, i.e. at the barrier position. For simplicity, in our plots we almost always show the vortex ring mean radius without considering the vortex ring core which would have added an error bar to our numerical results without changing the physics we explain as other effects govern the vortex ring dynamics.

3.5.1 Phase-slippage mechanism

We follow the first vortex ring, for $V_0/\mu = 0.8$ and $z_0 = 0.25$, during its early-stage dynamics by plotting the renormalized 2D density and phase profiles in Fig. 3.13 from the time it is nucleated, until it enters the left reservoir. The renormalised 2D density $\Delta\rho$ is obtained by substracting the equilibrium density from the condensate density at certain time, i.e. $\Delta\rho = \rho(t) - \rho(t = 0)$. The VR radius and position as found from our tracking code is indicated with a 'x' in each plot. It coincides with the coordinates of the 2D density minimum (Fig. 3.13 (a)) and a phase winding of around 2π at the 2D phase profile (see Fig. 3.13 (b)). This picture is consistent with the phase slippage concept for superfluid helium [12]. The horizontal error bars are due to the uncertainty coming from the size of the vortex core (estimated by the mean value of the healing length), which for simplicity are shown only along x axis but they are present also along the y axis. The vortex ring in a 2D plane can be imagined as a vortex and antivortex which have opposite sign circulation. As the time goes, the vortex-antivortex distance becomes smaller (i.e. the VR shrinks its radius) remaining near $x = 0$ until $t = 8.7$ms. After that, the VR radius becomes so small that it is quite difficult to resolve the vortex and antivortex pair and then the VR starts moving in the negative x axis. At $t = 10$ms, the VR has left the barrier and a relative phase near $x = 0$ is constructed again due to the remaining $\Delta\mu$. Fig. 3.14 shows the relative phase calculated along the x axis but for different y axis values: $y \simeq 0.7l_x$, $y \simeq 0.5l_x$ and $y \simeq 0.3l_x$ and for $z = 0$. We observe that there is a phase slippage of around 2π later in time for $y \simeq 0.3l_x$ as the VR core comes at that position later in time with respect to the other higher y values, following the initial shrinking mechanism (as shown in Fig. 3.13).

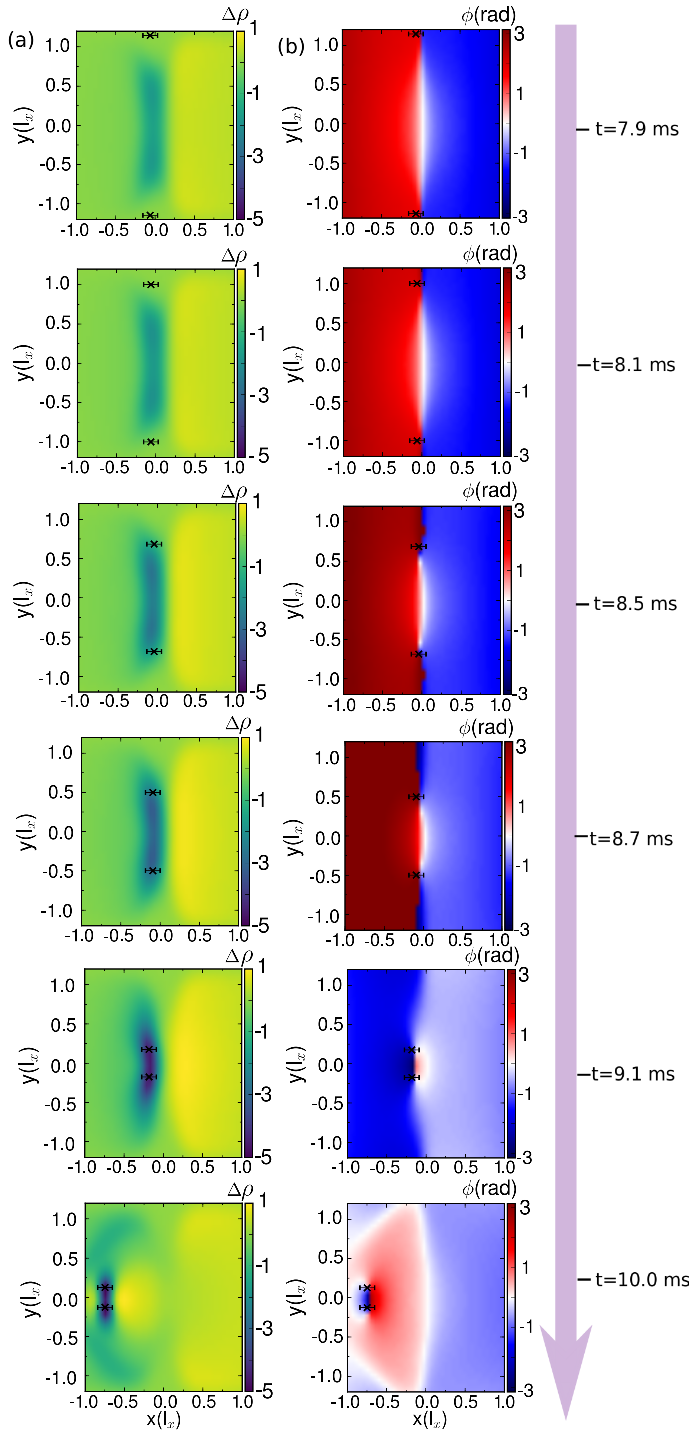

Figure 3.13: Planar ($z = 0$) 2D snapshots of (a) the BEC densities after substracting the equilibrium density, and (b) the corresponding 2D phase profiles at different times, selected to cover the temporal window from the moment the VR enters the Thomas-Fermi surface at the barrier position, until when it leaves the barrier. The radii and positions of the tracked VR and their numerical error bars, associated with the uncertainty in the determination of the position due to the finite size of the vortex core, are denoted by 'x' in the 2D phase profiles. For this simulation the data are $V_0/\mu = 0.8$ and $z_0 = 0.25$.

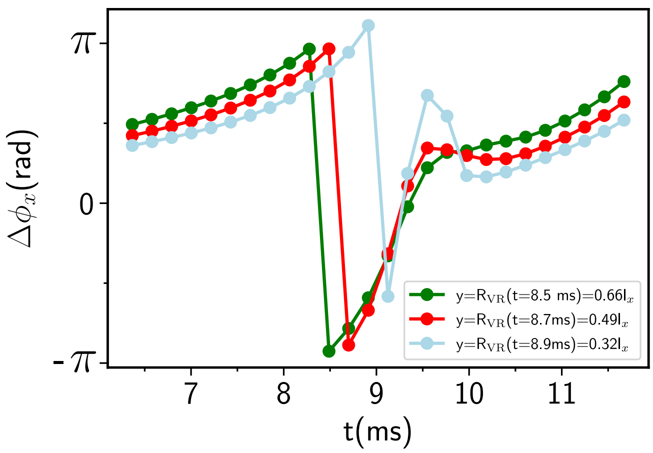

Figure 3.14: The relative phase calculated along the x axis and for $y = 0.7l_x$, $y = 0.5l_x$ and $y = 0.3l_x$ (at $z = 0$). For this simulation the data are $V_0/\mu = 0.8$ and $z_0 = 0.25$.

3.5.2 The presence of backflow

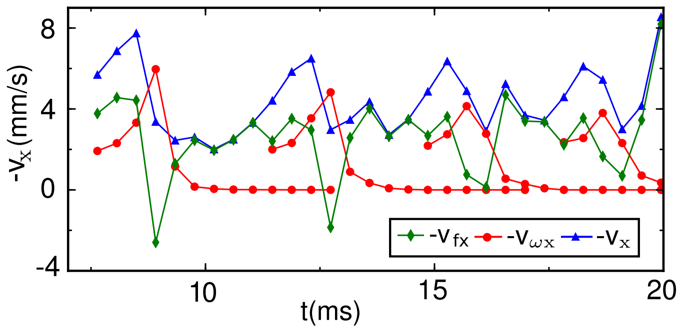

Figure 3.15: Temporal evolution of the total superfluid axial velocity v_x, the vortex ring induced axial velocity $v_{\omega x}$ and the axial potential flow velocity v_{fx} in the center of the trap for the first four rings generated in the case $V_0/\mu = 0.8$ and $z_0 = 0.25$.

Given the presence of an initial imbalance, the superfluid accelerates across the barrier and its coherent or frictionless flow is limited by the critical velocity for the VR emission. Before the nucleation of a VR, the superfluid velocity is only due to the particle flow through the barrier. At the moment a VR is generated the superfluid velocity $\mathbf{v}$ can be decomposed into a superfluid potential flow $\mathbf{v}_f$ and in the flow generated by the superfluid singular vorticity distribution $\mathbf{v}_\omega$, via

$$\mathbf{v} = \mathbf{v}_f + \mathbf{v}_\omega. \tag{3.19}$$

Given the complexity of the system studied, as a first approximation we neglect the density gradient effects on the superfluid velocity. In addition, we do not consider the velocity field generated by the images of the VRs with respect to the boundaries of the condensate [215–217]. In order to calculate the superfluid potential flow $\mathbf{v}_f$ at each time t in the center of the trap $O(0,0,0)$, we subtract the velocity field $\mathbf{v}_\omega(O,t)$ generated by the reconstructed VRs from the total superfluid velocity $\mathbf{v}(O,t)$, *i.e.* $\mathbf{v}_f(O,t) = \mathbf{v}(O,t) - \mathbf{v}_\omega(O,t)$, where $\mathbf{v}(O,t)$ is obtained from the density current of probability by using Eq. (3.8) and Eq. (3.9) (as described in Sect. 3.2). The $\mathbf{v}_\omega$ instead is calculated [1] via the Biot-Savart integral defined in Eq. (2.30) [175] that we express as

$$\mathbf{v}_\omega(O,t) = -\frac{\kappa}{4\pi}\sum_{i=1}^{N_{VR}} \oint_{\mathcal{C}_i(t)} \frac{\mathbf{s}'(\zeta,t)\times\mathbf{s}(\zeta,t)}{|\mathbf{s}(\zeta,t)|^3}\, d\zeta \ , \tag{3.20}$$

where $\kappa = h/m$ is the quantum of circulation, N_{VR} is the number of VRs present in the BEC, $\mathcal{C}_i(t)$ is the closed curve corresponding to the i-th VR reconstructed via an

[1] This calculation was performed by one of my collaborators, Dr. Luca Galantucci.

algorithm based on the pseudo-vorticity vector [210, 211], $\mathbf{s}(\zeta, t)$ is the position of the VR line-element corresponding to arclength ζ and $\mathbf{s}'(\zeta, t)$ its unit tangent vector. Fig. 3.15 shows the temporal evolution of the axial (x) components of $\mathbf{v}_f$, $\mathbf{v}_\omega$ and $\mathbf{v}$ in the centre of the trap O for $V_0/\mu = 0.8$ and $z_0 = 0.25$. We observe that in the event of a vortex ring generation, the superfluid flow v_{fx} slows down and even reverses its sign for the first two rings generated: the nucleation of vortex rings leads to a reduction in the main flow, thus slowing down the population imbalance dynamics. The vortex ring induced velocity $-\mathbf{v}_\omega(O, t)$ instead increases initially as the VR reduces its radius, achieves a maximum value and then decreases as the VR leaves the $x = 0$ position. This process repeated itself until the population imbalance becomes smaller than the critical value, which means until the superflow initial accelation is not large enough in order to allow the superfluid velocity to achieve the critical value again.

3.5.3 The effect of early stage dynamics on the population imbalance

To demonstrate the relation between the observable dips in the population imbalance at early times, and the vortex ring dynamics, Fig. 3.16 plots the population imbalance initial time evolution and the first four VRs radius profile in time for $V_0/\mu = 0.8$ and $z_0 = 0.25$. This figure also shows the local transversal spatial condensate extent at the instantaneous position of each generated vortex ring. We observe that the onset of dips happens at exactly the moment the VR radius becomes equal or slightly smaller than the TF radius, i.e. at the moment the VR enters the condensate density near $x = 0$. This happens due to the VR induced swirling velocity $\mathbf{v}_\omega$, which causes the superfluid flow to slow down and even reversing its sign. Even though only the first four VRs are shown in such figure, the mechanism repeated itself even for the subsequent other three VRs which are not shown here. Moreover, as long as $V_0/\mu \lesssim 1$, these results are valid independently on the value of initial imbalance if $z_0 \geq z_{\rm cr}$. In fact, Fig. 3.17 confirms this picture even for $z_0 = 0.13 > z_{\rm cr}$. We indicate with grey dashed lines the times when the mean radius of each generated VR becomes $R_{\rm VR} \simeq R_{\rm TF}$ where $R_{\rm TF} = (R_{\rm TF,y} + R_{\rm TF,z})/2$ is the mean TF radius near x=0.

Moreover for $z_0 = 0.25$, the $z(t)$ achieves its zero value later in time with respect to $z_0 = 0.13$. This is because of two reasons: firstly the initial imbalance in the first case ($z_0 = 0.25$) is higher and it means that the $z(t)$ needs more time to reach its zero value. Moreover a VR causes a backflow everytime it is generated, i.e. , a larger number of VRs (seven for $z_0 = 0.25$ and one for $z_0 = 0.13$) give a cumulative effect slowing down the population imbalance decay. This is clearer in Fig. 3.18, where we show the temporal evolution of the population imbalance scaled to the initial imbalance for three different values of $z_0 = 0.2$, $z_0 = 0.3$ and $z_0 = 0.4$ for fixed $V_0/\mu = 0.8$. Even here we observe that for higher z_0 the population imbalance decays slower in time due to the cumulative

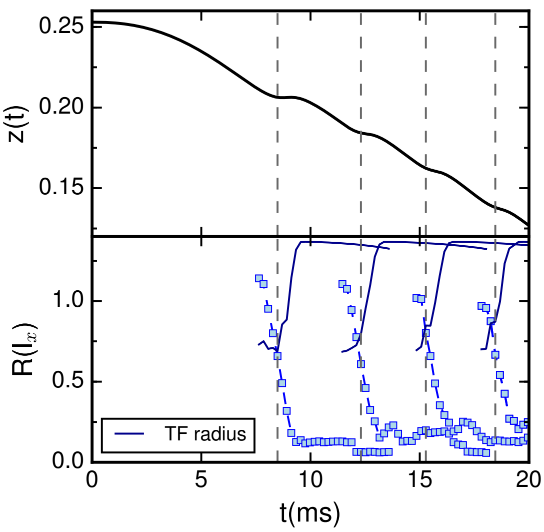

Figure 3.16: Temporal evolution of the population imbalance (a) and of the vortex ring radius (b) for $V_0/\mu = 0.8$ and $z_0 = 0.25$. In (b) we also show (solid blue lines) the TF mean radius calculated at each VR x-position. For such initial imbalance there are in total 7 VRs generated but here we show only the first four.

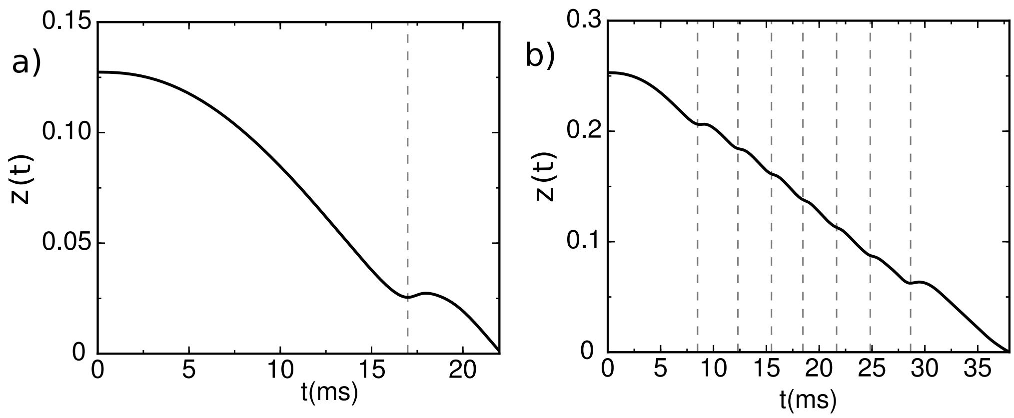

Figure 3.17: Temporal evolution of the population imbalance for $z_0 = 0.13$ (a) and $z_0 = 0.25$ (b) both for $V_0/\mu = 0.8$. The dashed grey line show the moment at which different VRs enter the Thomas-Fermi surface.

backflow effect.

3.5.4 The kinetic energy decomposition

In this section we show the effect of the vortex ring nucleation and early-stage dynamics on the kinetic energy components. The total energy of the system can be decomposed as

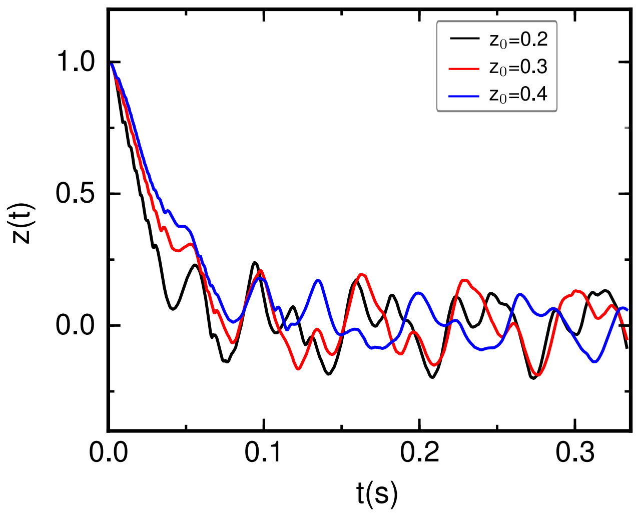

Figure 3.18: Temporal evolution of the population imbalance scaled to the initial imbalances, for $z_0 = 0.2$, $z_0 = 0.3$ and $z_0 = 0.4$ for fixed $V_0/\mu = 0.8$.

follows:

$$E = \int [e_{int}(\mathbf{r},t) + e_k(\mathbf{r},t) + e_V(\mathbf{r},r)]\, d^3\vec{r}, \tag{3.21}$$

where $e_{int}(\mathbf{r},t) = (g/2)\rho^2$ is the interaction energy density, $e_V(\mathbf{r},t) = \rho V_{trap}$ is the potential energy, and

$$e_k(\mathbf{r},t) = \frac{1}{2}|\nabla\psi|^2 = \frac{1}{2}\rho\mathbf{v}^2 + \frac{1}{2}|\nabla\sqrt{\rho(\mathbf{r},t)}|^2 \tag{3.22}$$

$$= \frac{1}{2}\rho\mathbf{v}^2 + e_q(\mathbf{r},t) \tag{3.23}$$

is the kinetic energy density, with $e_q(\mathbf{r},t)$ the quantum pressure term. The quadratic term involving the velocity of the flow can be split into incompressible $e_k^i(\mathbf{r},t)$ and compressible $e_k^c(\mathbf{r},t)$ contributions as follows:

$$\frac{1}{2}\rho\mathbf{v}^2 = \frac{1}{2}\left[(\sqrt{\rho}\mathbf{v})^i\right]^2 + \frac{1}{2}\left[(\sqrt{\rho}\mathbf{v})^c\right]^2 = e_k^i(\vec{r},t) + e_k^c(\vec{r},t), \tag{3.24}$$

where $\nabla\cdot(\sqrt{\rho}\mathbf{v})^i = 0$ and $\nabla\mathrm{x}(\sqrt{\rho}\mathbf{v})^c = 0$. The fields $(\sqrt{\rho}\mathbf{v})^i$ and $(\sqrt{\rho}\mathbf{v})^c$ are calculated employing the Helmholtz decomposition [218–221]. Fig. 3.19(a) shows the temporal evolution of the integrals of $e_k^i(\mathbf{r},t)$, $e_k^c(\mathbf{r},t)$ and of $e_q(\mathbf{r},t)$, called E_k^i, E_k^c and E_q respectively. The quantum energy E_q, that is related to the density inhomogeneities due to the trapping potential, is larger than E_k^i and E_k^c, and it is slightly affected by the VR nucleation. However when each VR enters the TF surface (vertical grey shadow areas in Fig. 3.19), the E_q has local peaks at the times the VR enters the TF surface. At those times, we see also

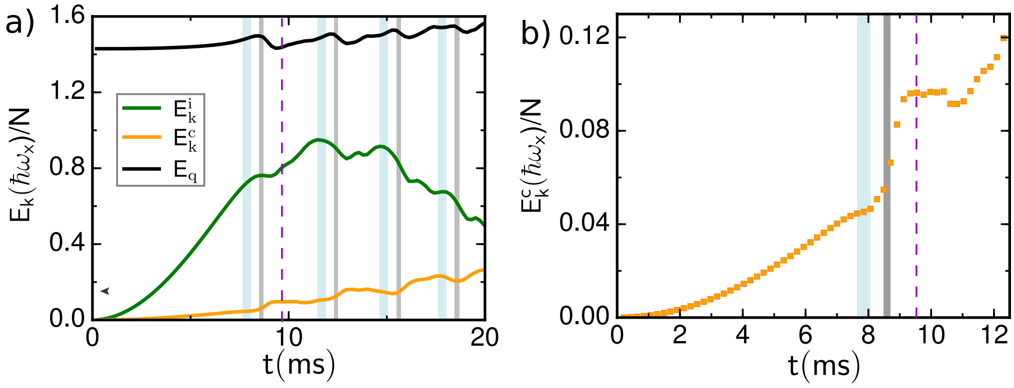

Figure 3.19: a) The temporal evolution of E_k^i, E_k^c and E_q. Showing also the three stages of the VR nucleation. b) The temporal evolution of E_k^c till the nucleation of the second VR. Vertical blue shaded areas in both subplots highlight the moment when each VR is nucleated and the grey shaded areas the moment when each VR enters the local Thomas-Fermi surface. Vertical dashed line indicates the moment during the axial propagation of the VR, when it reaches the point of largest transversal spatial extent corresponding to the edge of the barrier, after which time the background density begins decreasing very slowly due to the underlying external harmonic trap along x axis.

an increase of the compressible energy. This step-like increase is shown better in Fig. 3.19 (b) where only E_k^c is shown until the second VR is nucleated. The step-like increase starts when the first VR enters the Thomas-Fermi surface and stops (reaches a 'plateau') when the VR is at the position corresponding to maximum transverse Thomas-Fermi spatial extent, which for this case occurs around t$\sim$ 9.5 ms. This is shown by the vertical dashed lines in Fig. 3.19 and also in Fig. 3.12. Moreover, the ratio of the increase of E_k^c to the compressible energy before the first VR nucleation takes the values 1.09 , 1.36 , 1.57 for the nucleation of the 1$^{\text{st}}$,2$^{\text{nd}}$, 3$^{\text{rd}}$ VRs, respectively.

3.5.5 The interplay between the vortex ring and superfluid dynamics

In this section we analyse in detail the connection between the vortex ring nucleation and early-stage dynamics and superfluid transport properties across the barrier. In order to do so, we consider the x-component of the superfluid velocity, weighted over the transverse density in the $x = 0$ plane, $\langle v_x \rangle$ defined as

$$\langle v_x \rangle = \frac{\int v_x \cdot |\psi(x=0,y,z)|^2 dydz}{\int |\psi(x=0,y,z)|^2 dydz}. \tag{3.25}$$

We identify three distinct dynamical stages in the nucleation process of the first VR: these are shown in Fig. 3.20 and labelled as I, II and III. We also note at this stage that the emerging pattern applies to subsequent VRs. Summarizing from what we have described

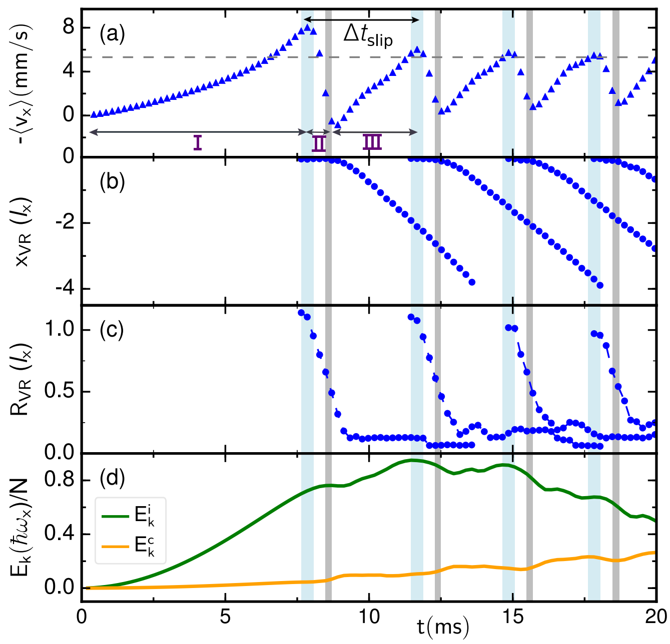

Figure 3.20: Vortex ring generation and early-stage dynamics. (a) Density-weighted x-component of superfluid velocity at the barrier (dashed line denotes mean speed of sound $\langle c\rangle = \sqrt{\mu/2M}$). (b) Position and (c) mean radius of the first few generated vortex rings (units of $l_x = \sqrt{\hbar/M\omega_x}$). (d) Temporal evolution of the incompressible (E_k^i) and compressible (E_k^c) kinetic energy of the BEC. Vertical shaded blue areas denote the maxima of superfluid velocity when VRs are generated, while grey areas indicate the times when the VRs enter the Thomas-Fermi surface. The data are for $V_0/\mu = 0.8$ and $z_0 = 0.25$.

in previous sections, in stage I, the chemical potential gradient $\nabla\mu$ drives an accelerated superfluid flow across the barrier. When $-\langle v_x\rangle$ reaches a critical value, exceeding the mean sound speed $\langle c\rangle = \sqrt{\mu/2M}$ (Fig. 3.20(a)), a VR is nucleated, associated with a relative-phase jump of 2π (as shown previously). After its nucleation [stage II], the VR moves axially very slowly away from its nucleation region $x_{\mathrm{VR}} = 0$ (Fig. 3.20(b)) with its mean radius R_{VR} rapidly shrinking (see Fig. 3.20(c)) due to the strong radial density inhomogeneity in the barrier region, until it is comparable to the transversal TF radius of the BEC, and enters the bulk superfluid [209]. During such evolution, $-\langle v_x\rangle$ exhibits a rapid decrease, possibly even changing sign. Then, in stage III, the VR gradually leaves the barrier region with the axial superfluid velocity $-\langle v_x\rangle$ re-accelerated by the remaining $\nabla\mu$ (see Fig. 3.20(a)), until at some time later ($\Delta t_{\mathrm{slip}} \simeq h/\Delta\mu$), when it has already travelled a considerable distance from the barrier edge, another VR is nucleated at the trap centre. Note that early on in stage III, before the VR exits the barrier region (i.e. before reaching the point of maximum transversal TF radius), R_{VR} continues decreasing due to the strong background density gradient.

For a deeper insight into the underlying superfluid dynamics, we make use of the decomposition at $\mathbf{x} = \mathbf{0}$ of the total axial superfluid velocity $v_x = v_f + v_\omega$ (see Sect. 3.5.2) for more details). By the end of stage II, the shrinked VR has just left the trap centre, and so the vortex contribution v_ω evaluated at $\mathbf{x} = \mathbf{0}$ (where the local superfluid velocity $\langle v_x \rangle$ shown in Fig. 3.20(a) is calculated) tends to 0 (as shown previously). This leads to a drop of $\langle v_x \rangle$ with amplitude $\Delta\langle v_x \rangle \sim \kappa/R_{\mathrm{VR}}$, corresponding to the change in the axial superfluid velocity at the trap centre due to the lost vortex contribution. This sawtooth-like profile of $\langle v_x \rangle$ (Fig. 3.20(a)) is typical of phase slippage phenomena seen in superfluid helium [12, 14, 39, 15] (as also described in Sect. 1.4.1), with the less abrupt drop found here stemming from the initial persistence of the VR within the barrier region. As shown previously, the drop $\Delta\langle v_x \rangle$ can even overcome the generating flow velocity, leading to flow reversal (i.e. backflow) in the post-nucleation dynamics, in agreement with Biot-Savart calculations. The amplitude of each subsequent velocity drop is reduced due to the overall decay of $z(t)$. In Fig. 3.20(d) is also shown the temporal evolution of two of the kinetic energy components, the incompressible E_k^i and compressible E_k^i kinetic energy. E_k^i and E_k^c correspond respectively to the kinetic energy of the flow (both potential flow driven by $\nabla\mu$ and vortex generated swirls) and to the sound wave energy in the superflow. When each VR enters the TF surface (end of stage II), and while still propagating within the barrier's region of increasing density, sound waves are emitted and E_k^c increases at the expense of E_k^i (Fig. 3.20(d)). The dissipation of Josephson oscillations [12, 14, 15, 20] thus stems from two effects: the incompressible kinetic energy transferred from the axial flow to the vortex swirling flow and the phonon-emission occurring during vortex nucleation and propagation within the barrier region.

3.6 Superfluid Current through the barrier

There are two ways to calculate the superfluid current: the first one is from the time derivative of the population imbalance as defined in Eq. (1.15) and can be written as

$$I = -\frac{dN_L}{dt} = \frac{N}{2}\frac{dz}{dt} \tag{3.26}$$

and the second one from the transverse integral of the probability current density at $x = 0$

$$I = \int_{R_{TF,z}} \int_{R_{TF,y}} j_x(x = 0, y, z)\, dy\, dz. \tag{3.27}$$

Knowing that j_x is the x component of the density current of probability the superfluid current can also be written as:

$$I = \int_{R_{TF,z}} \int_{R_{TF,y}} |\psi(0, y, z)|^2 \cdot v_x(x = 0, y, z) dydz. \tag{3.28}$$

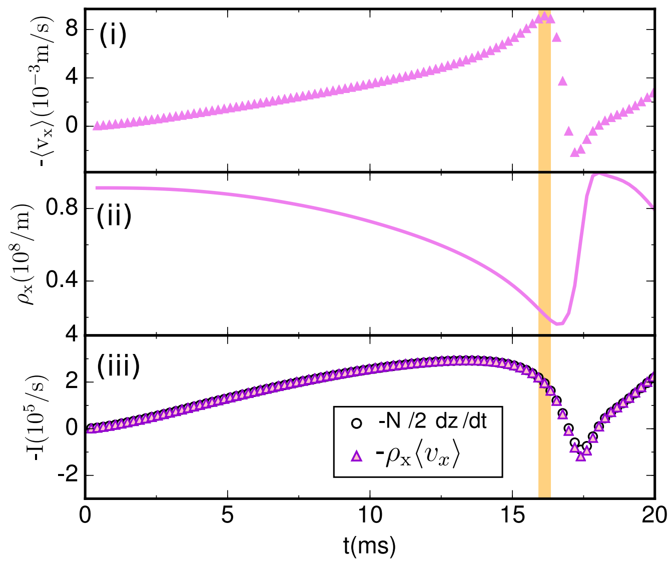

Figure 3.21: Density-weighted superfluid velocity along the x direction (i), the transverse integrated density (ii), and their product (violet symbol in (iii)) calculated at the trap center for $V_0/\mu = 0.8$ and $z_0 = 0.13$. In the (iii) we also show the current calculated from the time derivative of the population imbalance (black symbols). Vertical shaded area highlight the maximum value of $-\langle v_x \rangle$.

Given the expression for the superfluid density-weighted velocity $\langle v_x \rangle$ in Eq. (3.25) we thus obtain

$$I = \rho_x \langle v_x \rangle \ , \tag{3.29}$$

where

$$\rho_x = \int |\psi|^2 (x=0, y, z) dydz. \tag{3.30}$$

Fig. 3.21 shows the time profile of $-\langle v_x \rangle$ in the subplot (i), of the transverse integrated density ρ_x calculated at $x = 0$ in (ii) and of the superfluid current in (iii) for $V_0/\mu = 0.8$ and $z_0 = 0.13$. For these parameters only one VR is generated and the time interval in Fig. 3.21 is chosen slightly larger than the time when such VR is generated. As described previously, the superfluid starts flowing along the negative x axis with its velocity increasing until it achieves a maximum value (shown in Fig. 3.21(i)) and a VR is generated. During this time, the superfluid density ρ_x, which is shown in the subplot Fig. 3.21(ii), contrary to the superfluid velocity, decreases in time until it achieves a local minima. Such minima happens in time slightly later than the $-\langle v_x \rangle$ maxima at the time when the VR enters the condensate transversal density (becoming so a hydrodynamical vortex). As the VR starts moving, i.e. its position $|x|_{VR}$ increases, the density ρ_x starts increasing due to the superfluid flow driven by the $z(t)$. The superfluid current can be calculated by Eq. (3.26) or by Eq. (3.29) and these two methods are equivalent as shown in Fig. 3.21 (iii) (in the figure is shown $-I$). It increases initially in time and it achieves a local maxima which is not pronounced and more similar to a 'plateau'. In fact, during such time when the current profile is almost flattened the transverse integrated density decreases due to the increase of superfluid density-weighted velocity as $\rho_x = I/\langle v_x \rangle$. Moreover, at the time $-\langle v_x \rangle$ is maxima the current is slightly reduced with respect to its local maxima due to the varying density.

As described in Sect.3.5.2, in the event of a vortex ring generation, the superfluid flow slows down; the nucleation of a vortex ring leads to a reduction in the main flow (visible also in Fig. 3.21(i)), thus slowing down the population imbalance dynamics. In fact, the corresponding reduction in I following the VR generation is clearly visible in Fig. 3.21(iii) where it can even reverse its sign (i.e. $-I < 0$).

3.6.1 Second order term in current-phase relation

In the two-mode model (described in detail in Sect.2.3.2) the current-phase relation is a sinusoidal function written as $I = I_c \sin(\Delta\phi)$ where only one sinusoidal term is present, thus the population imbalance oscillates in time with one single frequency. As shown from F. Meier and W. Zwerger in [65] (described also in Sect. 2.4), this is an approximation that is valid in the limit of $V_0/\mu \gg 1$. In fact if the barrier height is not much larger than μ other terms must be considered in the tunneling Hamiltonian which takes into account also the condensate-noncondensate tunneling process and thus they add other terms to the current-phase relation such as the non-dissipative term $J_1 \sin(2\Delta\phi)$. If such term is present the current-phase relation, where we call now the relative phase as ϕ in order to use same symbols as [65], becomes

$$I(\phi) = I_c \text{sin}(\phi) + J_1 \text{sin}(2\phi). \tag{3.31}$$

In the paper of Ref. [65] an analytic model was developed in order to calculate the second-order term J_1 for homogeneous Bose gases and rectangular barriers. Recently, M. Zaccanti and W. Zwerger [159] extented such model to the harmonically trapped case with a Gaussian barrier, relevant for our study. In the following we briefly summarize how such model extension has been obtained.

Based on a perturbative approach valid in the limit $V_0 > \mu$, Meier and Zwerger [65] obtained explicit predictions for the first and second order contributions to the superfluid current (for a homogeneous, $T = 0$ weakly interacting BEC) respectively denoted by I_c and J_1, yielding a current-phase relation of the kind Eq. (3.31) that can also be written as:

$$I(\phi) \equiv I_c \cdot (\sin(\phi) + \bar{g} \cdot \sin(2\phi)), \tag{3.32}$$

where $\bar{g} = J_1/I_c$. Notably, these terms solely depend upon the bulk condensate density and the boson tunneling amplitude, which in turn can be recast in terms of the bulk chemical potential and the single-particle transmission coefficient across the barrier [65]. As such, within this framework, predictions for the maximum current supported by a generic junction can be obtained from the knowledge of the bulk properties of the superfluid, and by evaluating the single-particle transmission coefficient associated with the specific barrier under consideration.

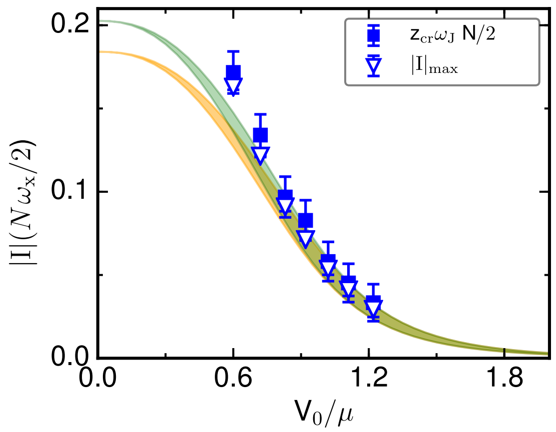

Figure 3.22: The prediction of the maximum superfluid current taking only the first order term in the current-phase relations (yellow profile) and including also the second order terms (green profile). The blue triangles indicate the value of the maximum current extracted by the GPE simulation for $z_0 = z_{\mathrm{cr}}$ and the blue squares show another way to calculate $|\mathrm{I}|_{\mathrm{max}}$ from the critical imbalance and the Josephson 'plasma' frequency extracted from the profile of $z(t)$ for $z_0 < z_{\mathrm{cr}}$.

To proceed with obtaining the theoretical curves, we modify the analytic results given in Ref. [65] in the following ways [2]: Firstly, we derive an analytic expression for the tunneling amplitude $t_{cc}(V_0, \mu)$ (using the notation of [65]) across our Gaussian barrier, by approximating the Gaussian profile with a symmetric Eckart potential of the kind $V_{Ec} = V_0/\cosh^2(x/d)$ with $d = 0.6w$. Secondly, we employ the local density approximation to recast the first and second order currents within an integral form, in order to account for the inhomogeneous density distribution featured by our trapped samples. From the knowledge of I_c and J_1, we then obtain the maximum current enabled by our junction, up to first and second order, respectively. These are shown in Fig. 3.22. In the former case, the critical current is simply given by I_c.

The yellow shaded area in Fig. 3.22 is delimited by the trend of I_c predicted by our analytic model, assuming a $\pm 5\%$ relative variation of the peak chemical potential μ_0 of the trapped Bose gas at $T = 0$, around the nominal value of μ_0 based on the measured molecule number and trapping frequencies. Fig. 3.22 shows the maximum value of the

[2]This calculation was performed by one of my collaborators Dr. Matteo Zaccanti and it is described in detail in [159].

absolute value of the current extracted for $z_0 = z_{\rm cr}$ for each V_0/μ in the range $[0.6, 1.22]$ from the GPE simulations. While I_c provides an excellent description of $I_{\rm max}$ derived from the numerical simulations for $V_0/\mu \geq 0.9$, it systematically underestimates the maximum current found for lower barrier heights. This mismatch is expected in light of the fact that second order contributions become increasingly important for progressively lower V_0/μ values [65]. In order to account for second order corrections to $I_{\rm max}$, we exploit our model prediction for J_1 in connection with the analytic results obtained in Ref. [222] for a generic current-phase relation with first and second harmonics Eq. (3.32). For any value of $\bar{g} = J_1/I_c$, it can be shown [222] that the maximum current will read:

$$\frac{I_{\rm max}}{I_c} = \frac{(\sqrt{1+32\bar{g}^2}+3)^{3/2}(\sqrt{1+32\bar{g}^2}-1)^{1/2}}{32|\bar{g}|}. \tag{3.33}$$

By comparing corresponding first (yellow area) and second order (green area) contributions in Fig. 3.22, one can notice how inclusion of second harmonics generally increases $I_{\rm max}$, and enables to excellently reproduce both experimental (shown in Chapt. 4) and GPE results, down to barrier heights as low as $V_0 \sim 0.6\mu$. Numerically, $|I|_{\rm max}$ is also well approximated by $z_{\rm cr}\,\omega_J\,N/2$ as shown in Fig. 3.22.

3.6.2 The Josephson current profile in different dynamical regimes.

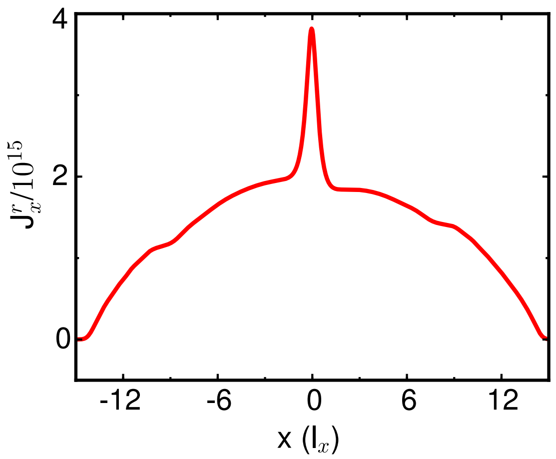

Figure 3.23: The x component of the density current profile along the x axis for $y = z = 0$ for $V_0/\mu = 0.8$ and $z_0 = 0.13 > z_{\rm cr}$ at $t = 14.9$ ms, before the VR is nucleated.

The density current along x axis has the profile shown in Fig. 3.23, with a local maxima (given by the tunneling current) at the barrier region (i.e. at the barrier center $x = 0$) superimposed to an almost Gaussian background at the time shown in Fig. 3.23. In order to extract only the tunneling current, we subtract the term $n(\hbar/M)a_L$ from the total density current, where a_L is the slope of the linear fitting function of the relative phase profile $\Delta\phi(x)$ and n the condensate density. We estimate so the tunneling density current as $J_x^r = j_x - n_x(\hbar/M)a_L$ from which we extract its value at $x = 0$. As discussed in the previous section, for the range of the barrier heights explored in this chapter $[0.6, 1.22]\mu$, the second order term in the current-phase relation is expected to be important, thus we write the local current-phase relation as:

$$J_x^r(\Delta\phi) = J_c \sin(\Delta\phi) + \tilde{J}_1 \sin(2\Delta\phi) = J_c \cdot (\sin(\Delta\phi) + g_{\text{loc}} \cdot \sin(2\Delta\phi)). \tag{3.34}$$

Here we often use also the expression 'current' or 'local current' for the density current but what we calculate locally is the density current which expresses the number of particles flowing through the barrier per unit time and unit area, such that its units are those of current divided by an area. Fig. 3.24 shows the profile of the density current J_x^r versus

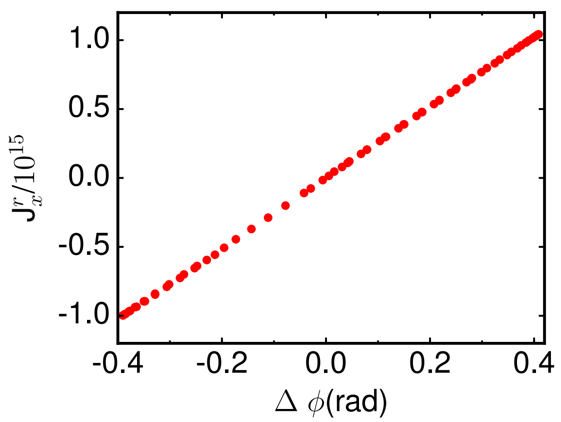

Figure 3.24: The density current versus relative phase profile for $V_0/\mu = 0.8$ and $z_0 = 0.05 < z_{\text{cr}}$. The values of j_x^r are expressed in units of time and area.

the relative phase for $V_0/\mu = 0.8$ and $z_0 = 0.05 < z_{\text{cr}}$ in the Josephson 'plasma' oscillation regime. The current profile is linear as the relative phase maximum value is much smaller than π ($\Delta\phi_{\max} \simeq 0.4$ rad) and thus we can approximate the density current defined in Eq. (3.34) as

$$J_x^r(\Delta\phi) \approx (J_c + 2\tilde{J}_1)\Delta\phi. \tag{3.35}$$

In the case when the second order term $2\tilde{J}$ is much smaller than J_c the inclination of the $J(\Delta\phi)$ gives the critical density current. If instead the initial imbalance is such that $z_0 \geq z_{\text{cr}}$, the relative phase achieves a maximum value of around π and thus the current-phase relation is sinusoidal. When the relative phase becomes equal to π, the phase jumps by 2π, due to the VR emission, and thus the local current jumps at its value $J_x^r(\Delta\phi = -\pi) = -J_x^r(\Delta\phi = \pi)$. This process repeats itself until the population imbalance becomes smaller than the critical value. Fig. 3.25 shows the current-phase relations for different

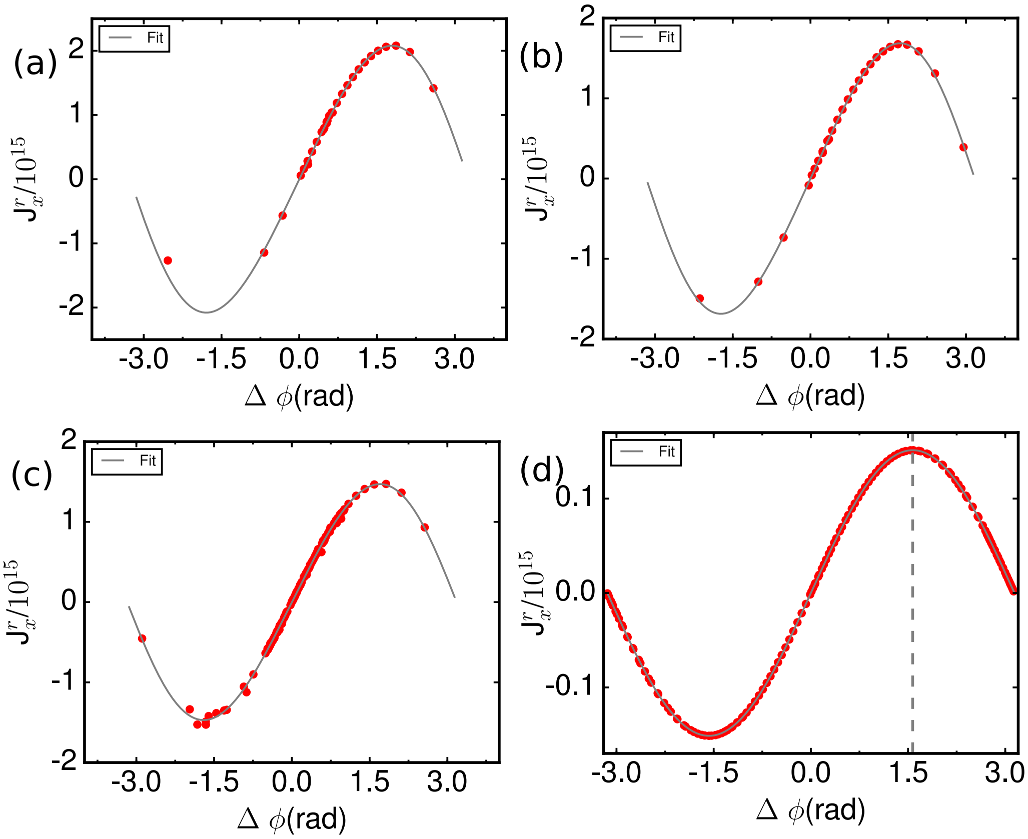

Figure 3.25: The density current versus relative phase profile for $V_0/\mu = 1$ (a), $V_0/\mu = 1.1$ (b), $V_0/\mu = 1.17$ (c) and $V_0/\mu = 2$ (d) at $z_0 = z_{\rm cr}(V_0)$.

values of barrier height near μ and at $z_0 = z_{\rm cr}(V_0)$ and the corresponding sinusoidal fit profiles (a)-(c). We find that the second order term $\tilde{J}_1$ is negative (as expected for J_1 from [65]), which means that the maximum value of the current is obtained for larger values than $\pi/2$. Moreover for smaller values of barrier heights, the importance of the second order increases (as shown previously) with a local ratio $|g|_{\rm loc} = |J_1|/j_c \simeq 0.14$ for $V_0/\mu = 1$ and $|g|_{\rm loc} \simeq 0.08$ for $V_0/\mu = 1.17$. Fig. 3.25 (d) shows just for comparison the current-phase relation for $V_0/\mu = 2$ (outside the experimental range of parameters) where the second order term contribution is $|g|_{\rm loc} \simeq 7 \times 10^{-4}$ and the current has its local maximum at exactly $\pi/2$. We note that, in this section, the density current and the relative phase are calculated during a relatively short-time evolution; usually the time evolution explored is until or slightly larger than the time when the generation of the first VR occurs.

The current profile for $V_0/\mu = 0.8$ and $V_0/\mu = 1.1$ are shown together in Fig. 3.26 at $z_0 = z_{\rm cr}$. For higher V_0/μ the maximum value of the density current is smaller as the density at the trap center is smaller too. Moreover, by looking at the value of the relative phase at the maximum of J_x^r we observe that it is shifted more towards values larger than $\pi/2$ for smaller V_0, consistent with the increasing importance of the negative second order term.

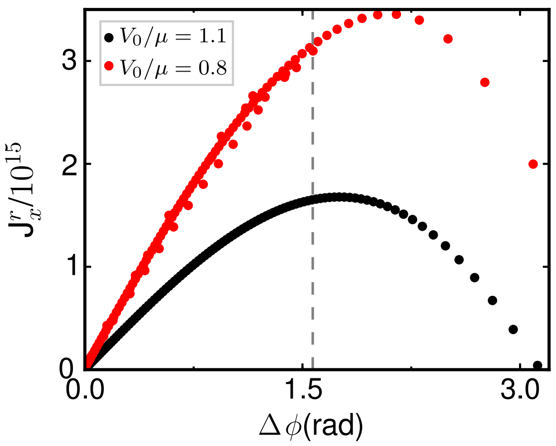

Figure 3.26: The density current versus relative phase profile for $V_0/\mu = 0.8$ (red line) and $V_0/\mu = 1.1$ (black line) at $z_0 = z_{\rm cr}(V_0)$. The vertical grey line is at $\pi/2$.

The superfluid critical current is expected to be dependent on the value of z_0 (as described in Refs. [65, 59]) and this dependence is expressed as $I_c\sqrt{1-z_0^2}$ [59, 65] in the case when only the first order term is present in the current-phase relation. We investigate such dependence in our case by showing in Fig. 3.27 the comparison between the density current versus relative phase profile $j_x^r(\Delta\phi)$ for $V_0/\mu = 0.8$ and for two different values of z_0: for $z_0 = 0.05 < z_{\rm cr}$ (shown also in Fig. 3.24) and $z_0 = 0.13 \gtrsim z_{\rm cr}$. We observe that the values of the density current for $z_0 = 0.05$ cover a short range (linear part) of the overall sinusoidal current-phase profile for $z_0 = 0.13$ and the inclinations of the current profiles for small $\Delta\phi$ are almost the same showing negligible dependence of the critical current on the initial imbalance in our case.

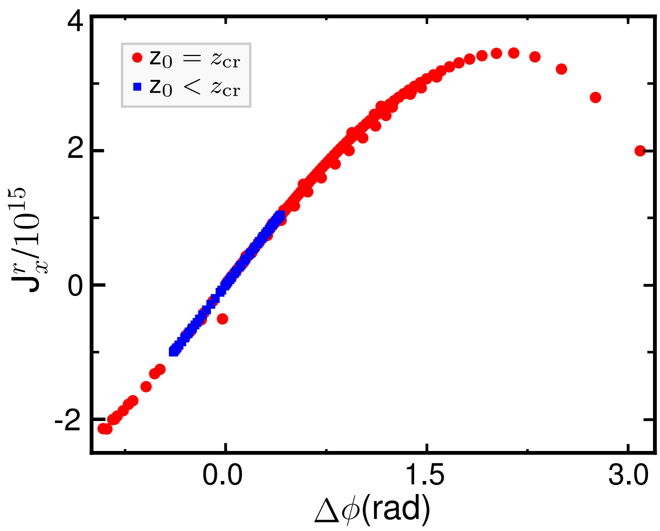

Figure 3.27: The comparison between the density current versus relative phase profile for $V_0/\mu = 0.8$, $z_0 = 0.05 < z_{cr}$ (blue circles) and $z_0 = 0.13 \simeq z_{cr}$ (red circles).

3.7 Dependence on initial imbalance

In this section we show the dependence of the vortex ring dynamics and the amount of dissipation present in the system on the initial population imbalance in the case when the barrier height value is kept fixed at $V_0/\mu = 0.8$ and the z_0 is variable taking values in the range $z_0 \in [0.13, 0.37]$. The presence of an initial imbalance induces an initial chemical potential difference between the two condensates found as $\Delta\mu_0 = E_c z_0 N/2$. Thus an initial chemical potential gradient is present in the system across the barrier which induces an initial superfluid acceleration through the barrier, expressed by Eq. (3.7). Such initial acceleration is higher for larger z_0, as observed in Fig. 3.28 which shows the temporal evolution of the x component superfluid velocity (calculated at the trap center) for different initial population imbalance from $z_0 = 0.13$ to $z_0 = 0.37$. Thus for higher z_0 the critical velocity is obtained earlier in time and the VR nucleation time becomes shorter as we will show later. Only the first jump $-\Delta v_x$ of the superfluid velocity is shown in Fig. 3.28 in correspondence to the first nucleated VR but other jumps are present depending on the number of the VRs generated, i.e. on the value of $z_0 - z_{\rm cr}$. Interestingly, the velocity jump Δv_x is not independent on z_0 and it follows a definite trend becoming smaller as z_0 increases. This can be related to the slightly larger VR size when it leaves the barrier for larger z_0 (discussed further in the next section) as $\Delta v_x \propto \kappa/R_{\rm VR}$.

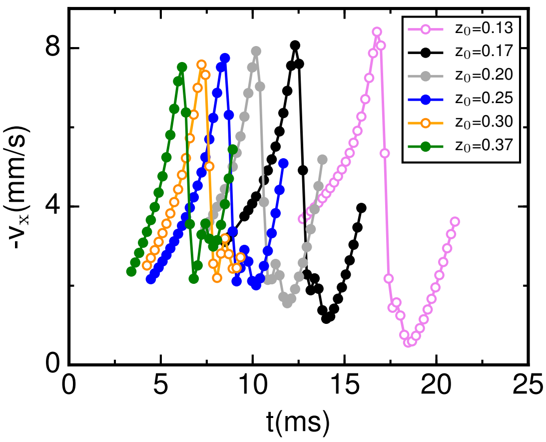

Figure 3.28: Time evolution of the x component superfluid velocity calculated at the trap center for different z_0 (as described in the legend) and for fixed $V_0/\mu = 0.8$.

3.7.1 First vortex ring dynamics

We focus here on the study of the dynamics of the first vortex ring generated for each z_0 in the range $[0.13, 0.37]$. Fig. 3.29 shows the time evolution of the first VR position and mean radius for different z_0. In the previous sections we analysed the early-stage dynamics

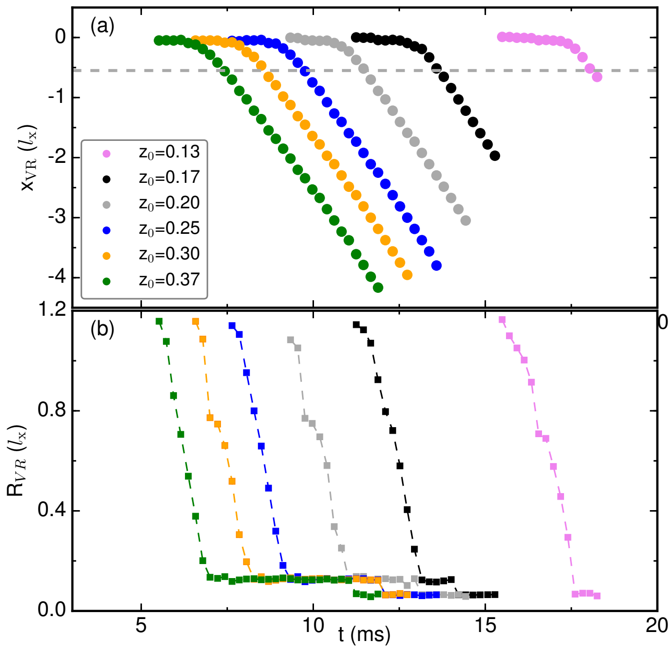

Figure 3.29: Time evolution of (a) the first vortex ring axial position, and (b) of its semiaxes mean value, generated for different initial imbalances. Horizontal grey line in (a) at $x = -0.55l_x$ indicates the temporal value from which we start extracting the linear fit, v_{VR}.

of the VR and its effect on the macroscopic quantities such as superfluid current. Here instead we analyse the dynamics of the VR after leaving the barrier, i.e. its position becomes larger than $2w$ and it propagates in the left condensate with almost constant velocity. Firstly, we observe that the VR is generated earlier in time with higher population imbalance confirming the results of Fig. 3.28: the dependence of the nucleation time, called t_0, on the initial population imbalance z_0 is shown in Fig. 3.30. Moreover the lifetime of the first VR increases with increasing z_0 as shown in Fig. 3.30. At the position $x_1 = |x|_{VR} \simeq 0.55l_x$ the VR mean radius, after the initial fast shrink, achieves its 'plateau' value and it maintains such values for certain time interval during its propagation until it slightly shrinks its radius again and in the end of its lifetime the VR disappears in rarefaction pulses. Interestingly the position x_1 corresponds to the position at which the TF radius achieves its maximum extent and after that it stays almost flat for certain x axis interval (as visible in Fig. 3.12). Therefore, following the condensate density profile the VR radius shrinks until the condensate density is maximum and then the VR radius stays for a while constant reflecting the density profile. For such barrier height, the Kelvin waves have small amplitude and thus it slightly affects the short lifetime of such VR. We will show in Chapt. 4 and Chapt. 5 that in the case of barrier removal or in the case of smaller barrier heights where the VR lives more and has larger mean radius the presence

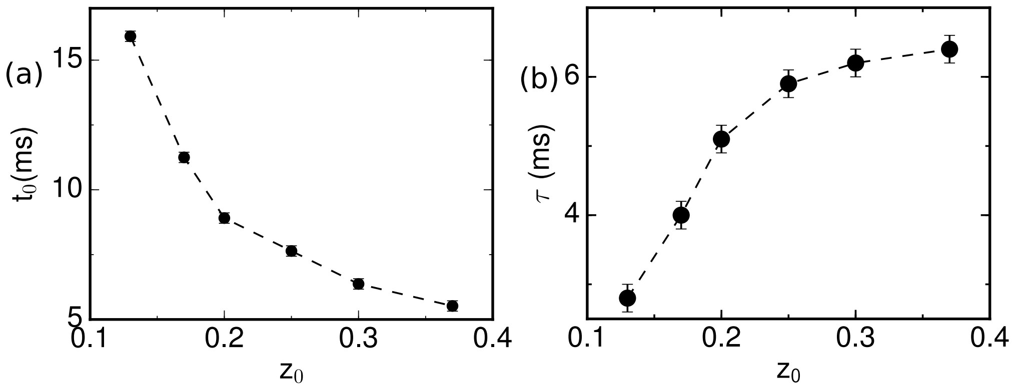

Figure 3.30: (a) The dependence of the VR nucleation time t_0 and (b) the lifetime of the first VR on the initial imbalance z_0. The barrier height is kept fixed at $V_0/\mu = 0.8$ while the z_0 changes in the range [0.13, 0.37].

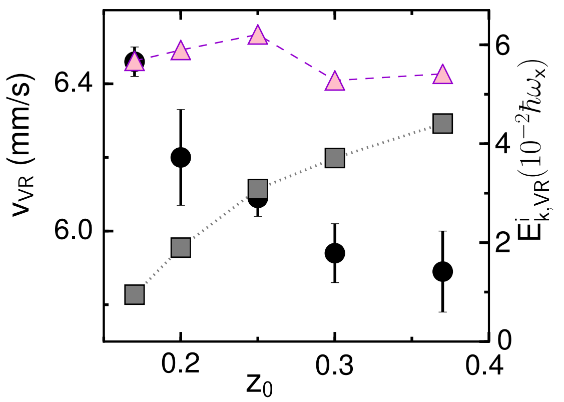

Figure 3.31: Role of initial population imbalance z_0 (for fixed $V_0/\mu = 0.8$ for which $z_{cr} = 0.11$) on: velocity v_{VR} (left axis, black circles) and incompressible kinetic energy $E^i_{k,VR}$ (right axis, grey squares) of 1st nucleated VRs. Pink triangles indicate the VR energy calculated with the analytical formula for homogeneous unbounded BECs.

of larger amplitude Kelvin waves have strong effects on the VR dynamics.

We extract the VR velocity by performing a linear fit from $|x_{VR}| \geqslant 0.55 l_x \simeq 2w$. and we find that increasing z_0 leads to a decreasing v_{VR} as shown in Fig. 3.31. As a result of this, the first VR for higher z_0 propagates further into the left reservoir (the one with smaller condensate density) (Fig. 3.29(a)), maintaining a constant radius during this propagation for longer time than the smaller z_0 cases (Fig. 3.29(b)). Moreover the first VR radius for $z_0 = 0.37$ during its propagation is larger than the one at $z_0 = 0.13$, which is consistent with its smaller propagation velocity value. Fig. 3.31) shows also the dependence on z_0 of the value of the incompressible kinetic energy $E^i_{k,VR}$ of the first nucleated VR together with the VR energy calculated by the formula for homogeneous

BECs [3] and will be described in the following section.

3.7.2 The VR kinetic energy

The incompressible kinetic energy of the VR, $E^i_{k,VR}$, which depends on v_ω only, is obtained by the following procedure: we first integrate the incompressible kinetic energy density per unit mass e^i_k on the volume $\mathcal{R}$ encompassing the vortex ring. The region $\mathcal{R}$ is defined as follows [4]

$$
\begin{aligned}
R = \quad & \{(x,y,z) : x_{VR} - \Delta x < x < x_{VR} + \Delta x \;\; ; \\
& -R^{TF,y}(x) < \;y\; < R^{TF,y}(x) \quad ; \\
& -R^{TF,z}(x) < \;z\; < R^{TF,z}(x) \;\; \} \;,
\end{aligned}
$$

where $x_{VR} = -l_x$ and $\Delta x = 4R_{VR}$, where R_{VR} is the VR radius when $x_{VR} = -l_x$. The values of x_{VR} and Δx are chosen stemming from the following considerations. First, in a homogeneous and unbounded BEC, a cylindrical region, coaxial with respect to a VR, of height $8R_{VR}$ (the VR center being placed in the center at $4R_{VR}$) and radius $5R_{VR}$ contains more than 90% of the incompressible kinetic energy of the VR. Second, the flow velocity is negligible in $\mathcal{R}$, *i.e.* $\mathbf{v}_f \approx 0$ and hence $\mathbf{v} \approx \mathbf{v}_\omega$. Therefore, the incompressible kinetic energy present in $\mathcal{R}$ only originates from the VR. As a consequence, $E^i_{k,VR} = \int_{\mathcal{R}} e^i_k d\mathbf{x}$ (with e^i_k defined in Eq. (3.24) is a reasonable estimate of the VR incompressible kinetic energy. Moreover, the VR is still close to its nucleation region and therefore $E^i_{k,VR}$ can, at least qualitatively, be considered as proxy for the VR initial incompressible kinetic energy. Investigating the dependence of $E^i_{k,VR}$ on the initial population imbalance z_0, shown in Fig. 3.31 we find that $E^i_{k,VR}$ is an increasing function of z_0.

To assess the impact of confinement and inhomogeneity, we also evaluate the corresponding energies of the first nucleated VRs if they had been immersed in an unbounded and homogeneous BEC, employing the analytical formula derived by Roberts and Grant [171] (expressed also in Eq. (2.33)):

$$
E^{i,RG}_{k,VR} = \frac{1}{2}\, n\, \kappa^2 R_{VR} \left[\ln\left(\frac{8R_{VR}}{\xi} \right) - 1.615 \right] \;, \tag{3.36}
$$

where the density n and the healing length ξ have been evaluated on the x axis for $x \sim x_{VR} = -1l_x$. The result of this calculation is reported in Fig. 3.31 (pink triangles) showing that confinement and inhomogeneity play a fundamental role in the energetics of the system studied [223, 224].

[3] The calculations of $E^i_{k,VR}$ for both our inhomogeneous system and for homogeneous BECs were performed by one of my collaborators, Dr. Luca Galantucci.

[4] This calculation was performed by one of my collaborators, Dr. Luca Galantucci.

3.7.3 The dissipation of the kinetic energy

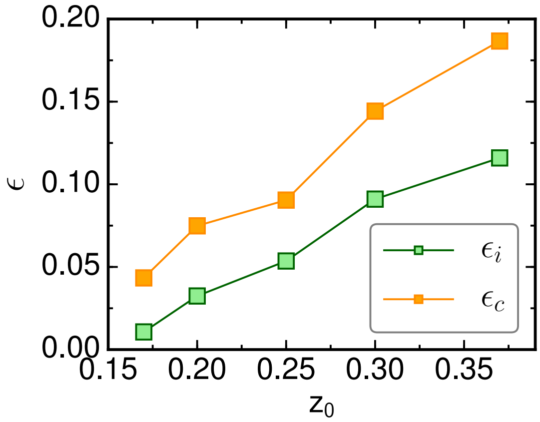

Figure 3.32: Vortex induced dissipations ϵ_i and ϵ_c as a function of z_0 for $V_0/\mu = 0.8$.

To quantify the irreversible dissipation of Josephson oscillations, we define the acoustic dissipation ϵ_c and the incompressible dissipation ϵ_i as follows:

$$\epsilon_c = \Delta E^c_k / E^{tot}_{k,[0,1]} \tag{3.37}$$

$$\epsilon_i = E^i_{k,VR} / E^{tot}_{k,[0,1]} \tag{3.38}$$

where $E^{tot}_{k,[0,1]}$ is the total kinetic energy flowing through the junction until the nucleation of the first VR, $E^i_{k,VR}$ is the incompressible kinetic energy of the first VR (as shown in Sect. 3.7.2) and ΔE^c_k is the increase of compressible energy in the system observed during the early stage dynamics of the VR (described in Sect. 3.7.2). After calculating the fraction of the total kinetic energy flowing through the junction until the nucleation of the first VR which is dissipated in sound (ϵ_c) or transferred to the first VR (ϵ_i), we find that both sources of dissipation increase as z_0 gets larger. This is shown in Fig. 3.32 which also demonstrates that they can cumulatively account for a significant fraction of the total energy. Surprisingly, the acoustic dissipation ϵ_c is always larger than the incompressible contribution ϵ_i.

3.7.4 Josephson junction as a tool for controlled vortex ring generation

Depending on the initial value of the population imbalance, or better on the difference between the z_0 and the critical imbalance $z_{\rm cr}$, different number of VRs can be nucleated, from one to many. Also in this section we keep fixed the barrier height to $V_0/\mu = 0.8$ and we study the role of increasing initial imbalance from $z_0 \simeq z_{\rm cr} = 0.11$ to $z_0 = 0.37$. The total number of VRs ($N_{\rm VR}$) propagating in the left well, is found by looking at the 3D density plots. However different methods can be used as comparison to check for consistency: $N_{\rm VR}$ can be also found by counting the number of -$\langle v_x \rangle$ time evolution maxima. Another way to estimate $N_{\rm VR}$ is by the expression [12]:

$$\langle(\mu_L - \mu_R)\rangle = h\langle\frac{dn}{dt}\rangle, \tag{3.39}$$

where the $\langle\cdots\rangle$ indicate time-averaged values, $(\mu_L - \mu_R)$ is the chemical potential difference and dn/dt is the rate of VRs crossing a certain path inside the condensate whose time-average gives $N_{\rm VR}$. The chemical potential in the left (right) well is estimated by using Eq. (2.18), upon replacing N with $N_L = (1 - z)/2$, $(N_R = (1 + z)/2)$. Increasing z_0 leads to more nucleated vortices $N_{\rm VR}$, due to the larger time-averaged chemical potential difference [12]. This is clearly shown in Fig. 3.33 and is consistent with Ref. [20] and with earlier studies of controlled vortex generation [225, 226].

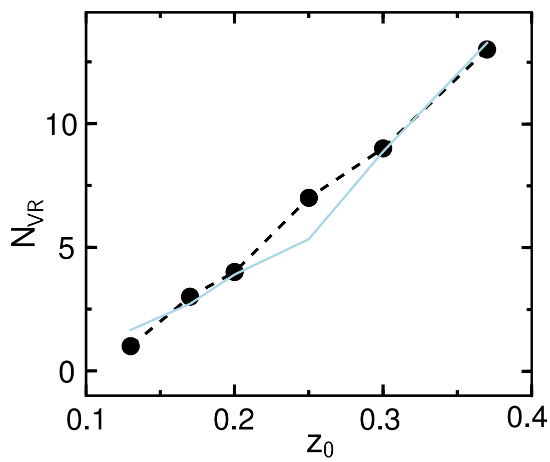

Figure 3.33: Total number N_{VR} of VRs penetrating the bulk as a function of z_0. Blue line connects $N_{\rm VR}$ estimates from the time-averaged phase-slippage rate $\Delta\mu(t)/h$ [12].

3.7.5 The effect of trap asymmetry

Due to the transverse axes asymmetry in our chosen geometry (set by the LENS experiment), i.e. $\omega_y = 2\pi \times 148$ Hz$\simeq 0.8\omega_z$ where $\omega_z = 2\pi \times 187$ Hz, the vortex ring has a slightly elliptic shape when it is generated. To investigate further the role of the transverse trap asymmetry, we consider two more cases, in which the product of transverse trap frequencies $(\omega_y \cdot \omega_z)$ is kept fixed, so that the system chemical potential is not affected. Specifically, we consider the cases: $\omega_y = 2\pi \times 130$Hz $\simeq 0.61\omega_{\rm z}$ with $\omega_z = 2\pi \times 213$ Hz, and $\omega_y = 2\pi \times 100$Hz $\simeq 0.36\omega_z$ with $\omega_z = 2\pi \times 277$ Hz. In order to refer to each of the three cases of different values of transverse trap frequencies and ratios we define the quantity $\lambda_{as} = 1 - \omega_y/\omega_z$ that represents the asymmetry between such frequencies. The quantity

λ_{as} takes a value equal to 0.2 for LENS experimental parameters, $\lambda_{as} = 0.39$ in the second case and $\lambda_{as} = 0.64$ for the most asymmetric case. The barrier height and initial imbalance are kept the same in all the three cases with $V_0/\mu = 0.6$ and $z_0 \simeq z_{cr} = 0.19$. Fig. 3.34 shows the population imbalance short time evolution for the LENS experiment transverse asymmetry $\lambda_{as} = 0.2$ and for the case of larger asymmetry $\lambda_{as} = 0.64$. We firstly observe that the initial part till $t = 0.05$ s of the relative imbalance time evolution is almost unaffected by the trap transverse asymmetry with a small effect in the size of the 'dip' which is more pronounced for the less asymmetric case. However, the subsequent dynamics of $z(t)$ are instead affected.

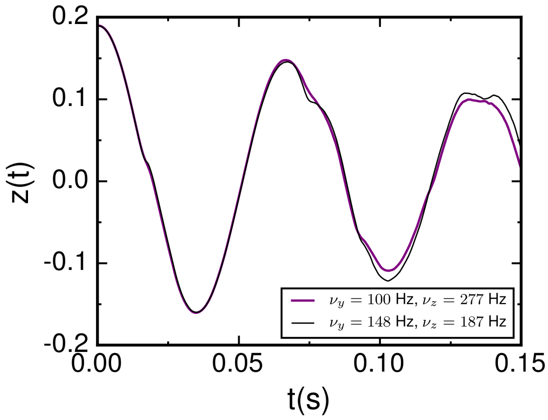

Figure 3.34: The time evolution of the population imbalance for the trasverse trap frequencies $\omega_y = 2\pi \times 148$ Hz, $\omega_z = 2\pi \times 187.5$ Hz and $\omega_y = 2\pi \times 100 Hz$ and $\omega_z = 2\pi \times 277$ Hz.

Increasing the transverse trap asymmetry λ_{as} leads to the generation of more elliptic VR as it is visible from the 3D iso-contour density profile shown in Fig. 3.35(a) at time $t = 19.1$ ms where the VR almost reach the condensate boundary for $\lambda_{as} = 0.39$ [(a),(ii)].

The fact that the VR shape differs from a circular profile induces the emergence of $m = 2$ Kelvin wave excitations (as will be shown in Chapt. 4). The amplitude and frequency of such waves increases with the transverse trap asymmetry, i.e. λ_{as}. In fact, at a slightly later fixed time $t = 22.2$ms, the VR generated for $\lambda_{as} = 0.39$ has already inverted the axes of symmetry while the VR in the case $\lambda_{as} = 0.2$ has still the same symmetry axis. In the presence of Kelvin wave excitations the VR dissipates its energy via phonons which are visible in the density surface of Fig. 3.35(b),(i)-(ii). Furthermore more sound waves propagates in the case $\lambda_{as} = 0.39$ with respect to the case of lower asymmetry $\lambda_{as} = 0.2$.

Increasing further λ_{as} leads to the nucleation of higly elliptic VR which can even, almost immediately after its generation, breaks in two vortex lines as happens for $\lambda_{as} = 0.64$ shown in the subplot [(a),(iii)]. Moreover at a later time $t = 22.2$ms as shown in (b)-(iii) the two vortex lines have also change their axes of symmetry from along y axis to along z axis due to the vortex-reconnections mechanism that happens in the time interval between the chosen times.

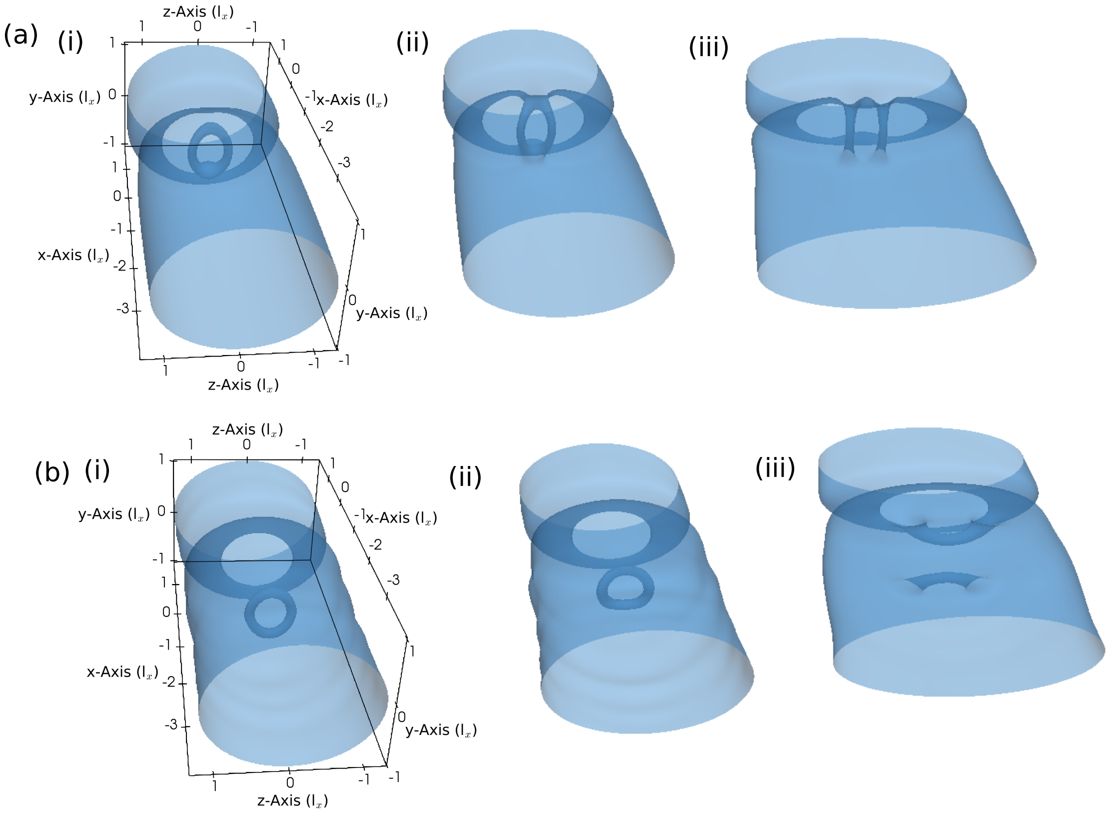

Figure 3.35: The 3D iso-contour density profile at 27% of the maximum density for the three cases of transverse trap frequencies asymmetry (i) $\lambda_{as} = 0.2$, (ii) $\lambda_{as} = 0.39$ and (iii) $\lambda_{as} = 0.64$ at fixed time (a) $t = 19.1$ ms and at (b) $t = 22.2$ ms. These numerical data are for $V_0/\mu = 0.6$ and $z_0 = 0.19$.

3.8 Conclusions and future works

3.8.1 Conclusions

In this chapter we have studied the dynamical regimes in an elongated atomic Josephson junction for the experimental parameters of ^{6}Li experiment at LENS in Florence [49, 20] in the limit of molecular BEC of lithium. Our Josephson junction consists of two molecular BECs separated by a thin Gaussian barrier which are trapped in an anisotropic three-dimensional harmonic trap with an aspect ratio of around 11. As in the experimental set-up, the $1/e^2$ Gaussian barrier width is set at $w/\xi = 4$ with variable barrier height in the range $[0.6, 1.22]\mu$. The superfluid dynamics through the barrier are triggered by an initial population imbalance between the two-wells z_0 which induces an initial chemical potential difference across the barrier. Driven by the chemical potential gradient the superfluid accelerates while flowing in the negative left direction [12]. We showed that when the superfluid velocity local maxima are smaller than the local speed of sound, the system is in the Josephson 'plasma' regime. This regime is characterized by coherent oscillations of both the population imbalance and the relative phase around a zero mean value at a characteristic 'plasma' frequency. If instead the superfluid velocity local maximum exceeds a critical value the system enters the dissipative regime, where the population imbalance decay initially fast in time and then oscillates around a zero mean value with different frequencies. On the other hand, the relative phase shows jump of around 2π everytime a VR is generated (known as phase-slippage mechanism). Once the VR emission ceases, the relative phase oscillates around a zero mean value with the same frequencies as the population imbalance (conjugate variables).

Further to this analysis we showed that in the current-phase relation, apart for the term in $\sin(\Delta\phi)$, there is a second one that depends on $\sin(2\Delta\phi)$ and thus the current-phase relation can be written as $I = I_1 \sin(\Delta\phi) + J_1 \sin(2\Delta\phi)$. The second order term is shown in [65] to arise from considering the second-order term in the tunneling Hamiltonian. It has a negative sign and a small contribution which decreases as the barrier height increases. We then extracted the critical parameters for the onset of the dissipative regime such as critical population imbalance and the critical current for each barrier heights from the GPE simulations and we showed that the critical current is well-predicted by the model of Ref. [65, 159] as long as we consider the second-order term in the current phase relation.

We then investigated further the origin of dissipation. We showed that in our 3D trap, vortex rings (VRs) are generated every time the superfluid velocity maxima exceeds a critical velocity threshold. The vortex ring, which is nucleated outside the local Thomas-Fermi radius (as a 'ghost' vortex), shrinks initially fast its radius (due to the density inhomogeneities) by entering the condensate, thus becoming a hydrodynamical vortex ring. The vortex ring swirling velocity, which increases initially as the VR radius decreases, induces a reduction of the superfluid potential flow which can even invert its sign, that we termed the backflow. As the VR leaves the barrier, the VR swirling velocity at the barrier position starts decreasing until it becomes equal to zero and then the total superfluid velocity is only due to the potential flow. Due to the remaining chemical potential difference $\Delta\mu(t)$, the superfluid velocity increases again until it exceeds again the critical velocity and another VR is nucleated with a rate given by the phase-slippage rate $\Delta\mu/h$.

We also showed that everytime a VR enters the local Thomas-Fermi surface it causes a local 'dip' in the otherwise monotonic decay of $z(t)$. Thus the number of dips in the short-time evolution of the population imbalance are directly related to the number of the generated VRs. The number of vortex rings which can be generated in the junction depends on how far the initial imbalance is from its critical value.

In order to give further insight into the irreversible dissipation mechanism of the Josephson oscillation we then carried out a further analysis of two of the components of the kinetic energy; the incompressible E_k^i and compressible kinetic energy E_k^c. We found that at early stage dynamics of the VR, specifically from the moment that it first enters the local TF surface until the moment when it reaches the axial position at which the TF radius is maximum, sound wave are released, which cause E_k^c to have a step-like increase. We thus showed that the dissipation originates from two irreversible effects: phonon emission during VR early stage dynamics, and incompressible kinetic energy transfer from the superfluid flow to the swirling one of the nucleated vortex rings.

We then followed the vortex ring dynamics after leaving the barrier. Depending on the value of the barrier height with respect to the chemical potential value, we found that the VR either have a long lifetime– during which it travels a long distance into the left reservoir before expanding and breaking into two vortex lines– or it can shrink after a short distance giving rise to rarefaction pulses. In this chapter we analysed the second case, for $V_0/\mu = 0.8$, and showed the dependence of the first VR dynamics on the initial population imbalance. Furthermore, the dependence of the amount of dissipation on z_0 was investigated, finding that the fraction of the total kinetic energy until the nucleation of the first VR that is dissipated in sound or transferred to the first VR, increases as z_0 gets larger.

Finally, we considered the effect of varying the trasverse trap asymmetry at fixed value of $(\omega_y \omega_z)$ and demonstrated that increasing the difference between the transverse frequencies leads to a more elliptical VR with higher elliptic geometries even causing it to break into vortexlines almost immediately after being generated. Despite such findings which influence the long time evolution, the transverse trap asymmetry was found to have no effect in the initial decay of $z(t)$.

3.8.2 Future works

Vortex-vortex interaction

The number of vortex rings depend on the difference $(z_0 - z_{cr})$ and as these differences increase more vortex rings are generated. For one of the cases we studied with $V_0/\mu = 0.8$ and $z_0 = 0.25$ there are in total seven vortex rings generated. The temporal evolution of their position along the x axis is shown in Fig. 3.36. The seven VR are well separated from each other in time and space and their distance along the x axis is almost unchanged with time. This seems to suggest that the interaction between VRs in this regime was small as it scales with $1/d^2$, where d is the distance between two subsequent VRs. However we note that the third and the fifth VRs live more and propagate further in the left reservoir. Looking at one of the components of the kinetic energy, the incompressible kinetic energy E_k^i, its value at the moment the third VR enters the local TF surface at the barrier is smaller with respect to its value when the second VR enters the TF surface. In this way more kinetic energy can go to the third VR and it can live more but this is not what happens. Even though the VRs are well separated from each other, everytime a VR enters the left reservoir and/or shrinks, sound waves are emitted which can affect the VR motion. As a future goal it would be interesting to quantify the effect of the sound waves to the VR motion and to investigate further the reasons why some of the subsequent VRs can live even more than the first VR.

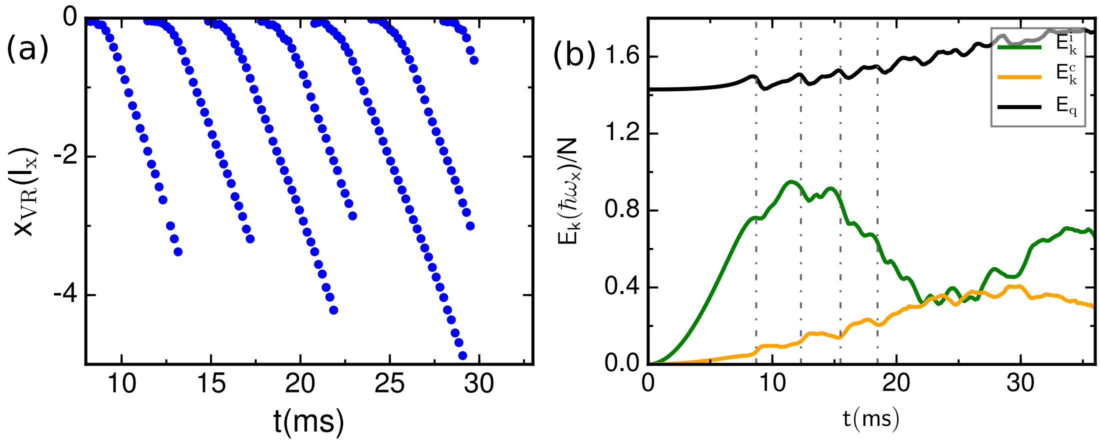

Figure 3.36: (a) The time evolution of the x axis position of the seven VRs generated and (b) the time evolution of the kinetic energy components; quantum, incompressible and compressible kinetic energy. The VR tracking in (a) starts slightly before the VR enters the local TF surface. The vertical dashed line indicate the moment the first four VR enters the local TF surface. The data are for $V_0/\mu = 0.8$ and $z_0 = 0.25 > z_{cr} = 0.11$.

If instead we study a case of a lower V_0/μ, the VR lives more (the effect of the value V_0/μ on the VR dynamics will be shown in Chapt. 4 and Chapt. 5) moving in the presence of a density gradient where the density decreases along the x axis. So, in order to conserve its kinetic energy, the VR expands and thus slows down its motion [5]. In this way, the distance between the two consecutive VRs decreases in time and interesting phenomena can occur such as 'leapfrogging' [227, 228]. Fig. 3.37 shows the 3D isocontour density surface for $V_0/\mu = 0.6$ and $z_0 = 0.3$ at different times. From these density plots we can see that there are several co-axial vortex rings; however we firstly focus on the two vortex rings in the region $[-6, -4]l_x$ in (a). These two VRs get closer to each other in (b), the left VR becomes larger while the right VR becomes smaller passing through the largest VR

[5]During the VR propagation, Kelvin waves are present which makes the VR to dissipate but it is not the dominant effect for relatively low V_0/μ.

in (c). This process is the so called ‘leapfrogging’. In our case, the smallest VR shrinks immediately after going across the largest VR (still present in (d)). Moreover in (d) the largest VR has also a wider core with respect to (c) maybe due to the presence of more sound waves at the VR position. After the leapfrogging, the largest VR increases further its radius until it breaks into two vortex lines which reconnect [229, 214] as shown in the Fig. 3.38. From Fig. 3.37(a) we also observe another interesting phenomenon in which a vortex ring near the trap center (where there is the largest density gradient) seems to break in three vortex ring, one in the center being larger and the other two at the two sides being smaller and near the condensate boundaries.

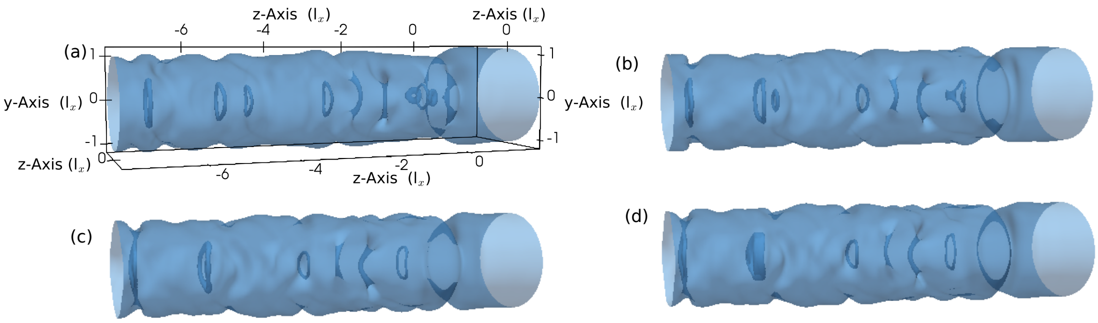

Figure 3.37: The 3D iso-contour density profile at 10% of the maximum density at $t = 26.5$ ms (a), at $t = 27.6$ ms (b), at $t = 28$ ms (c) and at $t = 28.2$ ms for $V_0/\mu = 0.6$ and $z_0 = 0.30$.

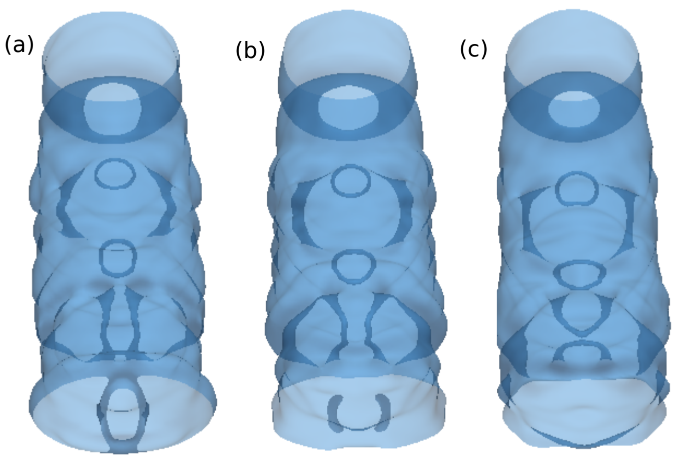

Figure 3.38: The 3D iso-contour density profile at 10% of the maximum density at $t = 30.4$ ms (a), at $t = 31$ ms (b) and at $t = 31.9$ ms (c) for fixed $V_0/\mu = 0.6$ and $z_0 = 0.30$.

We have shown that in an atomic Josephson junction other interesting phenomena can happen such as vortex ring ‘leapfrogging’ and vortex lines reconnections and that these phenomena can be somewhat ‘controlled’ by changing the system initial parameters such

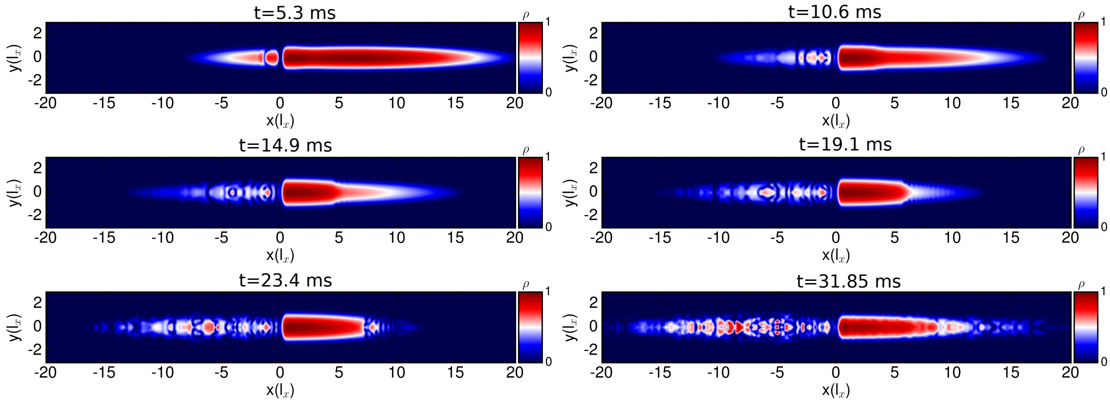

Figure 3.39: The 2D density along xy-plane ($z = 0$) at different times for $V_0/\mu = 0.8$ and $z_0 = 0.8$. The density is scaled to its maximum value.

as barrier height and initial imbalance. An interesting future work could thus be to give further insight into such rich phenomena, and their relation to system parameters.

Towards Quantum Turbulence

Further increasing the initial imbalance can lead to many vortex rings generated, and an interesting question is how many vortex should be generated in order for the system to enter a quantum turbulence regime. Fig. 3.39 shows the 2D density plots along xy-plane (for $z = 0$) for $V_0/\mu = 0.8$ and $z_0 = 0.8$ at different times. Initially the condensate particles are mostly occupying the right well as it is also clearly visible at $t = 5.3$ ms 2D images. Once the dynamics start, the superfluid flow exceeds the critical velocity many times and many VRs are generated at the trap center and subsequently propagating in the left side.

On the right side instead a dispersive shock wave is generated which propagate from the barrier to the right condensate edges similar to what was found in 2D geometry [221]. When such dispersive shock wave is at the position where the condensate transverse extension is small, the entrance of ghost vortices into the condensate is facilitated which subsequently become hydrodynamic vortices (as occurs at $t = 23.4$ ms, for example).

Fig. 3.40 shows the 3D isocontour density plot at two different time evolutions showing mostly the left condensate. In the left condensate there are many vortex rings/vortex lines. However having many vortices is not a sufficient condition for the quantum turbulence; the energy transfer from small to large scale constitutes the condition for quantum turbulence. Fig. 3.41 shows the time evolution of the population imbalance. The question is if the turbulence destroys totally the coherent flow of the particles or the population imbalance at long time evolution (after the initial decay) is still characterised by harmonic oscillations at the characterised Josephson 'plasma' frequency. Interestingly, the initial decay of $z(t)$ in Fig. 3.41 is still followed by harmonic oscillations around a zero mean value, even for

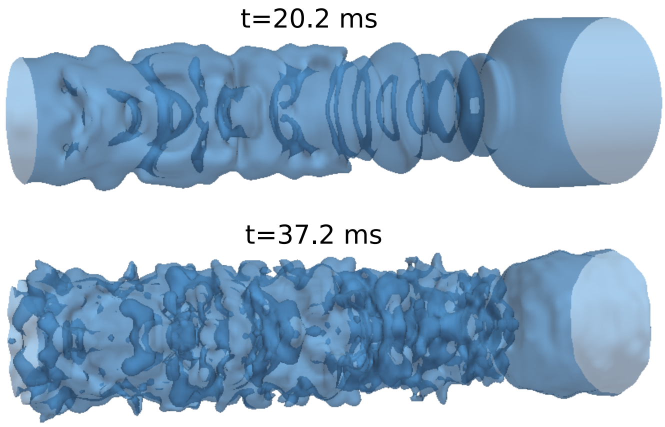

Figure 3.40: The 3D isocontour density profile at 5% of the maximum density at different times for $V_0/\mu = 0.8$ and $z_0 = 0.80$.

such large $z_0 = 0.8$ when many vortex rings are generated. Such plot suggests that even in the regime of many VRs generated there is still a small-amplitude coherent flow of the superfluid across the barrier (after the $z(t)$ initial decay). Moreover, differently from Ref. [221] in our system, during the initial decay, $z(t)$ shows some pronounced peaks which would correspond to a significant effect of the backflow and their frequency is around 22 Hz. Understanding more this behaviour, if it is connected or not to the onset of quantum turbulence would be useful because currently it is experimentally challenging to characterise the turbulence regime in such junctions, while it is relatively easy to measure the population imbalance.

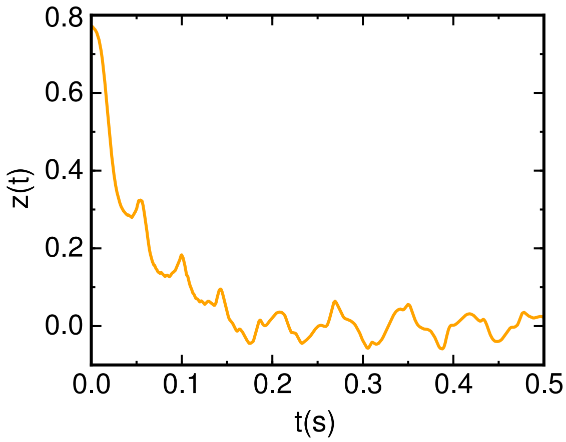

Figure 3.41: The time evolution of the population imbalance for $V_0/\mu = 0.8$ and $z_0 = 0.8$.

Chapter 4

Comparison with an ultracold atom experiment (^{6}Li experiment in Florence)

This chapter focuses on the comparison between the numerical data (obtained on modeling the atomic Josephson junction of Ref. [49, 20]) with the experimental data. The experiment of Ref. [49, 20] consists of two weakly coupled ^{6}Li fermionic superfluid through a Gaussian barrier which we model in the limit of molecular BEC (as described in Sect. 3.1) where $1/(k_F a) \simeq 4.6$. For the experimental range of parameters two different dynamical regimes are found: the Josephson 'plasma' oscillations regime and the vortex-induced dissipative regime as described in Chapt. 3. Firstly, we show here the direct comparison between the experimental and numerical time evolution profiles of the population imbalance both in the Josephson 'plasma' and dissipative regimes.

Then the critical parameters, which set in the onset of the dissipative regime, such as the critical current and critical imbalance (described in Sect. 3.3 and Sect. 3.6), are compared with the experimental values [90]. As the experiment is done at low, but finite temperature, we also consider the presence of a small thermal cloud. Specifically, we choose $T \simeq (0.3 - 0.4)T_c$ in our numerical simulations, as this is a relevant temperature range for many ultracold atom experiments. At finite temperatures we make use of the Zaremba-Nikuni-Griffin (ZNG) kinetic model (described in Sect. 2.5) in the collisionless limit. However a detailed analysis of the thermal cloud effect on the condensate dynamics is shown in the Chapt. 6.

Next, in order to connect with Ref. [49, 20], we implement in our simulations the protocol of barrier removal which was implemented in the experiment before observing the vortices in time of flight (TOF) images. In particular, we show the effect of barrier removal on the vortex rings dynamics and we demonstrate that the barrier removal process can be an efficient experimental tool for producing larger vortex rings with larger lifetime travelling a longer distance. This facilitates the direct observation of Kelvin-wave oscillations as it is shown in this chapter. Moreover, during its propagation the vortex ring can even expand and it can break into two vortex lines when its radius becomes comparable to the condensate transverse extent. This is found to be consistent with experimental observation of individual vortices after the barrier removal.

Furthermore, in the experiment off-center single vortex images were observed and we show that this could be explained by considering the effect of the thermal cloud on the vortex ring dynamics. In fact, even though in the experiment the thermal fraction is less than 15% (consistent with our chosen temperature range $T \simeq (0.3 - 0.4)T_c$) we show that the presence of thermal fluctuations (even though small) destabilizes the VR motion making it go off-center and breaking into one single vortex line when the VR hits the condensate boundary.

4.1 Dynamical regimes and the phase diagram

As we showed in the Chapt. 3, for the range of experimental values of barrier heights $V_0 \in [0.6, 1.22]\mu$ and barrier width $w/\xi = 4$, only two dynamical regimes were found numerically; the Josephson 'plasma' oscillations regime and the dissipative regime. These findings are consistent with the experimental results which showed the presence of Josephson 'plasma' oscillations regime, characterized by coherent sinusoidal oscillations of the population imbalance and relative phase [49] around a zero mean value, and the dissipative regime characterized by an initial decay of the population imbalance (followed by harmonic oscillations around a zero value) induced by the generation of vortices which leads to phase-slippage mechanism [20]. We validate our numerics by comparing here the time evolution of the condensate imbalance $z_{\mathrm{BEC}}(t)$ with the experimental data for the same parameters both in the Josephson 'plasma' regime (shown in Fig. 4.1(a)) and in the dissipative regime (shown in Fig. 4.1(b)-(c)). Initially we show only the numerical results at $T = 0$. The experimental parameters are not the same at different subplots in Fig. 4.1 so also in our numerical simulations we use different parameters in order to match the experimental values in each subplot.

Apart for the experimental error associated to the population imbalance values, there is an error bar on the experimental measured value of V_0/μ. Thus, in our numerics we achieve simulations for different values of V_0/μ within such experimental error bar. However, in Fig. 4.1 we show the results for only two values of V_0/μ for each subplot, chosen such that their corresponding population imbalance profiles are closer to the experimental data.

For example, Fig. 4.1(a) shows the numerical $z_{\mathrm{BEC}}(t)$ for $V_0/\mu = 0.89$ and $V_0/\mu = 0.8$. Although, for both values of the barrier height the agreement with experimental data is

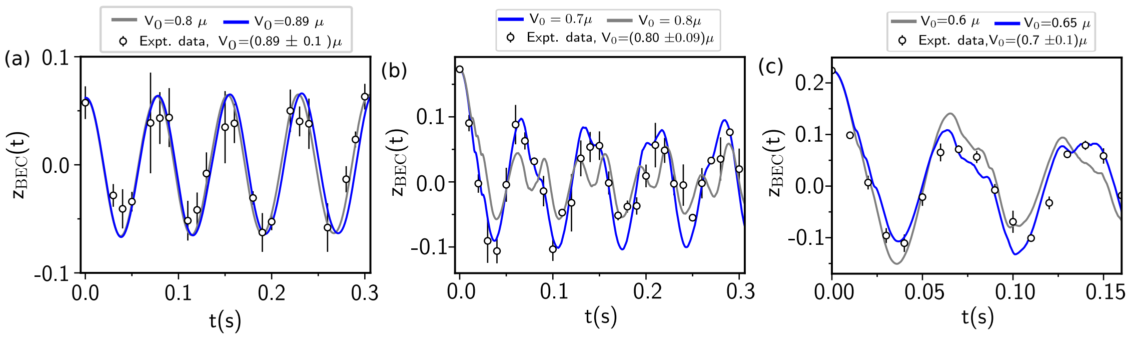

Figure 4.1: Comparison of numerical population imbalance time evolution (blue and grey lines) for two different values of V_0/μ (defined in the legend) with the experimental data in Josephson 'plasma' (a) and dissipative (b),(c) regimes. The molecule number is $N_{\rm BEC} = 64000$ in (a), $N_{\rm BEC} = 60700$ in (b) and $N_{\rm BEC} = 61500$ in (c) both for the numerical and experimental data. The experimental barrier heights are $V_0 = (0.89 \pm 0.10)\mu$ in (a), $V_0 = (0.80 \pm 0.09)\mu$ in (b) and $V_0 = (0.7 \pm 0.1)\mu$ in (c).

very good, we find that the $z_{\rm BEC}(t)$ for $V_0/\mu = 0.89$ better fits the experimental data and we choose such value for the following study of the effect of finite temperature. In the dissipative regime instead, a small change in the value of V_0/μ can lead to a non-negligible effect on the initial decay of $z_{\rm BEC}(t)$. In fact, as oberved from Fig. 4.1(b), where the $z_{\rm BEC}(t)$ is shown for $V_0/\mu = 0.7$ and $V_0/\mu = 0.8$, the largest value of the barrier height leads to a slower decay of the $z_{\rm BEC}(t)$. Moreover, the experimental imbalance decay time and short-time evolution profile (for $t \leq 0.17s$) are perfectly captured by the numerical $z_{\rm BEC}(t)$ for $V_0/\mu = 0.7$, with some small mismatches at later times (t > 0.17s) maybe due to the experimental particle loss. Thus we choose the imbalance profile for $V_0/\mu = 0.7$ as the best representative of the experimental data for our following analysis at small finite temperature. Fig. 4.1(c) shows instead the numerical data for $V_0/\mu = 0.6$ and $V_0/\mu = 0.65$ finding that the second V_0/μ better fits the experimental data.

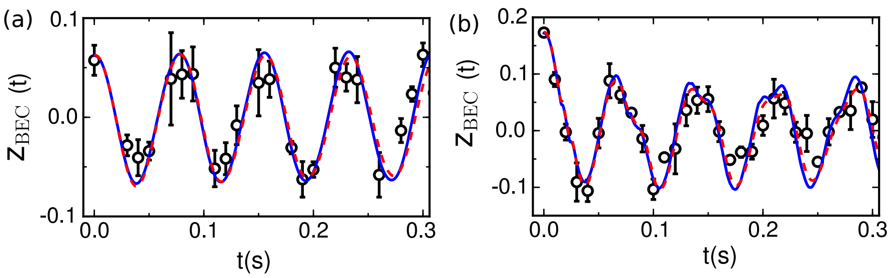

Figure 4.2: Comparison of numerical (blue line for $T = 0$ and red lines for $T = 0.3T_c$) condensate imbalance and experimental population imbalance evolution in Josephson (a) and dissipative (b) regimes. The numerical barrier heights are $V_0 = 0.89\mu$ in (a) and $V_0 = 0.7\mu$ in (b).

For the numerical simulations in Fig. 4.1(a) $V_0/\mu = 0.89$ and (b) $V_0/\mu = 0.7$ we then consider further the effect of a small thermal fraction for $T = 0.3T_c$ (near the experimental temperature), with results shown in Fig. 4.2. We keep fixed the condensate number when comparing $T = 0$ with finite T results. The small thermal cloud has small effect on damping the long-time imbalance evolution and on shifting slightly the frequency (the effect of larger thermal cloud on the condensate population imbalance is considered in the Chapt. 6).

4.1.1 Critical parameters

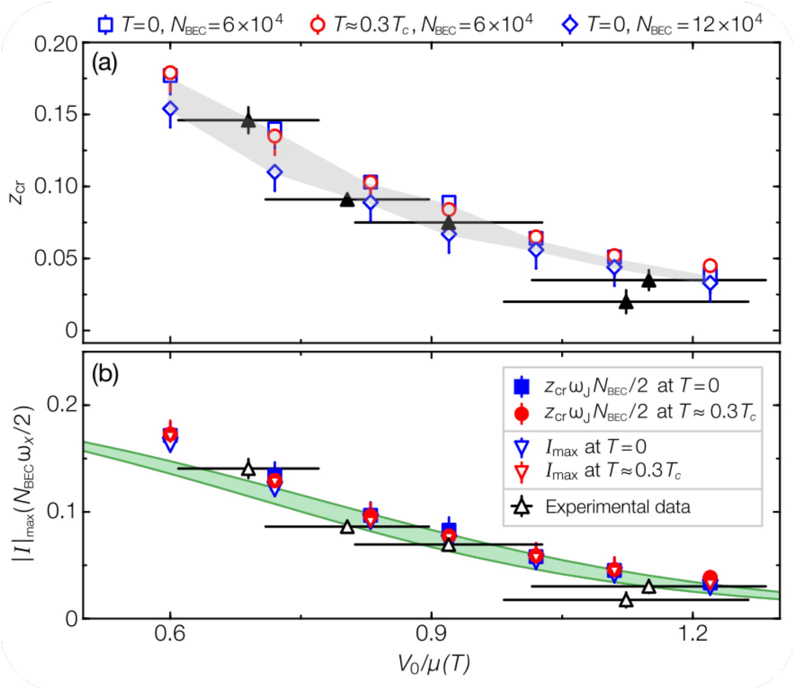

Figure 4.3: (a) Critical population imbalance $z_{\rm cr}$ as a function of $V_0/\mu(T)$, via numerical simulations at $T = 0$ (blue symbols) and $T = 0.3T_c$ (red circles), and experimental data (black triangles). Grey shaded area accounts for the experimental range of particle number. Vertical error bars are set by the discreteness of the numerically-probed z_0 values (simulations) and the standard deviations over at least four measurements (experiments); horizontal experimental error bars are set by the combined uncertainties in measuring barrier width, particle number and laser power. (b) Maximum superfluid current, $|I|_{\rm max}$, based on the numerical time derivative of population imbalance (down triangles), and on the numerical/experimental estimate $|I|_{\rm max} \simeq z_{\rm cr}\,\omega_J\,N_{\rm BEC}/2$. Green shaded area: predicted maximum supercurrent (including second-order harmonics in the current-phase relation), accounting for the uncertainty in V_0/μ.

Combining calculated and newly extracted experimental $z_{\rm cr}$ values, we map out the phase diagram delimiting Josephson and dissipative regimes as a function of the normalized barrier height $V_0/\mu(T)$ [Fig. 4.3(a)], where $\mu(T)$ is the chemical potential including the thermal mean-field contribution [28], also defined in Eq. (2.104). Increasing $V_0/\mu(T)$, the onset of dissipation appears at smaller $z_{\rm cr}$ for both numerical (shown also in the previous chapter) and experimental data. This reproduces the observed boundary within experimental uncertainty up to $T = 0.3\,T_c$ upon keeping the *condensate* number equal to the $T = 0$ case. Our findings can also be interpreted in terms of the critical current $I_{\rm max}$ across the junction, defined as the maximum value of $I = \dot{z}_{\rm BEC}\,N_{\rm BEC}/2$ at $z_0 = z_{\rm cr}$ [figure 4.3(b)]. Knowing that from the numerical simulation (Chapt. 3), $|I|_{\rm max}$ is well approximated by $z_{\rm cr}\,\omega_J\,N_{\rm BEC}/2$ we compare these results with the experimental values of the production $z_{\rm cr}\,\omega_J\,N_{\rm BEC}/2$. The very good agreement found with the experimental data suggested a simple way to estimate the maximum current that sets in the transition to the dissipative regime in an atomic Josephson junction. In Chapt. 3 we showed that the overall trend of the numerical $|I|_{\rm max}$ against $V_0/\mu(T = 0)$ is also quantitatively captured by considering second order terms in the current-phase relation [65, 159]. Fig. 4.3 shows that this model captures also the profile of the experimental maximum current as a function of V_0/μ.

4.2 The experimental versus the numerical findings on vortices

In this section we address some of the main different features found from the comparison between the experimental [20] and the numerical results shown in Chapt. 3 at $T = 0$ regarding the topological defects, which can be classified as two main topics:

- In the previous chapter we showed that the main cause for the resistive superflow dynamics even at $T = 0$ is the nucleation and dynamics of topological defects, which take the form of vortex rings for the experimental 3D set-up. When visualized in terms of two-dimensional density plots the VR will appear as a vortex-antivortex pair if the VR radius is large enough. An example of this is shown in Fig. 4.4(a) for $V_0/\mu = 0.6$. Instead for smaller radii VR, they appear as a 'single' vortex if the radius is too small for the vortex-pair to be resolved visibly as shown in Fig. 4.4(b) for $V_0/\mu = 0.8$. However in both cases the vortex pair is centered at $y = 0$.

  In the experiments instead the time of flight images shows often single or several off-center vortices, with two examples shown in Fig. 4.5 which were taken from the experimental paper [20]. We note that in this specific figure an experimental image is shown in the unitarity limit of the Feshbach resonance (Fig. 4.5(ii)), but in this thesis we focus only in the limit of BEC of molecules: an experimental image in the limit of molecular BEC is shown instead in Fig. 4.5(i).

- In the experiments the presence of vortices was found even for initial barrier heights

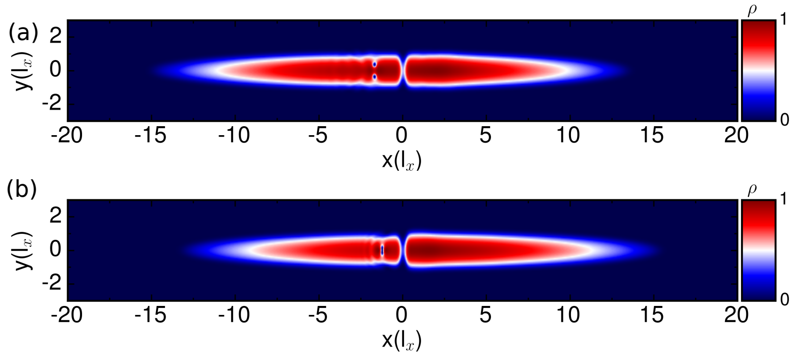

Figure 4.4: Density profile at $T = 0$ and along the xy plane ($z = 0$) for $V_0/\mu = 0.6$ and $z_0 = 0.19$ (a) and for $V_0/\mu = 0.8$, $z_0 = 0.25$ (b) showing only the first vortex ring (there is only one VR generated in (a) while there several vortex rings generated in (b)). The density is rescaled to its maximum value.

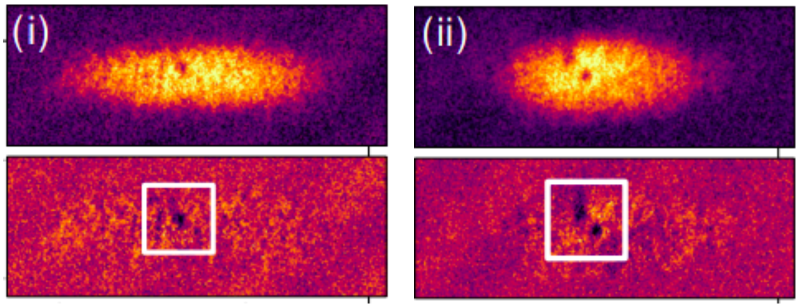

Figure 4.5: This figure is taken from the experimental paper [20] and shows time-of-flight images after 20 ms of evolution, where vortices are present (indicated within the white rectangle). Lower subplots show residual images, obtained by subtracting the density distribution of a cloud without excitations. The data are for $z_0 = 0.2$ and for $V_0/\mu = 1$ (i) in the limit of molecular BEC and for $V_0/\mu = 0.9$ (ii) for the unitarity Fermi gas. [Copyright (2018) by The American Physical Society [20]].

larger than the chemical potential. In our numerical simulations , even though the VR is nucleated at the barrier position, it does not leave the barrier and thus no VR is found outside the barrier for $V_0 \geq \mu$ (as will be shown in Sect. 4.3.3).

The experimental density images shown in Fig. 4.5 revealing the presence of vortices are taken after removing the barrier; in fact, in such images there is no barrier at the center. In the experiment, in order to image the topological defects they need to remove the barrier before time of flight imaging. Based on this last consideration and in order to explain the main different features between the experimental and numerical findings on vortices we firstly implement the barrier removal process in our simulations and we then study its effect on vortex ring dynamics for two cases of initial barrier heights; for barrier height smaller than the chemical potential and in particular for $V_0/\mu = 0.8$ and for the case of barrier height larger than μ and more specifically for $V_0/\mu = 1.2$. Secondly, we study the effect of a small thermal cloud ($T = 0.4T_c$) on the vortex ring nucleation and dynamics. These two main topics will be adressed in the following sections.

4.3 The barrier removal effect at $T = 0$

To connect with Ref. [49, 20], we implement in our simulations the same experimental protocol of barrier removal: we let the system evolve for 13ms with the barrier on at a chosen value V_0/μ, after that we gradually remove the barrier, reducing its height to zero over 40 ms. Specifically, the barrier height is decreased linearly in time and thus its time-dependent value for $t \geq 13$ ms$= t_0$ can be expressed as:

$$V(t) = V_0 \left(1 - \frac{t - t_0}{T_{\text{off}}}\right) \tag{4.1}$$

with $T_{\text{off}} = 40$ms.

4.3.1 Relatively low barrier heights

We firstly present the numerical results for initial barrier height $V_0/\mu = 0.8$ and initial imbalance $z_0 = 0.25$, which is one of the cases studied in Chapt. 3. Fig. 4.6 shows the temporal evolution of the generated VRs position along the x axis for both the two cases of barrier kept on (filled blue circles) and barrier removal (brown empty circles). In the latter case, the time interval during which the barrier is removed is indicated by an arrow in Fig. 4.6.

The first and the second vortex rings are generated before the time t_0 and thus they do not feel the effect of barrier removal. The dynamics of subsequent (third, fourth and fifth) VRs instead is strongly affected. In fact, in the case of barrier removal, when the third VR is nucleated or better when it enters the transverse condensate density near $x = 0$ (occurring at time t$\simeq$ 16 ms) the barrier height, expressed by Eq. (4.1), is around 0.74μ. This means that the superfluid density within the barrier is already larger with respect to the value before the start of the barrier removal process and thus the third VR is surrounded by larger condensate density having so a larger kinetic energy[1]. Consequently, the VR has a larger lifetime, propagating further into the condensate with smaller velocity (defined from the slope of the $\mathrm{x_{VR}(t)}$ profile) in the case of barrier removal. The same applies also for the fourth and fifth VR which are generated when $V(t)/\mu$ is even smaller, i.e. even larger condensate density within the barrier, and thus they live much longer

[1]The study of the dependence of the vortex ring incompressible kinetic energy on the value of the barrier height is described in Chapt. 5

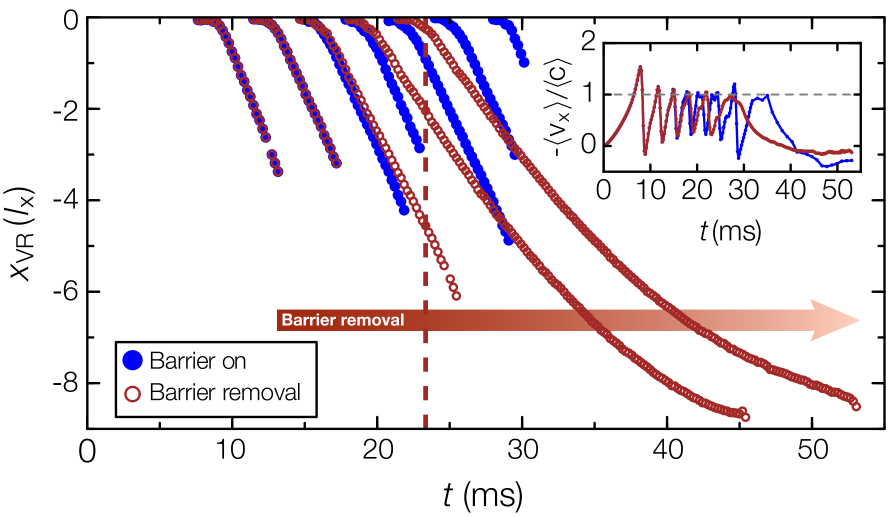

Figure 4.6: The temporal evolution of all the generated vortex rings x axis position in the case of barrier kept on (blue circles) and barrier removal (brown circles) for $V_0/\mu = 0.8$ and $z_0 = 0.25$. The inset shows the temporal evolution of the ratio of the x component density weighted superfluid velocity to the mean value of the speed of sound $\langle c \rangle = \sqrt{\mu/2M}$. The arrow goes from the moment the barrier starts to be removed until the moment the barrier is at zero, i.e. indicating the time interval [13, 53] ms. The vertical line indicates the time $t = 23.4$ ms chosen for the 3D density plot shown in Fig. 4.8.

with respect to the third VR. Furthermore the first three VRs in both cases shrinks into rarefaction pulses while the fourth and fifth VRs break into two vortex lines in the case of barrier removal (as will be shown later for one of them).

Another important feature arising from Fig. 4.6 is that the number of VRs generated is different in the two cases; specifically seven VRs are generated in total when the barrier is kept on at the initial value $V_0/\mu = 0.8$ and only five vortex rings are nucleated in the case of barrier removal. In order to explain such difference, we estimate the ratio of the density-weighted superfluid velocity (its x axis component), calculated on the $x = 0$ plane as in Sect. 3.5.5, to the mean value of the speed of sound given by $\langle c \rangle = \sqrt{\mu/2M}$. The temporal evolution of $-\langle v_x \rangle/\langle c \rangle$ is shown in the inset of Fig. 4.6. As the barrier is removed, the density at the center increases, which means that the superfluid velocity local maxima achieve smaller values, as $\langle v_x \rangle$ is proportional to the inverse of the transverse integrated density at $x = 0$ as shown in Sect. 3.6. Vortex rings are generated for as long as the ratio $-\langle v_x \rangle/\langle c \rangle$ is larger than one. When $-\langle v_x \rangle/\langle c \rangle$ becomes smaller than one, a VR can no longer be generated; this happens earlier in time for the case of barrier removal with respect to when the barrier is kept on, and thus less vortex rings are generated in the former case. Our estimation of the critical velocity for the VR generation of the order of the mean speed of sound is consistent with the results found in Ref. [209], in which they increased the barrier height starting from zero value until reaching a value when vortices generation occurred.

Effect of barrier removal on the VR dynamics

We now analyse in more detail the dynamics of the fourth generated VR in both cases. Fig. 4.7(a) shows the comparison between the temporal evolution of the semiaxes of the fourth VR in the case of including (orange line[2]) or excluding (blue line) the barrier removal procedure. The shadowed areas around the mean radius mark limiting values of the semiaxes along the y and z directions. The Thomas-Fermi radius along the y direction calculated at x_{VR} by Eq. (3.18) (where the barrier height is time-dependent in the barrier removal case) is also shown in Fig. 4.7 (a).

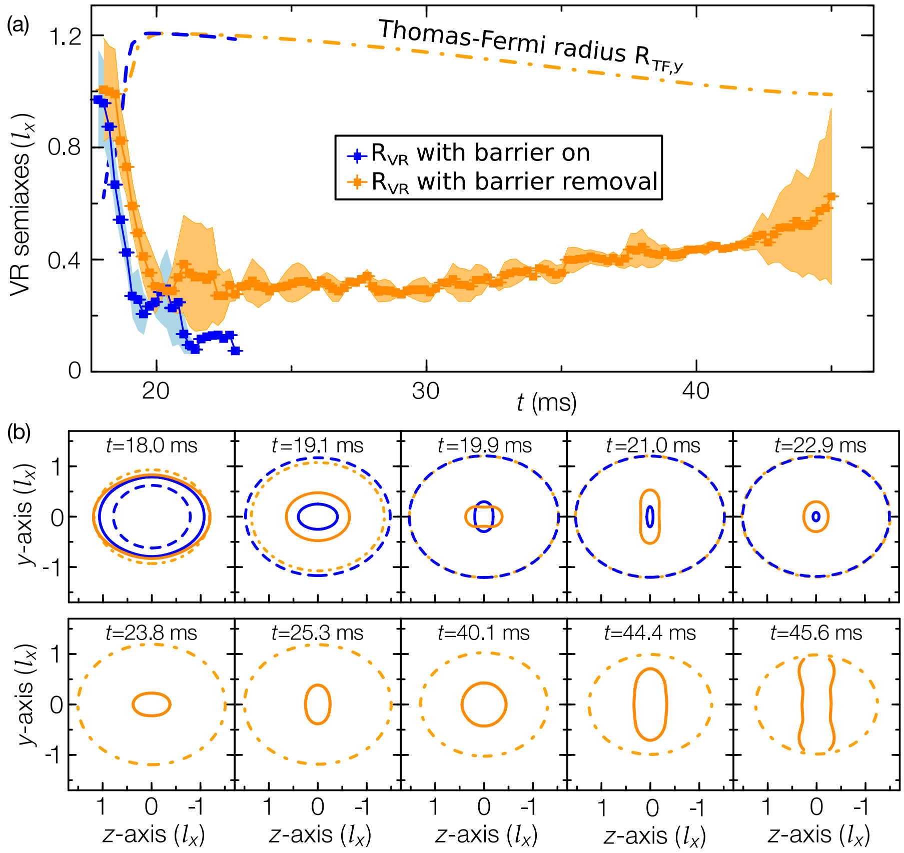

Figure 4.7: (a) Evolution of the semiaxes and mean radius of the 4$^{\text{th}}$ VR ($z_0 = 0.25$, $V_0/\mu = 0.8$), with barrier kept on (blue line) or removed during [13,53] ms (orange line). Shadowed areas mark limiting values of the two semiaxes. Dashed blue/orange lines on top: transverse TF radius at the instantaneous VR location. (b) Dynamical 2D VR profiles with barrier on (blue) and removed (orange) plotted alongside the corresponding transverse TF surface (dash-dotted lines).

Firstly, we observe that the fourth VR is nucleated (outside the local TF surface) at a

[2]instead of brown color of the Fig.4.6

time $t \simeq 17.5$ ms in the case of barrier on and slightly later for the barrier removal case. This is consistent with the temporal profile of $-\langle v_x \rangle / \langle c \rangle$ shown in the inset of Fig. 4.6 where the fourth local maxima is obtained at slightly later time in the case of barrier removal. After its nucleation, in both cases, the VR shrinks initially fast its mean radius within the barrier region until it reaches a relatively small value; then the VR leaves the barrier propagating in the left condensate with such radius for a while. The VR propagating radius is larger in the case of barrier removal consistent with smaller propagation velocity found from Fig. 4.6.

In both cases, the VR has an initial elliptical profile due to the radial trapping asymmetry ($\omega_y \neq \omega_z$) as visible in Fig. 4.6(b) where the VR 2D profile is shown, together with 2D Thomas-Fermi profile in the yz plane. Thus, the two semiaxes of the VR along the y and z directions oscillate in time as observed in Fig. 4.6(a)-(b). Such oscillations correspond to a $m = 2$ Kelvin wave excitation on a circular VR [178]. In fact, the VR survival during its propagation in the superfluid bulk is determined by two competing effects: On the one hand, the VR tends to expand [212] to conserve its incompressible kinetic energy as it moves towards lower-density regions with decreasing transverse size (as shown by the $\mathrm{R_{TF,y}}$ profile in Fig. 4.7(a)). On the other hand, the Kelvin wave excitation induces dissipation of the VR incompressible kinetic energy via the emission of phonon-like excitations, reducing the VR radius [213, 214]: When $R_{\mathrm{VR}} \sim \xi$, with ξ being the superfluid healing length, the VR loses its circulation and annihilates in a rarefaction pulse [209]. In the case of barrier removal the first effect dominates and the VR expands until it reaches the condensate boundaries (i.e. $R_{\mathrm{VR}} \simeq R_{\mathrm{TF,y}}$ which is the smallest TF radius corresponding to the largest transverse frequency) during its propagation towards the axial condensate edges; there it breaks up into two anti-parallel vortex lines as clearly seen in the final snapshot of Fig. 4.7(b) [209, 230, 212]. In the case when barrier is kept on, the vortex ring gradually shrinks, giving rise to rarefaction pulses. The analysis of Kelvin-wave oscillations, which can already be seen in Fig. 4.7(a)-(b), is performed in the following section.

A direct comparison of appropriate 3D density isosurfaces is shown in Fig. 4.8, revealing the presence of vortex rings in the case of barrier kept on (a) and barrier removal (b) at two different times: $t \approx 19.5$ ms (i) and at $t \approx 23.4$ ms. At time $t = 19.5$ ms the third and the fourth (indicated by the white box) generated VRs are shown in both cases while propagating in the left reservoir. While the third VR shape is near circular, the fourth VR has an elliptical shape instead. Moreover, the suggested smaller velocity from the slope of the $x_{\mathrm{VR}}(\mathrm{t})$ in Fig. 4.6 in the case of barrier removal is consistent with the larger propagating VR radius, an effect clearly visible also in Fig. 4.8[(a),(b)]-(i) for the fourth VR. A few ms later, at time $t = 23.4$ ms, we see clearly that only one VR remains in the case of barrier on (Fig. 4.8(a)-(ii)). Referring back to Fig. 4.6, where the time $t = 23.4$

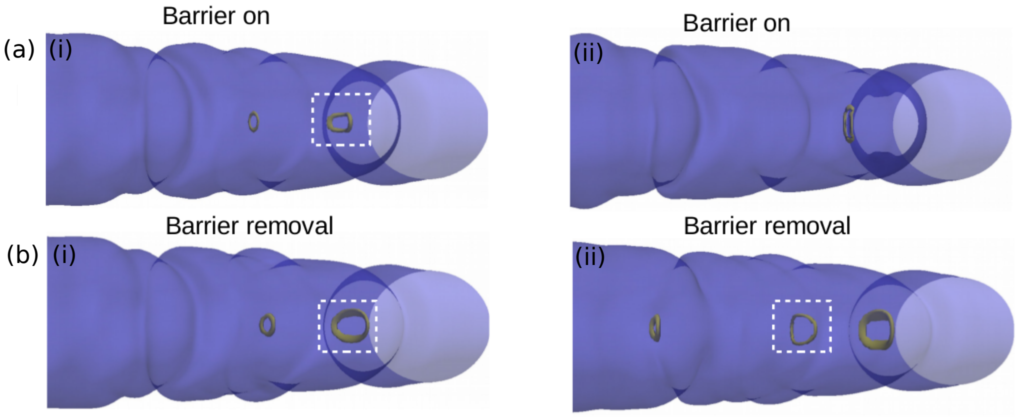

Figure 4.8: Density isosurface (taken at 5% of maximum density) for (a) barrier on, and (b) barrier removal at (i) $t = 19.5$ ms and at (ii) $t = 23.4$ ms for initial $V_0/\mu = 0.8$ and $z_0 = 0.25$. In both cases the fourth VR is the one inside the white box.

ms is indicated by a vertical line, we note that the fourth VR has already disappeared at such time and the VR observed in Fig. 4.8(a)-(ii) is the fifth generated VR. On the other hand, in the case of barrier removal, the fourth VR is still present at such time and it has even changed its axes of symmetry (from along z in (i) to along y direction in (ii)). Moreover, the fifth VR (rightmost VR) is also propagating, which is generated at a slightly later time with respect to the case of barrier kept on. The longer lifetime of the VRs in the case of gradual barrier removal makes possible the observation of three vortex rings simultaneously as shown in Fig. 4.8(b)-(ii).

4.3.2 Kelvin waves excitations

Here we provide further details on the characterization of Kelvin waves (KW) by analysing the 4th generated VR dynamics for the parameters of the previous section, i.e. initial barrier height $V_0/\mu = 0.8$ and $z_0 = 0.25$, and in the case of barrier removal.

The small asymmetry in the transverse direction leads to VRs with elliptical 2D profiles. During its propagation the VR shape oscillates by inverting its elliptical semiaxes, in the form of an $m = 2$ KW excitation of the circular shape. In fact, the 2D VR profile is best fit by the function $(y/a)^2 + (z/b)^2 = 1$. Based on our definition in Chapt. 3 of the mean VR radius as $R_{VR} = (a + b)/2$, the deformation of the elliptic VR from its ideal circular shape with radius R_{VR} can be characterised as $(a - R_{VR})$ along the y direction and $(b - R_{VR})$ along the z direction. Fig. 4.9 shows the time evolution of these quantities in the case of the 4th VR undergoing the barrier removal process over the relevant post-generation temporal window $t \in [17.5, 45]$ ms. After such time the VR is destroyed by interacting with its images, an effect already studied in different contexts in [215, 216, 231, 232].

In the limit of a VR radius much larger than the core size, the period of the KW

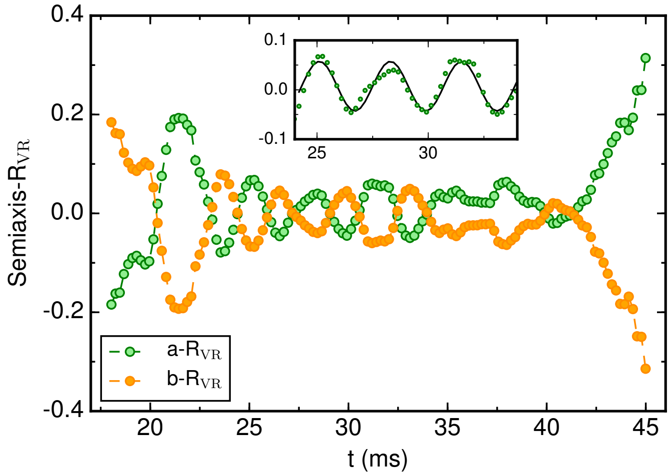

Figure 4.9: Evolution of deviations $(a - R_{VR})$ (green points) and $(b - R_{VR})$ of the VR semiaxes from their average value. Inset: sinusoidal fit (black line) to $(a - R_{VR})$ in the time interval [24,34] ms, confirming the KW nature of the VR excitations.

oscillations is given by the dispersion relation [178], expressed by Eq. (2.36) as :

$$\omega(k) \sim \kappa k^2/(4\pi)[\ln(2/(ka_0) - 0.5772], \tag{4.2}$$

with k the wavenumber, a_0 the vortex core size and $\kappa = h/M$ the quantum of circulation. The KW wavenumber k is found from the wavelength $\lambda = 2\pi/k$, which satisfies the relation $\lambda m = 2\pi R$ for $m = 2$, where R is the VR radius. Estimating the vortex core size inside the bulk as being comparable to the molecular BEC mean healing length ($\xi \simeq 0.5\mu$m) and approximating R as the mean value of the 4th VR radius in the time interval $[24, 34]$ ms, the above dispersion relation predicts a KW period $\tau \simeq 3.3$ ms, which is found to be in excellent agreement with a sinusoidal fit to our numerically extracted values of $(a - R_{VR})$ in the range $[24, 34]$ ms (black line in inset of Fig. 4.9) which yields $\tau = (3.19 \pm 0.03)$ ms; we note that this agreement is excellent, even though the VR radius is only five times the vortex core.

4.3.3 Higher barrier height case

Another crucial point to note in relating our findings to experimental observables is that in the experiment [20] they observe vortices propagating in the system even for initial barrier height $V_0 > \mu$. In our simulations when the barrier is kept on at $V_0 > \mu$, the VRs generated at the barrier position shrink fast within the barrier, i.e. without entering in the left reservoir (or bulk), whereas the experimentally relevant barrier removal enables their detection in the bulk. In fact, Fig. 4.10(a)-(b) shows that for such high barrier amplitude

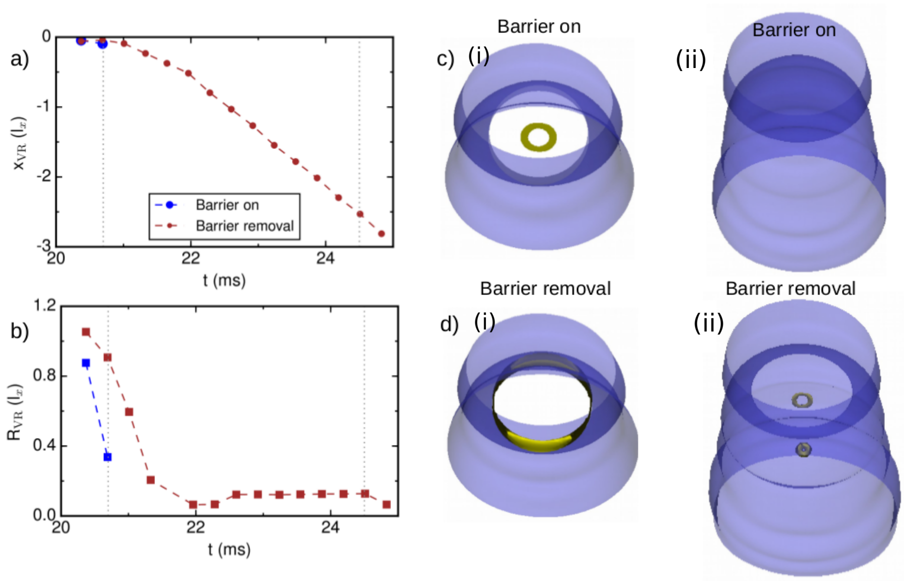

Figure 4.10: (a)-(b) Comparison of (a) x position, and (b) VR radius in the case when barrier height is kept fixed (blue points), or gradually decreased (red points) for initial value $V_0/\mu = 1.2$ and $z_0 = 0.25$. Density isosurface (taken at 5% of maximum density) in the case of (c) barrier kept on and (d) barrier removal at (i) $t = 20.7$ ms and (ii) $t = 24.5$ ms.

and in the case of barrier kept on, the VR position remains near $x_{VR} \approx 0$ and its radius shrinks fast within the barrier. Such shrinking time is much faster than the case when the barrier is removed. This picture is confirmed from Fig. 4.10[(c),(d)]-(i) where the 3D density plots are shown in the case of (c) barrier on and (d) barrier removal at the same time $t = 20.7$ ms; the VR in the former case has already reduces its radius to a small value while in the latter case the VR has still a large radius but slightly smaller than the the condensate transverse extension.

Moreover in the case of barrier removal, after shrinking initially its radius, the VR can have enough kinetic energy to leave the barrier and to travel a significant distance in the bulk before it disappears in rarefaction pulses.

Specifically, during the process of gradual decrease of the barrier amplitude, we observe that once the barrier height reaches some characteristic value ($V(t)/\mu \sim 0.9\mu$) the VR is able to escape the barrier region and propagates in the left reservoir[3] (red points in Fig. 4.10(a)-(b)), in stark contrast to the corresponding case of constant barrier height $V_0 > \mu$ (blue points).

In fact, at the subsequent time $t = 24.5$ ms, the 3D density plots in Fig. 4.10(c)-(d) reveal no VR in the case of barrier kept on (Fig. 4.10(e)) as it has already disappeared,

[3]We note that this result is also confirmed by our detailed study on the dependence of the VR dynamics on the barrier height (the barrier is kept on) to be presented in Chapt. 5.

and it reveals the presence of two VRs in the case of barrier removal; one of them is the VR that was at the barrier position in (i) which has now propagated inside the left condensate. The second VR is another VR which has enough energy to leave the barrier. Thus, in this case the barrier removal process facilitate the simultaneous observation of two VRs, in stark contrast to the case of barrier kept on which reveals none.

4.4 The effect of the thermal cloud on the vortex ring dynamics

Fig. 4.11 shows an example of the axial condensate (black) and thermal cloud density (red) for $V_0/\mu = 0.8$, $z_0 = 0.25$ and $T = 0.4T_c$. In this figure, the density is plotted along the x direction (for $y = z = 0$) both (a) at equilibrium, and (b) at a later time ($t = 10.6$ ms) when the first VR has already entered the left well (visible at $x \sim -1.4l_x$).

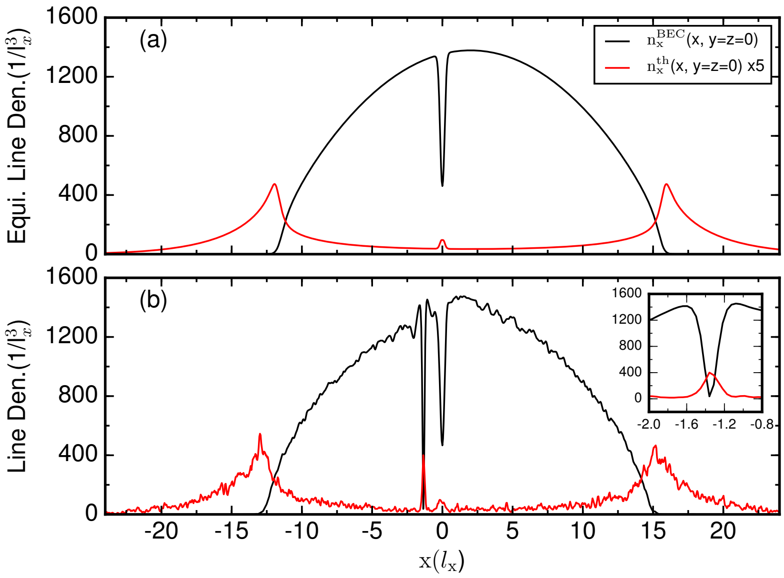

Figure 4.11: Density profile along x-direction (y=z=0) of the condensate (black line) and thermal cloud (red line) at equilibrium (a) and at 10.6 ms time evolution (b) where a VR is present (at $x \sim -1.4l_x$) for $V_0/\mu = 0.8$, $z_0 = 0.25$ and T= $0.4T_c$. The inset in (b) shows the condensate and thermal density around the VR position.

As expected, the thermal cloud has local maxima at both the barrier position, and at the edges of the condensate where the BEC density has local minima. This is because of the repulsive interaction between the thermal cloud and the condensate. Moreover when a VR is present, its core is filled by thermal molecules, as seen clearly in Fig. 4.11(b) where there is a thermal cloud density local peak at the VR position (around $x \sim -1.4l_x$). This effect has already been reported in [112, 115, 116].

4.4.1 The VR nucleation mechanism and early-stage dynamics

As we did for $T = 0$, we extract the transverse density weighted condensate velocity for $T = 0.4T_c$ and we show the comparison with the $T = 0$ results in Fig. 4.12 for the same condensate number $N_{\rm BEC} \simeq 6 \times 10^4$, the same barrier height $V_0 = 90\hbar\omega_x = 0.8V_0/\mu(T = 0)$ and for the same initial condensate imbalance $z_0 = 0.25$.

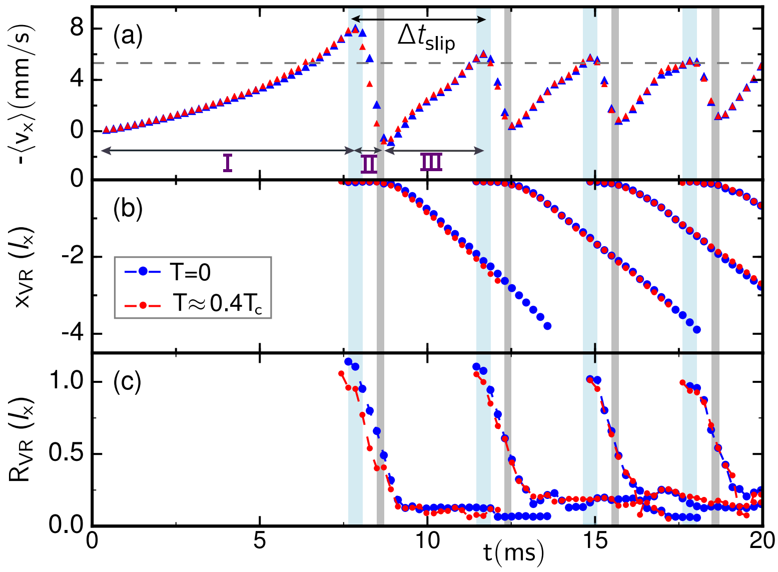

Figure 4.12: (a) Density-weighted x-component of superfluid velocity at the barrier (dashed line denotes mean speed of sound $\langle c\rangle = \sqrt{\mu/2M}$). (b) Mean radius and (c) position of the first few generated vortex rings. Vertical shaded blue areas denote the maxima of superfluid velocity when VRs are generated, while grey areas indicate the times when the VRs enter the Thomas-Fermi surface. Shown are both $T = 0$ (blue symbols) and $T = 0.4\,T_c$ (red symbols) for $z_0 = 0.25$, $V_0/\mu = 0.8$ and $N_{\rm BEC} \simeq 6 \times 10^4$.

We observe that the small temperature considered here (for which $0.4V_0 < k_BT < 0.8V_0$) has practically no effect on the superfluid velocity and on the VR generation process. In this case, the main effect of the thermal cloud is the addition of an extra potential to the BEC (Eq. (2.92) with $R = 0$ in the collisionless limit considered here), as previously observed in the context of vortex dynamics and reconnections [112, 115, 116]. This is because such timescales are typically much shorter than the corresponding ones for dissipation due to the relative motion between the BEC and the thermal cloud. At the same time, temperature has a notable cumulative effect on the overall post-generation VR dynamics which will be analysed in the following section.

4.4.2 Instability of the vortex ring due to the thermal cloud

In Sect. 3.7.1 we study the effect of the initial imbalance on the first VR dynamics at $T = 0$. We perform the same analysis at finite temperature $T = 0.4T_c$ for the same value of the barrier height and condensate number. From the slope of $x_{\mathrm{VR}}(\mathrm{t})$ profiles we thus extract the VR propagation velocity for $|x|_{\mathrm{VR}} \geq 2w$ and these results are shown in Fig. 4.13 both at $T = 0$ and at $T = 0.4T_c$.

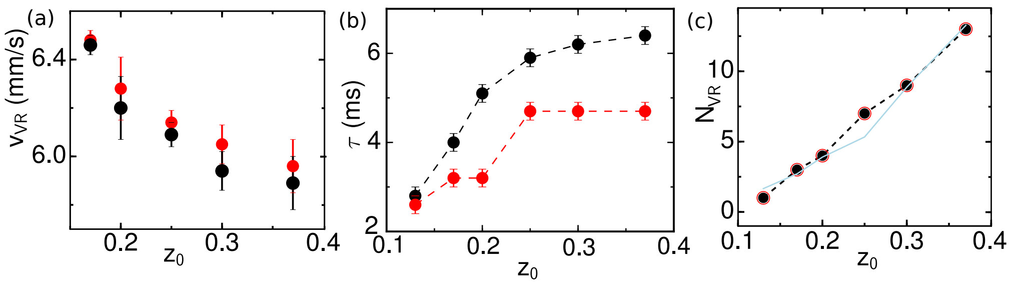

Figure 4.13: Role of initial population imbalance z_0 (for fixed $V_0/\mu = 0.8$ for which $z_{cr} = 0.11$) on: (a) velocity v_{VR} of 1$^{\mathrm{st}}$ nucleated VRs, (b) lifetimes, τ, of 1$^{\mathrm{st}}$ nucleated VRs and (c) total number N_{VR} of VRs penetrating the bulk with the blue line connecting N_{VR} estimates from the time-averaged phase-slippage rate $\Delta\mu(t)/h$ [12]. Each subplot shows $T = 0$ (black symbols) and $T = 0.4\,T_c$ (red symbols) results.

The VR velocity at finite T coincides with the one at $T = 0$ within the errorbars. For the case considered of $V_0/\mu = 0.8$ and for all the different values of z_0, both at $T = 0$ and at finite T, the first VR, after a certain propagation time, disappears by shrinking into rarefaction pulses. The thermal cloud effects stand on reducing the VR lifetime as shown in Fig. 4.13 (b). As the small T considered ($k_BT < 0.8V_0$) does not cause thermally activated VRs, the number of VRs nucleated at $T = 0.4T_c$ is the same as at $T = 0$ (as shown in Fig. 4.13 (c)). Even though the considered temperature range has a small effect on the VR generation process, nonetheless it does exert a ‘drift force’ causing the VR to go off-center while propagating along the negative x-direction, breaking so its motional symmetry. In fact, Fig. 4.14 shows the first VR center along the y and z directions for $z_0 = 0.25$ and $V_0/\mu = 0.8$ at finite T, which becomes different from zero in time. However, the vortex ring disappears before reaching the condensate transversal boundary. This behaviour is highly distinct to what happens at $T = 0$, where the VR remains centered at $y = z = 0$. This effect becomes more pronounced in the cases of barrier removal, because in such cases the VR lifetimes are considerably longer. The 2D profiles of the fourth VR at $T = 0$ (also shown in Fig. 4.7) and at $T = 0.4T_c$ in the case of barrier removal are shown in Fig. 4.15. In the case of barrier removal, at $T = 0$, the considered vortex ring has a longer lifetime and in the end of its lifetime it breaks into two vortex lines.

At finite T instead the thermal fluctuations destabilize the VR, going off-axis while

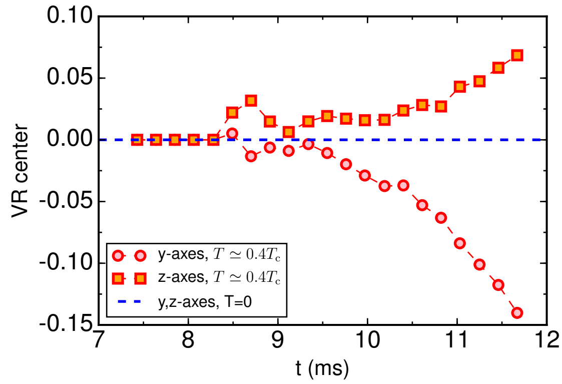

Figure 4.14: The first VR center along the y and z directions at $T = 0$ (horizontal dashed line) and at $T = 0.4T_c$ (red symbols) for $V_0/\mu = 0.8$ and $z_0 = 0.25$.

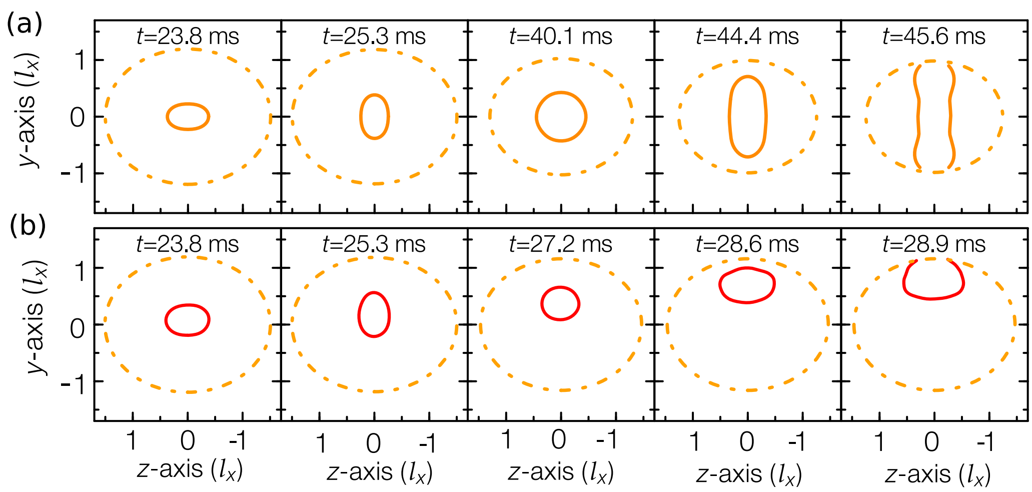

Figure 4.15: Evolution of the 2D profile of the fourth VR in the case of barrier removal at $T = 0$ (a) and at $T = 0.4T_c$ (b). The VR moves off-axis at finite T, generating a single vortex handle at the boundary. The time interval of the images is chosen close to the moment the VR breaks in each case.

propagating and this time it reaches the transversal boundary (condensate edges) asymmetrically [Fig. 4.15]. There, it reconnects with its image and forms a 'vortex handle' [229, 231, 232]. This could explain why a single vortex line is typically detected in each experimental run after barrier removal [49, 20]. A clear visualization of this effect is observed in Fig. 4.16 where the corresponding three dimensional isocontour density profiles are shown for the barrier removal case, clearly contrasting the $T = 0$ to the $T > 0$ case. Note that while the lifetime is well predicted within our kinetic model, the precise details of the VR trajectory – i.e. exactly how it goes off-center and approaches the boundary – are sensitive to the numerical realisation (here we show the results of a single realisation).

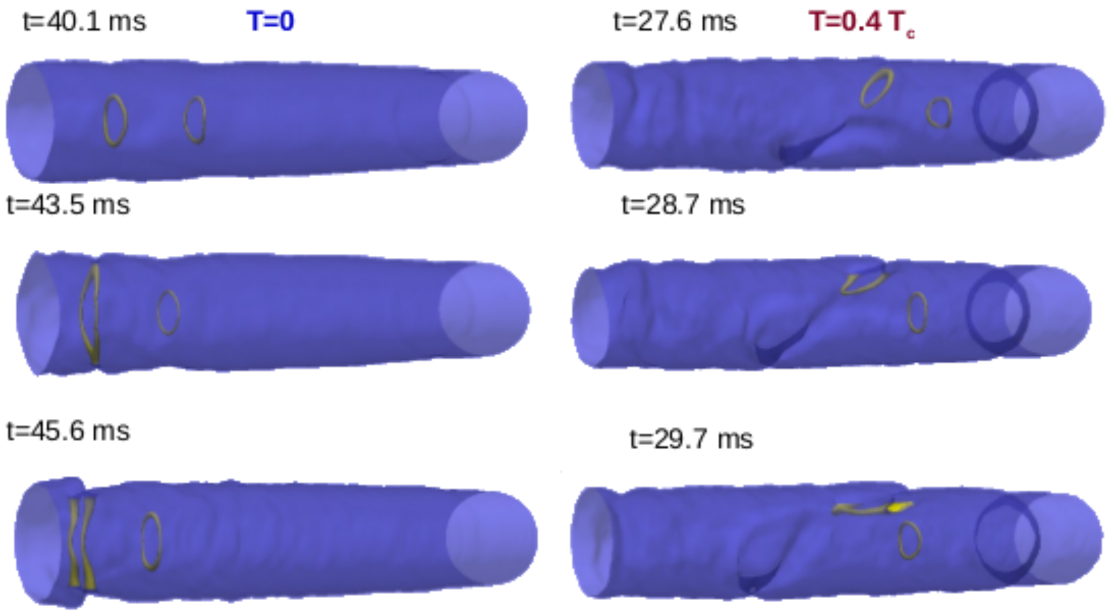

Figure 4.16: Density isosurface (taken at 5% of maximum density) in the case of barrier removal with initial barrier height $V_0/\mu = 0.8$, $z_0 = 0.25$ at $T = 0$ (left column) and at $T = 0.4T_c$ (right column) showing 'final trajectory' of the left VR (i.e. close to the moment it breaks).

4.5 Conclusion and future works

Conclusions

In this chapter we compared our numerical simulation results on the study of the onset of a vortex-induced dissipative regime in an elongated atomic Josephson junction with the experimental results from the LENS experiment in Florence [20] in the limit of BEC of lithium molecules. The two condensates were separated by a Gaussian barrier which had a fixed barrier with $w/\xi = 4$ and a variable V_0/μ in the range $[0.6, 1.22]$. In particular our prediction of the critical imbalance and critical superfluid current across the barrier, defining the transition to the dissipative regime was found to be in very good agreement with the experimental data. Furthermore, we showed that the maximum current delimitting the two regimes can also be calculated in a simpler way by the product of the population imbalance oscillations frequency ω_J (found for $z_0 < z_{cr}$), of the critical imbalance z_{cr} and of half the condensate number $N_{BEC}/2$. This finding is of significant importance for experiments as the ω_J and z_{cr} can be easily extracted.

The experimental condensate fraction was larger or equal to 85% suggesting that in the experiment the temperature was in the range $[0.3, 0.4]T_c$. For this reason, we also considered the effect of a small thermal fraction at such temperature on the critical parameters and temporal evolution of the condensate population imbalance. We showed that the thermal cloud has no significant effect on the critical parameters defining the onset of the vortex-induced dissipative regime as long as we keep fixed the condensate number when comparing the $T = 0$ and finite T results (which are thus done at variable total particle number). This suggests that, at such low temperature, the onset of the vortex-induced dissipative regime is essentially defined by the condensate dynamics and, as it happens on very short time-scale, the small thermal cloud has practically no effect, apart for a small change in the effective trap felt by the condensate.

We also showed that our numerical data at $T = 0$ produced by using the GPE equation for a molecular BEC reproduces very well the experimental data. Moreover a comparison was done by adding also the effect of the small thermal cloud which was found by using the ZNG model in the collisionless limit. Even at finite T the comparison was very good with the experimental data and the small thermal cloud slightly shifted the condensate frequency exerting a very small damping of the condensate imbalance oscillations for the relatively short experimental time evolution. However the presence of a small non-zero temperature is fundamental in understanding and explaining the experimental observation of single off-center vortices. In fact, from our numerical simulations we showed that the thermal cloud causes the vortex ring to go off-center until it breaks into one long single vortex line when it ‘hits’ the condensate boundaries asymmetrically.

In the experiments, the barrier is removed prior to time of flight imaging, which reveals the vortices. So we included the effect of barrier removal on vortex rings dynamics. Remarkably, we found that the barrier removal protocol is an efficient way for producing longer living vortices with larger propagation radius, and thus making it easier to be observed experimentally. On the other hand a smaller number of vortices are produced with respect to the case of the barrier kept unchanged for the same initial barrier height, as the vortex ring emission ceases once the density-weighted superfluid velocity $\langle v \rangle$ becomes smaller than a critical value. In fact, the barrier removal process permits us to also give an estimation of the critical velocity for the vortex ring generation in our 3D inhomogeneus system. We defined it as the value such as for $\langle v \rangle \geq v_c$ the vortex ring are generated, and it was found to be equal to the mean speed of sound $\langle c \rangle = \sqrt{\mu/2M}$. We also showed that another advantage of the barrier removal process is that it permits the vortex ring to leave the barrier and propagate in the cases of high barrier heights $V_0/\mu > 1$ which would otherwise shrink within the barrier if the barrier removal process was not applied.

Future works

In the context of the comparison with experiment and the onset of a vortex-induced dissipative regime there are two experiments that are mostly relevant for us. The first one is the experiment performed by L. J. LeBlanc *et al.* in Ref. [48] in 2011 where they studied the population dynamics of a Bose-Einstein condensate in a double-well potential in an atomic chip. They found a population imbalance profile which decays in time; their experimental results are reported in Fig. 4.17(a). They compared their data with the numerical results performed by using the Gross-Pitaevskii equation at $T = 0$ (shown in Fig. 4.17)(b)). The GPE numerical results did not capture the decay of the population imbalance in time so the authors concluded that such damping could be due to thermal or other stochastic events or from other technical experimental sources. J. Allen in her Phd Thesis [203] adressed the effect of the thermal cloud on the population imbalance and she found that, if the presence of the thermal cloud added a damping to the BEC oscillations, the corresponding damping time is larger with respect to the experimental values. However, the question that puzzles us is if the initial fast damping of $z(t)$ amplitude for $t < 3$ms which is also present in the GPE simulations at $T = 0$ can be associated with the generation of vortices which happens in a very short time-scale. As a future work it would be interesting to investigate further along this direction.

The second experiment is the experiment performed by Albiez *et al.* in [42] in 2005 where they studied dynamical regimes in a single bosonic Josephson junction consisting in two weakly linked Bose-Einstein condensates of ^{87}Rb in a double-well potential. Their geometry was almost a spherical trap with frequency $\omega_x = 2\pi \times 78$ Hz, $\omega_y = 2\pi \times 66$ Hz and $\omega_x = 2\pi \times 90$ Hz with the x axis being the tunneling axis. For the experimental parameters of barrier height and barrier widths they showed the presence of the Macroscopic Quantum

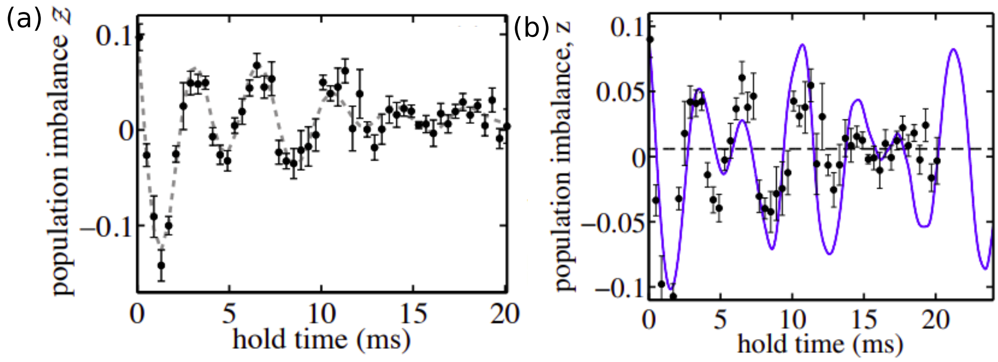

Figure 4.17: L. J. LeBlanc *et al.* [48]: (a) The temporal evolution of the population imbalance for a number $N = 5900 \pm 150$ of ^{87}Rb atoms. The dashed line is a decaying two-frequency sinusoidal fit to the data. Their trap frequency are $\omega_z = 2\pi \times 425$ Hz, $\omega_y = 2\pi \times 95$ Hz and along the x-axes the frequency goes from $\omega_x = 2\pi \times 350$ to $\omega_x = 2\pi \times 770$ Hz depending on the value of the barrier height. (b) The experimental data shown also in (a) and the GPE simulations profile (blue line). [Copyright (2011) by the American Physical Society [48]].

Self-trapping (MQST) regime. An interesting study would be to investigate if even for their geometry, interaction strength and particle numbers, a dissipative regime could be found for an appropriate choice of parameters, where vortices are generated. Our study in Chapt. 5 suggests that we can find all the three-dynamical regimes Josephson 'plasma', dissipative and MQST regimes for any geometry but it would be interesting to show it for parameters of the experiment of [42].

From a theoretical point of view, a future goal is to extend our study of the onset of dissipation to fermionic superfluids controllably tuned across the BEC-BCS crossover. In the experiment of ^{6}Li at LENS [20, 49], which we studied in the BEC limit of tightly bound fermion pairs (i.e. BEC of molecules), the existence of a dissipative regime was also found in the unitary and BCS superfluid. While in the BEC limit the main reason for dissipation was the generation of vortices, as we go towards the BCS limit, other dissipative mechanisms set in, such as the pair-breaking mechanism. While in the experiment [20] the onset of dissipation was attributed mainly to the generation of vortices which was revealed by TOF images even in the unitarity and BCS limit, it would be very interesting to investigate to what extent the vortex-induced dissipation dominates with respect to damping coming from unpaired fermions due to pair breaking mechanism, for a broad parameter range and specific experimental values probed.

Part III

Beyond the LENS experiment

Chapter 5

Full phase-diagram for a three-dimensional Josephson junction

In ultracold atoms, the most commonly studied distinct regimes of population transfer across the weak link are the Josephson 'plasma' and Macroscopic Quantum Self-Trapping (MQST) regimes [59–61]. The Josephson 'plasma' oscillations regime features periodic oscillations of both relative population imbalance and relative phase about zero (as shown also in Chapt. 3). The MQST regime instead sets in for higher population imbalance: this is connected to asymmetric population imbalance oscillations, with a bias towards the initially more populated well, such that the sign of the relative population imbalance remains unchanged, despite the existence of low amplitude population transfer across the weak link due to the tunneling [59, 61] (also described in Sect. 2.3.2). The MQST regime is characterised by a running relative phase (i.e. a relative phase which grows with time). Notice that in general, for long times, the self-trapped regime is eventually destroyed by thermal or quantum fluctuations [61, 62, 64, 63, 60, 233, 234] and/or by higher order tunneling processes [65]. Both these regimes, discussed for ultracold bosons in double- and multi-well potentials [59–61, 66, 235, 236] have been clearly observed both in ultracold ^{87}Rb [42] (described also in Sect. 1.3) and ^{39}K [47] bosonic atomic clouds trapped in a harmonic potential perturbed by a shallow optical lattice which creates a weak link across two well-separated minima, and in the presence of a deep optical lattice [41, 43].

Recent experiments with fermionic ^{6}Li have investigated these phenomena in an elongated fermionic superfluid across the BEC-BCS regime [49, 20]. The molecular BEC regime observed in such experiments (which we modelled in the previous chapters) has a direct correspondence with the experiments in atomic BECs. One of the interesting findings of the experiment [49, 20] – based on a thin Josephson junction – was the explicit observation (across the entire BEC-BCS regime) of a transition from Josephson 'plasma' oscillations to a dissipative regime with increasing initial population imbalance – with no evidence of the existence of self-trapping found in the probed parameter space.

The existence of several experimental studies of the Josephson effect in ultracold superfluids observing either a transition from the Josephson plasma oscillation regime to self-trapping [42, 43, 47], or a transition from Josephson to a dissipative regime [49, 20, 90], raises the interesting question of what distinguishes between such transitions/regimes, and whether a particular experimental set-up could be found that would allow for all three regimes to be observed upon careful control of the relevant parameters distinguishing between such physical regimes. In this chapter, we construct such a full phase diagram clearly demonstrating the crossover between Josephson 'plasma', dissipative and self-trapping regimes in a 3D ultracold superfluid, upon careful control of the parameters (height, width) of the barrier separating the two superfluids. Specifically, we firstly identify the parameter regime for which self-trapping is expected to arise in the LENS experiment geometry [49, 20] in the BEC limit. We then generalize our studies to an isotropic harmonic trap (i.e. spherical condensate), and explicitly show – beyond the expected Josephson 'plasma' and self-trapping regimes (observed and studied for a spherical trap in [42, 83]) – the emergence of a dissipative regime also in such a geometry.

Analysing the compressible and incompressible kinetic energy emission during the superflow, and the properties of the vortex rings – when emitted – we characterize the microscopic processes controlling the regime crossover, even in the absence of any thermal dissipation. The results that we present in this chapter are obtained at $T = 0$ by solving the Gross-Pitaevskii equation for the molecular BEC of lithium defined in Eq. (3.2) and the numerical simulations are described in Sect. 3.1. Some of the results of this chapter are also included in our recent paper [237].

5.1 Phase diagram for fixed barrier width $w = 4\xi$

For the LENS experimental parameters whose barrier width was $w = 4\xi$ we found two dynamical regimes: Josephson 'plasma' and dissipative regime (described in previous chapters). The experiment was done for a barrier height V_0/μ in the range $[0.6, 1.22]$. In our numerical investigations, we explore even higher barrier heights searching for the self-trapping regime predicted by Smerzi et al [59, 61]. and indeed we find (for the considered parameters) the onset of the self-trapping regime for barrier height $V_0/\mu \gtrsim 1.6$.

We define the self-trapped regime as the regime where the population imbalance oscillates around a non zero value for at least 0.4s; in general, for long times, the self-trapping regime can eventually be destroyed. One of the possible reasons for the destruction of the self-trapping regime, for our 3D geometry and in the case $T = 0$ considered here, could be

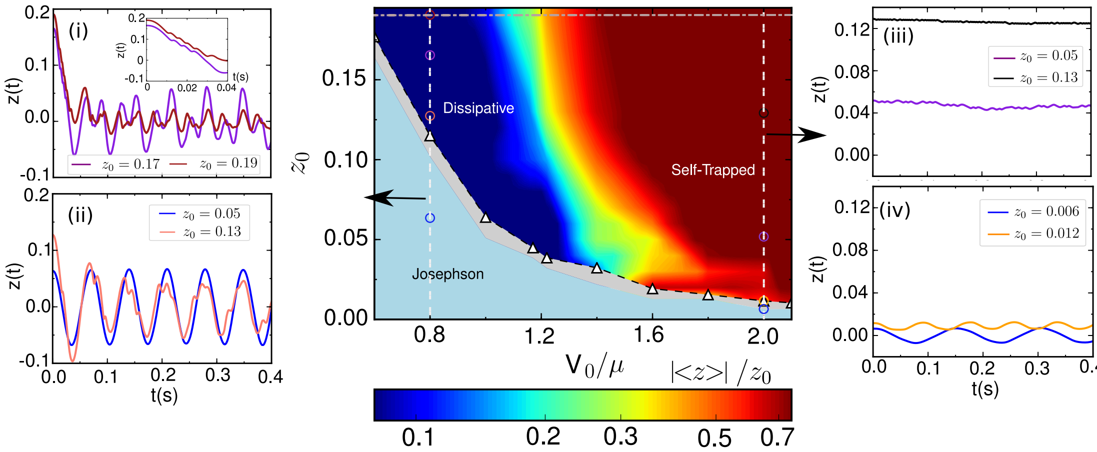

Figure 5.1: Main Panel: Josephson junction phase diagram of dynamical regimes arising across a Gaussian barrier of variable height $V_0/\mu \in [0.6, 2.1]$ and fixed $w/\xi = 4$ for different initial fractional population imbalances $z_0 = z(t = 0)$. The Josephson plasma oscillation regime is found for $z_0 < z_{cr}$ and, beyond a narrow transition regime (indicated by the grey shaded area) the system transitions to the dissipative ($V_0/\mu \lesssim 1.2$), or the self-trapped ($V_0/\mu \gtrsim 1.6$) regime, with the empty black triangles (and connected dashed black line) indicating the critical imbalance. Such regimes are characterized by the coloured regions displaying the absolute value of $\langle z(t)\rangle/z_0$ where $\langle z(t)\rangle$ is the temporal mean value of $z(t)$ in the time interval [0, 0.4]s; the colormap is in logarithmic scale ranging between 0.08 and 0.75. In the lateral figures we plot the evolution of the population imbalance $z(t)$ for different z_0 and (i)-(ii) $V_0/\mu = 0.8$ at $w/\xi = 4$, showing the transition from the Josephson 'plasma' oscillations to the dissipative regime; and (iii)-(iv) $V_0/\mu = 2$ at $w/\xi = 4$, showing the transition from the Josephson to the self-trapping regimes. The location of such points on the phase diagram are highlighted by the hollow circles (with the connecting white vertical lines simply a guide to the eye). The horizontal dot-dashed line at the top of the phase diagram indicates the value of $z_0 = 0.19$ chosen for the following study of the vortex ring dynamics (described in Sect. 5.5).

higher order dissipative tunneling processes [65].

The full phase diagram highlighting the distinct dynamical regimes for the particular inhomogeneous geometry and a narrow barrier width $w/\xi = 4$ is shown in Fig. 5.1. The central panel of Fig. 5.1 highlights the different 'Josephson', 'Dissipative' and 'Self-Trapped' regimes, and their crossover for barrier heights in the range $[0.6, 2.1]\mu$. While the Josephson regime can be clearly identified in Fig. 5.1 [blue-shaded region], and despite the existence of clear regimes where dissipative dynamics, or self-trapped, dominate, the interplay between all such regimes poses challenges on how to best present the complete phase diagram. To achieve this, the regimes beyond Josephson 'plasma' (i.e. for $z_0 \geq z_{cr}$) are characterised in terms of the absolute value of $\langle z\rangle/z_0$, where $\langle z\rangle$ denotes the temporal mean value of the population imbalance over our entire numerically probed range (corresponding here to 0.4s). The (necessarily) limited temporal evolution window probed to construct all phase diagrams in this chapter ($0 \leq t \leq 0.4$s) implies a weak sensitivity of calculated values $\langle z(t)\rangle$ around a zero mean in the dissipative/crossover regime: for these reasons, we consider instead the quantity $|\langle z(t)\rangle|/z_0$, which is plotted by colour in Fig. 5.1 and similar subsequent figures.

To better understand this behaviour, we look at the different dynamical regimes shown in subplots (i)-(ii) [left panels] and (iii)-(iv) [right panels] of Fig. 5.1. These show the dynamical evolution of the population imbalance $z(t)$ for increasing values of initial imbalance z_0 and for fixed $V_0/\mu = 0.8$ [(i)-(ii) Josephson 'plasma' to dissipative transition] and $V_0/\mu = 2.0$ [(iii)-(iv) Josephson 'plasma' to self-trapped transition]: for both values of V_0/μ, the location of the displayed cases on the phase diagram are highlighted by hollow circles. The blue symmetric oscillations shown for the lowest z_0 values in both (ii) and (iv) [lower panels] correspond to pure Josephson oscillations (with a single dominant plasma frequency).

For $V_0/\mu = 0.8$, increasing the initial population imbalance and for z_0 exceeding a critical value ($z_0 \geq z_{cr}$), the $z(t)$ presents 'kinks' or 'dips' during the first transfer cycle of population across the weak link (Fig. 5.1(i)-(ii) and inset in Fig. 5.1(i)). As shown in [90] and in Chapt. 3, such kinks are related to the generation of vortex rings which temporarily slows down (potentially even momentarily reversing) the evolution of $z(t)$. For this low V_0/μ, the vortex ring starts propagating along the long condensate axis (described in Sect. 3.7.1). These kinks during the early time evolution of $z(t)$ are always observed in the dissipative regime. For $z_0 = z_{cr}$ there is only one kink in the initial decay of $z(t)$ as only one vortex ring is generated [orange curve in Fig. 5.1(ii)] . The generation of the vortex ring and associated acoustic emission, combined with the subsequent sound emission from the excited decaying vortex ring eventually lead to dissipation of $z(t)$ (as shown in Chapt. 3). After initially decaying, the population imbalance continues oscillating about a zero mean value on average, following a more complicated pattern, involving multiple frequencies during the subsequent dynamics[1]. As shown in the previous chapters, increasing z_0 to values much higher than z_{cr} [purple/red lines in Fig. 5.1(i) leads to the sequential emergence of multiple vortex rings – one at a time – visible in the current subplots by the small-amplitude kinks during the first $t \sim 40$ms. Thus, in the dissipative regime we expect $\langle z(t)\rangle \sim 0$, with such regime highlighted by the dark blue colour in Fig. 5.1. Such behaviour remains true for all values of $z_0 > z_{cr}$ when $V_0/\mu \lesssim 1$, and then – depending on the value of z_0 – we see a gradual change of behaviour with the dissipative regime persisting even beyond $V_0/\mu \sim 1$ for small z_0.

In the limit of $V_0/\mu \gg 1$ and more specifically $V_0/\mu \geq 1.6$, and for small enough z_0 which is slightly higher than z_{cr}, we see the clear emergence of the self-trapped regime [orange curve in Fig. 5.1 (iv)]. In this case, the population imbalance oscillations clearly maintain a positive value within the time interval explored, implying that despite the

[1] A more detailed analysis of such frequencies and their dependence on the temperature is shown in Chapt. 6.

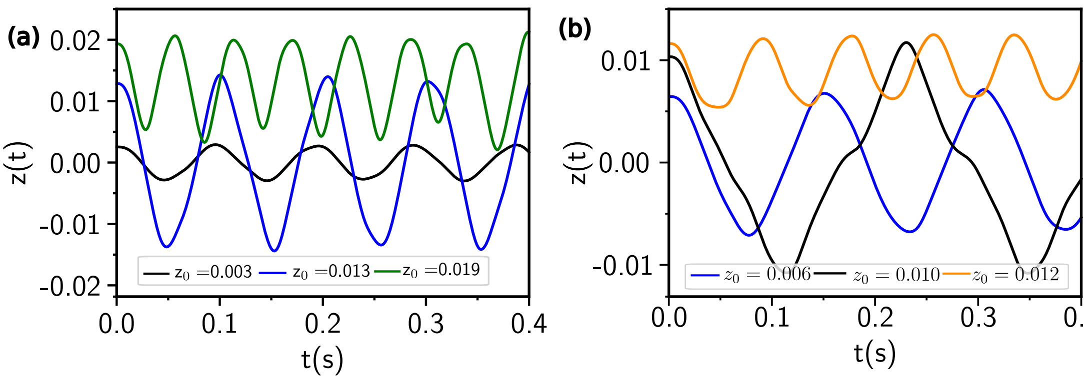

Figure 5.2: The time evolution of the population imbalance for $V_0/\mu = 1.6$ (a) and $V_0/\mu = 2$ (b) (both for $w/\xi = 4$) and for different z_0 (see legend).

periodic transfer of population across the two wells, the right well maintains a higher population compared to the left well at long time evolution. In fact, we refer to the self-trapped states for $z_0 = z_{cr}$ as pure self-trapped as the $z(t)$ oscillates with a single dominant frequency and such regime is the so-called Macroscopic Quantum Self trapping regime in the Ref.[59, 61]. Increasing z_0 to values much beyond z_{cr} does maintain a dominant population in the right well, with $\langle z \rangle$ having a clear positive value, i.e. the system exhibits self-trapping, but with additional excitations becoming relevant to the system dynamics. Moreover in such case of $z_0 \gg z_{cr}$, the population imbalance changes only very mildly during such oscillations, tending towards values $\langle z(t) \rangle / z_0 \to 1^-$, which is labelled by the deep red regime in the phase diagram (it is described in more details in the following Sect. 5.1.2).

The grey area between the Josephson 'plasma' oscillations and the dissipative/self-trapped regimes corresponds to a regime where the pure Josephson 'plasma' oscillations are suppressed. The intermediate or crossover region, occurring at values $V_0/\mu > 1$ (broadly arising for our current parameters around $1.2 < V_0/\mu < 1.6$, but also dependent on z_0) exhibits more complicated behaviour, featuring reduced sound emission, a generated vortex ring which remains a 'ghost' vortex (without entering the condensate), and a complicated irregular pattern of population oscillations, during which $z(t)$ may exhibit kinks, or can change sign, but in a sufficiently irregular manner that does not meet the criteria for belonging to either of the three identified regimes (which will be fully characterised later). We next focus on better characterising the pure self-trapping or MQST regime.

5.1.1 Macroscopic Quantum Self-Trapping regime

Fig. 5.2 shows characteristic examples of the time-evolution of the population imbalance for different z_0, transitioning from the Josephson 'plasma' to the MQST regime for two different barrier heights, $V_0/\mu = 1.6$ and $V_0/\mu = 2$. The range of the barrier heights near $V_0/\mu = 1.6$ is explored by increasing V_0 with numerical steps of $\Delta V_0 \simeq 0.1\mu$ [2] Within such numerical resolution, we firstly obtain the MQST regime for $V_0/\mu = 1.6$: the $z(t)$ remains 'locked' at its initial value in the time interval $[0, 0.4]$ s while exhibiting small-amplitude oscillations around its mean value as shown in Fig. 5.2(a). Specifically, Fig. 5.2(a) shows the temporal evolution of the population imbalance as z_0 increases by gradually approaching the critical imbalance z_{cr} for the onset of the MQST regime. For z_0 smaller than z_{cr}, the Josephson 'plasma' regime is obtained whose oscillations amplitude increases with z_0 but its frequency decreases slightly with increasing z_0 (for the explored z_0 values such decrease is less than 1 Hz) (black and blue profiles in Fig. 5.2(a)). For $z_0 = z_{cr} = 0.019$ instead the system enters in the MQST regime and the $z(t)$ oscillates with a dominant frequency around 17 Hz (extracted by the Discrete-Fourier Transform as will be described later). The $z(t)$ oscillations frequency in the MQST regime (based on the two-mode model description in [59, 61] and in Sect. 2.3.2) can also be estimated as $\nu_{MQST} = \Delta\mu/h \simeq \Delta\mu_0/h$ (such frequency gives also the rate of phase-slippage as described in Chapt. 2) and it gives a value around 20 Hz for $z_0 = z_{cr}(V_0/\mu = 1.6)$ which is near but not exactly equal to the extracted value of 17 Hz.

Ref. [59, 61] showed that the onset of the MQST regime is proceeded by an intermediate regime characterised by high amplitude anharmonic oscillations of $z(t)$ around a zero-mean value. The presence of such regime is found in our case for the next chosen $V_0/\mu = 2$ shown in Fig. 5.2(b). In fact, if for $z_0 < z_{cr}$ the $z(t)$ exhibits harmonic Josephson 'plasma' oscillations (blue profile), as z_0 achieves value near z_{cr} but slightly smaller than z_{cr}, the $z(t)$ becomes anharmonic (black profile). The z_0 corresponding to such regime is classified inside the grey area of Fig. 5.1 main panel. For $z_0 = z_{cr} = 0.012$ instead we obtain the MQST regime where the $z(t)$, for $V_0/\mu = 2$, is characterized by single-frequency dominated oscillations around a non-zero mean value which is very well predicted by $\nu_{MQST} \simeq \Delta\mu_0/h \simeq 12$ Hz. In Fig. 5.2 it is also visible that the $z(t)$ oscillations frequency in the Josephson plasma regime become smaller at larger V_0/μ, consistent with the results presented in Sect. 3.4. In the Josephson 'plasma' regime the relative phase $\Delta\phi$ performs small-amplitude sinusoidal oscillations (with the plasma frequency) around a zero mean value as shown in Sect. 3.3.1. In the dissipative regime the $\Delta\phi$ undergoes one to many (depending on $(z_0 - z_{cr})$) phase-slippage mechanisms during its short-time evolution (as described in Sect. 3.3.2) which is followed by sinusoidal oscillations around a zero-mean value with several frequencies and with amplitude smaller than π. Here we show the ralative phase temporal evolution in the MQST regime. In particular, Fig. 5.3 shows both the population imbalance and the relative phase oscillations for the parameters of the subplot (b) in Fig. 5.2, i.e. for $V_0/\mu = 2$, and for a shorter time interval. The main

[2] However sometimes a higher resolution is required, for example $\Delta V_0 \simeq 0.05\mu$ in Sect. 5.3 for barrier heights near the MQST regime at different barrier widths and in some other cases lower resolution is sufficient, for example when studying the dissipative regime for $V_0/\mu \lesssim 1$ where $\Delta V_0 \simeq 0.2\mu$.

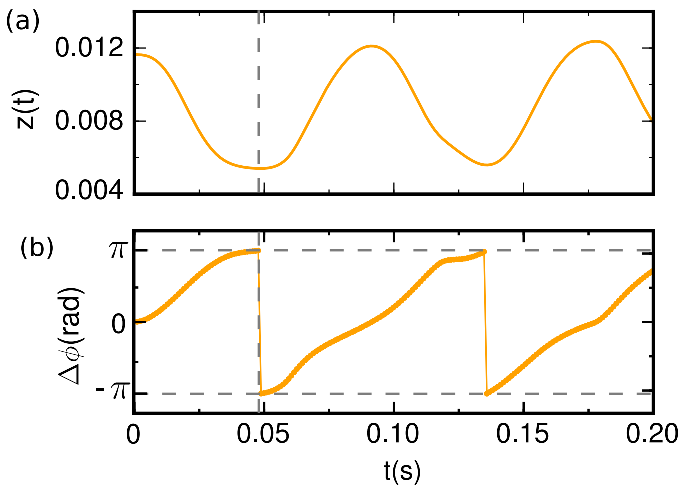

Figure 5.3: The temporal evolution of the imbalance (a) and the relative phase (b) for $V_0/\mu = 2$, $z_0 = z_{cr}$ and at fixed $w/\xi = 4$. The relative phase is calculated along the line $y = z = 0$ near the trap center. The vertical grey dashed lines show the moment the population imbalance has a local minima and the relative phase jumps by 2π.

features characterising the MQST regime consists of: the population imbalance oscillates about a non-zero value, and 2π jumps in the relative phase at the times of the $z(t)$ local minima, with a rate captured well by the two-mode model ($\nu_{\mathrm{MQST}} \simeq \Delta\mu_0/h \simeq 12$Hz). Abad *et al.* [83] (also described in Sect. 1.4) numerically related the self-trapping regime to phase slips created by the nucleated vortex rings which annihilate within the barrier region (but outside the region of observable condensate density). This picture is also confirmed by our simulations where, both our VR tracking code and the 2D phase profiles, reveals the presence of vortex rings at the trap center and outside the condensate density. In fact, Fig. 5.4 shows 2D phase profile along the $x-y$ plane (for $z = 0$) for $V_0/\mu = 2$, $z_0 = z_{cr}$ at time $t \simeq 46$ ms where a 2π phase windings is present around the vortex core at $y \sim \pm 1.6 l_x$.

The MQST regime is a metastable state and one of the possible causes of its destruction at relatively long-time evolution could be the presence of the dissipative second order terms in the current-phase relation (defined in Eq. (2.81)), which originates from considering also the tunneling between condensate and non-condensate states (noncondensate states can be low energy phonon-like excitation) across the junction that are finite even at $T = 0$ (described in Sect. 2.4). In fact, Meier and Zwerger in Ref. [65] showed that the presence of the normal current $J_n = G_n \Delta\mu$ leads to the destruction of the MQST regime even when it has a small contribution of around 3%. In fact, if we now look at longer time evolution, for example until $t = 1.6$s instead of $t = 0.4$s, the MQST regime for $V_0/\mu = 1.6$ decays within 0.55s while for $V_0/\mu = 2$ the MQST regime is stable until at least 1.6s. This is shown in Fig. 5.5. This is consistent with the Eq. (63) of Ref. [65] which states that the contribution

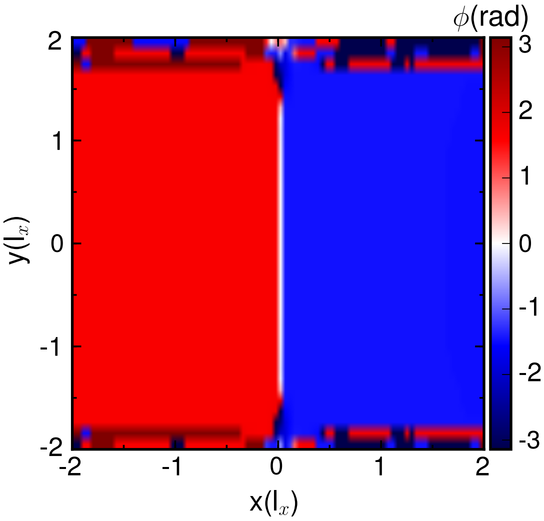

Figure 5.4: The 2D phase profile along the xy plane (for $z = 0$) for $V_0/\mu = 2$, $z_0 = z_{cr}$ at time $t \simeq 46$ ms revealing a phase-winding around the vortex core at $y \sim \pm 1.6 l_x$.

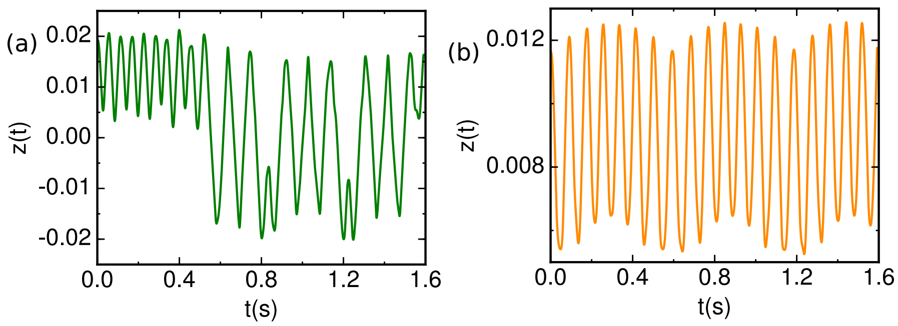

Figure 5.5: The long time evolution of the imbalance for $V_0/\mu = 1.6$ (a) and for $V_0/\mu = 2$, for $z_0 = z_{cr}(V_0)$, equal to $z_{cr} = 0.019$ and $z_{cr} = 0.012$ in (a) and (b), respectively, and at fixed $w/\xi = 4$.

of the second order dissipative term descreases with increasing V_0/μ. The Discrete Fourier Transform (DFT) of $z(t)$ extracted for both the barrier heights, shown in Fig. 5.6, shows a peak near the predicted ν_{MQST} (around 20 Hz) for $V_0/\mu = 1.6$ and at exactly the predicted value for $V_0/\mu = 2$. Except for the peak near zero, which comes from having a non-zero mean value of the imbalance, the MQST frequency is the dominant frequency for $V_0/\mu = 2$ while it is not the most important frequency for $V_0/\mu = 1.6$. In particular, for $V_0/\mu = 1.6$ the population imbalance, after the decay at $t \simeq 0.55$s, oscillates around zero value with several frequencies. Thus, we extract the DFT spectrum at two different time intervals: for $t < 0.55$s, which gives the frequency values of the MQST regime (black profile in Fig. 5.6(a)) and for $t \geq 0.55$s (grey profile), which gives the oscillation frequencies of the

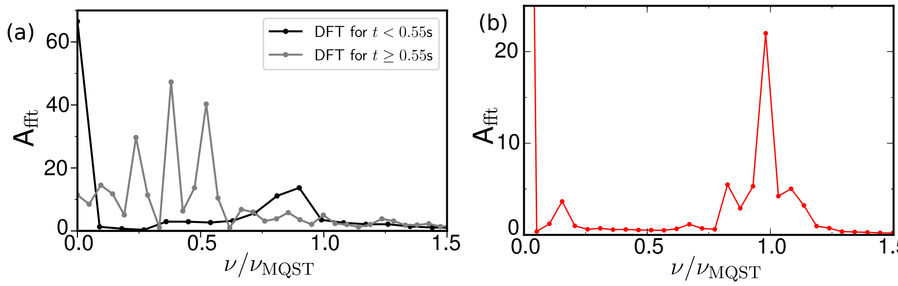

Figure 5.6: The DFT amplitude of the $z(t)$ for $V_0/\mu = 1.6$ (a) and for $V_0/\mu = 2$ (b) at $z_0 = z_{cr}$, equal to $z_{cr} = 0.019$ and $z_{cr} = 0.012$ in (a) and (b), respectively. The barrier width in both cases is $w/\xi = 4$. The frequency is scaled to $\nu_{MQST} = \Delta\mu_0/h$. In (a) the DFT spectrum of the population imbalance extracted for $t < 0.55$s (black profile) and $t \geq 0.55$s (grey profile) is shown, where the time $t = 0.55$s is the time the population imbalance, shown in Fig. 5.5(a), reaches the zero value.

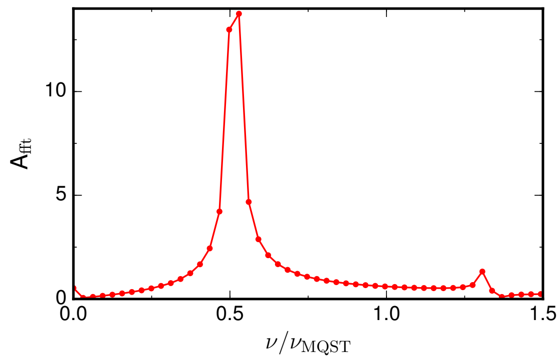

Figure 5.7: The DFT amplitude of the $z(t)$ for $V_0/\mu = 1.6$ and $z_0 < z_{cr}$. The frequency is scaled to the MQST frequency for $z_0 = z_{cr}$. The spectrum resolution is 0.6Hz.

population imbalance after the decay of the MQST regime. We observe that the DFT spectrum for $V_0/\mu = 1.6$ has a dominant peak at near 0.5 ν_{MQST}, which comes from the oscillations around the zero mean value. In fact, this is confirmed by looking at the DFT spectrum for $z_0 < z_{cr}$ shown in Fig. 5.7, where the peak at 0.5 ν_{MQST} is the dominant frequency of the imbalance in the Josephson 'plasma' oscillations regime. Thus after the decay at around 0.55s the $z(t)$ oscillates mainly with the Josephson 'plasma' frequency.

5.1.2 Self-Trapped State

Near critical imbalance

For $V_0/\mu > 1.6$, as z_0 (i.e. $\Delta\mu_0$) increases to higher values (beyond z_{cr}), the amplitude of the oscillations decreases and its corresponding frequency significantly increasing. These features are clearly visible in Fig. 5.8 where some examples of $z(t)$ profiles are shown for

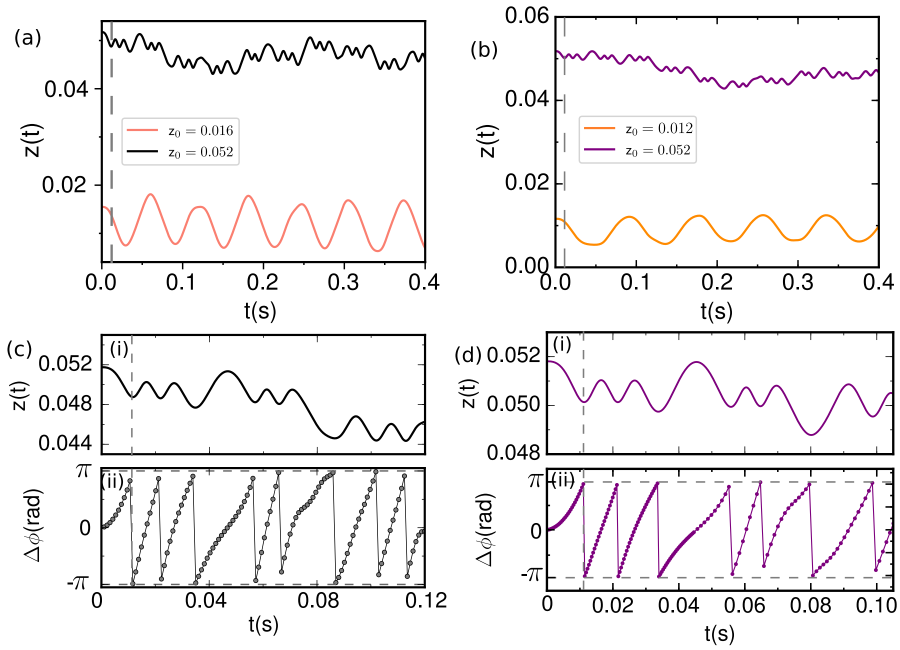

Figure 5.8: The temporal evolution of the population imbalance for $V_0/\mu = 1.8$ (a) and for $V_0/\mu = 2$ (b) for two different values of the initial imbalance: $z_0 = z_{cr}(V_0)$, that is $z_{cr} = 0.016$ and $z_{cr} = 0.012$ for (a) and (b) respectively, and for the same initial imbalance $z_0 = 0.052$. (c)-(d) The zoomed-in time evolution of $z(t)$ (i) and the relative phase (ii) for the profiles in (a) and (b) with the same value of $z_0 = 0.052$. The numerical data are at fixed $w/\xi = 4$. The vertical grey dashed lines show the moment the population imbalance for $z_0 = 0.052$ has a local minima. The time resolution in (c) is 1 ms while in (d) is 0.2 ms.

$V_0/\mu = 1.8$ [(a)-(b)] and $V_0/\mu = 2$ [(c)-(d)] for different z_0 values. Furthermore, the $z(t)$ pattern becomes increasingly less regular than the pure self-trapped states (or MQST). The origin of this is the co-existence of multiple modes, corresponding to additional higher-level excitations and complicated couplings [238, 239], which result in less regular dynamics than those discussed in the pure two-mode self-trapping regime [59].

Nonetheless, closer inspection even in this regime (Fig. 5.8(b)-(d)), still reveals the existence of (irregular) 2π phase jumps at the relative population minima, thus allowing us to still characterise this regime as 'self-trapped' (depicted by the dark red colour in the various phase diagrams shown in this chapter).

Self-trapped modes

Here we analyse the spectrum of the population imbalance for $V_0/\mu = 2$ at different initial population imbalances z_0. In the limiting case of z_0 marginally exceeding the critical value z_{cr}, one recovers the well-known MQST state (as shown previously): this features both single-frequency biased population oscillations between the two wells, and corresponding phase slips of 2π with the same period (Fig. 5.9 (a) and Fig. 5.3). As z_0 increases in the same system we observe a number of features, which can be clearly seen in Fig. 5.9: Firstly, the population oscillations become more complicated, with the gradual emergence of numerous frequencies associated with higher-order excitations [238, 239]. Secondly, the $z(t)$ can even decrease initially its value in time as happened in (b) for $t \lesssim 0.2s$ or for larger time in (c), while remaining different from zero for at least 1.1 s (which is the time interval explored here). This behaviour can be associated to the coupling with phonon modes as found in Ref. [238]. Importantly, the MQST frequency $\nu_{MQST} \simeq \Delta\mu_0/h$, which is the dominant frequency for $z_0 = z_{cr}$ (Fig. 5.9 (a)-(ii)), becomes increasingly less relevant with higher z_0, with all dominant frequencies in such extended self-trapped states being smaller than the corresponding ν_{MQST}.

The higher the initial z_0, the more reduced the total oscillation amplitude of $z(t)$ becomes. For sufficiently large value of z_0/z_{cr}, the evolution of $z(t)$ resembles to good approximation a nearly flat line with features only becoming discernible when one zooms into the plot (as for example in Fig. 5.9 (d)).

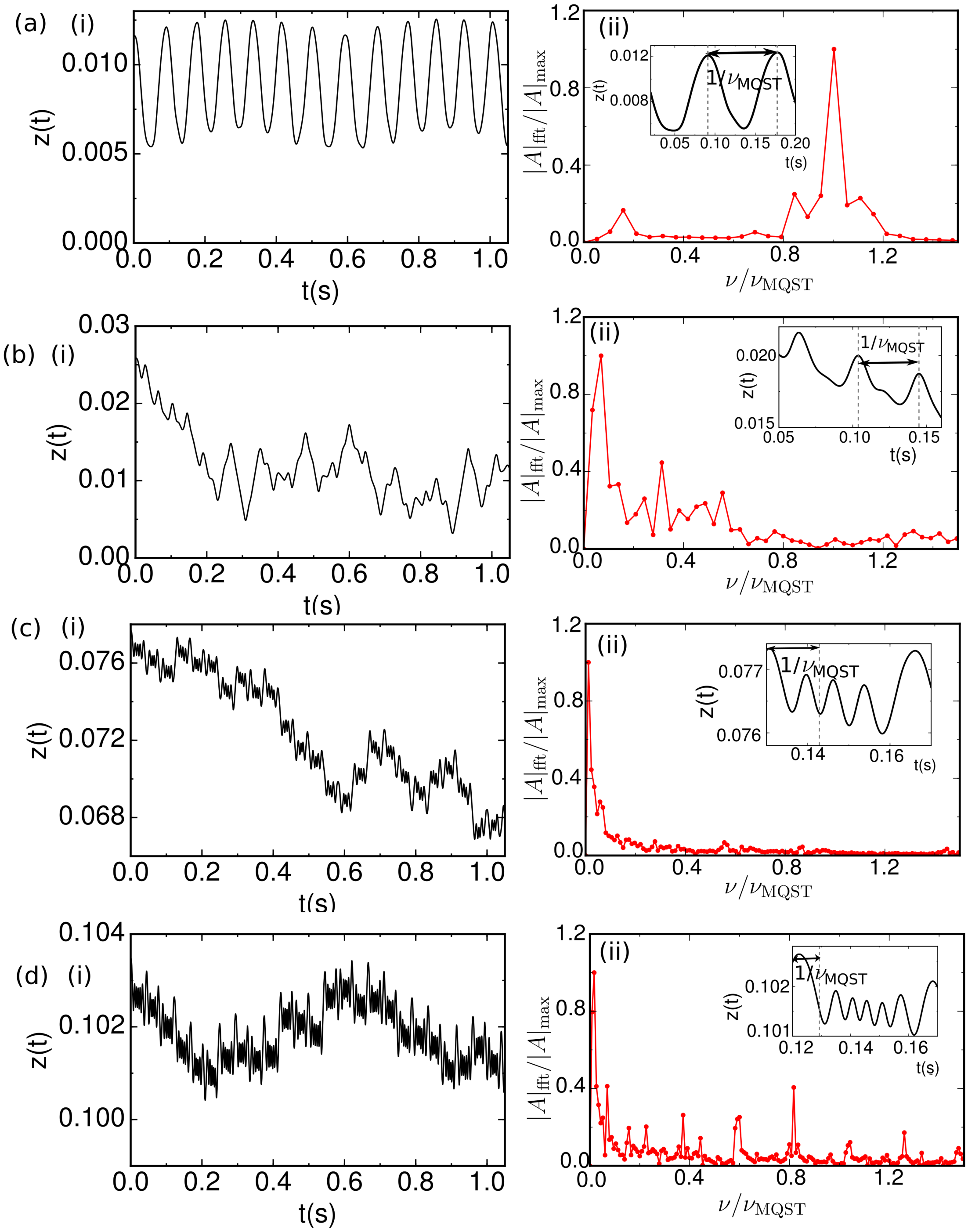

Figure 5.9: (a)-(d)(i) Temporal evolution of the population imbalance, $z(t)$, for different initial imbalances z_0 and for $V_0/\mu = 2$, $w/\xi = 4$. Plots (a)-(d)(ii) show the corresponding DFT amplitude of $z(t) - \langle z(t)\rangle$, with the frequency scaled to the MQST prediction, and the amplitude scaled to the value of the DFT amplitude of the dominant frequency. The insets show the $z(t)$ profiles of (i) for shorter time evolution where the arrows indicate the time interval $1/\nu_{\rm MQST}$ with $\nu_{\rm MQST} \simeq \Delta\mu_0/h$.

5.1.3 Further Dynamical Regime Details in an Elongated Trap

Next, we present more details about how the evolution of $z(t)$ can differ even within a particular regime, which allows us to highlight more clearly the nature of the different observed crossovers. In particular, Fig. 5.10 shows the complex dependence of the evolution of $z(t)$ for barriers with $w/\xi = 4$ and different values of the parameters z_0/z_{cr} and V_0/μ, as clearly identified in the individual subplots. Specifically, this figure is organised across 3 rows, with the ratio of z_0/z_{cr} increasing from bottom to top: from values $z_0/z_{cr} < 1$ (bottom row; Josephson regime), through $z_0/z_{cr} \sim 1$ (middle row; crossover regime from Josephson to other dynamical behaviour) to $z_0/z_{cr} > 1$ (top row).

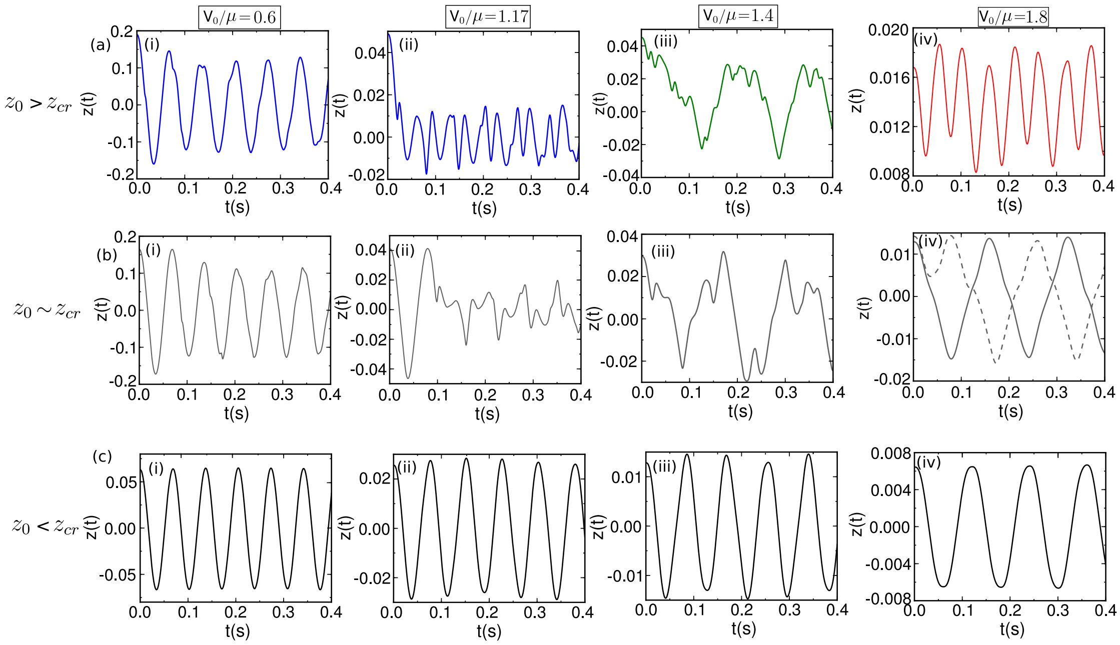

Figure 5.10: Dependence of the temporal evolution of the population imbalance in an elongated harmonic trap on different values of $z_0/z_{\rm cr}$ and V_0/μ at fixed $w/\xi = 4$, corresponding to the phase diagram of Fig. 5.1.

Specifically, the bottom row [(c)] has $z_0/z_{cr} < 1$, with the system exhibiting Josephson plasma oscillations, with a frequency that becomes smaller at higher V_0/μ. The intermediate row [(b)], depicting the behaviour of $z(t)$ at values $z_0/z_{cr} \sim 1$ but just below 1, corresponds to the 'grey' crossover regime of Fig. 5.1, during which the system transitions from Josephson plasma oscillations to the dissipative or self-trapped regime. The top row corresponds to cases $z_0/z_{cr} > 1$, the system exhibits a smooth crossover from dissipative regime (left two columns, $V_0/\mu \leq 1.2$) to self-trapped regime (right column; $V_0/\mu = 1.8$).

This figure displays a range of interesting behaviours, which are briefly commented upon below:

1. For $z_0/z_{cr} > 1$ and relatively low V_0/μ [left 2 columns], the dynamical behaviour in the dissipative regime exhibits either a rapid decay of the amplitude of $z(t)$ to 0 [subplot (a)(ii)], or to a more gradual decay as V_0/μ decreases further below 1 [subplot (a)(i)].

2. As the system transitions from Josephson plasma to a distinct dynamical regime with increasing z_0 approaching z_{cr} from below – and for intermediate values of V_0/μ of order 1 (here the value corresponds to $V_0/\mu = 1.4$) – the evolution of $z(t)$ becomes somewhat irregular, and hard to classify as belonging to a particular regime [e.g. subplot (b)(iii)]. Such features are somewhat obscured by our chosen coloured representation of the phase diagram shown in Fig. 5.1 but are important to note: it is precisely such behaviour of $z(t)$ which reveals the irregular crossover denoted by different colours in the presented phase diagram plots.

3. In the 'crossover regime' occurring for $z_0 > z_{cr}$ and 'intermediate' $V_0/\mu \geq 1.2$ [subplot (a)(iii)] we see behaviour which is somewhat reminiscent of the dissipative regime, as there are multiple dips in the early-time decay of $z(t)$, followed by a periodic-like oscillation around zero mean value; at the same time, it also bears features of the behaviour seen for high z_0/z_{cr} and large $V_0/\mu > 1$: indeed increasing z_0/z_{cr} even more for fixed $V_0/\mu = 1.4$ gradually leads to the appearance of a self-trapped state. This behaviour further justifies the slightly curved contours shown in the phase diagrams. The study of the origin of those frequencies in the crossover regime goes beyond the scope of this thesis.

4. Finally, we note some interesting observations in the Josephson regime $z_0 < z_{cr}$ [subplots (c)(i)-(iv)]. The Josephson regime in ultracold atoms is typically associated with a single dominant frequency, the plasma frequency, determined by the two-mode model.

   However, the two-mode approximation is expected to be valid if the condensate wavefunctions in the left and right wells are localized in each well, i.e. if the barrier height and width are such that the overlapping of the left and right condensate wavefunctions is small in the barrier region. In our case, both the Josephson plasma frequency and the critical imbalance are well predicted by the two-mode model in our elongated trap, only for a specific parameter subspace, as will be shown later. Specifically, the predictions of the two-mode model appear to agree with those of our GPE simulations at fixed $w/\xi = 4$ only for $V_0/\mu \geq 1.6$. For $V_0/\mu \leq 1.4$, we actually see higher frequencies emerging, at approximate integer multiple values of the fundamental Josephson oscillation frequency, and with a significantly lower weighting, consistent with Refs. [65, 222, 159] (the study of second-order term in the current-phase relation is performed in Sect. 3.6.1).

5.2 Dependence on barrier width

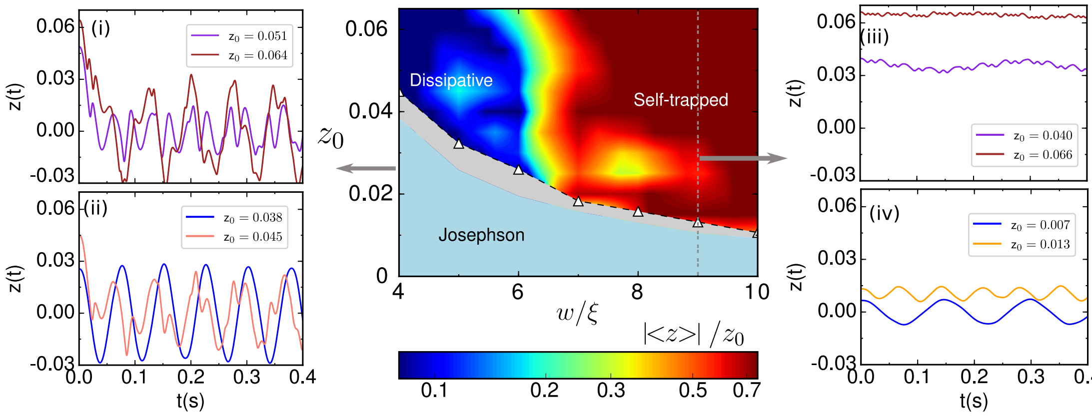

Figure 5.11: Phase diagram of dynamical regimes arising across a Gaussian barrier of variable width $w/\xi \in [4, 10]$ and fixed $V_0/\mu = 1.17$ for different initial population imbalances $z_0 = z(t = 0)$ [main panel]. The Josephson plasma oscillation regime dominates for $z_0 \lesssim z_{cr}$ and, beyond a narrow transition regime (indicated by the grey shaded area) the system transitions to the dissipative ($w/\xi \leq 6$), or the self-trapped ($w/\xi > 6$) regime, with the empty black triangles (and connected dashed black line) indicating the critical imbalance. Such regimes are characterized by the coloured regions which display the absolute value of $\langle z(t)\rangle/z_0$ where $\langle z(t)\rangle$ is the temporal mean value of z(t) in the time interval [0, 0.4]s; the colormap is in logarithmic scale ranging between 0.08 and 0.75. Evolution of the population imbalance $z(t)$ for different z_0 and (i)-(ii) $w/\xi = 4$ at $V_0/\mu = 1.17$, showing the transition from the Josephson 'plasma' oscillations to the dissipative regime, and (iii)-(iv) $w/\xi = 9$ at $V_0/\mu = 1.17$, from the Josephson to the pure MQST regime and higher self-trapped states. The dashed grey line in main panel indicate the value $w/\xi = 9$.

Many experiments that showed the presence of the MQST regime had a barrier width larger than the one of the experiment at LENS in terms of its ratio to the superfluid healing length. Being motivated by these experiments, we study the effect of the barrier width, firstly on the phase diagram. We keep fixed the barrier height $V_0/\mu = 1.17$– which we would still classify as belonging to the dissipative regime – and different values of the barrier width compared to the healing length ξ.

The corresponding plot is shown in Fig. 5.11[main panel], and clearly reveals the same behaviour as found above. When the width is narrow ($w/\xi \lesssim 6$), and for population imbalances $z_0 > z_{cr}$ such that the system transitions away from the Josephson plasma regime, the barrier acts more like a perturbing force to the initial superfluid flow, leading to significant acoustic energy emission and vortex ring(s) generation – with the system thus entering (in agreement with earlier findings) the dissipative regime (as shown in Fig. 5.11 (i)-(ii) for $w/\xi = 4$). Increasing the barrier width at constant height, leads to a stronger effective barrier which isolates the two wells more, thus decreasing the Josephson coupling energy E_J in comparison to the self-interaction energy (for fixed z_0) $E_c z_0^2 N^2/8$: the system now transits to the self-trapped regime. For small values of z_0 which only slightly exceed z_{cr}, the system finds itself in the pure self-trapped regime, with higher z_0 leading to the more complicated self-trapped states discussed above (examples shown in Fig. 5.11 (iii)-(iv) for $w/\xi = 9$).

5.3 Critical parameter Phase Diagram

To gain further insight on the generality of the results presented previously, we next investigate the dependence of the critical population imbalance, local density and healing length (appropriately scaled, as described later), at the transition from Josephson plasma to the other (dissipative; self-trapped) dynamical regimes, in terms of both barrier height V_0/μ and barrier width w/ξ. This is shown in Fig. 5.12, and clearly characterizes the key parameters in terms of the transition between dissipative and self-trapped regimes.

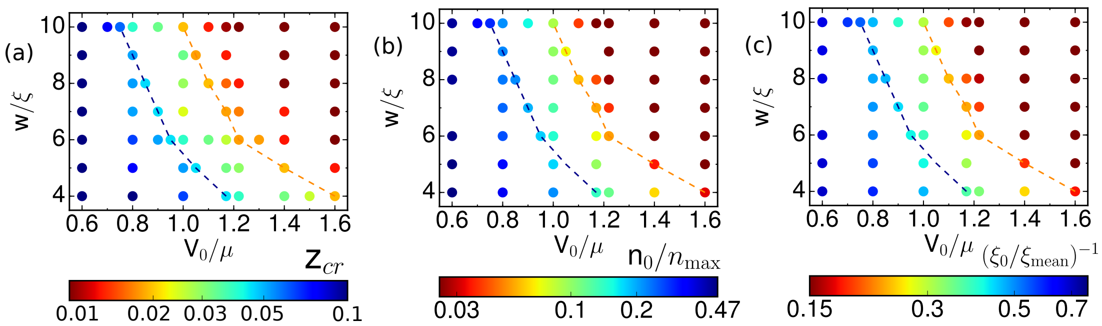

Figure 5.12: (a) Alternative phase diagram in the $V_0/\mu - w/\xi$ space of parameters depicting (a) the value of the critical population imbalance, z_{cr}, (b) the scaled density, and (c) the scaled inverse healing length, as a function of $V_0/\mu \in [0.6, 1.6]$ and $w/\xi \in [4, 10]$. Their values are represented by the colorbar shown in logarithmic scale. For each value of w/ξ there exists a maximum value of the barrier height $V_0 = V_{dissip}$ (denoted by the dashed blue line) below which we find a pure dissipative regime at $z_0 \approx z_{cr}$, and another value of the barrier height $V_0 = V_{MQST}$ (denoted by the dashed orange line), above which the system transitions to a self-trapped regime, and specifically to a pure self-trapped regime for $z_0 \approx z_{cr}$. The numerical data between the dark-blue and the orange lines correspond to the intermediate, or 'crossover', regime. In (b) the density at the trap center is scaled to the maximum value of the density in the absence of the barrier, while in (c) the mean healing length is correspondingly scaled to the healing length at the trap center.

Specifically, Fig. 5.12(a) shows the value of the critical population imbalance, z_{cr}, for each probed V_0/μ and w/ξ combination, which is represented by the color of the points. For each w/ξ there exists a specific (maximum) threshold value V_{dissip}, such that for $V_0 \leq V_{dissip}$ the system transits from Josephson plasma to the dissipative regime. Likewise, there exists a specific (minimum) threshold value of the barrier height V_{MQST}, such that for $V_0 \geq V_{MQST}$ there is a transition to the (pure) self-trapped regime. These crossover behaviours are respectively mapped out by the dashed blue, and dashed orange lines. The dissipative regime can be found for relatively low and narrow barriers but also for wide and small enough barrier heights (left of the dashed blue line). On the other side the self-trapped regime can be achieved for relatively high and wide barriers but also for narrow and large enough barrier heights (right of the dashed orange line). By varying the barrier heights and widths the system enters the crossover regime (for the values between the dashed blue and orange lines in Fig. 5.12(a)), where the population imbalance features irregularly-oscillating decaying dynamics, as showed in Sect. 5.1.3 for the case of $w/\xi = 4$ but it applies for any w/ξ.

From Fig. 5.12(a), we see that the dissipative regime occurs at a higher z_{cr} than the self-trapped regime. For the elongated experimental parameters Refs. [49, 20] the critical population imbalance at which the interesting crossover dynamics emerges is rather low, placing strong constraints on its experimental observation. However, the actual value of z_{cr} at such boundaries is very geometry-dependent, and we later show how an isotropic trap can significantly enhance the observable relevant region. An important comment regarding Fig. 5.12(a) is that the value of z_{cr} at which the transition to (pure) self-trapping takes place, i.e. along the transition line, is rather independent of the values of V_0/μ and w/ξ. This also occurs, although to a lesser extent, along the dissipative transition line. Interestingly, a similar qualitative picture emerges when looking at the value of the density along the x axis at the trap centre, scaled to its corresponding value in the absence of the barrier. Another way to plot this information is as the inverse of the ratio of the healing length calculated at the trap center to the mean value healing length ξ_{mean} extracted by the maximum density in the absence of the barrier (both calculated from the x axis density). These are respectively shown in Figs. 5.12(b)-(c).

Although these considerations clarify the weak dependence of such (dimensionless) quantities on V_0/μ and w/ξ, we note here that the *specific* value of z_{cr} marking such crossovers actually depends on the trap geometry. Nonetheless, the above findings raise the interesting question of how much the *structure* of the phase diagram depends upon the microscopic details of the junction and of the bulk system. We will comment more on this point in the final section on 'Conclusions and future works' (Sect. 5.9.1).

5.4 The two-mode model validity

As described in Sect. 2.3.2 and Sect. 3.4, in the two-mode model the two condensates are considered as weakly-linked, i.e. there is a a small overlapping of their wavefunctions in the barrier region. In the linear two-mode model the wavefunction is written as in Eq. (3.12) where the time-dependence of the wavefunction is separated by its spatial-dependence while in the non-linear two-mode model the time-dependence appears on the spatial part of the system wavefunction which is then expressed by Eq. (3.13). An atomic Josephson junction is characterised by the onsite interaction energy and by the tunneling energy. Their ratio defines the critical imbalance for the onset of MQST regime and it is expressed by Eq. (3.15) for $z_0^2 \ll 1$:

$$z_{cr} \simeq \sqrt{\frac{8K}{UN}}. \tag{5.1}$$

In our simulations the tunneling energy is extracted from the difference ΔE between the antisymmetic-state energy and the symmetric-state energy; in particular the term $2K$ in Eq. (5.1) is substituted by $\Delta E/N$. As described in Sect. 3.4, the symmetric and antisymmetric states are numerically found by solving the GPE equation for a linear tilted potential $\epsilon = 0$ and imposing the symmetry/antisymmetry condition of the wavefunction under space coordinates inversion (along the x axis). The Josephson coupling energy E_J is defined as $E_\mathrm{J} = \Delta E/2$. The onsite interaction energy U can be calculated *either* from the linear two-mode model [59], via $U_\mathrm{lin} = g \int \eta_L^4 d\mathbf{r}$ *or* from the nonlinear two-mode model [187] as $U_{NL} = 2(\partial\mu/\partial N)$. From the tunneling and the onsite interaction energy, the Josephson 'plasma' oscillations frequency can be estimated from Eq. (3.17) as

$$\omega_J = \frac{\sqrt{\Delta E U_{\mathrm{lin(NL)}}}}{\hbar} . \tag{5.2}$$

The two-mode model did not accurately predict the critical imbalance and especially the Josephson 'plasma' frequency in the range of the experimental parameters, i.e. for $w/\xi = 4$ and $V_0/\mu \leq 1.2$ (as shown in Sect. 3.4). The two-mode model prediction of z_{cr} was not expected to fit the numerical data well in the dissipative regime because its expression is valid in the MQST regime. It instead fails to predict the ω_J as for $V_0/\mu \leq 1.22$ we are not in the deep tunneling regime. In fact, as we showed in Sect. 3.6, second-order term in the current-phase relation at twice the Josephson frequency are present for V_0 on the order of μ and their importance increases with decreasing V_0/μ. We here instead explore barrier heights and widths beyond the experimental range, i.e. $V_0/\mu > 1.2$ for fixed $w/\xi = 4$ and barrier width w in the range $[4, 10]\xi$ for fixed $V_0/\mu = 1.17$. The extracted values of the z_cr from the two-mode model and from the GPE results are shown in Fig. 5.13(a)(i) for the first case of fixed barrier width $w/\xi = 4$ and barrier heights $0.6 \leq V_0/\mu \leq 2.1$ while Fig. 5.13(b)(i) shows the corresponding results for the second case

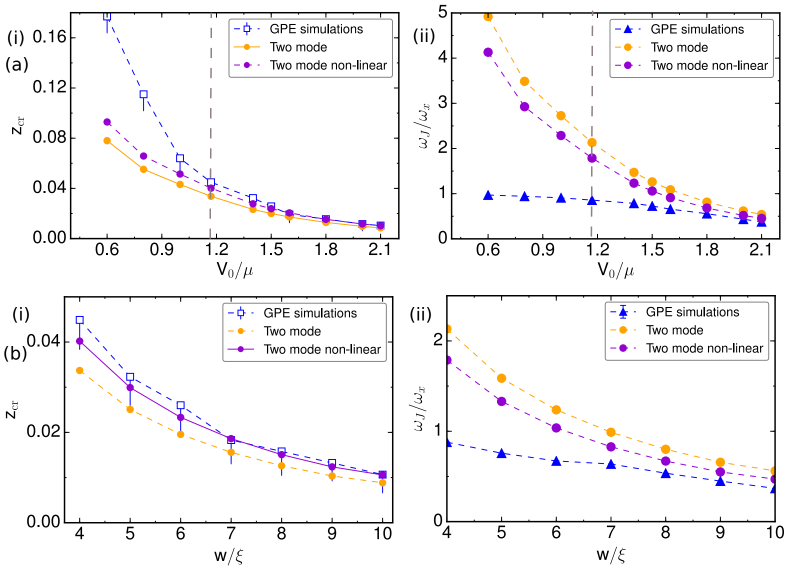

Figure 5.13: (a) Critical initial population imbalance (i) for different barrier height V_0/μ and for fixed $w/\xi = 4$ extracted from GPE simulations, from linear (orange circles) and nonlinear (violet circles) two-mode model and the predicted Josephson 'plasma' (ii) frequency at different values of barrier heights from the two-mode model and the value extracted from the GPE simulations by fitting with a sinusoidal function $z(t)$ for $z_0 < z_{cr}$. (b) The critical imbalance (i) and the Josephson frequency (ii) for different values of the barrier widths and for fixed barrier height $V_0/\mu = 1.17$ (indicated by the vertical grey dashed line in (a)) extracted by the GPE simulations and the predictions from the two-mode model. The data are for the elongated trap.

of fixed $V_0/\mu = 1.17$ and a variable barrier width $4 \leq w/\xi \leq 10$. We note that the MQST regime emerges when $V_0/\mu \geq 1.6$ in the first case, and for $w/\xi \geq 7$ in the second case. We find good agreement for $V_0/\mu \geq 1.2$ in the case of fixed barrier width at $w/\xi = 4$ and for all the explored barrier widths in the case of fixed $V_0/\mu = 1.17$.

The behaviour of the Josephson 'plasma' frequency is shown in the right subplots of Fig. 5.13 ((a)(ii), (b)(ii)). Specifically, we plot ω_J/ω_x as a function of V_0/μ at fixed $w/\xi = 4$ [(a)(ii)] and as a function of w/ξ at fixed V_0/μ [Fig. 5.13(b)(ii)], showing both two-mode model predictions, and corresponding numerical GPE results. The two-mode model predicts the Josephson plasma frequency well for $V_0/\mu \geq 1.6$ in the case of fixed $w/\xi = 4$ and for $w/\xi \geq 7$ for fixed $V_0/\mu = 1.17$.

5.5 Microscopic description

To understand the macroscopic processes described in previous sections which lead to distinct dissipative, self-trapped regimes and their crossover, we perform here a detailed microscopic analysis of compressible and incompressible kinetic energies and the corresponding vortex ring dynamics – for cases where a vortex ring is indeed generated. We apply our analysis to the entire relevant regime of $V_0/\mu = [0.6, 1.6]$ for the specific case of $w/\xi = 4$, corresponding to the crossover shown in Fig. 5.1.

5.5.1 Effect of the barrier height on the vortex rings dynamics

A vortex ring is generated when $z \geq z_{\rm cr}$, i.e. when the initial acceleration driven by the population imbalance is such that the superfluid velocity locally exceeds a critical value within the barrier (as described in Chapt. 3). After its nucleation the VR enters the condensate transverse density by shrinking initially its radius. Then the VR starts travelling into the left reservoir by increasing its position $|x|_{VR}$. For $|x|_{VR} \leq 2w$ the VR shrinks further its radius due to the increasing density along the x axis. We start by noting that for rather low values of V_0/μ, e.g. $V_0/\mu = 0.2 - 0.4$, the density gradient within the barrier region is small and thus the VR radius does not shrink much. The large vortex ring then interacts strongly, and on a relatively short timescale after commencing its axial propagation, with its image vortices [228] and, as a result of the radial anisotropy of the trap, it almost immediately breaks up into two vortex lines.

Shortly after, the vortex structure reverses its motion, travelling towards the barrier (which it can even surpass for $V_0/\mu = 0.2$).

The analysis of the vortex ring motion presented in this section is therefore limited to values $V_0/\mu \geq 0.6$ for which the vortex ring does not break up immediately [3]. In this section we characterize the dependence of vortex dynamics and relevant energies as a function of V_0/μ for two cases: Firstly we consider a variable initial population imbalance equal to the critical value, *i.e.* $z_0 = z_{cr}(V_0/\mu)$: such a curve corresponds to the dashed black line in Fig. 5.1 delimiting the transition from Josephson plasma to dissipative/self-trapped regimes. Secondly, we consider the case of a fixed initial imbalance $z_0 = 0.19$, illustrated with a horizontal white dashed-dotted line in Fig. 5.1. In both cases, for $V_0/\mu \leq 1$ a vortex is clearly observed and its dynamics within the atomic cloud is subsequently monitored (whereas for values $V_0/\mu > 1$ the generated vortex ring at $x = 0$ always remains a 'ghost' vortex outside the condensate region, where the density is negligible). Specifically, Fig. 5.14 shows the time evolution of the radius $R_{\rm VR}$ (a(i), b(i)) and axial position $x_{\rm VR}$ (a(ii), b(ii)) of the clearly discernible vortex ring for $V_0/\mu \in [0.6, 1.0]$ for (a) a variable $z_0 = z_{cr}(V_0/\mu)$ [left], and (b) a fixed $z_0 = 0.19$ [right]. Fig. 5.14 (a) and (b) show a similar behaviour in this range of parameters. If $z_0 = z_{cr}(V_0/\mu)$ (left), the system exceeds the critical velocity once, and thus only one vortex ring is generated, while for $z_0 = 0.19$ multiple vortex rings can be nucleated, their number depending on the value of $z_0 - z_{cr}(V_0/\mu)$ [90] (also described in Chapt. 3). However, for simplicity, here we only study the dynamics of the first generated vortex ring.

[3]Note that for $V_0/\mu = 0.6$, the vortex ring still breaks into two vortex lines, but this only occurs after a long evolution within the left condensate.

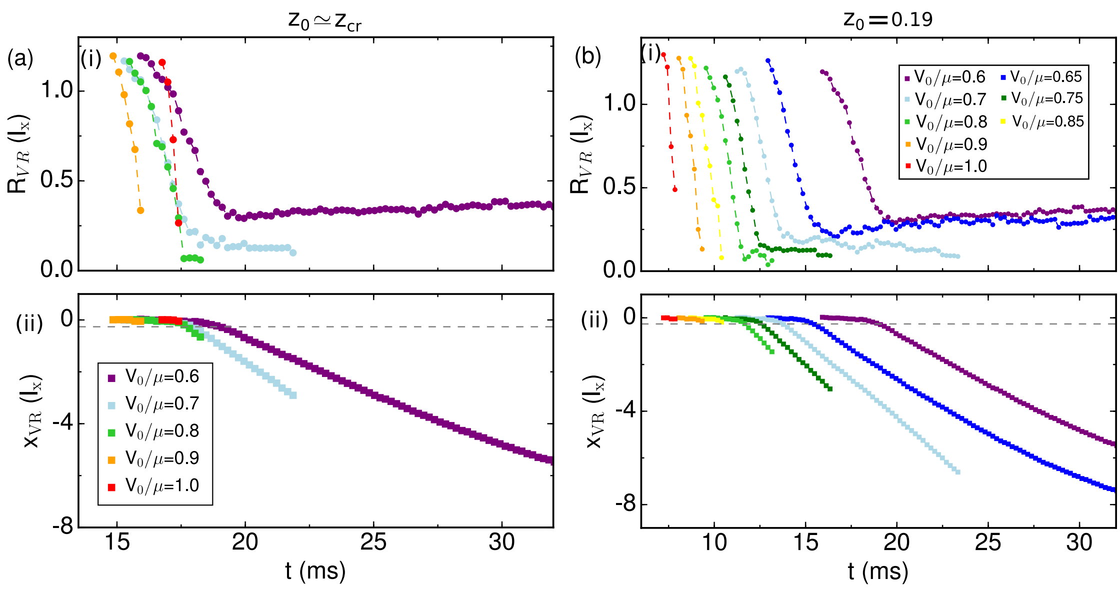

Figure 5.14: Dependence of the evolution of the first generated vortex ring for fixed value of the barrier width $w/\xi = 4$ and barrier height values $0.6 \leq V_0/\mu \leq 1$. Shown are the cases of (a) $z_0 = z_{cr}$, or (b) $z_0 = 0.19$. The grey dashed horizontal lines indicate the value of the barrier width.

In the case $z_0 \simeq z_{cr}$, the vortex rings are nucleated almost after the same time interval since the start of the dynamics, independently of the value of V_0/μ (the observed minor shift is due to the numerical tracking uncertainty and numerical finite resolution in identifying the z_{cr}). For $z_0 = 0.19$ and variable V_0/μ we clearly observe that larger values of V_0/μ lead to earlier nucleation of the first vortex ring. This is because the critical velocity in the barrier is reached earlier by the superfluid, as the junction is thinner.

In both cases, we observe that as the barrier height V_0/μ decreases, the vortex ring lives longer, overcomes the barrier region and propagates further into the left well. In fact, as V_0/μ decreases, the nucleated vortex ring has a larger energy (described later) hence a larger radius and a smaller velocity, as shown in Fig. 5.14. We next characterise in more detail the effect of the barrier height on the VR initial shrinking dynamics within the barrier region and subsequent VR dynamics occurring within the left condensate and after leaving the barrier for the case of fixed $z_0 = 0.19$.

The analysis is performed for $0.6 \leq V_0/\mu \leq 0.8$. As observed in Fig. 5.14 the VR mean radius decays initially almost exponentially in time and we thus fit the VR radius with the function:

$$R_{VR}(t) = a \cdot \exp(-(t - t_0)/\tau) + c \tag{5.3}$$

The fit is done starting from the moment the VR radius is smaller or equal to the mean TF radius until the moment it achieves its 'plateau' value. From the extracted value of τ shown in Fig. 5.15(a)), and a, we estimate the initial VR shrinking velocity as shown in

Fig. 5.15 (b)). These calculations show that the VR shrinks faster for the largest barrier height.

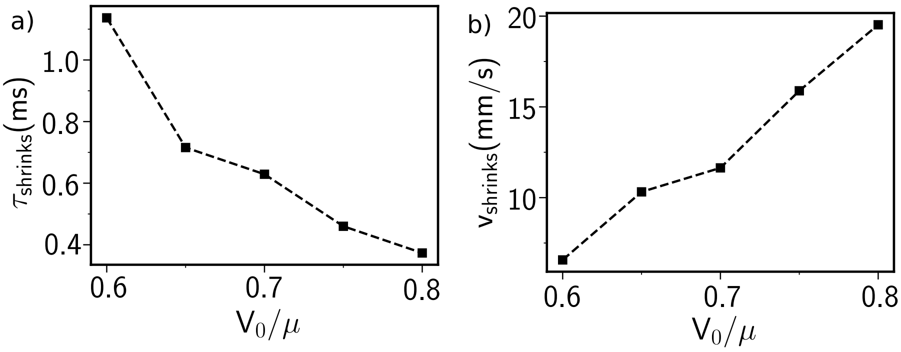

Figure 5.15: The dependence of the first VR shrinking time τ (a) and shrinking velocity (b) on the barrier height for the case of fixed $z_0 = 0.19$ and $w/\xi = 4$.

The initial shrinking stops when the VR is at the position ($x_{VR} \simeq -0.55 l_x$) where the TF radius is maximum. At this position the VR radius is smaller for larger barrier heights (as shown in Fig. 5.16(b)). After that it moves for a while with constant velocity, i.e. constant radius. The VR velocity is extracted from a linear fit of the time evolution of the VR x position in the range $[-3, -0.5] l_x$ (Fig. 5.16(a)) and its larger value at higher V_0 is consistent with the smaller radius at higher V_0.

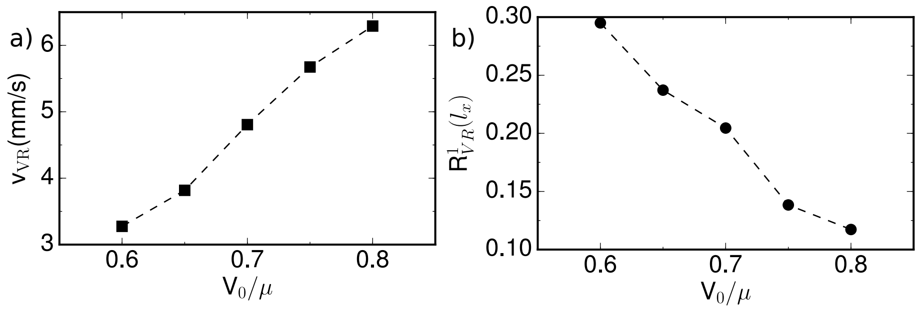

Figure 5.16: (a) The first VR propagation velocity for different barrier heights and (b) the VR mean radius at the position when the TF radius is maximum. The data are for fixed $z_0 = 0.19$.

For $V_0/\mu \geq 0.8$, the energy of the vortex ring is insufficient to overcome the barrier and thus it shrinks within the barrier itself. This behaviour is evident in Fig. 5.14 (bottom), which shows x_{VR} remaining close to 0 (the motion of the vortex ring towards negative x_{VR} being too slow to be noticeable on this scale): for $0.8 < V_0/\mu \leq 1$ the vortex ring fails to reach the edge of the barrier $x \sim -0.55 l_x$, and so decays before entering the left superfluid.

5.5.2 Energetic consideration

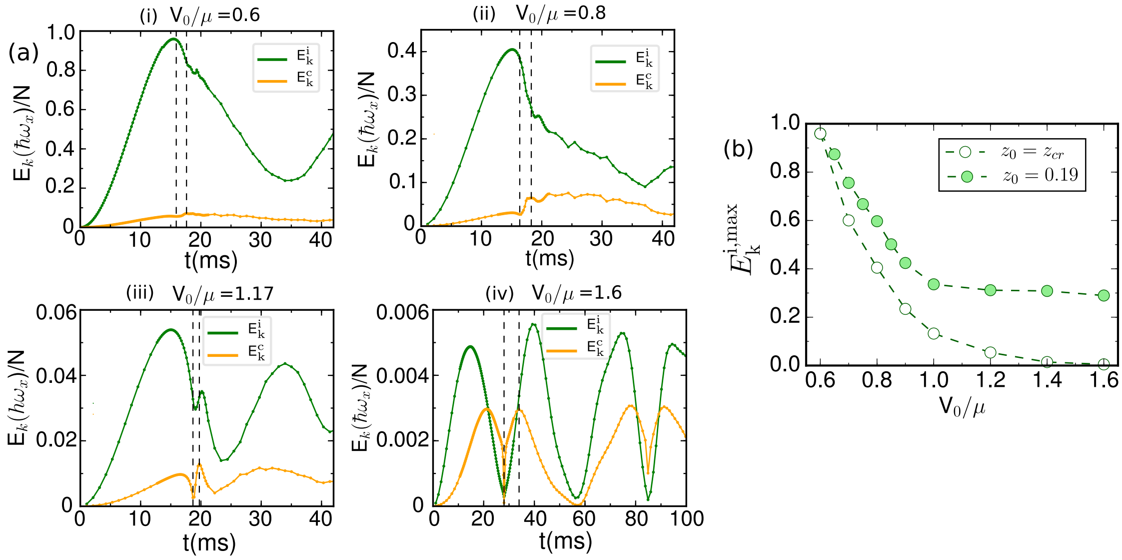

Figure 5.17: (a) The time evolution of the incompressible E_k^i (green) and compressible E_k^c (orange) kinetic energy for $z_0 = z_{\mathrm{cr}}(V_0/\mu)$ and (i) $V_0/\mu = 0.6$, (ii) $V_0/\mu = 0.8$, (iii) $V_0/\mu = 1.17$, (iv) $V_0/\mu = 1.6$. The vertical dashed black lines mark the boundaries of the time intervals during which E_k^c has a step-like increase, labelled here as $\Delta E_k^c = \epsilon_c$. (b) The dependence of the maximum value of E_k^i on the barrier height V_0/μ for $z_0 = z_{\mathrm{cr}}(V_0/\mu)$ (hollow circles) and $z_0 = 0.19$ (filled circles), for fixed $w/\xi = 4$.

Having identified the parameter regime of vortex ring generation, and characterised their dynamics, we now provide information about the energy which gives insight into the observed dynamics. Building on our earlier analysis [90] and Chapt. 3, we decompose the total energy of the BEC into potential, interaction, quantum and kinetic contributions. We concentrate our attention on the compressible and incompressible kinetic energy components, which are defined in Sect. 3.5.4. We focus initially on the case $z_0 = z_{\mathrm{cr}}$, and calculate the time evolution of these contributions for different values of $V_0/\mu \in [0.6, 1.6]$, with our results shown in Fig. 5.17(a). This enables us to extract, for each V_0/μ, the maximum value of E_k^i, whose dependence on V_0/μ is shown by the hollow points in Fig. 5.17(b).

For completeness, this plot also shows the corresponding E_k^i maxima for the fixed $z_0 = 0.19$ case (filled points). In both cases, we clearly observe that the maximum values of E_k^i decrease with increasing V_0/μ. The energy of the vortex ring stems from the E_k^i of the flow: hence the larger E_k^i, the larger the available energy for the vortex ring. This effect is visible in Fig. 5.14(a(i), b(i))-5.16.

Until now we have been concerned with the vortex nucleation and its motion, in particular whether it can go beyond the barrier. Now we focus on the energy dissipated by

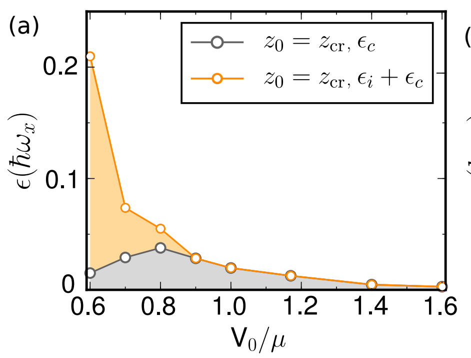

Figure 5.18: Compressible energy dissipation ϵ_c (grey circles) in the time interval bounded by the two vertical black lines in Fig. 5.17, and total energy dissipation $\epsilon_{tot} = \epsilon_c + \epsilon_i$ (orange circles) as a function of V_0/μ, for fixed $w/\xi = 4$ and for (a) $z_0 = z_{\rm cr}(V_0/\mu)$ and (b) $z_0 = 0.19$.

the vortex.

For small values of V_0/μ ($V_0/\mu \leq 0.8$), the vortex overcomes the barrier and some energy of the Josephson oscillation is turned into (incompressible kinetic) energy of the vortex ring. In addition, acoustic emission takes place when the vortex, nucleated in the barrier region outside the condensate, enters a region of higher density [90]. For $V_0/\mu > 0.8$ the vortex shrinks and vanishes within the barrier, as illustrated in Fig. 5.14 (a(i), b(i)): its incompressible kinetic energy is transformed in compressible kinetic energy (sound waves). To better characterize the compressible dissipation ϵ_c, we calculate the

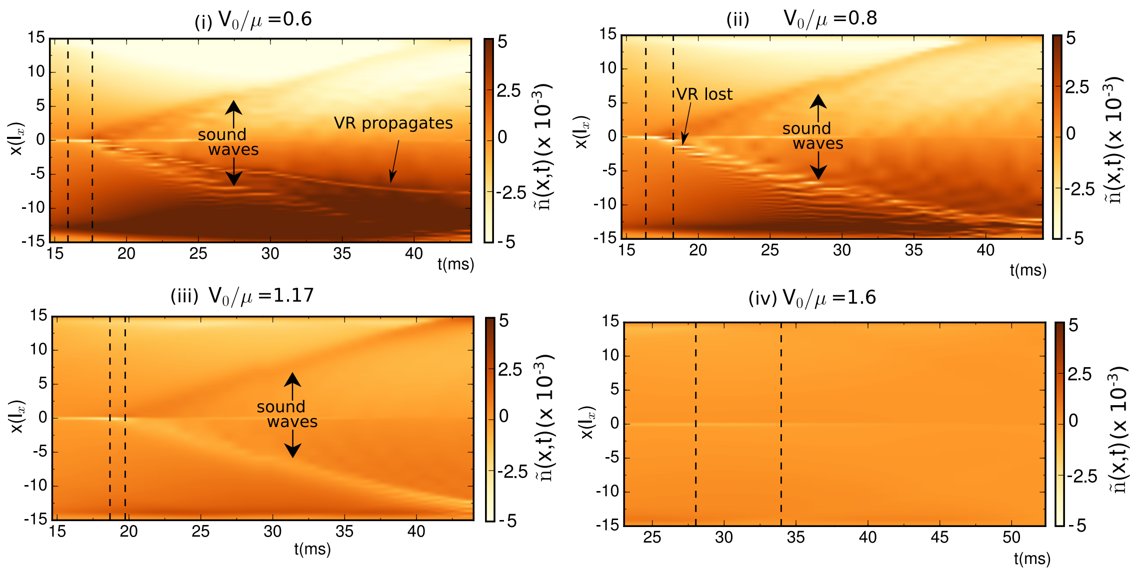

Figure 5.19: Carpet plots of renormalised density $\tilde{n}(x,t)$ for $z_0 = z_{cr}$ and (i) $V_0/\mu = 0.6$, (ii) $V_0/\mu = 0.8$, (iii) $V_0/\mu = 1.17$ and (iv) $V_0/\mu = 1.6$, for fixed $w/\xi = 4$. Vertical dashed lines bound the time intervals between which the compressible kinetic energy is measured, and correspond to those shown in Fig. 5.17(a)(i)-(iv).

corresponding *change* in the compressible kinetic energy, ΔE_k^c, experienced during the nucleation and early-stage dynamics of the vortex ring [90] (also shown in Chapt. 3) this time interval corresponds to the region between the two vertical dashed lines in panel (a)(i)-(iv). We identify this change in compressible energy with the compressible dissipation, *i.e.* $\epsilon_c = \Delta E_k^c$. We observe a local maximum of ϵ_c at $V_0/\mu = 0.8$ for both $z_0 = z_{cr}$ and $z_0 = 0.19$, as it is evident from the grey circles (and corresponding grey-shaded region) in Fig. 5.18 panels (a)-(b).

As for the incompressible dissipation ϵ_i, we define it as the incompressible kinetic energy density integrated in a small volume [4] (as described in Chapt. 3) surrounding the vortex ring when $x_{\mathrm{VR}} \simeq -l_x$. We choose this value of x_{VR} as here the velocity of the Josephson flow is negligible and hence the calculated incompressible kinetic energy stems only from the vortex. When applying this definition of ϵ_i to our system, we observe that the incompressible energy of the vortex ring increases as V_0/μ decreases. This is consistent with the features illustrated in all panels of Fig. 5.14-5.16. If we combine the behaviour of ϵ_i and ϵ_c, we find a monotonic decrease of $\epsilon_{tot} = \epsilon_i + \epsilon_c$ with V_0/μ over the entire probed range [0.6, 1.6] for both $z_0 = z_{cr}$ [Fig. 5.18 (a)] and $z_0 = 0.19$ [Fig. 5.18 (b)]. It must be noted that for $z_0 = z_{cr}$ and $V_0/\mu = 0.8$ the vortex ring goes beyond the barrier but shrinks to zero and vanishes before reaching $x_{\mathrm{VR}} \simeq -l_x$ (where its incompressible dissipation would have been defined): its incompressible energy is totally turned into sound immediately after entering the condensate. In this circumstance, to determine ϵ_c we also consider the second step-like increase of compressible energy which is observable in Fig. 5.17 (a,ii) at $t \sim 20$ ms.

In summary, our analysis demonstrates that for high barrier heights ($1 \leq V_0/\mu < 1.6$), the dominant dissipation mechanism is not the propagation of the vortex ring *per se*, but instead the sound waves generated by the vanishing vortex ring. To illustrate this effect graphically, Fig. 5.19 shows 'carpet plots' of the renormalised density $\tilde{n}$ along the x direction at four different characteristic values of V_0/μ for the case $z_0 = z_{cr}$. In these plots, the density $\tilde{n}$ is evaluated by subtracting from the instantaneous density along x (for $y = z = 0$), its background (equilibrium) value, *i.e.* $\tilde{n}(x,t) = n_x(x,t) - n_x(x,0)$ in units of $(1/l_x^3)$. Subplots (i)-(iii) show clearly the propagation of sound waves in both the negative and positive x-directions for $V_0/\mu \leq 1.2$. Subplot (i) also shows the presence of a slower moving feature, the vortex ring propagating along the negative x axis until -7.5 l_x, consistent with the vortex motion shown earlier in Fig. 5.14(a)-(ii). This vortex propagation can also be observed in Fig. 5.19(b) but only at early times, as in this case the vortex ring vanishes rather rapidly, at $t \sim 18$ ms. The vortex ring is absent in the subplots (iii),(iv) of Fig. 5.19: specifically, in subplot (iii) we observe only the propagating sound waves while in (iv), corresponding to the self-trapped regime, the density oscillations are

[4] This calculation was performed by one of my collaborators, Dr. Luca Galantucci.

barely visible.

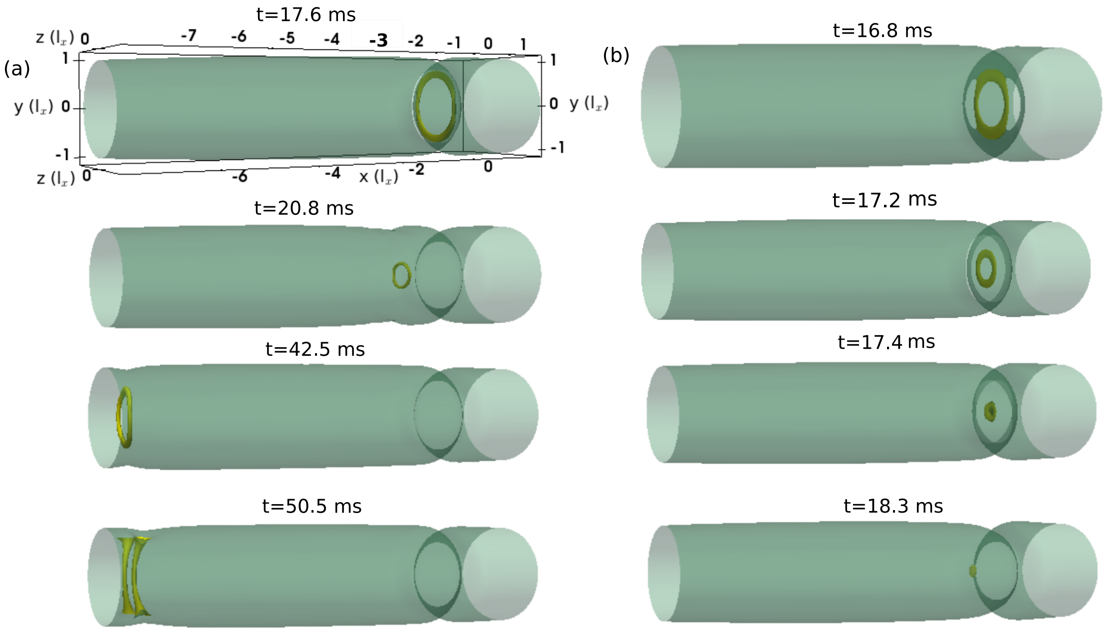

Figure 5.20: Snapshots of the three-dimensional isosurface density plots depicting the vortex ring generation and evolution for (a) $V_0/\mu = 0.6$ and (b) $V_0/\mu = 0.8$, taken at $z_0 = z_{cr}(V_0/\mu)$ and $w/\xi = 4$. Note the different evolution times in the two cases.

To clarify the vortex ring dynamics and, in particular, highlight the difference between $V_0/\mu = 0.6$ [Fig. 5.19(i)] and $V_0/\mu = 0.8$ [Fig. 5.19(ii)], Fig. 5.20 depicts the corresponding 3D density isosurface plots. While for $V_0/\mu = 0.6$ [Fig. 5.20(a)] the vortex ring propagates significantly along the negative x axis until $x_{\rm VR} \sim -8l_x$, eventually breaking into two vortex lines when it reaches the boundary, for the slightly higher $V_0/\mu = 0.8$ the vortex ring shrinks and vanishes before reaching $x_{\rm VR} \sim -1l_x$.

These results complete our study of the microscopic differences between the dissipative regime for $0.6 \leq V_0/\mu \leq 1.17$ and the pure self-trapped regime at $V_0/\mu = 1.6$.

5.6 Fixed z_0 Crossover due to Variable Barrier Height/Width

The evolution of $z(t)$ at fixed initial population imbalance z_0 as the system transits from Josephson plasma to dissipative and then to self-trapped regimes is shown in Fig. 5.21 by increasing either (a) V_0/μ at fixed $w/\xi = 4$, or (b) w/ξ at fixed $V_0/\mu = 1.17$. This corresponds to horizontally traversing the phase diagram of, respectively, Figs. 5.1 and 5.11.

In both plots we see a clear transition from Josephson plasma oscillations (blue), to a dissipative regime (purple plots), followed by a rather complicated transition to a self-

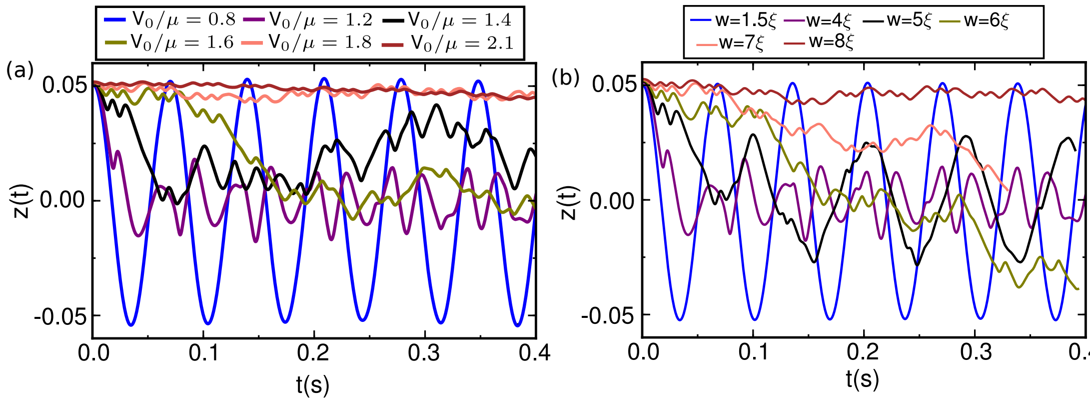

Figure 5.21: Temporal evolution of the population imbalance, $z(t)$, for fixed initial imbalance z_0: Shown are the cases of (a) fixed $w/\xi = 4$ and variable V_0/μ; and (b) fixed $V_0/\mu = 1.17$ and variable w/ξ.

trapped state. Due to the previously identified dependence of z_{cr} on V_0/μ (largely related to the profile of the maximum current versus V_0/μ found by considering first and second order terms in the tunneling Hamiltonian [90] which is also described in Chapt. 3), a simple inspection of the phase diagram of Figs. 5.1 and 5.11 reveals that such horizontal cuts through the phase diagrams imply that the system will enter the self-trapped regime with a value of $z_0 \gg z_{cr}$, such that we do not expect to observe the emergence of the pure self-trapped regime, but rather the multi-frequency self-trapped state analyzed below.

In fact, the imbalance for $V_0/\mu = 1.8$ in the first case of fixed $w/\xi = 4$ and the imbalance for $w/\xi = 8$ in the second case of fixed V_0/μ shows similar profile where there is almost no decay in time of $z(t)$, which oscillates around a non-zero mean value with complicated profiles and multi-modes; a feature characteristic of self-trapped states for $z_0 \gg z_{cr}$. We thus define these values as the first barrier height and width value at which there is the onset of self-trapped states without the slow-decay in time (for fixed $z_0 = 0.05$) and we term them V_0^{ST} in the first case and w^{ST} in the second case. For $V_0/\mu = 2.1$ at fixed $w/\xi = 4$ the value of $(z_0 - z_{cr}(V_0/\mu = 2.1))$ is even larger and thus the $z(t)$ oscillates with many modes and reduced amplitude (appearing almost flatten). These features are consistent with the description of the self-trapped states given in Sect. 5.1.2.

Thus, these two subplots reveal the complicated intermediate region for large $z_0 > z_{cr}$ when the system transitions from the dissipative to the self-trapped regime, i.e. the transition from the blue to the red regions in Figs. 5.1 and 5.11 respectively.

We note that for all the cases of barrier heights and widths explored in this section, the VRs are 'ghost' vortices, in the sense that they do not enter the condesate density. For this reason the main differences between the dissipative and self-trapped states are given in terms of the incompressible and compressible kinetic energy. In fact, from the time profile of $E_k^i(t)$ and $E_k^c(t)$, we retrieve the maximum value of the first called $E_k^{i,max}$ (as previously done) and the step-like increase value of the second termed ΔE_k^c. This is done firstly for fixed $w/\xi = 4$ and is shown in Fig. 5.22. Both $E_k^{i,max}$ and ΔE_k^c decrease as V_0/μ increases, consistent with the results of Fig. 5.17 and Fig. 5.18 for $V_0/\mu \geq 1.17$.

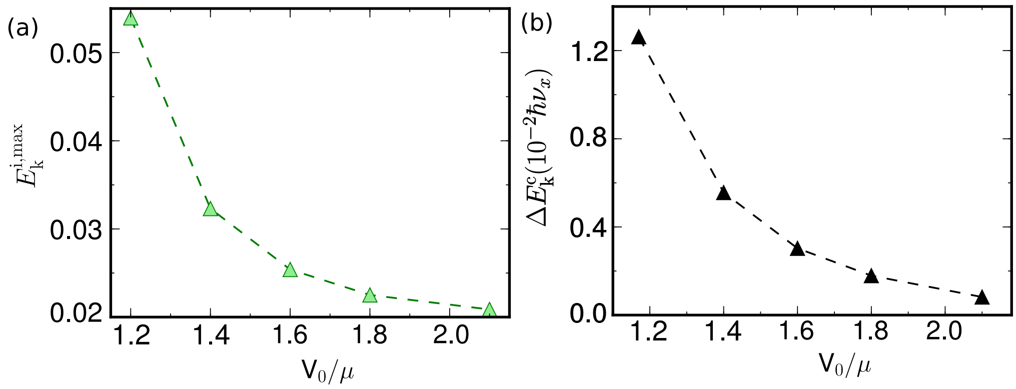

Figure 5.22: The maximum value of the incompressible kinetic energy $E_k^{i,max}$ (a) and the step-like increase of the compressible kinetic energy ΔE_k^c as a function of V_0/μ for fixed $w/\xi = 4$ and fixed $z_0 = 0.05$.

Then for each value of the barrier width at $V_0/\mu = 1.17$ we extract the maximum value of the incompressible kinetic energy in units of $\hbar\omega_x/N$ and we show it in Fig. 5.23. In such plot is shown both the dependence of $E_k^{i,max}$ on V_0/μ in the case of fixed w/ξ (the curve shown also in Fig. 5.22(a)) and the dependence of $E_k^{i,max}$ on w/ξ; the bottom x axis of the plot is V_0/μ and the upper x axes is w/ξ. As the E_k^i corresponds respectively to the kinetic energy of the flow – both potential flow driven by $\nabla\mu$ and vortex generated swirls– its smaller value as going towards self-trapped regime is consistent with a 'frozen' population dynamics with the right well remaining more populated than the left one in time. This is also related to the picture described in Sect. 5.3 where the effective density becomes smaller as the system enters the self-trapping regime. Such transition to the self-trapped states can be obtained in two different ways; by varying the Gaussian barrier height or its width. Fig. 5.23 shows that these two ways are equivalent obtaining similar profiles of $z(t)$ during the transition. Furthermore, an interesting feature arises from Fig. 5.23 showing that not only the $E_k^{i,max}(V_0/\mu)$ and $E_k^{i,max}(w/\xi)$ profiles are similar but the threshold value of $E_{k,max}^i$ for the onset of the self-trapped regime at V_0^{ST} and at w^{ST} respectively is exactly the same.

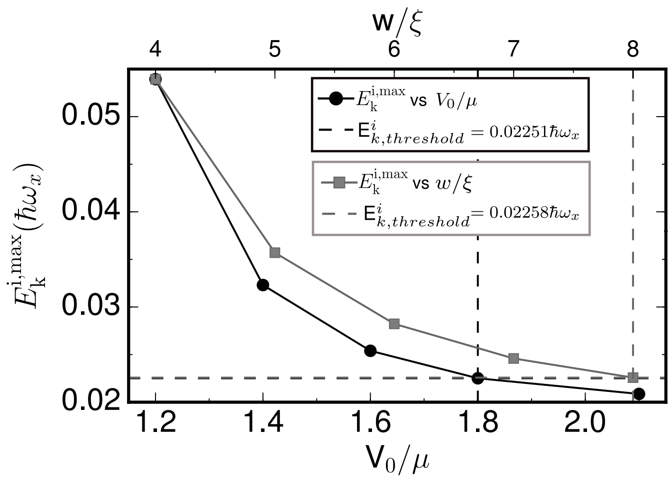

Figure 5.23: The maximum value of the incompressible kinetic energy at different values of the barrier heights for fixed barrier width $w/\xi = 4$ (the bottom x axis) and at different barrier width for fixed barrier heights $V_0/\mu = 1.17$ (the upper x axis). The dashed vertical and horizontal black (grey) line show the value of the V_0^{ST} (w^{ST}) and its corresponding value of $E_k^{i,max}$ labelled as the threshold energy for obtaining self-trapped states $E^i_{k,threshold}$.

5.7 Isotropic Trap

Here we demonstrate the broad relevance of our previously characterized phase diagram showing the emergence of different dynamical regime by performing the same analysis in the context of an isotropic (spherical) trap. For the spherical trap, the presence of the Josephson 'plasma' and MQST regime is already observed and studied in [42, 83]. In this section we will show that, in the 3D spherical trap, a dissipative regime can also be found in which $z(t)$ and vortex ring dynamics show similar features as for the elongated trap.

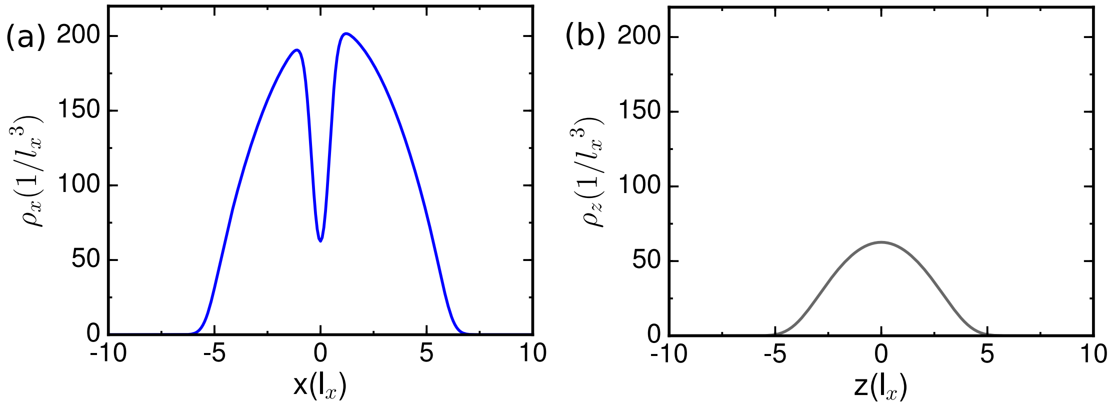

Figure 5.24: The density profile along (a) x-direction for $y = z = 0$ and the density profile along (b) z-direction for $x = y = 0$ at equilibrium for the spherical trap at $V_0/\mu = 0.9$, $w/\xi = 4$ and $z_0 = 0.15$. The density is shown in units of $1/{l_x}^3$ with $l_x = 7.5\mu m$.

To make a connection with the features already studied earlier, we keep the condensate number fixed to 60,000, and all three harmonic trap frequencies are fixed to the previously used $\omega_x = 2\pi \times 15$Hz. We thus set $\omega_y = \omega_z = \omega_x = 2\pi \times 15$ Hz which (for N=60,000) gives $\mu = 17\hbar\omega_x$ and $\xi = 1.3\mu m \simeq 0.17 l_x$. The grid size we choose is 10x10x10 with a number of grid points 128x128x256 along y,z and x axes respectively. Thus $\Delta x/\xi = 0.45$ and $dy/\xi = dz/\xi = 0.9$. The barrier width is kept fixed at four times the mean healing length, i.e. $w = 4\xi \simeq 0.68 l_x$ while the barrier height is changed in the range $[0.6, 1.8]$. Fig. 5.24 shows an example of the density plot along x- direction for $y = z = 0$ (a) and along z-direction for $x = y = 0$ (b). The Thomas-Fermi radius value for the spherical trap $R_{TF,spher}$ is around $5l_x$ along all the directions, being slightly larger along the x axis due to the presence of the barrier and the population imbalance between the two-wells. Referring back to the elongated trap, described in Sec. 3.1, the condensate extension along the x axis is smaller in the case of the isotropic trap. Contrary to this, the transverse condensate size is larger for the spherical trap. Furthermore the ratio of barrier width to the axial condensate extension, i.e. $(w/R_{TF,x})$, is such that $(w/R_{TF,x})_{spher} > (w/R_{TF,x})_{elong}$. Such differences would be the reason for obtaining different critical imbalance, as will be shown later, for the spherical and elongated trap even when V_0/μ and w/ξ are the same.

5.7.1 Characterization of Dynamical Regime Crossover for the Isotropic Trap

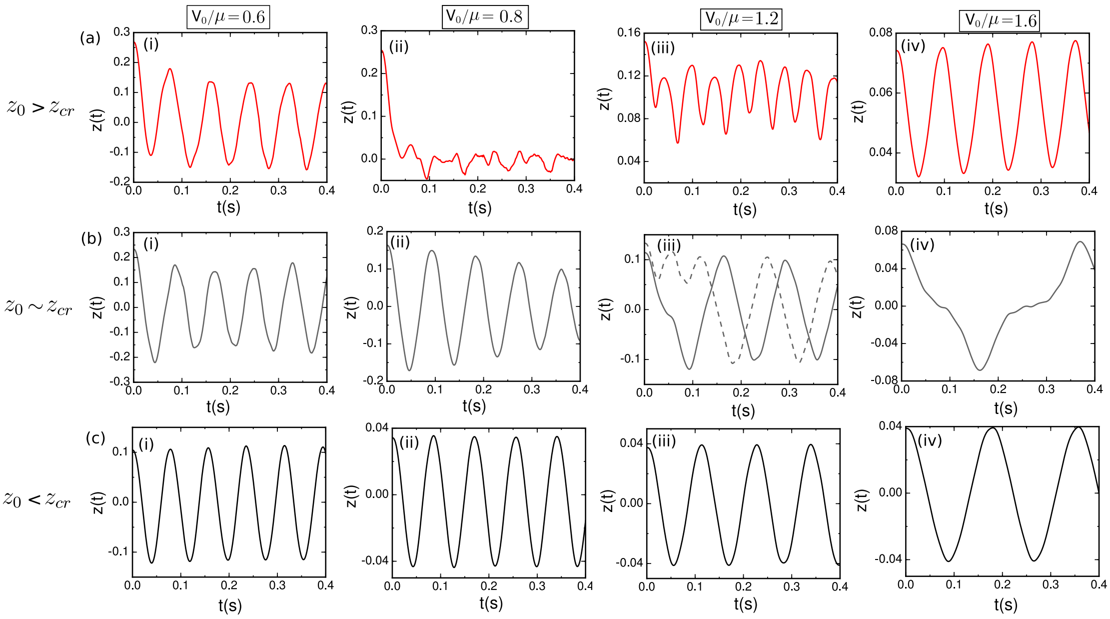

Figure 5.25: Dependence of the temporal evolution of the population imbalance in an isotropic trap on different values of $z_0/z_{\rm cr}$ and V_0/μ at fixed $w/\xi = 4$, corresponding to the following phase diagram of Fig. 5.26.

Fig. 5.25 shows the complex dependence of the evolution of $z(t)$ for barriers with $w/\xi = 4$ and different values of the parameters z_0/z_{cr} (increasing from bottom to top) and V_0/μ (increasing from left to right). Overall we find similar features to the corresponding figure for the elongated trap [Fig. 5.10]. This demonstrates the broad applicability of our findings.

In particular, in all the cases if $z_0 < z_{cr}$, $z(t)$ oscillates around zero mean value exhibiting Josephson 'plasma' oscillations, i.e. single-frequency dominated harmonic oscillation of $z(t)$ around zero value. The $z(t)$ oscillations frequency becomes smaller as V_0 is increased (as observed from Fig. 5.25 (a)) due to the reduced tunneling energy value. For values $z_0 \geq z_{cr}$ one instead transitions to either a dissipative regime ($V_0/\mu \lesssim 1.0$), or a self-trapped regime ($V_0/\mu \geq 1.2$), with a crossover occuring at intermediate values of V_0/μ. In fact, the transition to the self-trapped regime is found to occur for $V_0/\mu \geq 1.2$, i.e. at a slightly smaller value of V_0/μ with respect to the elongated trap (where it emerged around $V_0/\mu = 1.6$ for the same $w/\xi = 4$). In the dissipative regime, in Fig. 5.25 (a)-(ii), $z(t)$ shows similar profile as for the elongated trap, decaying initially fast in time and then oscillating around zero-mean value with several frequencies. However, in the dissipative regime obtained for relatively low barrier height, $V_0/\mu = 0.6$ and $z_0 \gtrsim z_{cr}$, the $z(t)$ shows some new features (as shown in Fig. 5.25 (a)-(i)); it presents a very pronounced 'kink' (which will be analysed more later) at the time interval between 0.03s and 0.1s.

Between the Josephson 'plasma' and dissipative/MQST regime exists an intermediate regime with some examples shown in Fig. 5.25 (b). For $V_0/\mu \gtrsim 1.2$ the intermediate regime consists of an MQST state which decays within 0.4 s (as shown in Fig. 5.25(b)-(iii)) or to a high amplitude anharmonic regime [5], as shown in Fig. 5.25(b)-(iii)-(iv). For the dissipative regime, in the example of Fig. 5.25(b)-(i), the $z(t)$ amplitude of the second local maxima is smaller than z_0 but there are only sound waves that propagate in the system. In Fig. 5.25 (b)-(ii) instead, the amplitude of oscillations seems to decay in time, for long time evolution. A more detailed analysis, and evolution over a longer time, shows in fact that the system does not present damping but beating between the Josephson 'plasma' frequency $\nu_J = 11.8$Hz and another mode (at around 10 Hz) (for $z_0 \lesssim z_{cr}$). This could be attributed to enhanced coupling of the Josephson plasma oscillations to other intra-well excitations [2] which is more pronounced in the spherical trap as the Josephson 'plasma' frequency is not much smaller than the trap frequencies.

5.7.2 Phase diagram for an isotropic trap

A plot revealing the emergence of the different dynamical regimes for variable z_0 as a function of $V_0/\mu \in [0.6, 1.8]$ (similar to that of Fig. 5.1) is shown in Fig. 5.26 which summarizes the results described in the previous section. The important main conclusion arising from this figure is that – despite huge differences in the values of z_{cr} in relation to the elongated phase diagram of Fig. 5.1 – qualitatively we recover the same picture. For z_0 smaller than a threshold value the system is in the Josephson plasma regime. As z_0 increases it can even transits in the dissipative or self-trapped regime depending on the value of V_0/μ. Differently from the elongated trap, the first value of the barrier height in which the onset of pure self-trapping states (for $z_0 = z_{cr}$) is obtained is $V_0/\mu = 1.2$, while in the elongated trap it was obtained for a larger value $V_0/\mu = 1.6$. Importantly, we observe that the critical imbalances for the spherical trap are higher with respect to those previously found in the elongated trap due to the increase of the ratio of the tunneling to self-interaction energy (related to the change in the geometry, i.e. to the different volumes of the condensate in each well and to the different ratio of the barrier width to condensate axial extension).

This parameter choice – which is within experimental reach – significantly increases the values of the population imbalance for which interesting dynamical crossovers can be observed (by about an order of magnitude compared to the small values encountered in the elongated geometry) – thus making the observation of our findings highly experimentally

[5]We note that in such anharmonic regime, and for the spherical trap, we find the presence of rugosities in the zero crossings of $z(t)$ similar to the one described in [83]

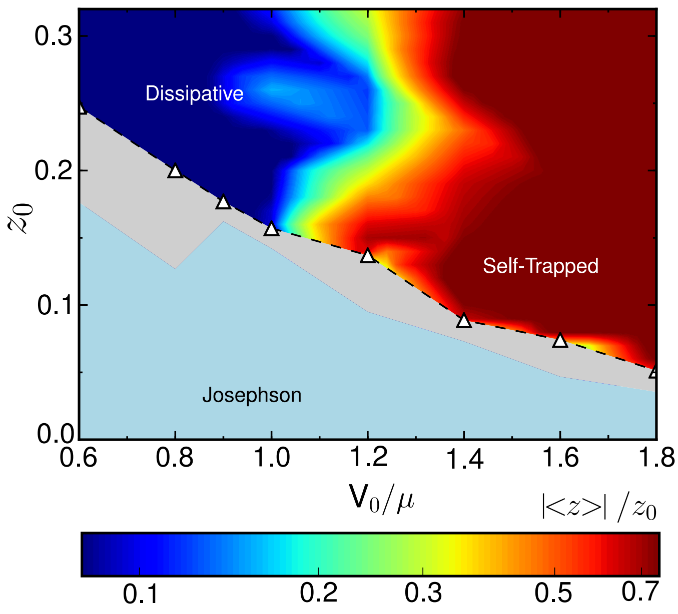

Figure 5.26: Josephson junction phase diagram of dynamical regimes arising across a Gaussian barrier with variable V_0/μ for fixed $w/\xi = 4$ for an isotropic trap. Hollow black triangles show the critical imbalance for the transition from Josephson 'plasma' to the dissipative regime (for $V_0/\mu \leq 1$) and to the MQST regime (for $V_0/\mu \geq 1.2$). Such regimes are characterized by the coloured regions which display the absolute value of $\langle z(t)\rangle/z_0$ where $\langle z(t)\rangle$ is the temporal mean value of $z(t)$ in the time interval [0, 0.4]s; the colormap is in logarithmic scale ranging between 0.08 and 0.75.

relevant.

We also note an interesting additional feature found within the slightly broadened grey-shaded area in this isotropic geometry. Specifically, we have found a narrow range of intermediate values of the population imbalance z_0 (as shown in Fig. 5.25 (b)-(ii)) – located between the low values leading to single-frequency undamped Josephson plasma oscillations, and those generating the transition to the dissipative regime – for which the observed oscillating population imbalances about a zero value can exhibit beating, which could be attributed to enhanced coupling of the Josephson plasma oscillations to intra-well excitations [2]. The further analysis of which goes beyond the scope of this thesis and can be subject of future studies.

Another similar behaviour with the elongated trap regards the vortex ring dynamics which will be the subject of the next following section. We anticipate that even in the spherical trap, for $0.6 \leq V_0/\mu \leq 1$, the vortex ring enters the local Thomas-Fermi surface at the trap center and can eventually propagate axially into the left well, with a lifetime which decreases with increasing barrier height, as found for the elongated trap.

5.8 Vortex rings dynamics

Fig. 5.27 shows the temporal evolution of $z(t)$ for $V_0/\mu = 0.8$ and $z_0 = z_{cr}$. This is a slightly smaller z_0 than the one shown in Fig. 5.25(a)-(ii) for the same barrier height. The pronounced 'kink' of the $z(t)$ starts at the moment the VR enters the local TF surface consistent with the elongated trap results. The reason why for the spherical trap the 'kink' is more pronounced could be related to the fact that the VR stays longer within the barrier. In fact, the VR radius when entering the condensate (as shown in Fig. 5.27(b)) is much larger for the spherical trap as its transverse extension is larger and thus the VR moves slowly. Moreover the barrier is wider.

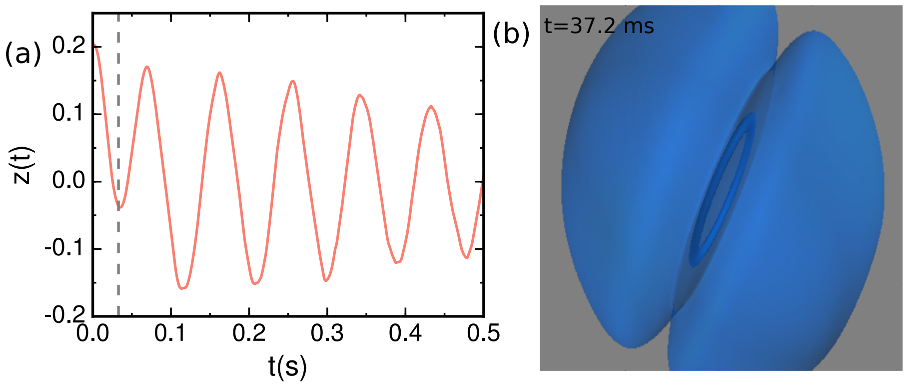

Figure 5.27: The time evolution of the population imbalance for the spherical trap at $V_0/\mu = 0.8$, $w/\xi = 4$ and $z_0 = z_{cr}$, with the vertical grey dashed line indicating the moment the VR enter the TF surface $t = 35$ms. (b) Three dimensional isocontour surface density at 5% of the maximum density at $t = 37.2$ms.

Fig. 5.28 shows the VR radius and x axis position (x_{VR}) time evolution for $V_0/\mu = 0.8$ and for $V_0/\mu = 1$ at $z_0 \simeq z_{cr}$ together with the transverse TF radius calculated at x_{VR} for $V_0/\mu = 0.8$. The increase of R_{TF} (extracted at x_{VR}) at the end is due to fact that the VR changes the direction of motion as observed from Fig. 5.28(b). As found for the elongated trap, the VR shrinks its radius (after entering the TF surface) due to the increasing density, remaining initially within the barrier (the barrier width is indicated by the horizontal line in Fig. 5.28(b)). When it achieves a certain radius it enters in the left side of the BEC and propagates. The time interval between the time the VR enters the TF surface and the time it leaves the barrier is much larger here with respect to the elongated trap. For $V_0/\mu = 0.8$, the VR continues propagating further in the condensate, but it travels a shorter distance here with respect to the elongated trap; while going towards the edge of the condensate it increases it radius (for $t \geq$63.7 ms) and after that reverses its motion. When the VR radius becomes comparable to the transverse TF radius, the VR does not break into two vortex lines as observed for the elongated trap (as shown in Appendix A); it instead becomes larger than the condensate size moving so at the surface without breaking. For $V_0/\mu \simeq 1$

the VR lives much less with respect to the VR for $V_0/\mu = 0.8$ being consistent with our findings for the elongated trap. Moreover, after leaving the barrier, the VR disappears almost immediately in rarefaction pulses for $V_0/\mu \simeq 1$. In the elongated trap instead the VR for $V_0/\mu \simeq 1$ disappears within the barrier. We find such behaviour for $V_0/\mu = 1.1$ for the spherical trap.

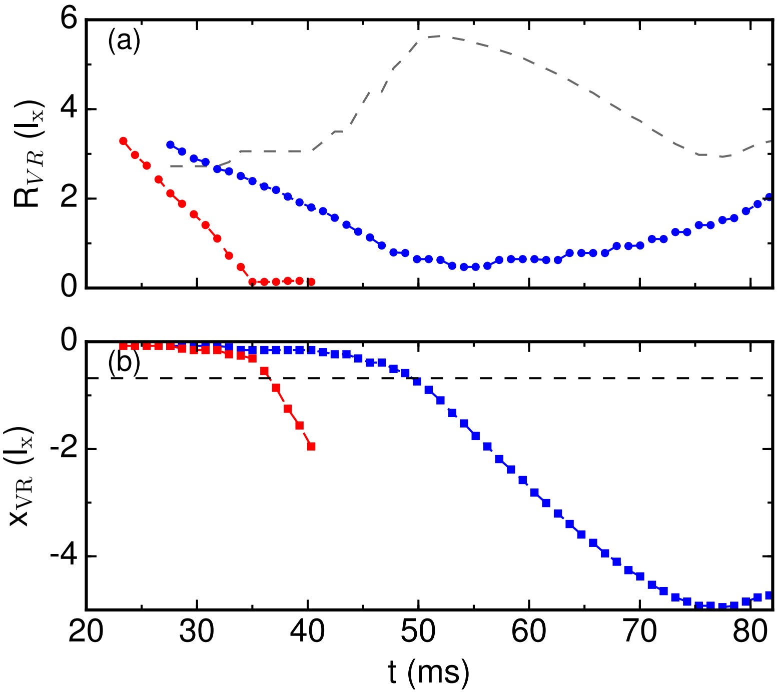

Figure 5.28: Evolution of (a) VR mean radius R_{VR} and (b) its x axis position x_{VR} for the spherical trap for $V_0/\mu = 0.8$ and $V_0/\mu = 1$ at fixed $w/\xi = 4$ for $z_0 = z_{cr}$. The horizontal dashed line indicates the barrier width while the grey dashed line in (a) shows the calculated transverse Thomas-Fermi radius at x_{VR} for $V_0/\mu = 0.8$.

5.9 Conclusions and future work

We have characterised the full phase diagram describing the dynamical regimes that can emerge across a Josephson junction created by a Gaussian barrier: Josephson plasma, self-trapping, and dissipative. Our analysis in this chapter bridges the gap between numerous previous studies depicting either a transition from Josephson plasma to macroscopic quantum self-trapping, or Josephson plasma to dissipative regimes.

As expected, we have found the existence of undamped symmetric Josephson plasma oscillations for initial population imbalances below their corresponding critical values. Increasing the initial population imbalance across the barrier leads to a transition to a different regime, which depends on a specific combination of barrier height and width.

Specifically, for relatively large barrier heights/widths, the system transits to a self-trapped state. Once the population imbalance exceeds a critical value, it exhibits the established macroscopic quantum self-trapping regime, which features regular symmetric oscillations about a non-zero value, and a running relative phase, whereas increasing the initial population imbalance much beyond that value leads to more complicated self-trapped states with oscillations at multiple frequencies. In the other extreme of small barrier widths/heights, the system transits – with increasing z_0 – to a dissipative regime, where the emission of acoustic (sound) energy and the generation and propagation of vortex rings take place, a distinctive feature associated with phase-slips known in other physical systems with Josephson junctions, and leading to the resistive superflow. The critical value of z_0 for which dissipative behaviour is observed is always larger than the corresponding one when the system transitions (for a higher/broader barrier) to the self-trapped regime as the tunneling energy becomes smaller.

We showed that for elongated traps such as the ones studied in [49, 20], where only the transition from the Josephson plasma regime to the dissipative one was observed, the self-trapping regime can in fact also be observed for higher and wider barriers, thus making concrete predictions which can be experimentally tested. As a counterpart, our result indicated that for traps in which only the transition from the Josephson plasma to the self-trapped regime has been seen (such as [42], which had an aspect ratio ~ 1), the dissipative regime can also be observed by lowering the barrier height (to values slightly below, but still a sizable fraction of, μ). Thus, our work presented in this chapter suggested that for any geometry we can find all three dynamical regimes, and that such regimes should be experimentally observable within a single experimental set-up by careful control of the barrier height or width.

Interestingly we also found – beyond a smooth, and rather irregular, crossover between dissipative and self-trapped regimes – that spherical traps have another regime that should be observable in current experiments, in which the coupling of the Josephson plasma frequency and other collective modes become relevant [2] and can lead to a beating. The latter becomes particularly noticeable as the system begins to transit from the pure single-frequency Josephson to the dissipative regimes. This feature was showed to be more pronounced in spherical geometries, rather than elongated ones, facilitated by the equal trapping frequencies. We showed that the spherical geometry leads to the emergence of such features, and other crossover behaviours, at higher critical population imbalances, which should make such features easier to investigate experimentally.

Our results in this chapter also clarified what distinguishes between the dissipative and macroscopic quantum self-trapping regimes, not just in terms of $z(t)$ and $\phi(t)$, but also in terms of vortex ring dynamics. As V_0/μ increases, the vortex rings go from a regime in which they can propagate (leaving the barrier region), to a regime where they shrink within the barrier. The value of the incompressible kinetic energy that is present in the system defines if the vortex ring leaves the barrier or not. We showed that in the crossover between the self-trapped and dissipative regimes, the main difference comes from sound waves: specifically, in the self-trapped regime (for z_0 values slightly larger than z_{cr})) there are practically no sound waves, while in the dissipative regime such sound waves propagate and make the condensate dissipate.

5.9.1 Towards a universal criterion

The comparison of the results obtained for the elongated trap and the isotropic one showed that the structure of the phase diagram is the same. Nevertheless, despite using rescaled units (e.g., the barrier width w in units of the healing length ξ and the height of the potential V_0 in units of the chemical potential μ), the phase diagrams are not the same, in the sense of exhibiting a dependence on the geometry of the trap itself. Since, from a qualitative point of view, the phase diagram structure depends on how vortex rings propagate, or not, in the bulk, one can draw an analogy (with the differences discussed below) with type-I/type-II superconductors [73]. In these latter systems, the penetration of an external magnetic field into the bulk of the superconducting sample depends on the ratio κ between the penetration depth λ and the healing length ξ: for $\kappa < \kappa_c$ (where κ_c denotes a critical threshold value) there is a perfect screening of the external magnetic field, which is thus unable to enter the sample until the critical magnetic field is reached, while in the opposite case $\kappa > \kappa_c$ a partial penetration of the magnetic field inside the superconductor takes place through vortices [73]. Relevantly for our present discussion, the critical value $\kappa_c = 1/\sqrt{2}$ can be considered universal, i.e. independent of the microscopic details of different superconducting samples. Coming to our case, where the different phases depend on the penetration of the vortex rings in the bulk, one could be tempted to conclude from the type-I/type-II transitions for superconductors that there may exist a combination of parameters which makes the phase diagram independent from the system's microscopic parameters. However, it is known that BECs behave as type-II, in the sense that vortices can penetrate the sample without breaking the superfluidity when under rotation (which is the equivalent to the magnetic field for neutral systems). The reason for such behaviour, as discussed e.g. in Ref. [240], is that they are chargeless and the rotation behaves as a fictitious magnetic field, and not as a *real* one (in contrast to the magnetic field acting on superconductors which is not fictitious).

Since BECs are of type-II, the possibility of vortex rings propagating within the bulk superfluid primarily depends on whether the seeded vortex inside the barrier can exit (overcome the barrier), or not. In turn, this depends sensitively on the details of the junction itself, making non-trivial the possibility to construct suitable rescaled quantities – depending on the parameters of the system – for which the transitions between different regimes would coincide across geometrically different junctions. The previous argument demonstrates the challenges in identifying appropriate dimensionless quantities, but does not show that one cannot in principle construct such suitable rescaled quantities.

In fact, we next present some possible candidates for such universal scaled quantities.

In analogy with superconductos we search for a characteristic length of the system such that it defines the 'transition' from a regime for which the VR leaves the barrier to a regime in which it shrinks within the barrier. In both elongated and spherical traps we found the existence of a critical value of the barrier height V_0^c/μ such that, for $V_0/\mu \geq V_0^c/\mu = 1$ for elongated trap and $V_0/\mu \geq V_0^c/\mu = 1.1$ for the spherical trap, the VR shrinks within the barrier, without entering the bulk (the left condensate). One possible candidate of λ in ultracold atoms can be the value of the healing length at the trap center ξ_0, i.e. at $x = 0$, extracted by the density along x axis (for $y = z = 0$), shown in Fig. 5.29 (a). While the analog of superconductor coherence length can be the value of the healing length extracted at the maximum value of the density ξ_{mean}, i.e. outside the barrier. The ratio of ξ_0 to ξ_{mean} is shown in Fig. 5.29 (b) at each value of the barrier height in the range $[0.6, 1.8]\mu$ for $w/\xi = 4$ and at $z_0 = z_{cr}$ for both the elongated and the spherical trap.

Firstly, we observe that in both cases the value of ξ_0 increases with V_0/μ as it is proportional to the inverse of the square root of the density at the trap center which is a decreasing function of V_0. Next, we observe that the value of the ξ_0 is larger for the spherical trap with respect to the elongated one. The ratio ξ_0/ξ_{mean} instead achieves almost the same values for both traps until $V_0/\mu = 1.2$, and becomes larger for the elongated trap for $V_0/\mu > 1.2$. Interestingly, ξ_0/ξ_{mean} at the characteristic barrier height of $V_0^c/\mu = 1.1$ and $V_0^c/\mu = 1$ for the spherical and elongated trap, respectively have similar values suggesting that it can be a good candidate of the analog of $\kappa = \lambda/\xi$ for ultracold atoms superfluids with the threshold value (the analogue of κ_c) defined by the value $(\xi_0/\xi_{mean})_{spher}(V_0 = 1.1\mu) \simeq (\xi_0/\xi_{mean})_{elong}(V_0 = 1\mu)$.

Furthermore, we note that the first value of V_0/μ at which the imbalance leads to a MQST regime (or pure self-trapped state) is for $V_0^{MQST}/\mu \simeq 1.2$ for the spherical trap and for $V_0^{MQST}/\mu = 1.6$ for the elongated trap. Interestingly from (a) the value of ξ_0 at the $V_0^{MQST}/\mu = 1.6$ for the elongated trap has a similar value as ξ_0 for $V_0^{MQST}/\mu \simeq 1.2$ for the spherical trap. From this argument, it seems that ξ_0 is suitable on defining a threshold for the onset of the MQST regime, such that if ξ_0 is larger than such threshold value, and thus the density at the center is smaller than a threshold value, then the MQST regime is obtained for $z_0 = z_{cr}$.

Finally, we extract the maximum value of the incompressible kinetic energy for each barrier height for both the spherical and elongated trap as shown in Fig. 5.29 (c). In contrast to the ratio ξ_0/ξ_{mean}, the $E_k^{i,max}$ becomes smaller as V_0/μ increases, i.e. as the density decreases for both traps. This is consistent with the fact that the generated

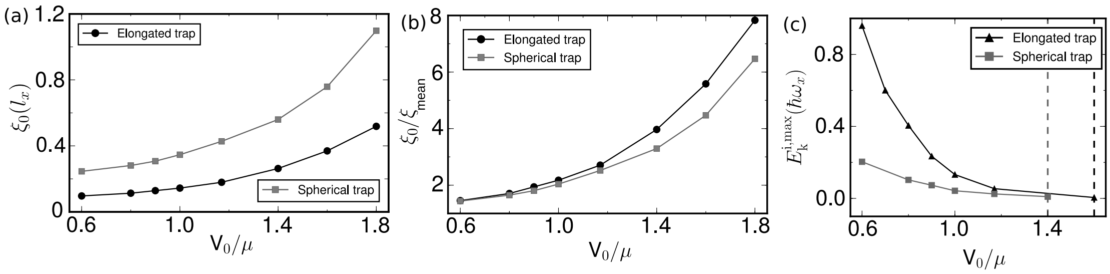

Figure 5.29: (a) Healing length ξ_0 calculated from the density at the center as a function of the barrier height for the elongated trap and for the spherical trap for $w/\xi = 4$ and $z_0 = z_{cr}$. (b) Dependence on the barrier height of the ratio of ξ_0 to the value of ξ_{mean}, calculated from the maximum value of the density. (c) The maximum value of the incompressible kinetic energy E_k^i as a function of the barrier heights for $w/\xi = 4$ for the elongated trap (the black points) and for the spherical trap (the grey points) for $z_0 = z_{cr}(V_0)$ (whose value depends also on the geometry).

vortex rings propagate less into the left condensate as V_0/μ increases until they do not have enough kinetic energy to leave the barrier. Such VR kinetic energy threshold is related to the value of the $E_k^{i,max}$ available in the system. Moreover, the $E_k^{i,max}$ value at $V_0^c/\mu = 1.1$ for the spherical trap is near to the value at $V_0^c/\mu = 1$ for the elongated trap and such value defines the threshold incompressible kinetic energy value $E_k^{i,threshold}$ for the propagation or not of the VR. In fact, for $V_0/\mu < V_0^c/\mu$ the $E_k^{i,max} > E_k^{i,threshold}$ and thus the VR has sufficient energy to overcome the barrier and to propagate further into the condensate.

Moreover, a second threshold of $E_k^{i,max}$ defines the onset of the MQST regime which achieves smaller values than the one for the propagation or not of VRs. It is defined by the value of $E_k^{i,max}$ for $V_0/\mu \simeq 1.2$ for the spherical trap and $V_0/\mu \simeq 1.6$ for the elongated trap which are comparable.

The results presented in this section are not conclusive and further future studies are required for the determination of universal scaled quantities which defines the 'transition' from a regime when VRs propagate to a regime when VRs disappear within the barrier or/and the transition from the dissipative to the self-trapped regime.

Part IV

Finite temperature effects

Chapter 6

Bose-Einstein condensates at finite temperature in an atomic Josephson-junction

In this chapter we show the effect of the thermal cloud on the condensate dynamics across a Gaussian barrier for the elongated Josephson junction of Ref. [49, 20], in the limit of molecular BEC. In particular, the role of thermal dissipation is studied for the three main dynamical regimes found at $T = 0$ in Chapt. 3 and Chapt. 5: Josephson 'plasma', vortex-induced dissipative (called only dissipative regime in Chapt. 3 to Chapt. 5) and pure self-trapped or MQST regimes. In order to model the finite temperature Bose gas we use the Zaremba-Nikuni-Griffin model, in which a generalized GPE describing the condensate evolution is solved self-consistently with a Quantum Boltzmann equation (QBE) describing the thermal cloud dynamics. Firstly, we perform our studies in the collisionless limit which neither includes the particle exchange between the condensate and thermal cloud due to collisions (C_{12}), nor considers the collision term within the thermal cloud (C_{22}). In the collisionless limit, the coupling comes from the presence of the thermal cloud mean field potential in the generalized GPE and viceversa (the presence of the condensate mean field potential in the QBE). The range of the temperature considered here is $[0.1, 0.7]T_c$.

In this chapter we mainly focus on the case of fixing the condensate number when comparing different temperatures as this ensures a fixed $R_{TF,x}/\xi$, where $R_{TF,x}$ is the Thomas-Fermi radius of the condensate in the axial direction. As the temperature is increased, the total atom number also increases and thus the same happens to the critical temperature, which is a function of N_{tot}.

After introducing the modelling scheme in Sect. 6.1, we next show the effect of the thermal cloud on the critical population imbalance for the onset of the vortex-induced dissipative and self-trapping regimes in Sect. 6.2. We then perform a detailed analysis of the effect of the thermal cloud on the Josephson 'plasma' and on the vortex-induced dissipative regimes in Sect. 6.3 and Sect. 6.4. In particular, we study the dependence on the temperature of the condensate/total/thermal population imbalance main frequencies, corresponding damping rates and initial phase of each component on the temperature. The dominant frequencies identified are the Josephson plasma frequency, its second order contributions, and a characteristic frequency of the thermal cloud, which is close to the underlying x axis harmonic trap frequency. We show that these frequencies are relevant in both the Josephson plasma and the dissipative regimes, but their relative contribution within each regime depends on the value of $V_0/(k_B T)$. Moreover we show that in the limit of high temperature the total population imbalance exhibits beating and damping.

Next, we study the effect of the thermal cloud on the MQST regime in Sect. 6.5. Ref. [65, 60, 2, 208, 63] showed that at finite temperature, the presence of the thermal cloud destroys the self-trapping state. Here, we show that not only the MQST regime is destroyed at relatively low temperature, but also that its decay time could differ from run to run. Thus it is necessary that the results are obtained from the average of several runs. Then we show the dependence of the MQST decay time on the temperature. In experiments, one typically works with an approximately constant total (rather than condensate) atom number. This means that at different T the condensate number is different too. In Sect. 6.6 we shortly show that by changing the temperature at fixed total number the condensate dynamics can undergo a transition to different dynamical regimes.

Next, we consider the effect of all collisional terms in all the three dynamical regimes (Sect. 6.7). Specifically, the effect of collisions on the condensate and total imbalance oscillation frequency is shown, both in the Josephson and vortex-induced dissipative regime. Furthermore, we study the effect of collisions on the decay time of the MQST regime. The results of this chapter form the basis of another intended publication [241], which is due to be submitted soon for publication.

In chapt. 3 we showed that at $T = 0$, vortex rings are generated when the superfluid velocity across the junction exceeds a critical value. At finite temperature the thermal cloud fills the vortex ring core and affects its dynamics. In fact, in Sect. 6.8 we consider the effect of the thermal cloud not only on the VR nucleation process but also on its long time evolution. In chapt. 4 such study was performed at $T \simeq 0.4T_c$; here we explore higher temperatures and both, the collisionless and collisional limit. The end of the chapter (Sect. 6.9) outlines our key conclusions and discusses possible future investigations.

6.1 Modelling Scheme Details

Below, we give a brief summary of the kinetic model used mostly in this chapter, which corresponds to the collisionless limit of the ZNG formalism described in more details in

Sect. 2.5:

At finite temperature, the system wavefunction is written as the sum of the condensate wavefunction and the non-condensate (thermal cloud in our case) wavefunction. The condensate wavefunction evolution is found by solving the generalized GPE Eq. (2.92), where the source term is $R = 0$ in the collisionless limit, expressed as:

$$i\hbar\frac{\partial\psi}{\partial t} = \left[-\frac{\hbar^2\nabla^2}{2M} + V_{\rm trap} + g(|\psi|^2 + 2n_{\rm th})\right]\psi \ , \tag{6.1}$$

which accounts for the thermal cloud mean field potential $2gn_{\rm th}$ [28] where $n_{\rm th}$ is the thermal cloud density. The latter is determined through $n_{th} = 1/(2\pi\hbar)^3 \int d\vec{p}\ f(\vec{p}, \vec{r}, t)$, where the phase-space distribution f satisfies the collisionless Boltzmann equation

$$\frac{\partial f}{\partial t} + \frac{\vec{p}}{M}\cdot\nabla_{\vec{r}} f - \nabla_{\vec{r}} V_{eff}\cdot\nabla_{\vec{p}} f = 0, \tag{6.2}$$

with $V_{eff} = V_{\rm trap} + 2g(|\psi|^2 + n_{th})$ the generalized mean-field potential felt by the thermal particles. In our case M is the mass of molecules of lithium, $V_{\rm trap}$ is the double-well potential defined above, $g = 4\pi\hbar^2 a_M/M$ is the interaction strength with a_M the s-wave scattering length between molecules. We recall here that the V_{trap} in our Josephson junction, defined in Eq. (3.3), is expressed as

$$V_{\rm trap}(x, y, z) = \frac{1}{2}M({\omega_x}^2x^2 + {\omega_y}^2y^2 + {\omega_z}^2z^2) + V_0\cdot e^{-2x^2/w^2}, \tag{6.3}$$

where the trapping frequencies are the same as the ones defined in Sect. 3.1. The Gaussian barrier, separating the two wells, has a fixed $1/e^2$ width of $w/\xi \simeq 4$ with variable barrier height. Our numerical study is conducted in a grid of $[-24, 24]\,l_x, [-4, 4]\,l_x, [-4, 4]\,l_x$ along the x, y and z directions respectively (based on $1024\times64\times64$ grid points for the condensate) and a grid that it is the double of the condensate grid (also the double of the number of the grid points) for the thermal cloud in order to capture the entire thermal cloud surrounding the condensate. The equilibrium condensate and the thermal cloud densities are found in an external potential $V_{ext} = V_{trap} - \epsilon x$ with the linear tilted potential along the x axes added in order to create an initial condensate (as also described in Sect. 3.1) and thermal cloud population imbalance across the junction. In fact the linear potential increases the potential minimum of one well with respect to the other and thus one of the well becomes more populated than the other. In our case of $\epsilon > 0$, the condensate number is larger in the right well than in the left well.

The equilibrium condensate density ψ_0 is obtained self-consistently via Eq. (2.104)

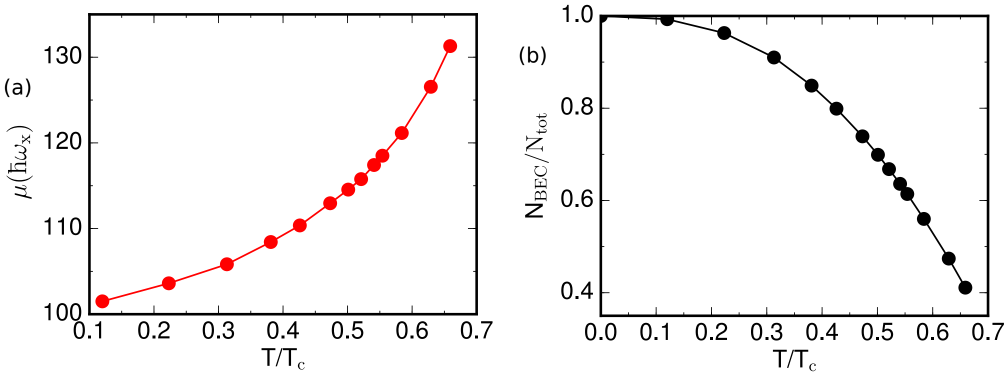

Figure 6.1: (a) The chemical potential and the condensate fraction (b) as a function of the temperature T/T_c for fixed condensate number $N_{\rm BEC} = 50400$ and the barrier height $V_0 = 104\hbar\omega_x$.

written here as

$$\mu(T)\psi_0 = \left(-\frac{\hbar^2}{2M}\nabla^2 + V_{\rm trap} + g(|\psi_0|^2 + 2n^0_{\rm th})\right)\psi_0, \tag{6.4}$$

where $n^0_{\rm th}$ is the equilibrium thermal cloud density, while $\mu(T)$ is the temperature-dependent system chemical potential counting for the thermal cloud equilibrium mean field potential.

As described in [28, 199] the initial thermal cloud density ansatz is based on a simple Gaussian for the required temperature. We then iterate those 2 equations self-consistently, until arriving at an equilibrium solution with the desired condensate, or total, particle number at each specified temperature. The presence of the thermal cloud changes also the chemical potential μ of the system which takes into account also the mean field potential of the thermal cloud. The main analysis in this chapter is conducted at fixed condensate atom number $N_{\rm BEC} = 5.04 \times 10^4$: for such parameters, the dependence of μ on the temperature is shown in Fig. 6.1(a). Changing the temperature while keeping $N_{\rm BEC}$ fixed also changes $N_{\rm tot}$, and hence the corresponding system critical temperature $T_c = T_c(N_{\rm tot})$, defined in Eq. (1.8) for a weakly-interacting Bose gas trapped in a harmonic potential. In our analysis, we specifically probe the temperature regime $T/T_c \lesssim 0.7$, for which the condensate fraction $N_{\rm BEC}/N_{\rm tot} \in [0.4, 1]$. Such correspondence between condensate fraction and scaled temperatures is shown in Fig. 6.1(b). In a trapping potential and in the Hartee-Fock limit, due to the presence of the condensate and thermal mean-field terms, the energy of a particle becomes (also called Hartee-Fock 'dressed' energies) (defined in Eq. 2.87):

$$\epsilon(\mathbf{r}, t) = \frac{\mathbf{p}^2}{2m} + V_{\rm ext}(\mathbf{r}) + 2g(n_{\rm BEC}(\mathbf{r}, t) + n_{\rm th}(\mathbf{r}, t)). \tag{6.5}$$

Thus the thermal particles feel an effective potential expressed by Eq. (2.88) as:

$$U_{\text{eff}}^{\text{th}}(\mathbf{r},t) = V_{\text{ext}}(\mathbf{r}) + 2g(n_{\text{BEC}}(\mathbf{r},t) + n_{\text{th}}(\mathbf{r},t)) \tag{6.6}$$

while the condensate atoms feel an effective potential given by Eq. (2.89), which is written as:

$$U_{\text{eff}}^{\text{BEC}}(\mathbf{r},t) = V_{\text{ext}} + g(n_{\text{BEC}}(\mathbf{r},t) + 2n_{\text{th}}(\mathbf{r},t)). \tag{6.7}$$

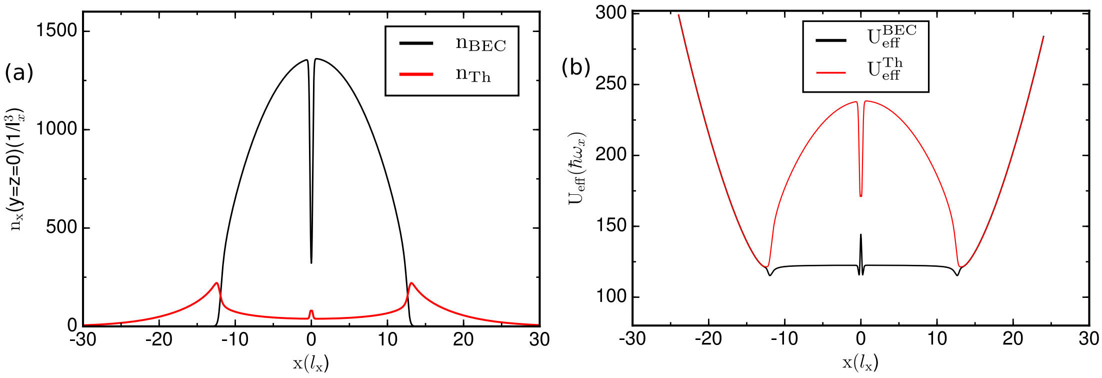

Figure 6.2: (a) The condensate (black line) and thermal (red line) cloud density along the x axis (for $y = z = 0$) and (b) the equilibrium effective potential felt by the condensate (black curve) and by the thermal cloud (red curve) at T =88nK= $0.58T_c$ for $V_0 = 104\hbar\omega_x$.

Fig. 6.2 shows the condensate, the thermal cloud density at finite temperature and the effective potential profile felt by the condensate and the thermal particles for a double-well potential. Due to the repulsive interaction between particles (i.e. g >0) the thermal cloud feels a larger potential where the condensate density is larger, which means that the thermal particles would have lower density. This explains why the thermal cloud density has local maxima at the barrier position (where the condensate density is minima) and at the edges of the condensate. To seed the oscillatory dynamics, at $t = 0$, the linear potential is instantaneously removed, and the subsequent dynamics of all components are analyzed in detail.

For comparison, Fig. 6.3 shows the equilibrium condensate and thermal density along the x axis for $y = z = 0$ for three different temperatures: $T = 0$, $T = 0.31T_c$ and $T = 0.63T_c$. The numerical data are obtained for $V_0 = 104\hbar\omega_x \simeq \mu(T = 0) \simeq 107\hbar\omega_x$ and in the presence of an initial imbalance. In all three case, the condensate number is kept fixed at $N_{\text{BEC}} = 5.04 \times 10^4$. We note that the presence of the thermal cloud at the edges of the condensate makes the condensate density to have a slightly smaller x axis extension with respect to the condensate at $T = 0$ where the thermal cloud is not present and thus a larger maximum density in order to keep the condensate number fixed. This effect is

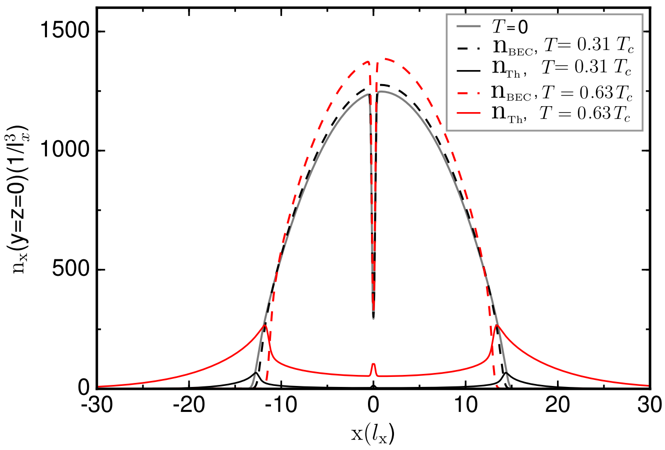

Figure 6.3: The condensate density profile along the x direction ($y = z = 0$) for three different temperatures: $T = 0$ (grey line), T =40nK $= 0.31T_c$ (black dashed line) and T =100 nK $= 0.63T_c$ (red dashed line) and the thermal cloud density shown as black solid line for $T = 0.31T_c$ and as red solid line for $T = 0.63T_c$. The barrier height is fixed at $V_0 = 104\hbar\omega_x$, $w/\xi = 4$ and $N_{\rm BEC} \simeq 5.04 \times 10^4$.

stronger at a higher temperature $T = 100\text{nK} = 0.63\text{T}_\text{c}$.

Our model corresponds to the collisionless limit of the "Zaremba-Nikuni-Griffin" (ZNG) kinetic theory which has been successfully used to model collective modes, vortex dynamics and evaporative cooling [112, 28, 139, 115, 116].

6.2 Effect of the thermal cloud on the critical imbalance

In Chapt. 5 discussing the full phase diagram for the elongated trap Josephson junction, we have defined the critical imbalance delimiting the transition from the Josephson plasma to the dissipative/MQST regimes at $T = 0$, while in Chapt. 4 discussing the comparison with experimental data we showed the effect of a small thermal fraction on z_{cr} ($T = 0.3T_c$) for the range of the experimental barrier heights. At $T = 0$, the critical imbalance in the dissipative regime is defined as the first explored value at which the system decays initially fast in time (within $t \sim 0.1$s) and the relative phase undergoes only one phase-slippage mechanism (i.e. only one VR is nucleated). In the MQST regime instead, it is the first value of z_0 where the $z_{\rm BEC}(t)$ remains 'self-locked' at its initial value while performing small amplitude oscillations around its non-zero mean value and maintaining a fixed sign for at least 0.4s. At $T = 0.3T_c$, z_{cr} was defined by looking at the condensate population imbalance (Chapt. 4) and, in this case only the transition from Josephson plasma to vortex-induced dissipative regime was studied. Here instead we consider a higher temperature T =88 nK $= 0.58T_c$ and we explore barrier heights beyond the experimental range. The dependence of the critical imbalance on the barrier heights at such temperature is shown in Fig. 6.4. We note that the time interval chosen for $z_{\rm BEC}(t)$ in order to exctract the critical imbalance is $[0, 0.4]$s but in the following sections the numerical data are usually obtained for a longer time interval $[0, 0.72]$s.

At this high T, even the condensate Josephson 'plasma' oscillations will be damped in time due to the mean-field coupling with thermal cloud but we keep calling this Josephson regime. Being consistent with our definition at $T = 0$, we call dissipative or vortex-induced dissipative regime the regime where $z_{\rm BEC}(t)$ presents 'dips' or 'kinks' during its initial fast decay (in correspondence of phase-slippage, i.e. vortex rings generation). So, the definition of Josephson or dissipative regime is based on the profile of $z_{\rm BEC}(t)$ within 0.1s, if it presents or not 'dips', i.e. if vortex rings are generated, or not, during the short-time evolution of $z_{\rm BEC}(t)$.

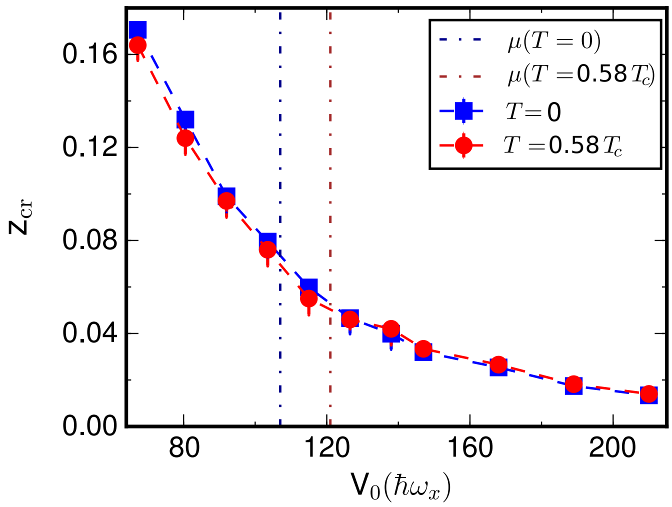

Figure 6.4: The critical imbalance delimiting the transition from the Josephson 'plasma' regime to the dissipative/crossover regime (for $V_0 < 192\hbar\omega_x \simeq 1.8\mu(T=0)$) or to the MQST regime (for $V_0 \geq 192\hbar\omega_x$) both at $T = 0$ (blue square symbols) and T =88 nK $= 0.58T_c$ (red circles), and for the same values of the barrier heights in the range $[67, 210]$ $\hbar\omega_x$ and same value of $N_{\rm BEC} \simeq 5.04 \times 10^4$. The vertical lines indicate the value of the chemical potential at $T = 0$ (dark-blue dash-dotted line) and at $T = 0.58T_c$ (brown dashed-dotted line).

As discussed in Chapt. 5, the MQST regime is a metastable state and even at $T = 0$ it could be destroyed, for example, by the presence of the dissipative second-order term in the current-phase relation originating by the tunneling between condensate and noncondensate states [65]. The latter at $T = 0$ could be phonon excitations. At finite temperature instead, it is the thermal cloud which damps the MQST state. As will be shown later, the MQST regime is highly unstable against thermal excitations and moreover its decay, or not, within 0.4s depends not only on the chosen temperature but also it can vary from run to run of the numerical simulation. However the critical imbalance shown in Fig. 6.4 is extracted from a single numerical simulation. At $T = 0$ and for $N_{\rm BEC} \simeq 5.04 \times 10^4$, the first numerically explored V_0 value at which the onset of the MQST regime is obtained (for $z_0 = z_{cr}$) is $V_0 = 192\hbar\omega_x \simeq 1.8\mu(T=0)$. For such values, the population imbalance oscillates around a non-zero mean value remaining different from zero for at least 0.4s. At finite T instead, for the same barrier height $V_0 = 192\hbar\omega_x$ the $z_{\rm BEC}(t)$ is in the MQST regime (for $z_0 = z_{cr}$), oscillating around a non-zero mean value for at least 0.3s. In fact, Fig. 6.4 shows also the comparison with the extracted z_{cr} at $T=0$ for the same condensate number and for the same value of barrier height. We note that, for temperature $T = 0.58T_c$ the condensate critical imbalance is almost not influenced (within the numerical error bars) by the presence of the thermal cloud as long as we keep fixed condensate number and barrier height. However, at $V_0 = 67\hbar\omega_x$ there is a small shift on the critical imbalance. As will be described in Sect. 6.8.1 for such relatively low barrier height and at relatively high temperature a thermally-induced vortex ring could be generated.

The system chemical potential depends on the temperature (as shown previously) and it is equal to 107 $\hbar\omega_x$ at $T=0$ and $\mu(T=0.58T_c) = 121.4\hbar\omega_x$. Thus, the range of the barrier heights V_0 explored $[67.2, 210]\hbar\omega_x$ corresponds to a range $[0.63, 1.96]$ $\mu(T=0)$, while at $T = 0.58T_c$ the range of barrier heights in terms of finite temperature chemical potential is $V_0/\mu(T=0.58T_c) \in [0.55, 1.73]$. In this chapter we decide to fix the barrier height V_0 instead of $V_0/\mu(T)$ (which was kept fixed in Chapt. 4) as the relevant parameter in our study here is $V_0/(k_BT)$ as will be described later. The range of temperatures that would be explored in the following sections is $[0.1, 0.7]T_c$ where the chemical potential at the highest explored temperature is $\mu(T \simeq 0.7T_c) = 131\hbar\omega_x$.

6.3 Effect of the thermal cloud on the Josephson 'plasma' oscillation frequencies

At finite T, the tilted linear potential $-\epsilon x$ added to our double-well potential at equilibrium creates also an initial population imbalance for the thermal cloud. Thus, in addition to the definition of the condensate imbalance $z_{\rm BEC}(t)$, we define the thermal cloud $z_{th}(t)$ and the total $z_{\rm tot}(t)$ population imbalance as follows:

$$z_{\rm BEC}(t) = \frac{N_R^{\rm BEC}(t) - N_L^{\rm BEC}(t)}{N_R^{\rm BEC}(t) + N_L^{\rm BEC}(t)}, \tag{6.8}$$

$$z_{th}(t) = \frac{N_R^{th}(t) - N_L^{th}(t)}{N_R^{th}(t) + N_L^{th}(t)}, \tag{6.9}$$

$$z_{\rm tot}(t) = \frac{N_R(t) - N_L(t)}{N_R + N_L} = \frac{N_R(t) - N_L(t)}{N_{\rm tot}}, \tag{6.10}$$

where $N_{R/L}^{\mathrm{BEC}}$ and $N_{R/L}^{th}$ is the number of the condensate and the thermal particles on the right/left sides of the barrier (centered at $x = 0$) while $N_{R/L}$ is the sum of the number of the condensate and the thermal particles on the right/left sides of the junction and the total particle number is conserved in the collisionless model. In fact, we model our partly condensed system by using the Zaremba-Nikuni-Griffin model, initially in the collisionless limit where the collisional integrals between the thermal-thermal particles (C_{22}) and between the thermal-condensate particles (C_{12}) are set to zero. Thus the total condensate number $N_{\mathrm{BEC}} = N_L^{\mathrm{BEC}} + N_R^{\mathrm{BEC}}$ and the total thermal cloud number $N_{th} = N_R^{th} + N_L^{th}$ does not change in time due to the absence of particle-exhange mechanisms between the thermal and the condensate cloud. The condensate and the thermal cloud dynamics are coupled together via the mean-field potential, which appears in the effective potential felt by the condensate and thermal cloud (as shown previously and in Chapt. 2).

Our analysis of the role of the thermal dissipation in both the Josephson and the dissipative regimes is performed at $V_0 = 104\hbar\omega_x$, which is comparable to the chemical potential at $T = 0$ but it is around $0.8\mu(T)$ for the highest probed temperature $T \simeq 0.7T_c$. Moreover, we can associate an effective temperature to such value of the barrier height expressed as $T_{eff} = V_0/k_B$ and we find that $T_{eff} = 70$nK$= 0.5T_c$. In order to also fix the initial condensate population imbalance when varying temperature, we use a fixed value of ϵ in the linear barrier shift contribution $-\epsilon x$ for each regime (Josephson, dissipative) studied.

6.3.1 Introduction to the main features of the system dynamics

We start by analyzing the dependence of system dynamics on temperature in the Josephson regime, upon fixing the initial *condensate* population imbalance $z_{\mathrm{BEC}}^0 = z_{\mathrm{BEC}}(t = 0) = 0.05 < z_{cr}$. The evolution of the fractional relative condensate and thermal population imbalance is shown in Fig. 6.5(a) and (b) respectively, from low to a relatively high temperature.

Initially the condensate density is larger in the right well with respect to the left well ($z_{\mathrm{BEC}}^0 > 0$), then the condensate population imbalance oscillates harmonically around a zero mean value with its frequency being shifted by the thermal cloud. Moreover the $z_{\mathrm{BEC}}(t)$ amplitude in time is more damped at higher T. Fig. 6.5(c)-(d) show the condensate, thermal and total imbalance temporal evolution for a relatively low temperature $T = 0.31T_c$ and a relatively high $T = 0.63T_c$ temperature. At low temperatures, the small thermal fraction (red) is moved by the condensate motion, with no significant distinction between the condensate (solid black) and total (dashed green) fractional population imbalances. Both the condensate and total imbalance are slightly damped through the mutual friction of the condensate in its motion through the thermal cloud. However, as the temperature increases to values $k_BT > V_0$ (as occurs for $T = 0.63T_c$), the increasing

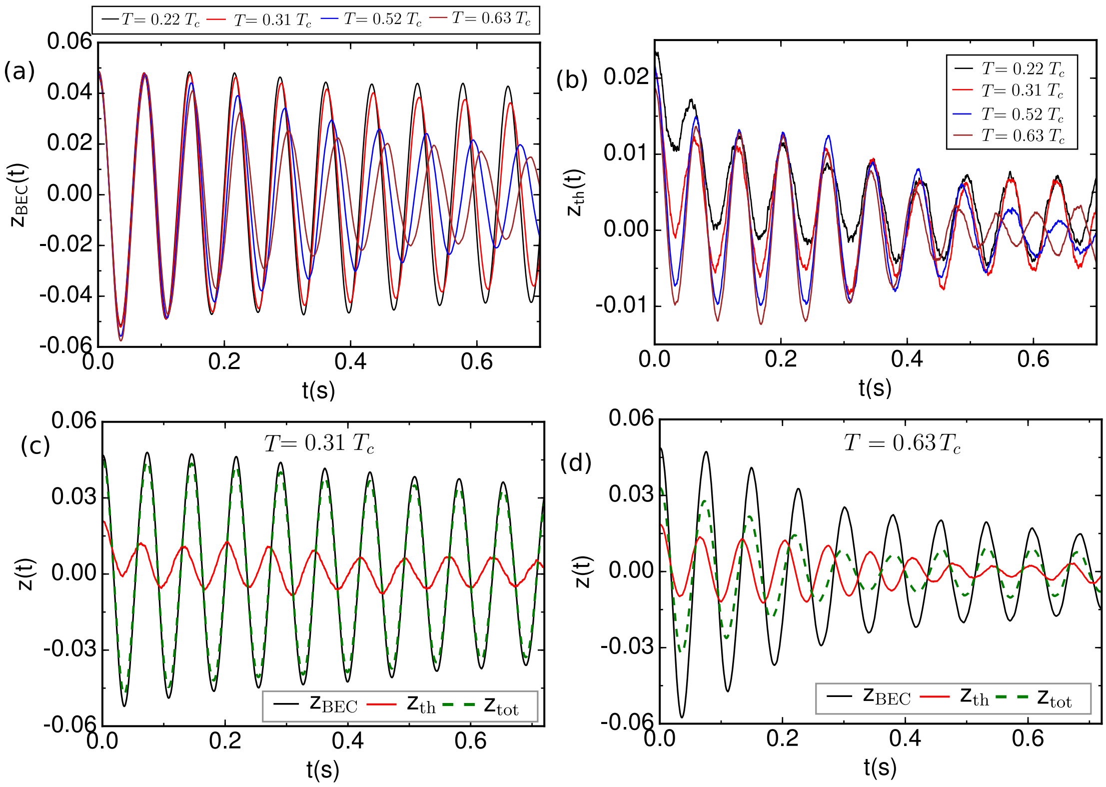

Figure 6.5: (a) The condensate and (b) the thermal cloud population imbalance time evolution for different temperatures. In (c)-(d) is shown the condensate, thermal and total imbalance temporal evolution for two of the temperatures shown in (a)-(b); $T = 0.31T_c$ and $T = 0.63T_c$. The numerical data are for fixed $N_{\rm BEC} = 50400$ and fixed $V_0 = 104\hbar\omega_x$ and for $z^0_{\rm BEC} = 0.05 < z_{cr}$.

thermal component is free to execute its own oscillations over the barrier, at a distinct frequency to that of condensate oscillations: relative condensate oscillations are significantly damped, and the total atomic population difference also appears to exhibit some beating. At low T the thermal cloud mean kinetic energy k_BT is not high enough for the thermal cloud to flow hydrodynamically through the barrier. Thus thermal particles would perform incoherent tunneling through the barrier. For relatively low T such that the thermal cloud mean kinetic energy k_BT is smaller or comparable to $(V_0 - \mu_0)$, the crossing rate of a thermal particle across the barrier is given by the Arrhenius-Kramer formula [60]:

$$P_{th} \simeq \frac{\omega_x}{2\pi}\exp\left(-\frac{(\mathrm{V}_0 - \mu_0)}{\mathrm{k_B}\,T}\right), \tag{6.11}$$

where $\mu_0 = \mu(N/2)$. In the case of $T = 0.22T_c$, shown in Fig. 6.5(b), the Eq. (6.11) estimates a crossing rate $P_{th} \simeq 8.6$Hz, to which corresponds to a time $t_{th} \simeq 0.12$s. This means that each 0.12s, a thermal particle cross the barrier via tunneling. Such result is consistent with the $z_{th}(t)$ profile in Fig. 6.5(b) at $T = 0.22T_c$ which oscillates initially around a non-zero mean value $\langle z_{th}(t)\rangle$ for at least ~ 0.13s and after that its mean value decays in time until it achieves a value near zero for $t \gtrsim 0.4$s.

6.3.2 Condensate imbalance dynamics

In this section, we focus on the condensate $z_{\mathrm{BEC}}(t)$ oscillation frequencies, and their dependence on the temperature.

Fitting function and the comparison with DFT results

Our fitting function of the condensate imbalance is choosen based on two main features: Firstly, we note that in our parameter regime, i.e. for $V_0 \simeq \mu$ and small barrier width $w/\xi = 4$, which is not in the deep tunneling regime, the superfluid current (thus the condensate imbalance) is expected to oscillate with two frequencies; a dominant Josephson plasma frequency and an additional second frequency arising from the second order-term in the tunneling amplitude [65] (as also described in Chapt. 2 and shown in Chapt. 3 for our parameters).

Secondly, at finite T, the presence of the thermal cloud introduces a normal component I_n to the Josephson current (an Ohmic-like contribution) [60, 65] $I_n = -G_{th} \Delta\mu$ where G_{th} is the junction conductance. In the limit of low T, the latter can be estimated from the Arrhenius-Kramers formula as $G_{th} = P_{th} N_{th} / k_B T$ [60], with $\Delta\mu$ the chemical potential difference between the two wells being proportional to the condensate imbalance (i.e. $\Delta\mu(t) \propto z_{\mathrm{BEC}}(t)$, as described in Chapt. 2 and Chapt. 3). For the chosen barrier height, the Arrhenius-Kramers formula is valid for very low temperature $T \lesssim 0.2 T_c$ as the barrier height here is not much different from the single-well chemical potential. Based on these two considerations and knowing that the condensate current is related to the condensate imbalance as $I = -(N_{\mathrm{BEC}}/2)\, dz_{\mathrm{BEC}}/dt$ (as described in Chapt. 3), we then choose as our fitting function of the condensate imbalance

$$\begin{aligned} F(t) = \; & a_J \cos(2\pi\nu_J t + \phi_J) \exp(-\gamma_J t) \\ & + a_i \cos(2\pi\nu_i t + \phi_i) \exp(-\gamma_i t), \end{aligned} \tag{6.12}$$

where we assign distinct damping rates $\gamma_.$ to the two components, and allow unconstrained phases $\phi_.$ to each contribution. The frequency ν_J is the main frequency, which corresponds to the Josephson 'plasma' frequency at $T = 0$ and will be henceforth called the Josephson frequency, with γ_J its corresponding damping term. Interestingly, the secondary oscillations (labelled here by $i = 1, 2$) correspond to distinct frequencies at low temperatures $k_B T/V_0 < 1$ (henceforth labeled as ν_1) and high temperatures $k_B T/V_0 \gtrsim 1$ (henceforth labelled as ν_2) (as will be described later) with γ_1 and γ_2 the corresponding dampings.

We cannot use the two-mode model or its modified version, which accounts for the presence of the normal current [65], because, as we showed in Chapt. 3 for $T = 0$, the two-mode model does not give good predictions of the Josephson 'plasma' oscillation frequency for $V_0/\mu \simeq 1$. Thus the frequencies would be extracted by fitting the condensate imbalance with $F(t)$ function at different T. We choose the time interval $[0.05, 0.72]$s for the fit, which does not start at $t = 0$. This choise is necessary in the study of the dissipative regime where the oscillation frequencies are extracted after the VRs generation, i.e. after the initial fast decay of the population imbalance. For our parameters, such decay ceases near $t \simeq 0.05$s and thus we start our fit from that time. For consistency the same interval is chosen also for the analysis performed in the Josephson regime. Beyond characterizing the oscillation frequencies and damping rates, we also investigate the relative contribution A of each component defined as:

$$A_J = \frac{a_J}{a_J + a_i} \qquad \text{and} \qquad A = \frac{a_i}{a_J + a_i}. \tag{6.13}$$

Finally we investigate the phases $\phi_{.}$ of the different contributions.

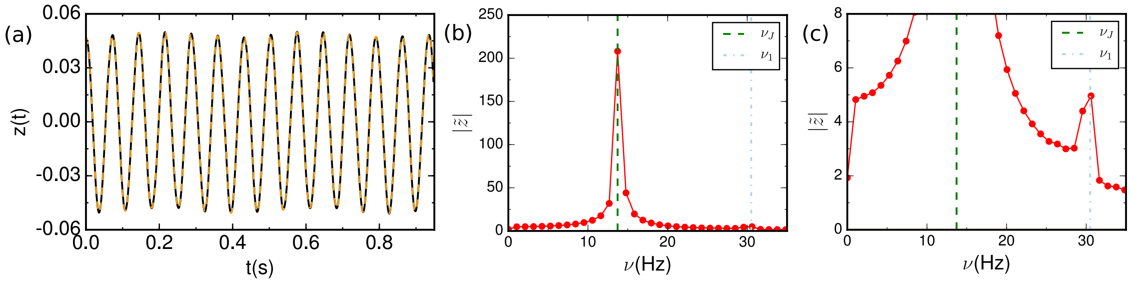

Figure 6.6: (a) The population imbalance time evolution at $T = 0$ and the corresponding fit (orange profile). (b) The corresponding DFT spectrum with a zoomed-in plot of shown in (c). The numerical data are for $V_0 = 104\hbar\omega_x$ and condensate initial imbalance $z^0_{\rm BEC} < z_{\rm cr}$.

Fig. 6.6(a) shows the temporal evolution of the population imbalance at $T = 0$ (black line) for initial imbalance $z_0 = 0.05 < z_{cr}$, i.e. in the Josephson plasma regime where the population imbalance exhibits periodic oscillations around a zero value. Such numerical data are perfectly fitted by the function $F(t)$ (Eq. 6.12) but with $\gamma_{.} = 0$ at $T = 0$ (the fitting function is indicated as orange dashed line). We find that the population imbalance oscillates at a dominant frequency ν_J, whose relative contribution is around 97% at $T = 0$. These results are also confirmed by examinating the Discrete-Fourier Transform (DFT) of the population imbalance time series defined as:

$$\tilde{z}(\omega_m) = \sum_{j=0}^{N} z_{\rm BEC}(t_j) e^{-i\omega_m t_j}, \tag{6.14}$$

where $\omega_m = 2\pi m/t_m$ which are shown in Fig. 6.6 (b)-(c). In fact, the DFT shows a large amplitude peak at ν_J and a very small component at ν_1 which can be just resolved in appropriate zoomed-in plot (Fig. 6.6(c)). The temperature range explored in the following analysis is $[0.1, 0.7]T_c$. Moreover, we would use the superscript 'BEC' in order to label the condensate frequencies and the corresponding damping.

Main oscillation frequencies

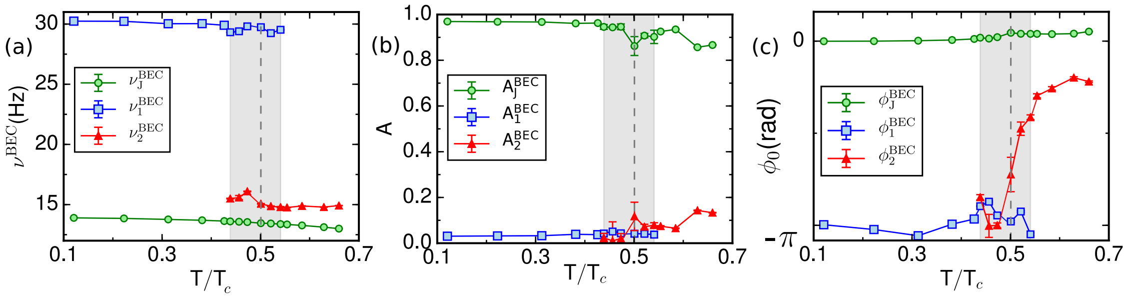

Figure 6.7: (a) The condensate imbalance frequencies (i), their relative amplitude (ii) and the corresponding initial phase (iii) as a function of the temperature for $V_0 = 104\hbar\omega_x$ and condensate initial imbalance $z_0^{\mathrm{BEC}} < z_{\mathrm{cr}}$. Outside the grey area the condensate imbalance is fitted by two-frequency fit while within the grey area is shown the mean value of the two and three-frequency fit and the corresponding error bars is given from their differences. The fit is done in the time interval $[0.05, 0.72]$ s. The vertical dashed line indicate the effective temperature corresponding to the barrier height, i.e. $T_{eff} = 70$ nK $=0.5T_c$.

The extracted main frequencies, relative amplitudes and initial phase of each component are shown in Fig. 6.7(a), (b) and (c) respectively for the condensate imbalance and for $T \in [0.1, 0.7]T_c$. Throughout all the temperature range explored by us, the dominant Josephson dynamics occurs at the frequency ν_J^{BEC} (labelled by green circles) with a relative weighting A_J^{BEC} exceeding 97% at low T and at around 85% at the highest temperature probed here ($T/T_c = 0.66$), with $N_{\mathrm{BEC}}/N_{\mathrm{tot}} \sim 0.4$. At low T the Josephson frequency is $\nu_J \approx 14$Hz and it exhibits a small monotonic decrease as the temperature increases. Interestingly, the role of the second component is played by different frequencies at low and high T (note that our high T is still far from the critical temperature) as shown in Fig. 6.7(a)-(b). For $T < 59$nK$= 0.44T_c$ the second component is around 30Hz (blue squares) and we call it ν_1^{BEC} with its damping γ_1^{BEC}. At high temperature limit $T > 78$nK$= 0.54T_c$ instead, the second component is a different frequency close to the axial trapping frequency (red triangles) and we call it ν_2^{BEC} with its damping γ_2^{BEC}.

In Fig. 6.7(c) we observe that, while the Josephson frequency initial phase ϕ_J remains near zero in all the range the of T explored, the second component for $T < 59$nK$= 0.44T_c$, ν_1^{BEC} has an initial phase ϕ_1^{BEC} shifted to $-\pi$ with respect to the Josephson frequency. This is consistent with the presence of second-order (non-dissipative) term with negative sign in the current-phase relation, as shown for our case in Chapt. 3, suggesting that ν_1^{BEC} comes from considering second-order term in the tunneling Hamiltonian through the barrier [65]. As the temperature increases and for $T > 0.54T_c$, the second frequency, which now becomes ν_2^{BEC}, has a relative initial phase with respect to the Josephson frequency of $|\phi_2^{\mathrm{BEC}} - \phi_J^{\mathrm{BEC}}| \approx \pi/4$.

In order to capture the transition from ν_1^{BEC} to ν_2^{BEC} with increasing temperature, the analysis in a narrow intermediate region $0.44T_c \leq T \leq 0.54T_c$ is extended to 3-frequency fits (ν_J, ν_1 and ν_2) to provide some continuity to our analysis. The three-component frequency fit is defined as:

$$\begin{aligned} G(t) = a_J \cdot \cos(2\pi\nu_J t + \phi_J) \cdot \exp(-\gamma_J t) \\ + a_1 \cdot \cos(2\pi\nu_1 t + \phi_1) \cdot \exp(-\gamma_1 t) + \\ + a_2 \cdot \cos(2\pi\nu_2 t + \phi_2) \cdot \exp(-\gamma_2 t). \end{aligned} \tag{6.15}$$

In order to avoid the problem of having the highest damped components with a large relative contribution, we set two of the three damping rates in Eq. (6.15) to be the same. We take for ν_1^{BEC} and ν_2^{BEC} the same damping, i.e. $\gamma_1 = \gamma_2$ as they are the less dominant component all-over the temperature range. In order to have an even more accurate estimate of the condensate imbalance component frequencies and damping rates, we plot the mean value between the two and three frequency fit in the intermediate region (indicated by the grey area in Fig. 6.7).

We note that in the intermediate region, the relative contribution A_2^{BEC} starts becoming larger than A_1^{BEC} for T$\simeq$ 70 nK = $0.5T_c$, which is exactly equal to the effective temperature T_{eff} associated to the barrier height and thus our intermediate region corresponds to $k_B T \sim V_0$. In fact, as T increases such that $T \geq T_{eff}$, the thermal particles have sufficient energy to overcome the barrier ($V_0/k_B T \lesssim 1$), and are thus allowed to execute oscillations in the underlying trap with a frequency close to the axial trap frequency $\nu_x = 15$Hz (as will be shown later).

Few examples of the DFT spectrum of the condensate imbalance are shown in Fig. 6.8 for a low temperature T =50nK= $0.38T_c$ such that $k_B T < V_0$ (a) and for a high temperature T =100 nK= $0.63T_c$ such that $k_B T > V_0$ (b), together with the results from the two-frequency fit (indicated by vertical lines). We firstly observe that the fit results are in very good agreement with the frequencies of the DFT peaks (the shift between the two results can be due to the finite temporal evolution of our numerical simulations). The DFT spectrum confirms the picture described above: at low temperature $k_B T < V_0$ the main frequencies are ν_J^{BEC} (around 14Hz) and ν_1^{BEC} (around 30Hz) with the latter one having a small contribution. In the opposite limit of relatively high temperature $k_B T > V_0$ the main spectrum components are the temperature shifted ν_J^{BEC} (around 13.2Hz at $T = 0.63T_c$) and ν_2^{BEC} at around the axial trap frequency (specifically, $\nu_2^{\mathrm{BEC}} \simeq 14.5$Hz at $T = 0.63T_c$). We anticipate here that, as will be shown in the following sections, the appearance of the component ν_2^{BEC} in the spectrum of the condensate imbalance is related to its coupling to the thermal cloud motion, with the latter oscillating mainly with a frequency near the axial trap, i.e. close to ν_2^{BEC}.

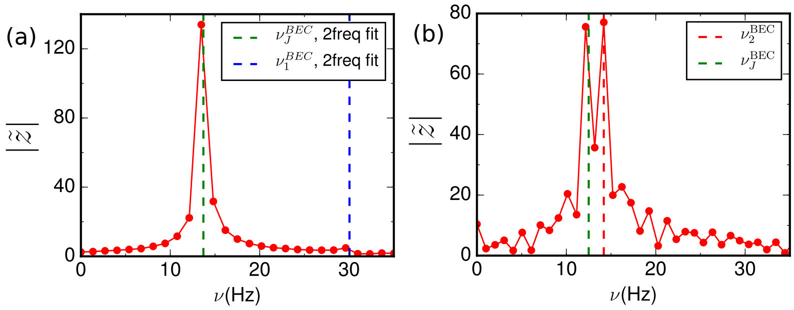

Figure 6.8: The Discrete Fourier transform (DFT) of the z_{BEC}(t) for $V_0 = 104\hbar\omega_x$ and $z^0_{\mathrm{BEC}} = 0.05 < z_{\mathrm{cr}}$ in the frequency domain for T =50nK= $0.38T_c$ (a) and T =100 nK= $0.63T_c$ (b) for fixed $N_{\mathrm{BEC}} = 50400$ and fixed $V_0 = 104\hbar\omega_x$. The y axis is the amplitude of the components of the DFT $|\tilde{z}|$ while the x axis is the frequency. The vertical dashed lines indicate the values of the frequencies obtained by the two-frequency fit.

However we make use of the two-frequency fit results in order to extract the relative amplitude instead of the DFT as our time evolution was not long enough to have a precise DFT spectrum.

More information on the properties of the dominant contributions to $z_{\mathrm{BEC}}(t)$ can be found in Fig. 6.9 which focuses on the dependence of the frequencies ν_J^{BEC}, ν_1^{BEC} and ν_2^{BEC} [top row] and corresponding damping rates [bottom row] as a function of scaled temperature T/T_c. We clearly see the monotonic decrease of ν_J^{BEC} over the entire temperature range probed, accompanied by an almost linear increase of the damping consistent with the results found by [203]. Frequency ν_1^{BEC} also decreases with increasing temperature, and its contribution damps at a faster rate than the ν_J^{BEC}-term, whereas ν_2^{BEC} displays a less clear dependence and a corresponding large damping which increases with decreasing temperature, eliminating that mode for $k_B T \lesssim V_0$: this somewhat counter-intuitive behaviour can be understood from the fact that at such lower temperatures, the thermal cloud cannot on its own move across the barrier, but can only do so mediated by the condensate which drags it along. Since the analysis here focuses on behaviour extracted from the condensate imbalance dynamics, and the small thermal component does not drag the condensate at low temperatures, it is understandable that no ν_2^{BEC} contribution can be found at such low temperatures.

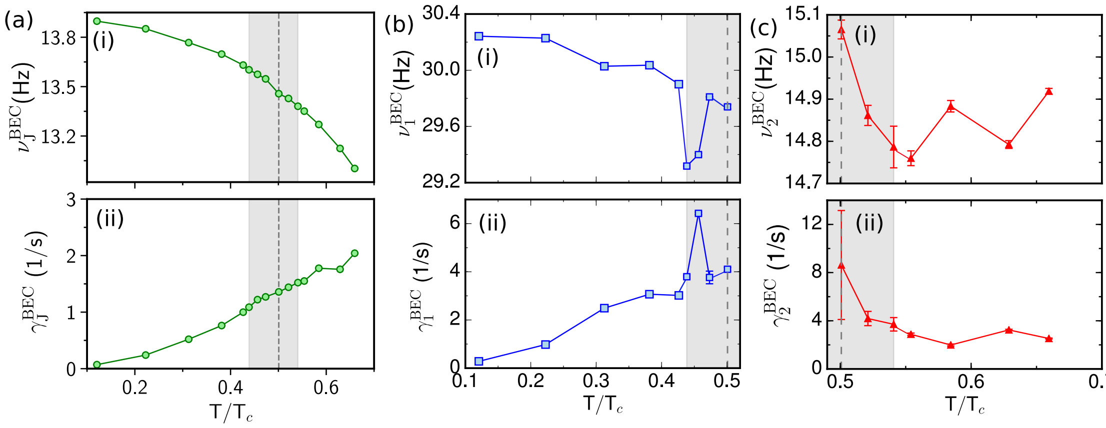

Figure 6.9: The condensate imbalance Josephson (a)-(i) and second frequencies (b)/(c)-(i) dependence on the temperature with the corresponding damping shown in (a)-(ii) and (b)/(c)-(ii) for $V_0 = 104\hbar\omega_x$ and $z_0 < z_{\rm cr}$. We use the label $\nu_1^{\rm BEC}$ for the frequency around 30Hz and the label $\nu_2^{\rm BEC}$ for the frequency around 15Hz, which is also the trap frequency along x axis. In the grey area the data shows the mean value between the two and three frequency fit while outside the grey area only the two-frequency fit is performed. The $\nu_1^{\rm BEC}$ and $\nu_2^{\rm BEC}$ are shown in the range of temperature where they are more important, i.e. at low T for $\nu_1^{\rm BEC}$ and at high T for $\nu_2^{\rm BEC}$.

6.3.3 The thermal cloud imbalance

Overview of the thermal cloud dynamics, from low to high T

As we discussed previously, at very low temperature $T \lesssim 0.2T_c$ the dynamics of the thermal cloud across the barrier occurs mainly via incoherent tunneling with a crossing rate for a thermal particle given by the Arrhenius-Kramers formula Eq. (6.11). For such low temperatures, the thermal imbalance oscillates around a non-zero mean value for relatively long time. As the temperature increases, the thermal cloud dynamics depends essentially on the thermal particles have sufficient energy to overcome the barrier, or not, i.e. on the ratio $V_0/(k_BT)$. At low T such that $k_BT < V_0$, the small thermal cloud cannot move on its own across the barrier but it is driven instead by the condensate motion. In fact, the back action that the condensate has on the thermal particles appears evident if we analyse the oscillations features of $z_{th}(t)$. In order to give a clearer picture of this process, Fig. 6.10(a) shows the time evolution of the thermal population imbalance (i) and the corresponding DFT spectrum (ii) at a selected $T = 0.31T_c < V_0/k_B$. The $z_{th}(t)$ profile is fitted by single-component frequency fit (orange line in (i)) and the extracted frequency is indicated by a vertical dashed line in the DFT spectrum. Interestingly, the extracted frequency value is around 14Hz, which is close to the condensate Josephson frequency; for this reason we keep calling it ν_J^{th}. The frequency extracted by the fit is close to the component of the DFT spectrum with the largest amplitude (the spectrum resolution is 1.2Hz). The DFT spectrum shows few components (apart of ν_J^{th}) with comparable amplitude. This means that perfoming a two-component frequency fit (instead of one-component fit) would not give reliable results for the second component. For this reason, we perform one-component frequency fit of $z_{th}(t)$ for $T < V_0/k_B$, specifically for $T \leq 0.46T_c$. As the temperature increases, a second-component appears in the thermal imbalance spectrum and thus a two-component frequency fit is necessary.

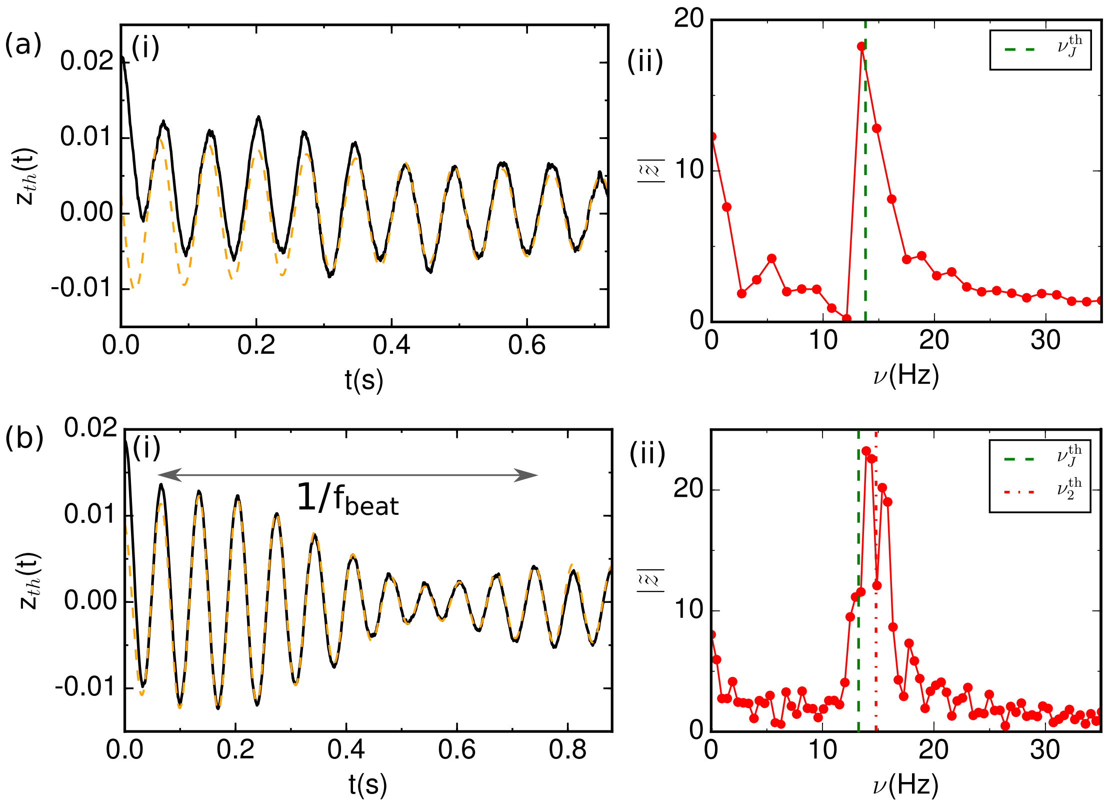

Figure 6.10: The temporal evolution (i) of the thermal population imbalance and its corresponding DFT spectrum (ii) for $T = 0.31T_c$(a) and $T = 0.63T_c$. The numerical data are for $V_0 = 104\hbar\omega_x$ and for fixed $N_{\rm BEC} \simeq 50400$. The orange curves in (a)-(i) and (b)-(i) are the one-component and two-component frequency fit respectively. The results from the fit are indicated by vertical dashed lines in (a)-(ii) and (b)-(ii).

At high T, such that the thermal cloud energy exceeds the barrier height value, the thermal particles move 'freely' over the barrier exhibiting their own motion with a frequency close to the axial trapping frequency. However, this motion is not quite 'freely' as the thermal dynamics is coupled to the condensate motion. In fact, as shown in Fig. 6.10(b), $z_{th}(t)$ oscillates with two-main frequencies; the first one has a value near the trap frequency, and in analogy with the condensate analysis, we term it ν_2^{th}–with a value $\nu_2^{th}(T = 0.63T_c) \simeq 14.8$Hz— and the second one has a value near the temperature-shifted Josephson frequency which we called ν_J^{th}–with a value $\nu_J^{th}(T = 0.63T_c) \simeq 13.3$Hz. The frequency values found from both the fit (orange curve) and from the DFT are in good agreement within the DFT spectrum finite resolution. Interestingly at such high T the thermal imbalance shows beating, which occurs between its two-components and the beating frequency is given by $f_{beat} = |\nu_2^{th} - \nu_J^{th}| \simeq 1.5$Hz and its inverse is indicated by an arrow in the $z_{th}(t)$ profile Fig. 6.10(b)-(i).

Main oscillation frequencies

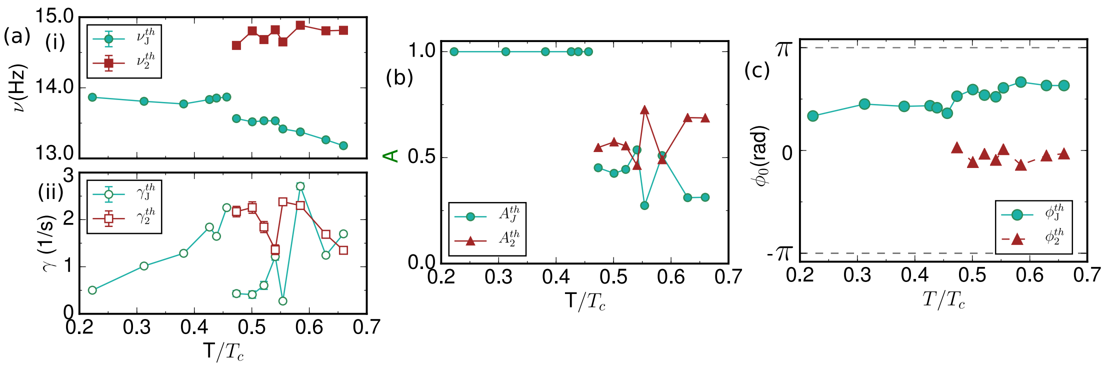

Figure 6.11: (a) The dependence of the thermal cloud imbalance main frequencies (upper plot) and their damping (lower plot) on the temperature obtained from the one (for T $\leq 0.46T_c$) and two-component frequency fit (for T $> 0.46T_c$) in the time interval [0.1, 0.72] s. (b) The corresponding relative contribution of the z_{therm}(t) components and their initial phase (c) at different temperatures. The data are for $V_0 = 104\hbar\omega_x$ and fixed $\text{N}_{\text{BEC}} = 50400$. The data are for $V_0 = 104\hbar\omega_x$.

Fig. 6.11 shows the results from the one-component frequency fit for $T \leq 0.46T_c$ and from the two-component frequency fit for higher temperatures for the frequencies (a)-(i), damping rates (a)-(ii), for the relative contributions (b) and for the initial phase of each-component (c). The error bars are the one obtained from the fit. We observe that as the temperature increases but for $T \leq 0.46T_c$, the ν_J^{th} slightly changes with temperature, remaining near 14Hz (slightly smaller); its damping rate instead increases almost linearly. For $T > 0.46T_c \approx V_0/k_B$, the ν_J^{BEC} is shifted to lower values as T increases while ν_2^{th} approaches the x axis trap frequency. Fig. 6.11(b) reveals that for $k_BT \sim V_0$, specifically for $0.46T_c \leq T \leq 0.58T_c$, there is an interplay between the ν_J^{th} and ν_2^{th}. For $T > 0.58T_c$ instead, the ν_2^{th} dominates. Moreover, we observe that the initial phase of ν_J^{th} is at around $\pi/2$ at low T and it is slightly shifted to larger values as T increases. The ϕ_2^{th} instead, remains near zero in the range of temperature where it is relevant.

In order to better understand the thermal cloud dynamics it is useful to show its frequencies, damping rates and initial phases alongside the condensate imbalance corresponding values.

6.3.4 Thermal vs condensate population imbalance

Fig. 6.12 shows together the thermal and the condensate imbalance oscillation frequencies and corresponding damping rates at different temperatures. Firstly, we observe that the thermal cloud and condensate imbalance main components frequencies (shown in Fig. 6.12 (a)) have almost the same values. Next, we initially comment the low temperature behaviour of both the condensate and thermal imbalance and then we focus on the high temperature limit.

For $T \leq 0.46T_c$ the thermal imbalance oscillates mainly with ν_J^{th}, which is close to the Josephson frequency of the condensate imbalance $\nu_J^{\rm BEC}$, as it is visible in Fig. 6.12 [(a)-(b),(i)]. On the other hand, the corresponding damping rate γ_J^{th} increases more rapidly with respect to $\gamma_J^{\rm BEC}$. At such low temperatures, as shown in Sect. 6.3.2, $\nu_J^{\rm BEC}$ is the dominant component of the condensate spectrum with a relative contribution of more than 97%, but a second-component is present too, $\nu_1^{\rm BEC}$. As the latter has a very small contribution in the condensate dynamics, it does not affect the thermal imbalance evolution, i.e. it does not appear in the $z_{th}(t)$ spectrum. Moreover, as it is evident from Fig. 6.12(d), the thermal cloud ν_J^{th} present a phase shift of around $\pi/2$ with respect to the condensate imbalance component $\nu_J^{\rm BEC}$, i.e. $|\phi_J^{th} - \phi_J^{\rm BEC}| \approx \pi/2$. Even though both the condensate and thermal cloud density are larger in the right well initially (due to the system preparation process), the thermal cloud during its dynamics would tend to have higher density where the condensate density is minimum, explaining so the relative phase shift of $\pi/2$.

At high enough temperature $T \gtrsim 0.5T_c = T_{eff}$, as the thermal particles have enough mean kinetic energy to overcome the barrier, a second component appears in the spectrum of the thermal imbalance which is near to the axial trap frequency and we termed it ν_2^{th}, as shown in Fig. 6.12 [(a)-(c),(i)]. The thermal cloud, which at these temperatures is a significant fraction of the total particle number, 'drives' the condensate dynamics influencing its oscillations features. This picture is confirmed by the results reported in Fig. 6.12(a). In fact, as the temperature increases further, in particular for $T > 0.58T_c$, ν_2^{th} becomes the dominant component of $z_{th}(t)$ and, as an effect of the thermal cloud back action on the condensate motion, $z_{\rm BEC}(t)$ second main component becomes $\nu_2^{\rm BEC}$ instead of $\nu_1^{\rm BEC}$; with the latter already damped at such temperatures. Furthermore, the initial phase $\phi_2^{\rm th}$ has a value near zero and it is close to the value of $\phi_J^{\rm BEC}$; specifically ϕ_2^{th} is in between $\phi_J^{\rm BEC}$ and $\phi_2^{\rm BEC}$ suggesting that initially the thermal and condensate clouds could be phase-locked. Interestingly, the initial phase ϕ_J^{th}, even though increasing slightly, it remains close to $\pi/2$. Throughout the range of temperatures, $\nu_J^{\rm BEC}$ is the dominant frequency and, as the condensate motion is coupled the thermal cloud dynamics, even $z_{th}(t)$ oscillates in time with a second component whose frequency is near the temperature-shifted condensate frequency $\nu_J^{\rm BEC}$, as it is visible in Fig. 6.12(a)-(b).

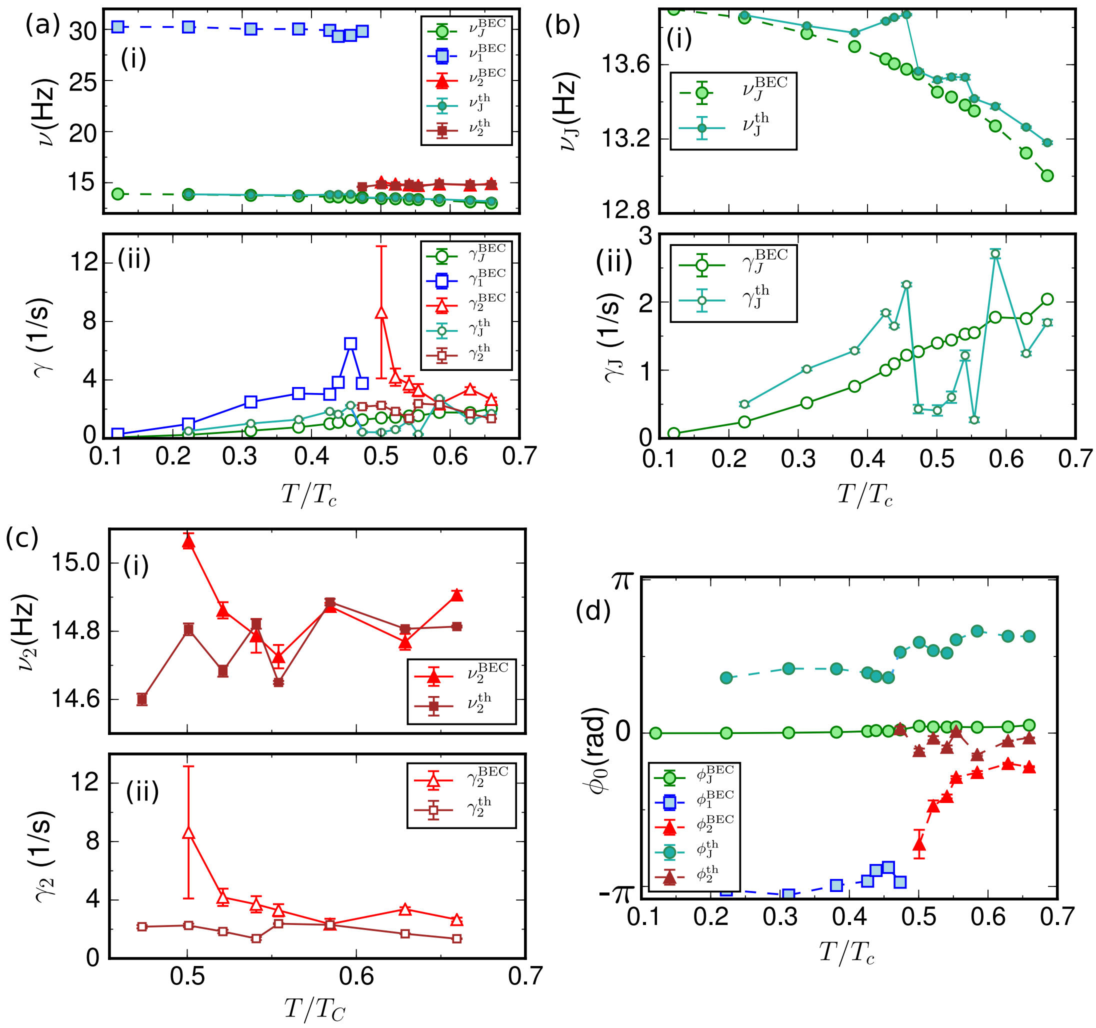

Figure 6.12: (a)-(b)-(c) The condensate and the thermal imbalance oscillations frequency at different temperatures. The dependence of the intial phase of the condensate and of the thermal cloud imbalance on the temperature. The data are for $V_0 = 104\hbar\omega_x$ and fixed $\mathrm{N_{BEC}} = 50400$.

6.3.5 The total imbalance

We analyse the total imbalance $z_{\text{tot}}(t)$ by fitting the data with two-component and three-component frequency fit, with the results of their frequencies and their damping rates shown in Fig. 6.13. The three-component fit results converges to the two-component fit ones in the limit of low and high temperatures, but for the intermediate temperatures $0.45T_c \le T \le 0.56T_c$ ($k_B T \simeq V_0$) there is a small shift between the results. For this reason, in the intermediate range of temperatures (shown as grey areas in Fig. 6.13), we calculate the mean value between the fits (as we did for the condensate imbalance) and show the final results for the frequencies, damping rates, relative amplitudes and each component initial phase in Fig. 6.13.

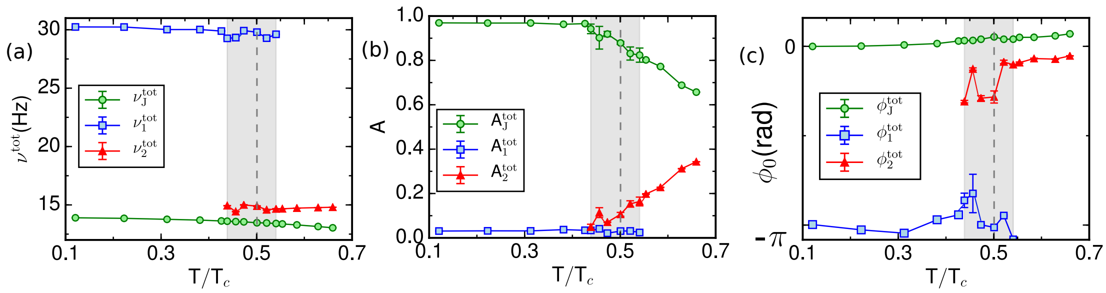

Figure 6.13: The total imbalance frequencies (a), their relative amplitude (b) and the corresponding initial phase (c) as a function of the temperature. Outside the grey area the total imbalance is fitted by two-frequency fit while within the grey area is shown the mean value of the two and three-frequency fit and the corresponding error bars is given from their differences. The fit is done in the time interval [0.05 : 0.72] s. The vertical dashed line indicate the temperature corresponding to the barrier height, i.e. $T = 70nK = 0.5T_c$. The data are for $V_0 = 104\hbar\omega_x$ and fixed $\mathrm{N_{BEC}} = 50400$.

We observe that the total imbalance oscillation properties are similar to the condensate one; at relatively low T the z_{tot} main components frequencies are similar with the condensate one so they are called ν_J^{tot} and ν_1^{tot}. The same happens at relatively high T with the appearance of a third-component near to the ν_2^{BEC}, which we label as ν_2^{tot}; it becomes the second dominant frequency for $k_B T > V_0$. As for the condensate imbalance, the ν_J^{tot} is the dominant frequency over the entire range of temperatures explored here. However, there is a main difference with respect to the condensate imbalance: in our simulations, the increase in temperature leads to an increase in the number of particles in the thermal cloud, while keeping the condensate particle number fixed: as such, while the Josephson frequency ν_J^{tot} is not significantly affected, its relative contribution (Fig. 6.13(b)) decreases rapidly as the total population becomes more dependent on the increasing thermal contribution. At $T/T_c \sim 0.66$ the Josephson contribution contributes only 65% of the total amplitude, while the initial phases of the two dominant contributions (ϕ_J^{tot} and ϕ_2^{tot}) approach each other, indicating phase-locking.

The significant contibution of the second component A_2^{tot} at high T gives rise to beating

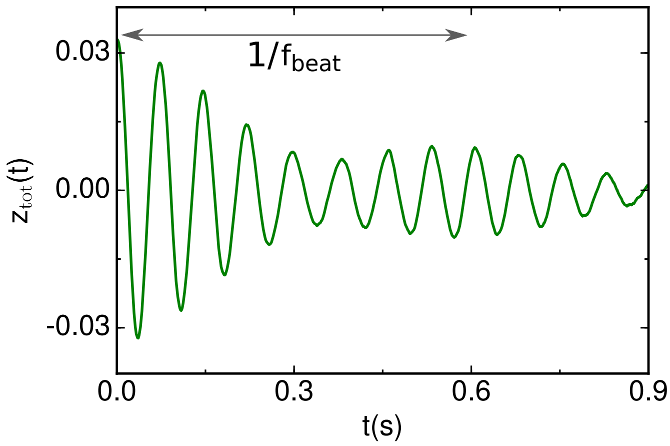

Figure 6.14: The total imbalance temporal evolution for $T = 100nK = 0.63T_c$. The data are for $V_0 = 104\hbar\omega_x$ and fixed $\mathrm{N_{BEC}} = 50400$.

modes between the ν_J^{tot} and ν_2^{tot} as shown in Fig. 6.14 with a beating frequency $f_{beat} = |\nu_J^{\mathrm{tot}} - \nu_2^{\mathrm{tot}}| \simeq 1.7Hz$ and the beating fastest oscillations frequency $(\nu_J^{\mathrm{tot}} + \nu_2^{\mathrm{tot}})/2 \simeq 13.96$ Hz (as occurs to the thermal imbalance shown in Sect. 6.3.3).

Fig. 6.15 shows only the dominant total imbalance frequency ν_J^{tot} which decreases its value with T, while its damping rate increases, similar to the condensate Josephson 'plasma' frequency.

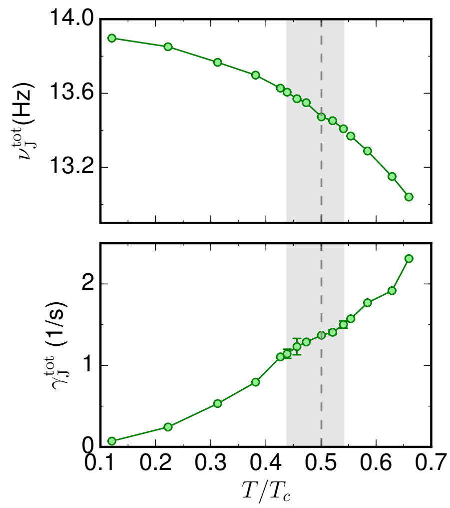

Figure 6.15: The total imbalance dominant frequency value as a function of the temperature. Outside the grey area the total imbalance is fitted by two-frequency fit while within the grey area is shown the mean value of the two and three-frequency fit and the corresponding error bars is given from their differences. The fit is done in the time interval $[0.05, 0.72]$ s. The vertical dashed line indicate the temperature corresponding to the barrier height, i.e. $T = 70nK = 0.5T_c$. The data are for $V_0 = 104\hbar\omega_x$ and fixed $\mathrm{N_{BEC}} = 50400$.

6.4 Effect of the thermal cloud on the vortex-induced dissipative regime

In order to study the effect of the thermal cloud in the dissipative regime, we choose the same barrier height as in the previous section, i.e. $V_0 = 104\hbar\omega_x \simeq \mu(T=0)$. With the term 'dissipative regime' we refer to the regime found at T=0 for $z_0 \geq z_{cr}$, where the dominant dissipation mechanism is the nucleation and subsequent dynamics of the vortex rings (described in Chapt. 3). At finite temperature instead, there is another source of dissipation which comes from the coupling of the condensate motion to the thermal cloud dynamics. At $T = 0$, the onset of the dissipative regime for the chosen barrier height happens for $z_{cr} = 0.08$ and in this section we choose a slightly larger $z_0 = 0.11$, in order to study the effect of the thermal cloud. The barrier shift creating the initial imbalance ϵ is kept fixed at the same value for all the simulations at different T.

6.4.1 Overview of the main characteristics of the system dynamics

Fig. 6.16 shows the condensate, the thermal cloud and the total imbalance time evolution in the collisionless regime for some of the temperatures explored here. The condensate imbalance profile at the lowest T shows two 'dips' for $t < 0.1$s, which suggests that there are two vortex rings generated.

We note that the initial decay of the condensate imbalance is only slightly influenced by the presence of the thermal cloud, as the timescale at which such decay happens is faster than the timescale for significant mutual friction effects. Thus, the main source of dissipation for short time evolution $t < 0.1$s is due to the VR nucleation and dynamics.

The thermal cloud has another effect in the early time evolution. Its presence at the barrier position and at the edges of the condensate shifts slightly the initial condensate imbalance produced for the same barrier shift ϵ compared to that at $T = 0$. Such thermally-induced shift in the $z^0_{\rm BEC}$ increases with temperature, even though is still very small such that it becomes visible only under appropriate zoomed-in of the $z_{\rm BEC}(t)$ profile (as will be shown later). However, at high T such initial shift can lead to the generation of another VR (another 'dip' is present in the $z_{\rm BEC}$) as shown in Fig. 6.16(a)-(d) and clearly visible in the inset of (d) at $t \sim 0.04$s. In this section we focus on the analysis of the oscillations after the initial decay, specifically in the time interval $[0.05, 0.72]$s.

At longer time evolution, the main features of condensate/thermal and total imbalance evolution shown in Fig. 6.16 are:

- At low T (even at $T = 0$ which is not shown in the figure), and after the shedding of the generated vortex rings, the condensate oscillates about a zero mean value at two frequencies (which will be shown to correspond to $\nu_J^{\rm BEC}$ and $\nu_1^{\rm BEC}$). As the

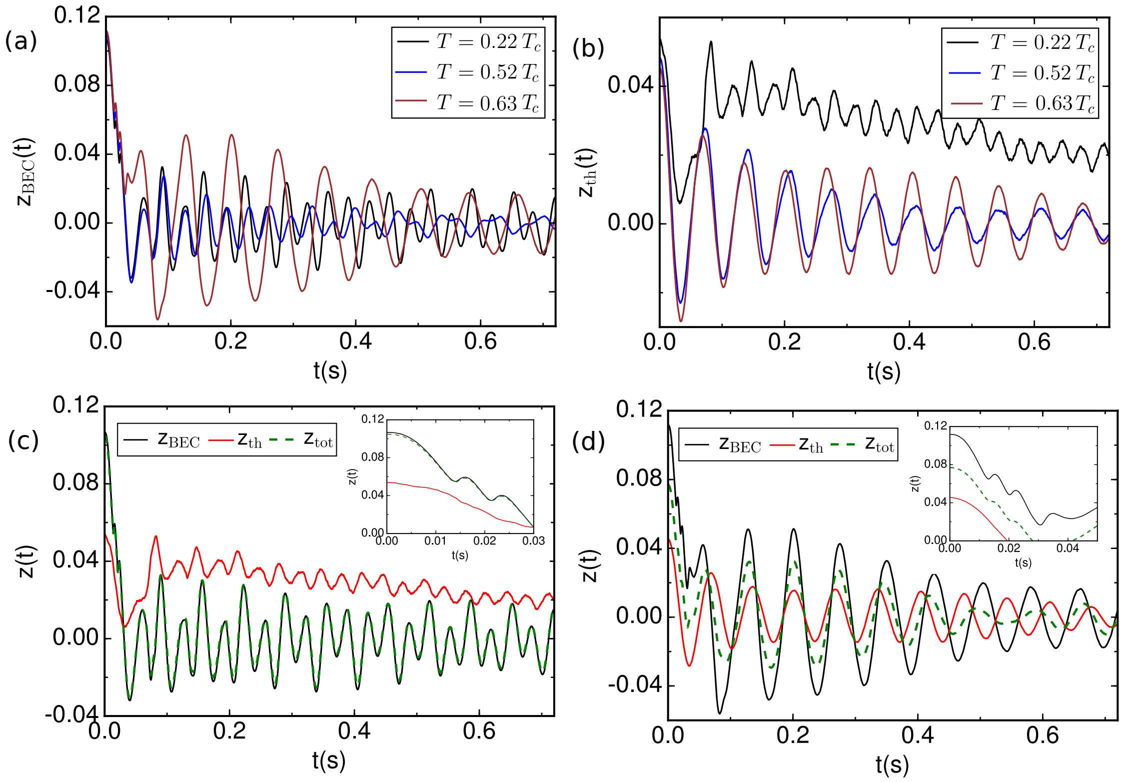

Figure 6.16: (a) The time evolution of the condensate and (b) the thermal cloud imbalance at different temperatures. In (c)-(d) is shown the condensate, thermal and total imbalance temporal evolution for two of the temperatures shown in (a)-(b); $T = 0.22T_c$ and $T = 0.63T_c$. In the insets in (c)-(d) is shown the short-time evolution of the condensate/thermal/total imbalance. The numerical data are for fixed $N_{\rm BEC} = 50400$, fixed $V_0 = 104\hbar\omega_x$ and $z^0_{\rm BEC} = 0.11 > z_{\rm cr}$.

temperature increases to values higher than the barrier, the thermal cloud exhibits its own oscillatory decaying dynamics across the barrier. Interestingly, the condensate mode exhibits enhanced damping (due to the relative motion through the dynamical thermal cloud) and at relatively high T (for example, $T = 0.63T_c$) the condensate starts oscillating mainly with a single dominant frequency.

- At low temperatures, where there is only a small thermal component, the total population imbalance is dominated by the corresponding condensate one (an example shown in Fig. 6.16 (c)). As T/T_c increases, i.e. as the thermal fraction increases, $z_{\rm tot}(t)$ starts deviating from $z_{\rm BEC}(t)$. This property is observed by looking both at short (zoomed-in inset in Fig. 6.16 (c)-(d)) and long time evolution of $z_{\rm BEC}(t)/z_{th}(t)/z_{\rm tot}(t)$.

- For $T = 0.22T_c$ the dynamics of the thermal cloud through the barrier happens via incoherent tunneling with a crossing rate of the barrier for a thermal particle given by the Arrhenius-Kramer formula Eq. 6.11. This means that for certain time evolution the thermal cloud remains 'trapped' in the right well (i.e. positive thermal imbalance mean value). Referring back to the $z_{th}(t)$ profile in the Josephson regime and for the same $T = 0.22T_c$ (shown in Fig. 6.5), we note that in that case the thermal imbalance mean value descreases in time and becomes near zero at $t \sim 0.3$s while in Fig. 6.16 is evident that the $\langle z_{th}(t)\rangle$ remains different from zero for at least 0.7s. The reason for such difference could be the following: In the dissipative regime, during the short time evolution, vortex rings are generated at the trap center and, as the thermal cloud fills in the vortex core, the initial tendency of the thermal cloud to equilibrate between the two wells (with a time estimated as $1/P_{th}$) is disrupted by the presence of the vortex rings. Consequently, at $t \sim 0.05$s the $\langle z_{th}(t)\rangle$ increases until it reaches a maximum value at $t \sim 0.1$s and then decreases slowly in time. During its long time evolution, the thermal imbalance shows some small oscillations following the condensate imbalance as observed from Fig. 6.16 (c).

6.4.2 The condensate imbalance

In this section we present the results from the analysis of the condensate population imbalance oscillations after the initial decay.

Main oscillation frequencies

Remarkably, the main oscillation frequencies of the condensate imbalance in the dissipative regime (see Fig. 6.17 (a)) have similar values as the condensate imbalance components in the Josephson regime. For this reason we also label them here as ν_J^{BEC}, ν_1^{BEC} and ν_2^{BEC}.

The two dominant frequencies at low T ($k_BT < V_0$) in the dissipative regime are ν_J^{BEC} and ν_1^{BEC}, while at high T ($k_BT > V_0$), ν_J^{BEC} and ν_2^{BEC} dominate as was also the case in the Josephson regime. In fact, once again the behaviour changes around $k_BT/V_0 \sim 1$, where the frequency ν_2^{BEC} emerges, due to the oscillations of the increasing thermal cloud in the underlying axial harmonic trap. On the other hand, there is a main difference with respect to the Josephson regime; the main component at low T is the ν_1^{BEC} and not ν_J^{BEC} (with the relative contribution shown in Fig. 6.17 (b)). Another important difference is that, at low T, the second-component has a relative initial phase of $\simeq \pi/2$ with respect to ν_J^{BEC}, differently from the Josephson regime where the $|\phi_J^{\mathrm{BEC}} - \phi_1^{\mathrm{BEC}}| \simeq \pi$.

In the Josephson regime, in all-over the range of T, the initial phase of ν_J^{BEC} remains at zero with a small shift at high T. Here instead, as shown in Fig. 6.17 (c) at low T limit the ϕ_J^{BEC} is near zero while as T increases, its distance from zero increases becoming smaller than $-\pi/2$ in the intermediate regime. Then at $T = 0.58T_c$ the ϕ_J^{BEC} jumps by more than

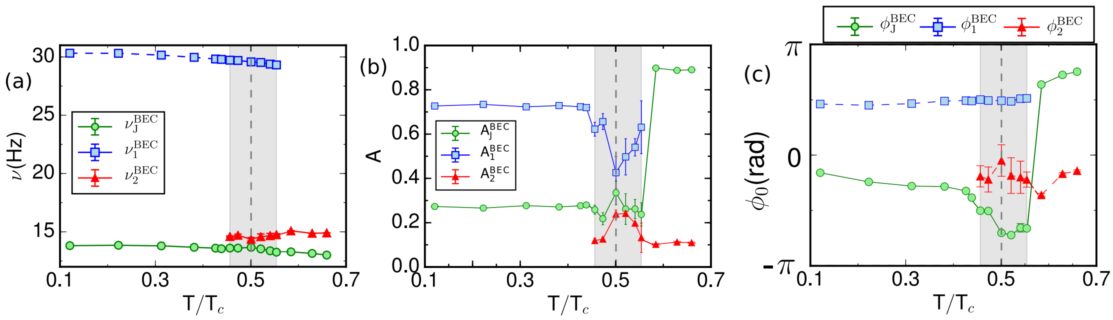

Figure 6.17: The condensate imbalance frequencies (a), their relative amplitude (b) and the corresponding initial phase (c) as a function of the temperature for $V_0 = 104\hbar\omega_x$ and condensate initial imbalance $z^0_{\rm BEC} = 0.11 > z_{cr}$. Outside the grey area the condensate imbalance is fitted by two-frequency fit while within the grey area is shown the mean value between the two cases of the three-frequency fits; in the first case the damping $\gamma_J^{\rm BEC} = \gamma_2^{\rm BEC}$ and in the second case for the damping $\gamma_1^{\rm BEC} = \gamma_2^{\rm BEC}$). The corresponding error bars is given from the differences between the fits. The vertical dashed line indicate the temperature corresponding to the barrier height, i.e. $T = 70nK = 0.5T_c$. The data are for fixed $z^0_{\rm BEC} = 0.11$, $N_{\rm BEC} = 50400$ and $V_0 = 104\hbar\omega_x$.

π, achieving a value near $\pi/2$. Moreover, from Fig. 6.17(b) we observe that another drastic change happens: For $T \leq 0.55T_c$, $\nu_1^{\rm BEC}$ is the dominant frequency (except for $T = 0.5T_c$ where it has a relative amplitude $A_1^{\rm BEC}$ comparable to the $A_2^{\rm BEC}$). Surprisingly, the $A_1^{\rm BEC}$ transits from having a value of more than 60% for $T = 0.55T_c$ to disappearing from the condensate imbalance spectrum at $T = 0.58T_c$. On the other hand, for $T \geq 0.58T_c$ the $\nu_J^{\rm BEC}$ becomes the dominant frequency. This drastic change at such temperature can be associated to two main reasons: Firstly, at $T \geq 0.58T_c$ the initial condensate imbalance is slightly larger than its value at $T = 0$ leading to the generation of a third VR. In both cases, the linear tilted potential $-\epsilon x$ is taken to be the same. If we instead fix the initial condensate imbalance at $T = 0$ to be the same (which means slightly different ϵ) as the one at $T \geq 0.58T_c$, we find that in this case $\nu_1^{\rm BEC}$ is not the dominant component at $T = 0$ (as will be shown in Sect. 6.4.7) and its contribution to condensate motion is less than $A_J^{\rm BEC}$. Secondly, these results seem to suggest that at high enough temperature the thermal cloud attenuates the sound wave's amplitude, helping the condensate to oscillate around zero value mainly with the temperature-shifted Josephson frequency.

In both Josephson and dissipative regime, at low T, there is a third component at around 45Hz with a relative contribution of few percent in the Josephson regime and less than 10 % in the dissipative regime. This third component damps very fast and is already damped at 0.31 T_c (as shown in Appendix B), for this reason we show the results only from the two-component frequency fit at low T (note that the frequencies and the damping rates of the main frequency are not at all affected by including or not the third term but the second component can be slightly affected). The fact that the frequencies 30Hz and 45Hz are exactly multiple of the x-axes trap frequencies seems to suggest that they can

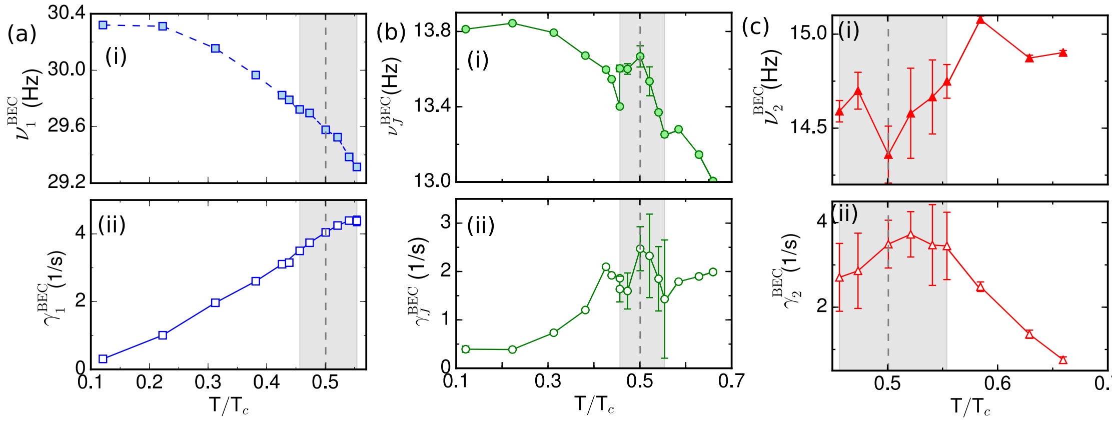

Figure 6.18: The condensate imbalance Josephson (a)-(i) and second frequencies (b)/(c)-(i) dependence on the temperature with the corresponding damping shown in (a)-(ii) and (b)/(c)-(ii) for $V_0 = 104\hbar\omega_x$ and $z_0^{\rm BEC} > z_{\rm cr}$. Outside the grey area the condensate and total imbalance are fitted by two-frequency fit while within the grey area is shown the mean value between the three-frequency fits (between the results with the two of the three damping fixed to be the same; in the first case the damping $\gamma_J^{\rm BEC} = \gamma_2^{\rm BEC}$ and in the second case for the damping $\gamma_1^{\rm BEC} = \gamma_2^{\rm BEC}$) and the corresponding error bars is given from their differences. The fit is done in the time interval $[0.05, 0.72]$s.

have different nature not connecting with tunneling, but in the section 'Future works' we are going to show some analysis of $z(t)$ a a function of V_0 which seems to rule out these alternative for $V_0/\mu \geq 1$.

Consistently with the condensate imbalance analysis in the Josephson regime, in the low and high T limits the $z_{\rm BEC}(t)$ is fitted via $F(t)$ (defined in Eq. (6.12)) two-component frequency fit with the fit performed in the same time interval $[0.05, 0.72]$s (some examples of the comparison between the condensate imbalance evolution and the corresponding fits are shown in Appendix B). We then perform a three-component frequency fit by using $G(t)$ (defined in Eq. (6.15) in the intermediate range of temperature for $0.45T_c < T < 0.56T_c$. Firstly we took all the damping rates to be different, but there was the problem that one of the component that had the highest damping rate, had also a high relative amplitude. Thus we resolve this problem by taking two of the three damping (corresponding to the frequencies with smaller relative contribution) to be the same as we did in the Josephson regime. However, there is a significant difference: while for the Josephson regime the $\nu_J^{\rm BEC}$ was the main frequency at all the temperatures, here instead the role of the main frequency changes between the $\nu_1^{\rm BEC}$ (for $T < 88{\rm nK} = 0.58T_c$) and $\nu_J^{\rm BEC}$ (for T $\geq 0.58T_c$). Thus we perform the three-component frequency fits in the first case by setting $\gamma_{\rm J}^{\rm BEC} = \gamma_2^{\rm BEC}$ and in the second case by imposing $\gamma_1^{\rm BEC} = \gamma_2^{\rm BEC}$. For $T < 0.45T_c$ and for $T > 0.56T_c$ the different three-component frequency fits results converges to each-other and to the two-component frequency fit, but at the intermediate range of temperatures they differ from each other. For this reason, in all the plots shown here, in the intermediate range of

T indicated as grey area, we show the mean value between the three-component frequency fit results.

Looking into more details to the three emerging frequencies, and the damping of the corresponding modes shown in Fig. 6.9, we note the similar ν_1^{BEC} and ν_J^{BEC} frequency dependence on T/T_c as found earlier in the Josephson regime, shown in Fig. 6.9. In fact, similar to the Josephson regime, the frequency value ν_1^{BEC} and ν_J^{BEC} decreases with temperature while the corresponding damping rates increases due to an increasing thermal cloud fraction. Moreover the frequency ν_1^{BEC} damps faster than ν_J^{BEC}.

Fig. 6.18(c) also shows the dependence ν_2^{BEC} and the corresponding damping rate on the temperature. The ν_2^{BEC} starts becoming important once the thermal cloud becomes large enough to strongly affect the condensate motion. This happens when the thermal cloud has sufficient energy to overcome the barrier, $k_BT > V_0$, and to 'drive' the condensate. As T increases, the ν_2^{BEC} value tends at the x axis trap frequency; interestingly, its damping rate decreases with temperature at $T > 0.55T_c$.

6.4.3 The origin of the second frequency

We pause here to briefly describe the origin of ν_1^{BEC}. As our barrier height is near the chemical potential, in the Josephson regime we attributed $\nu_1^{\mathrm{BEC}} \approx 2\nu_J^{\mathrm{BEC}}$ frequency to the presence of the second-order non-dissipative term [65] in the current-phase relation '$\sin(2\Delta\phi)$' term. Thus the superfluid current is then expressed by Eq. (2.79) (and Eq. 3.34 locally): $I(\Delta\phi) = I_c \sin(\Delta\phi) + J_1 \sin(2\Delta\phi)$ where $J_1 < 0$ and $\Delta\phi$ is the relative phase between the two condensates. In the dissipative regime instead, the generation of vortices and associated phonon emission leads to significant interaction between the condensate and excited sound waves. Meier and Zwerger in Ref. [65] showed that also dissipative terms could be present in the current-phase relation $I(\Delta\phi)$ (defined from Eq. (2.81), originating from second-order terms in the tunneling Hamiltonian which consider the transfer of a particle between a condensate state in right well (for example) to an excited state in the left well and viceversa. They also showed that, for $\Delta\mu \ll \mu$ (as in our case), the excited states that contribute to the condensate-noncondensate tunneling are phonon modes. In particular, there is a $\cos(2\Delta\phi)$ term which introduces a relative phase of $\pi/2$ with respect to ν_J, similar to our findings for ϕ_1^{BEC}. Based on these considerations and on our analysis reported in Fig. 6.17, we think that one possible scenario is the following: In the dissipative regime and for long time evolution (after the generation of vortices and in the presence of sound waves), the second-order non-dissipative current $J_1 \sin(2\Delta\phi)$ is negligible while the second-order dissipative current $J_2 \cos(2\Delta\phi)$ instead becomes important. The latter term is finite even at $T = 0$ as shown in [65] that is consistent with our findings. Moreover, in our case $\nu_1^{\rm BEC}$ could even become more important than the Josephson frequency [1]. At finite T, the condensate imbalance is damped due to the presence of the thermal cloud and this process is considered by adding to $I(\phi)$ a normal current $I_n = G_{th}\Delta\mu$ with the conductance G_{th} related to the thermal cloud dynamics. In our analysis, the presence of such normal current is taken into account by fitting the $z_{\rm BEC}(t)$ with an exponential decay. We note that $\nu_1^{\rm BEC}$, found from our analysis of the condensate imbalance, is not exactly twice the Josephson frequency, with $\nu_1^{\rm BEC}(T=0) \simeq 2.2\nu_J^{\rm BEC}$. Even though more analysis will be given in the section 'Future works', one possible explanation could be that in our study we are analysing the population imbalance and not the current-phase relation. Thus a more detailed study is needed on analysing the current-phase profile obtained by the $z_{\rm BEC}(t)$ and $\Delta\phi(t)$ at long time evolution (i.e. after the VRs generation), which goes beyond the scope of this thesis and would be part of future works.

6.4.4 The thermal cloud imbalance

The analysis of the thermal clound imbalance frequencies starts from $T \geq 0.22T_c$ while the condensate analysis started at $T = 0.1T_c$. The reason for that is that $T = 0.1T_c$ the thermal fraction is negligible.

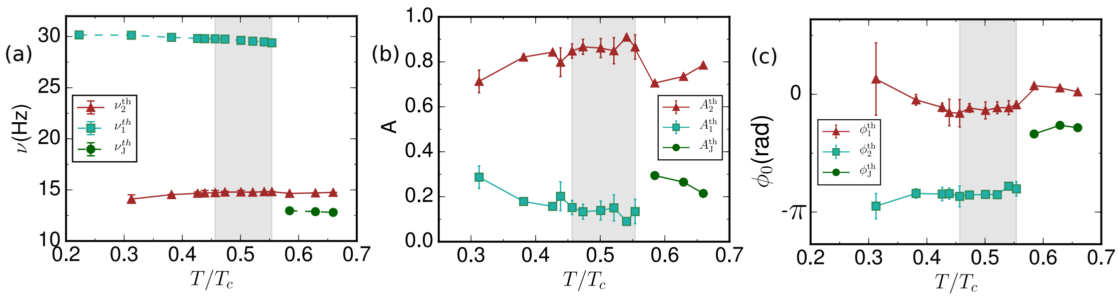

Figure 6.19: (a) The thermal imbalance frequencies, (b) their relative amplitude and (c) the corresponding initial phase as a function of the temperature. The data points and their errorbar are estimated by the mean value between the two-component frequency fit done in different time intervals. The data are $z^0_{\rm BEC} = 0.11$, $N_{\rm BEC} = 50400$ and $V_0 = 104\hbar\omega_x$.

Moreover at $T = 0.22T_c$, z_{th}(t) temporal mean value is different from zero and thus one of the two main components of the fit is close to zero. For this reason, for $T = 0.22T_c$ we show only one of the two frequencies, the one different from zero. Furthermore for $T \leq 0.56T_c$ the thermal cloud imbalance fit is performed in different time intervals $[0.05, 0.35]$s and $[0.25, 0.72]$s. From these results we calculate the mean value and the corresponding error bars shown in Fig. 6.19. For $T \geq 0.58T_c$ the two-component frequency fit in the

[1] We note that the relative contribution of $\nu_1^{\rm BEC}$ depends on z_0: for $z_0 \geq z_{cr}$, the second-order term is not always the dominant frequency; for example, for $z_0 = z_{cr}$ and $V_0 = 104\hbar\omega_x$ its contribution is smaller with respect to that of the Josephson frequency.

range $[0.05, 0.72]$s fits better our numerical data than the two fits in shorter time interval so we choose the long-range fit results to show in Fig. 6.19 for these temperatures.

Fig. 6.19(a) shows that for $T \leq 0.56T_c$, the thermal cloud oscillates with two main components termed ν_2^{th} and ν_1^{th} as their values are similar to the condensate main components (as will be shown in the next section). In the opposite limit instead,i.e. for $T > 0.56T_c$, the thermal imbalance oscillates mainly with ν_2^{th} and ν_J^{th}, where the latter is termed so as its value is close to the Josephson frequency $\nu_J^{\rm BEC}$. Moreover, Fig. 6.19(b) reveals that ν_2^{th} has the largest contribution to the thermal dynamics along the whole range of temperatures probed. Interestingly, we note that the change in the second-component role from ν_1^{th} to ν_J^{th} occurs at exactly $T = 0.58T_c$. Referring back to our analysis of the condensate imbalance, at such temperature there is a drastic change of the main condensate component from $\nu_1^{\rm BEC}$ to $\nu_J^{\rm BEC}$. In fact, similar to the Josephson regime, the thermal cloud spectrum shows a component close to the condensate dominant frequency all-over the range of temperatures. Each component initial phase is shown in Fig. 6.19(c). The ϕ_2^{th} remains close to zero for all the temperatures. As ν_2^{th} is the the thermal cloud dominant frequency, we compare its initial phase with the one of the condensate dominant frequency. At relatively low T, ϕ_2^{th} is shifted by around $\pi/2$ with respect to $\phi_1^{\rm BEC}$ shown in Fig. 6.17. Thi happens because, due to repulsive interaction between the thermal and condensate particle, the thermal particles density is larger where the condensate density is smaller and viceversa. In the opposite limit instead, ϕ_2^{th} has a relative shift of more than $\pi/2$ with respect to $\phi_J^{\rm BEC}$. The temperature dependence of the thermal imbalance main components frequencies and damping rates are shown in the following section.

6.4.5 The thermal cloud vs BEC imbalance

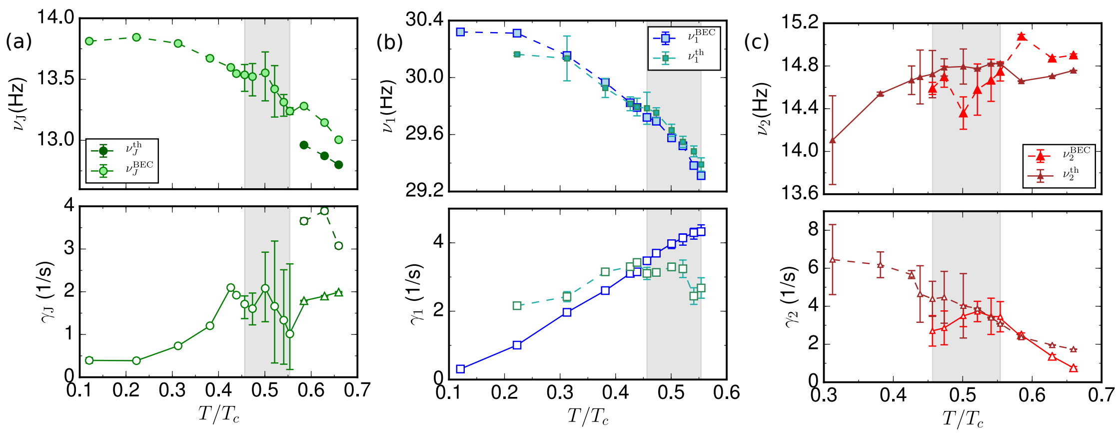

Figure 6.20: The comparison between the condensate and the thermal cloud imbalance oscillation frequencies and the corresponding damping rates at different temperatures. The data are for fixed $z^0_{\rm BEC} = 0.11$, $N_{\rm BEC} = 50400$ and $V_0 = 104\hbar\omega_x$.

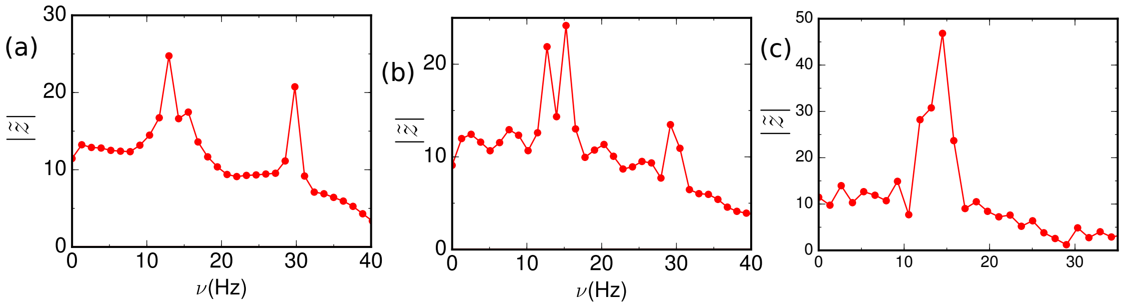

Figure 6.21: The DFT spectrum of the $z_{\text{tot}}(t)$ in the frequency domain for $T = 0.44T_c$ (a), $T = 0.5T_c$ (b) and $T = 0.66T_c$ (c). The data are for $N_{\text{BEC}} \simeq 50400$ and $V_0 = 104\hbar\omega_x$.

Fig. 6.20 shows together the BEC and the thermal cloud imbalance oscillation frequencies and their corresponding damping. As described previously and as it is evident from this figure, the components of the thermal imbalance are termed based on their similarity to the condensate frequencies value. In fact, for $k_B T > V_0$, the thermal imbalance frequencies ν_J^{th} and ν_2^{th} have similar values to the condensate imbalance frequencies ν_J^{BEC} and ν_2^{BEC} respectively. This is clearly visible in Fig. 6.20(a)-(c). Interestingly, not only the frequencies ν_2^{th} and ν_2^{BEC} acquire similar values for $T > 0.5T_c$ but also the corresponding damping rates γ_2^{th} and γ_2^{BEC}. In the entire range of temperature where it is relevant, ν_1^{th} values coincides with ν_1^{BEC}. The latter one exhibits a faster damping with respect to the corresponding thermal component, until it is overdamped at $T = 0.58T_c$, 'disappearing' so from the condensate spectrum.

Moreover we note that the ν_2^{th} value increases, converging at the trap frequency, as the temperature increases while its damping decreases instead. This behaviour is similar to that of the condensate component ν_2^{BEC} for $k_B T > V_0$. At relatively low T, the second component frequency value ν_1^{th} shows the opposite behaviour, i.e. decreasing with the temperature, while its damping increases initially until reaching a 'plateau'.

6.4.6 The total imbalance

We analyse the total fractional population imbalance $z_{\text{tot}}(t)$ with the two-component frequency fit at the low and high T limit and the three-component frequency fit for the intermediate temperatures $0.43T_c \leq T \leq 0.55T_c$, with the intermediate temperature started at lower T with respect to the condensate imbalance analysis that started at $T = 0.45T_c$. In fact, in the total imbalance spectrum, shown in Fig. 6.21, appear clearly three components even at temperature T $= 0.44T_c$. Also for $T = 0.5T_c$ the spectrum has three well-resolved peaks while for $T = 0.66T_c$ the spectrum shows a single dominant peak but the DFT resolution is not high enough to clearly resolve the second component (found by the two-component frequency fit) as the two components are close to each other.

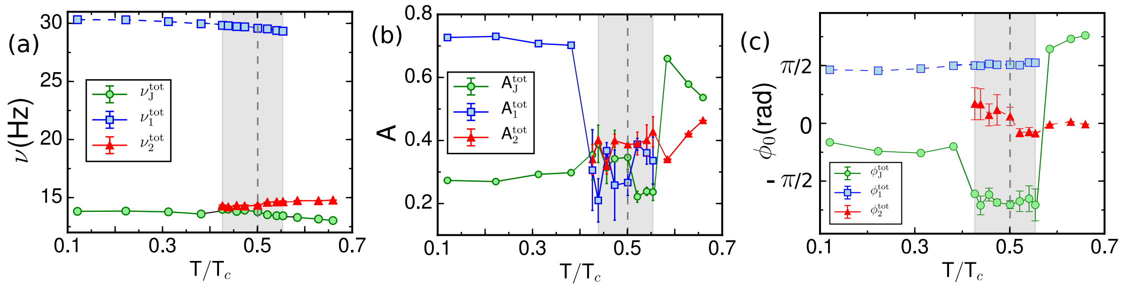

Figure 6.22: The total imbalance frequencies (a), their relative amplitude (b) and the corresponding initial phase (c) as a function of the temperature for $V_0 = 104\hbar\omega_x$ and condensate initial imbalance $z^0_{\rm BEC} = 0.11 > z_{\rm cr}$. Outside the grey area the condensate imbalance is fitted by two-frequency fit while within the grey area is shown the mean value between the two cases of the three-frequency fits; in the first case the damping $\gamma_J^{\rm tot} = \gamma_2^{\rm tot}$ and in the second case for the damping $\gamma_1^{\rm tot} = \gamma_2^{\rm tot}$). The corresponding error bars is given from the differences between the fits. The vertical dashed line indicate the temperature corresponding to the barrier height, i.e. $T = 70nK = 0.5T_c$.

The results from the fit are shown in Fig. 6.22. We observe that the same three frequencies emerges also from the total imbalance oscillations analysis; For $T \lesssim 0.4T_c$ the $z_{\rm tot}$ main components (Fig. 6.22 (a)-(b)) are $\nu_J^{\rm tot}$ and $\nu_1^{\rm tot}$ with the second one being the dominant frequency, as happens for the condensate. In fact, at such low T the small thermal fraction is moved by the condensate motion and the total population imbalance is again dominated by the corresponding condensate one. As T increases, another frequency start becoming important with a frequency value similar to the $\nu_2^{\rm BEC}$ and ν_2^{th}, so we label it $\nu_2^{\rm tot}$. In particular, this occurs for temperatures such that k_BT exceeds the barrier height V_0. The strong driving of the total particle number by the oscillating thermal cloud leads to approximately equal amplitudes for Josephson frequency $\nu_J^{\rm tot}$ and $\nu_2^{\rm tot}$ contributions to the total population at the highest temperatures probed (shown in Fig. 6.22 (b)) and the total population difference also exhibits some beating and damping. In the intermediate regime $0.4T_c < T < 0.56T_c$ there is an inteplay between the relative contribution $A_J^{\rm tot}/A_2^{\rm tot}/A_1^{\rm BEC}$ while for $T > 0.56T_c$ the $\nu_J^{\rm tot}$ dominates.

Fig. 6.22 (c) shows the initial phase of each component of $z_{\rm tot}$. We note that the total imbalance components $\phi_J^{\rm tot}/\phi_1^{\rm tot}/\phi_2^{\rm tot}$ shows similar behaviour and takes similar values as the corresponding ones for the condensate imbalance shown in Fig. 6.17(c).

Fig. 6.23 shows the profiles of the total imbalance main components as a function of T. Similar to the condensate $\nu_1^{\rm BEC}$ and $\nu_J^{\rm BEC}$ profiles, the frequency value decreases with T while its damping increases. The opposite happens to $\nu_2^{\rm tot}$, which increases with T showing a behaviour which is intermediate between the corresponding condensate $\nu_2^{\rm BEC}$ and thermal ν_2^{th}. These results confirm our previous description that, while at low T the total imbalance dynamics is defined mainly by the condensate time evolution, at high T when the thermal particle number becomes significant, the total imbalance shows an

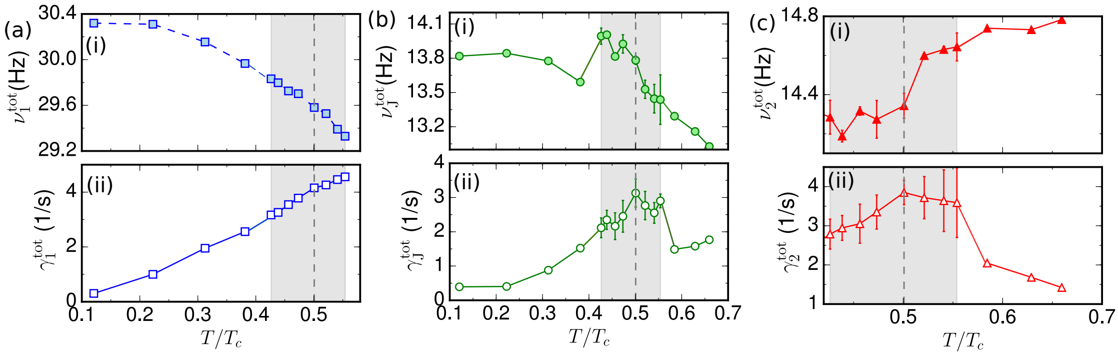

Figure 6.23: The total imbalance Josephson (a)-(i) and second frequencies (b)/(c)-(i) dependence on the temperature with the corresponding damping shown in (a)-(ii) and (b)/(c)-(ii) for $V_0 = 104\hbar\omega_x$ and $z_0^{\rm BEC} > z_{\rm cr}$. In the grey area the data shows the mean value between the three-component frequency fit while outside the grey area only the two-frequency fit results are shown. The $\nu_1^{\rm BEC}$ (b) and $\nu_2^{\rm BEC}$ (c) and their corresponding damping are shown in the range of temperature where they are more important, i.e. at low to intermediate T for $\nu_1^{\rm BEC}$ and at intermediate to high T for $\nu_2^{\rm BEC}$.

intermediate behaviour between condensate and thermal dynamics.

6.4.7 The role of thermal cloud on initial condensate imbalance

As we showed previously, for $T \gtrsim 0.58T_c$, there is a third 'dip' in the initial decay of the condensate population imbalace which occurs in the correspondence of the generation of a VR. We also noted that the concentration of the thermal cloud at the condensate edges and at the barrier induces a small shift in the condensate initial imbalance which slightly increases with temperature. The first question is whether the new shifted $z^0_{\rm BEC}$ would have been large enough at $T = 0$ to cause the transition to a regime when another phase slippage happens or it comes from the thermal induced fluctuations of the phase. The second question is related to the reason why at $T = 0.58T_c$ the $\nu_1^{\rm BEC}$ 'disappears' from the spectrum of the condensate imbalance when for $T < 0.58T_c$ its contribution is large, around 60%.

In order to answer such questions, we consider also the case when the initial condensate imbalance is fixed when comparing $T = 0$ and the selected $T = 0.66T_c$, instead of fixing ϵ of the lineal potential $-\epsilon x$. Fig. 6.24 shows together with the condensate imbalance for $T = 110{\rm nK} = 0.66{\rm T_c}$, the population imbalance at $T = 0$ for two slightly different $z_0 = 0.106$ and $z_0 = 0.113$, with the first one produced by the same barrier shift as $T = 0.66T_c$ while the second one is exactly equal to the initial condensate imbalance $z^0_{\rm BEC}$ at $T = 0.66T_c$. We observe that at $T = 0$, the condensate population imbalance for $z_0 = 0.113$, which is equal to the initial condensate imbalance at $T = 0.66T_c$, present a third 'dip', indicated by the white rectangle in the zoomed-in profile in Fig. 6.24(b). Thus this analysis explains the origin of the third generated VRs (for $V_0 = 104\hbar\omega_x$),

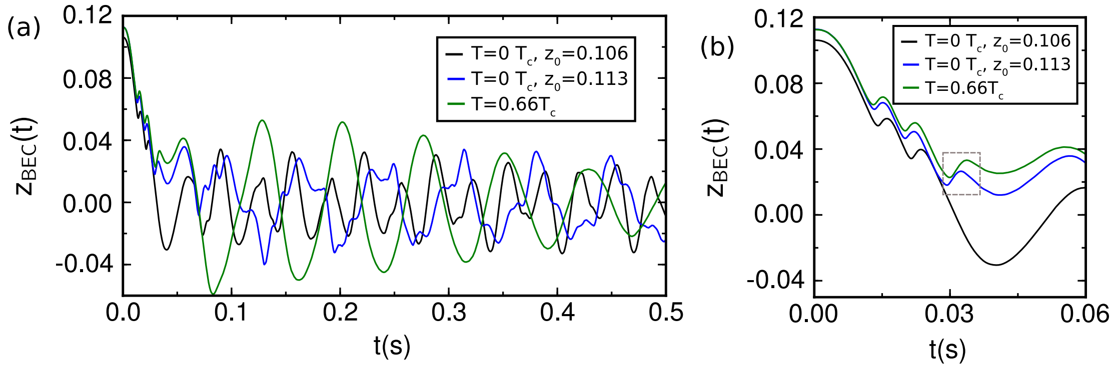

Figure 6.24: (a) The condensate population imbalance time evolution at $T = 0$ and for two slightly different z_0 and at $T = 110\mathrm{nK} = 0.66\mathrm{T_c}$ with a zoomed-in corresponding profile shown in (b). The data are for $V_0 = 104\hbar\omega_x$ and fixed $N_{\mathrm{BEC}} \simeq 50400$.

which is not related to the thermal induced phase-fluctuations. We note that the initial decay of the condensate imbalance is similar for $[T = 0,\ z_0 = 0.113]$ and $T = 0.66T_c$. Furthermore, the temporal profile of the population imbalance at $T = 0$, after the initial decay, shows different features for $z_0 = 0.113$ with respect to $z_0 = 0.106$. In particular in the first case the frequency near 30Hz, i.e. the ν_1^{BEC} frequency, is less important than the Josephson 'plasma' frequency. As we have shown previously, the opposite happens for $z_0 = 0.106$, where the ν_1 is the dominant frequency. Thus this answer to our second question. Moreover, from Fig. 6.24 we observe also that the long-time evolution differs between $[T = 0, z_0 = 0.113]$ and $T = 0.66T_c$, i.e. for the same initial condensate imbalance between $T = 0$ and $T = 0.66T_c$, due to the presence of a significant thermal fraction at this temperature which damps second-order term.

6.5 The effect of the thermal cloud on the Macroscopic Quantum Self-Trapping regime

So far we have studied the effect of the thermal cloud in the vortex-induced dissipative and the Josephson regimes. In this section we show how the thermal cloud affects the condensate population imbalance in the MQST regime. The barrier height value we consider here is $V_0 = 210\hbar\omega_x \simeq 2\mu(T = 0)$, that is around 1.7μ at the highest explored temperature. Fig. 6.25 shows the time profile of the population imbalance at $T = 0$ for two different values of z_0; for $z_0 \lesssim z_{cr}$ (the blue profile) and for $z_0 \simeq z_{cr}$ with $z_{cr} = 0.015$ being the critical imbalance for having the MQST regime. In the former case, the population imbalance exhibits high amplitude anharmonic oscillations around a zero mean-value as we found in Chapt. 5 and as predicted by [59, 61]. Such z_0 values would be in the grey area of the phase diagram shown in Chapt. 5. For $z_0 \simeq z_{cr}$ instead the population imbalance oscillates around a non-zero mean value being so in the MQST or pure self-trapped regime, i.e. it would correspond to the red part of the phase diagrams in Chapt. 5.

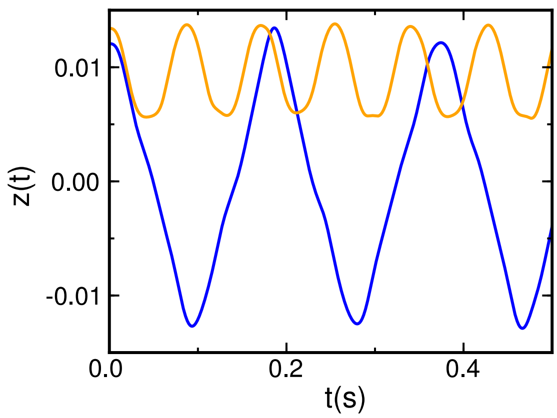

Figure 6.25: The population imbalance time evolution at $T = 0$, for $V_0 = 210\hbar\omega_x \simeq 2\mu(T = 0)$ and two different values of z_0. The orange profile is for $z_0 \simeq z_{\rm cr}$. The data are for $N \simeq 50400$.

We then, at different temperature, keep fixed the constant gradient of the linear potential $-\epsilon x$ at the value it has at $T = 0$ in order to give $z_0^{\rm BEC} \simeq z_{\rm cr}$. Even at $T = 0$, the MQST regime is a metastable regime (for example, it could be destroyed due to the presence of second-order term in the tunneling Hamiltonian as discussed in Chapt. 5) so the temperature has a stronger effect on de-stabilizing it with respect to the other regimes such as the Josephson 'plasma' oscillation and the dissipative regimes. Thus, even in the collisionless limit, different runs of the simulations can give different decay times of the condensate imbalance in the MQST regime, as shown in Fig. 6.26 for different temperatures. We note that in the cases when the MQST regime decays, the condensate imbalance exhibits high-amplitude anharmonic oscillations around a zero value after decaying. The latter regime usually proceeds the transition to the MQST regime, i.e. it is achieved for initial condensate imbalance smaller but near to the critical imbalance for the onset of the MQST regime as shown in Fig. 6.25.

For each temperature are shown five different runs in the time interval [0, 0.74]s. For each run we extract the decay time of the condensate imbalance τ_{MQST} defined as the time at which the condensate imbalance is almost zero, i.e. $|z_{\mathrm{BEC}}(\tau)| \leq 10^{-5}$. We then calculate the mean value of the τ_{MQST} from the different runs and estimate its error bar from the maximum deviation. The results are shown in Fig. 6.27 for different temperatures.

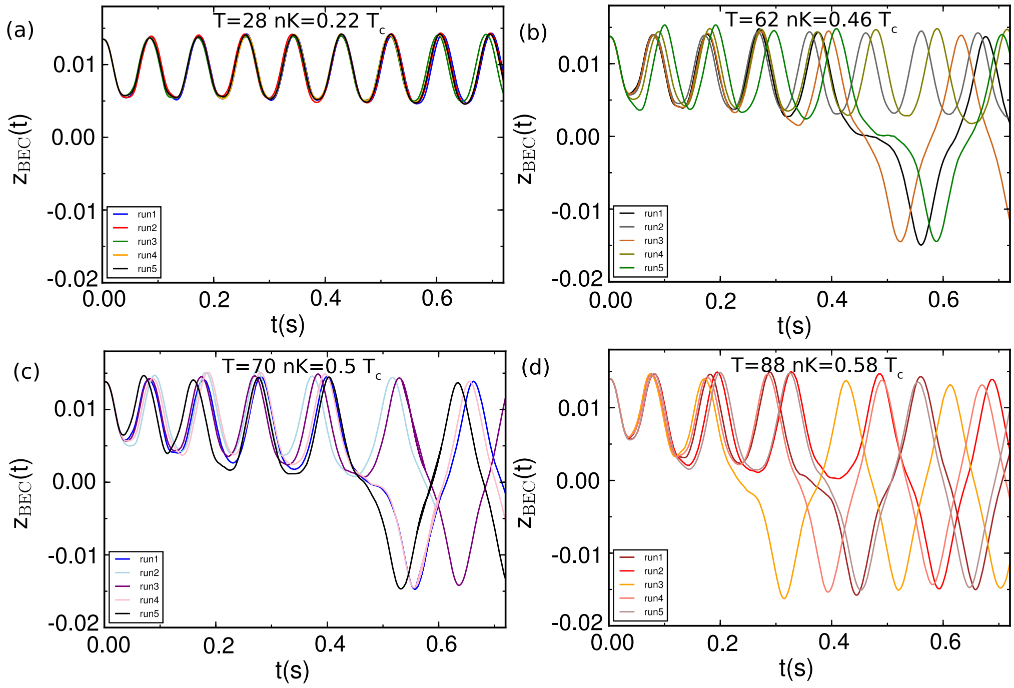

Figure 6.26: The condensate imbalance time evolution at different temperatures: (a) $T = 28\mathrm{nK} = 0.22\mathrm{T_c}$, (b) $T = 62\mathrm{nK} = 0.46\mathrm{T_c}$, (c) $T = 70\mathrm{nK} = 0.5\mathrm{T_c}$ and (d) $T = 88\mathrm{nK} = 0.58\mathrm{T_c}$, for $V_0 = 210\hbar\omega_x$ and $z^0_{\mathrm{BEC}} \simeq z_{\mathrm{cr}}$. In each subplot are shown five different runs.

For $T = 28\mathrm{nK} = 0.22\mathrm{T_c}$ and $T = 50\mathrm{nK} = 0.38\mathrm{T_c}$ the condensate imbalance does not decay in the chosen time interval so we set $\tau_{\mathrm{MQST}} \simeq 0.74$ s as a lower limit of the decay time. We observe that, the overall trend of the condensate imbalance decay time is to decrease with the temperature.

Fig. 6.28 shows some examples of the condensate and thermal cloud population imbalance time evolution at different temperatures. We observe that the $\langle z_{th} \rangle$ is different from zero at low T and it approaches zero as T increases. Nevertheless, it is different from zero even at relatively high $T = 88\mathrm{nK} = 0.58\mathrm{T_c}$. As we described previously, if the thermal particles have not sufficient kinetic energy to overcome the barrier, the thermal particles dynamics across the barrier occurs via tunneling. In particular, if $k_B T \lesssim (V_0 - \mu_0)$, a

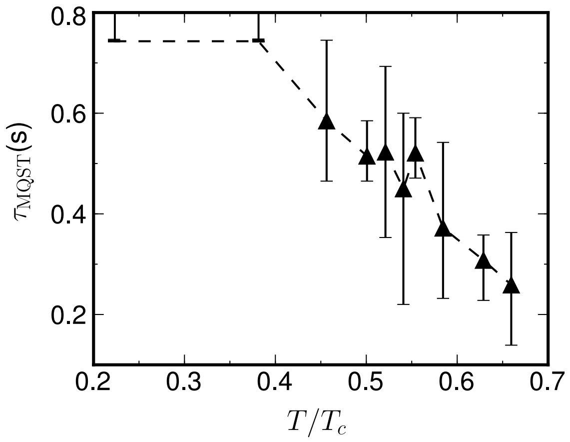

Figure 6.27: The condensate imbalance mean value of the decay time and its error bar given from the five different runs at each temperature for $V_0 = 210\hbar\omega_x$ and $N_{\mathrm{BEC}} \simeq 50400$.

thermal particle exhibit incoherent tunneling with a crossing rate expressed by Eq. (6.11). In this section, the chosen barrier height $V_0 = 210\hbar\omega_x$ is far from $\mu_0 = \mu(N/2) = 81\hbar\omega_x$. This means that even at $T = 0.58T_c$, where $k_BT \sim (V_0 - \mu_0)$, a thermal particle needs sometime to cross the barrier, in particular this each $1/P_{th} \simeq 0.18$s.

In fact, as shown in Fig. 6.28 the thermal cloud remains 'trapped' (i.e. $\langle z_{th} \rangle$ remains different from zero even though close to zero) in the right well for relatively long time even at $T = 0.58T_c$. Moreover we note that the effective temperature associates to such barrier height is $T_{eff} \simeq 140$nK. Thus, even at the highest temperature probed by us $T = 110nK = 0.66T_c$ the thermal particles mean kinetic energy is smaller than the barrier height and the thermal cloud is so 'driven' by the condensate.

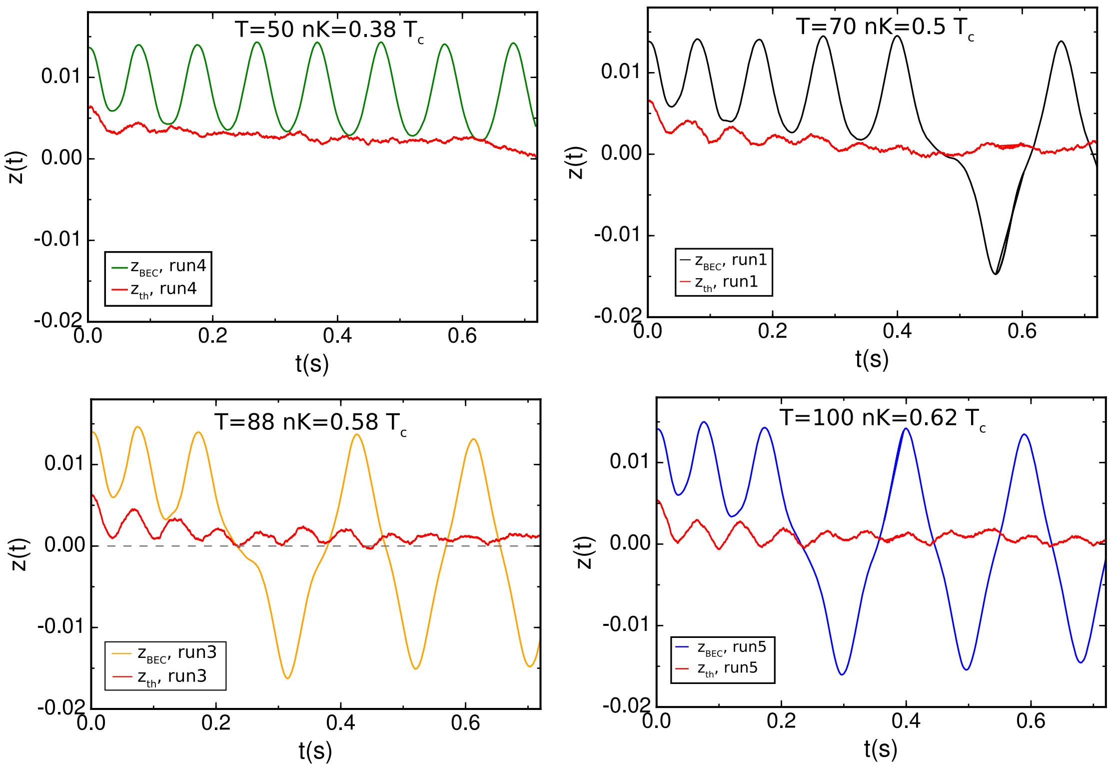

Figure 6.28: The condensate and the thermal cloud imbalance time evolution at different temperatures for $V_0 = 210\hbar\omega_x$ and $N_{\text{BEC}} \simeq 50400$.

6.6 Fixed total particle number

Our analysis so far has focussed on the role of temperature at variable particle number, which was essentially in order to fix the condensate particle number, and thus condensate chemical potential μ. Next, we consider the role of temperature at fixed *total* particle number.

In this section we set the barrier height $V_0 = 104\hbar\omega_x$. When fixing the total number in the system, the effect of temperature is to decrease the condensate number with increasing temperature, due to the increasing presence of particles in the thermal cloud. This is reflected by x axis condensate and thermal cloud densities (for $y = z = 0$) shown in Fig. 6.29 for fixed $N_{\text{tot}} = 106000$ and at different T. While the condensate density maxima decreases with T, the thermal cloud maxima instead (at the edges of the condensate), increases. Due to the presence of more thermal particles at the edges of the condensate and due to the repulsive interaction between the condensate and thermal particles, the condensate density extension along x axis decreases. Moreover the thermal cloud density at the barrier position increases causing a type of repulsive potential at the center for the condensate particle and as a consequence the condensate density at $x = 0$ decreases.

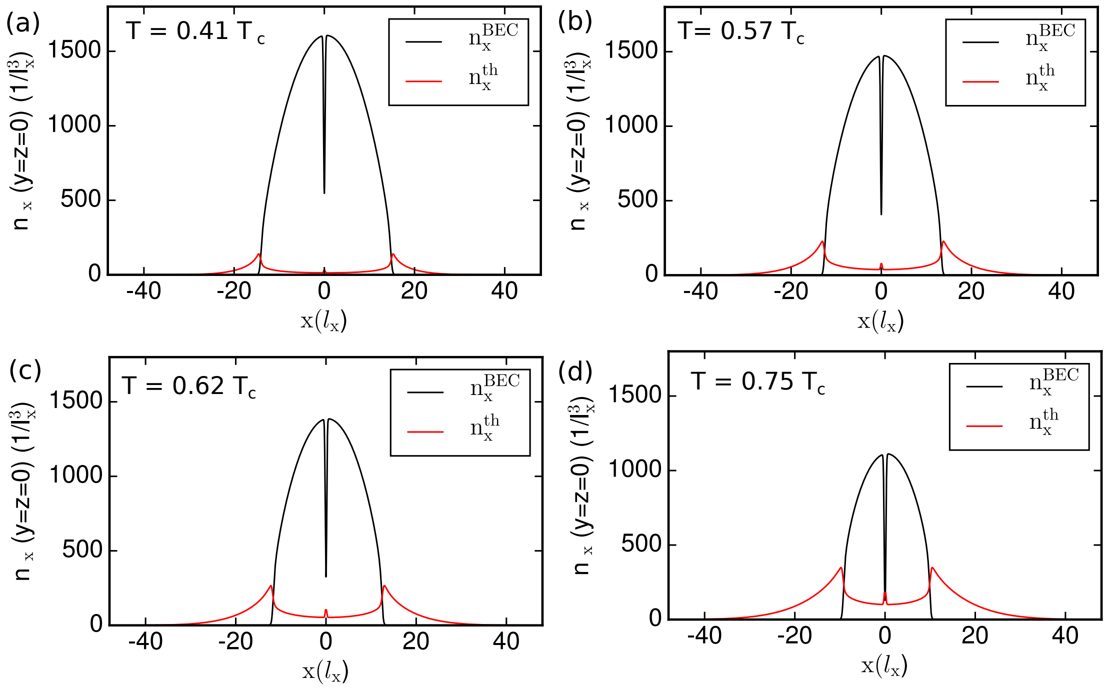

Figure 6.29: The condensate and the thermal cloud density along x axis ($y = z = 0$) profile at different temperatures going from around 0.4 T_c till around 0.75 T_c. The total particle number is kept fixed at $N_{\text{tot}} = 106000$, $V_0 = 104\hbar\omega_x$ and same barrier x axis shift.

The tilted linear potential $-\epsilon x$ which is added to the double-well potential at equilibrium in order to generate an initial population imbalance is initially taken to be the same at different T. Fig. 6.30 shows the condensate and thermal imbalance temporal evolution for $T = 65$ nK $= 0.41T_c$(a), $T = 100$ nK $= 0.63T_c$ (b) and for $T = 120$ nK $= 0.75T_c$ (c).

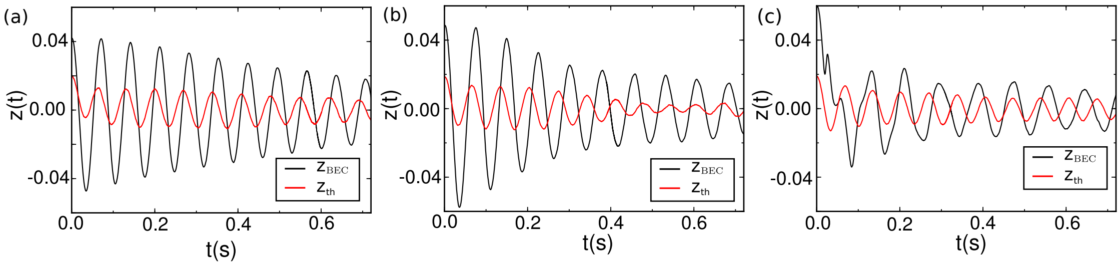

Figure 6.30: The time evolution of the condensate and the thermal cloud imbalance for $T = 0.41T_c$ (a), $T = 100$ nK $= 0.63T_c$ (b) and for $T = 120$ nK $= 0.75T_c$ (c). The data are for the same barrier height $V_0 = 104\hbar\omega_x$ and for fixed total particle number $N_{\text{tot}} = 106000$.

We firstly observe that the same shift ϵ does not give the same condensate initial imbalance, not only because of the presence of the thermal cloud (whose effect is described in Sect. 6.4.7) but also because the condensate number is different at different temperature. Moreover the condensate imbalance temporal profile shows different behaviour, being in the Josephson 'plasma' oscillations regime for $T = 0.41T_c$ and in the dissipative-like regime for $T = 0.75T_c$. This happens not only because $z_{\text{BEC}}(t = 0)$ is different but also because the ratio of the barrier height to the system chemical potential is different, leading to a different ratio of the barrier width to the system healing length. In fact, even when we set the condensate initial imbalance to be the same for $T = 0.41T_c$ and $T = 0.75T_c$ (i.e. choosing the constant gradient ϵ such that $z^0_{\text{BEC}}(T = 0.41T_c) \simeq z^0_{\text{BEC}}(T = 0.75T_c)$), as shown in Fig. 6.31, the condensate exhibits Josephson 'plasma' oscillation at $T = 0.41T_c$ and shows dissipative-like profile (characterized by an initial fast decay of condensate imbalance with 'dips') at $T = 0.75T_c$.

This means that the dominant effect should come from the change in the system chemical potential. In fact, for the case considered here of fixed N_{tot}, for larger temperature value $T = 0.75T_c$, the system chemical potential, which includes also the thermal cloud mean field potential, is smaller ($\mu \simeq 112\hbar\omega_x$) with respect to its value at $T = 0.41T_c$ ($\mu \simeq 137\hbar\omega_x$). Thus, for the same barrier height, the ratio $V_0/\mu(T)$ is larger in the case of higher temperature, and thus the corresponding z_{cr} would be smaller, implying that for the same initial condensate imbalance the system could be in the Josephson regime for smaller temperature $T = 0.41T_c$ and in the vortex-induced dissipative regime for higher T (for example $T = 0.75T_c$).

Moreover, we note that such differences in the chemical potential should be attributed to both the different thermal and condensate particle numbers. In fact, at $T = 0.75T_c$ and $T = 0.41T_c$ the condensate number is $N_{\text{BEC}} = 23656$ and $N_{\text{BEC}} = 86137$ respectively.

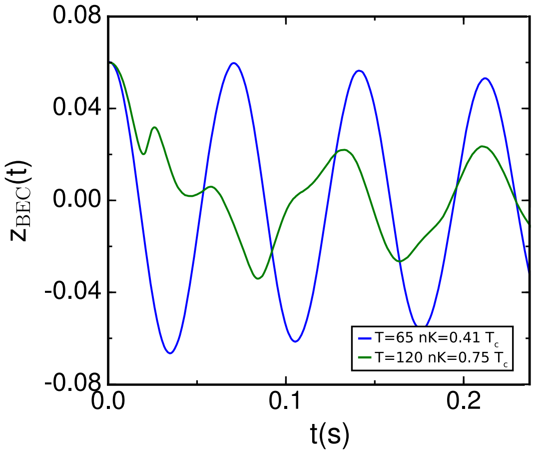

Figure 6.31: The time evolution of the condensate imbalance for $T = 65\text{nK} = 0.41\text{T}_\text{c}$ and $T = 120\text{nK} = 0.75\text{T}_\text{c}$ for the same z^0_{BEC}. The barrier height is kept fixed at $V_0 = 104\hbar\omega_x$ and fixed total number $N_{\text{tot}} = 106000$.

For the same condensate number, at $T = 0$ one would have obtained $\mu = 79.2\hbar\omega_x$ and $\mu = 132.9\hbar\omega_x$ respectively. Moreover, the $T = 0$ chemical potential values are smaller with respect to the chemical potential value at finite T for the same condensate number, which is consistent with our results in Sec. 6.1.

For $T = 0.75T_c$ the thermal cloud fraction is around 0.78 and the thermal imbalance oscillates mainly with a frequency around 14.83Hz (from the two-component frequency fit), consistent with our findings from the thermal imbalance analysis reported in the previous sections. Fig. 6.32 shows the DFT spectrum of the thermal imbalance time evolution showing a clear peak at the frequency found by the fit.

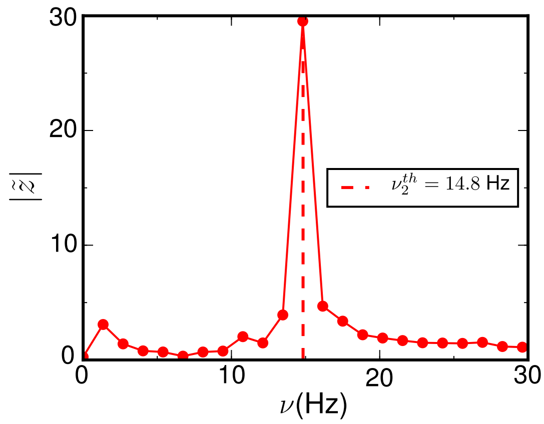

Figure 6.32: The DFT spectrum of the thermal imbalance time evolution $T = 0.75T_c$, for $N_{\text{tot}} = 106000$ and for the case of $z^0_{\text{BEC}} = 0.06$. The vertical dashed line indicate the main component frequency value found by two-component frequency fit in excellent agreement with the position of the main peak of DFT. The barrier height is kept fixed at $V_0 = 104\hbar\omega_x$.

Fixed total initial imbalance

As a next step, we fix the total initial imbalance (as usually done in experiments), for the same two different temperature as previously $T = 0.41T_c$ and $T = 0.75T_c$ as shown in Fig. 6.31. At the two-different T, the total imbalance shows different behaviour; for $T = 0.41T_c$ the total imbalance oscillates sinusoidally around zero mean value with mainly a single component damped due to the presence of the thermal cloud. On the other hand, for $T = 0.75T_c$ the total imbalance shows a 'dip' during its initial decay suggesting there are vortex rings nucleated, and thus the system is in the dissipative regime. After the initial decay, the total imbalance shows beating. In order to extract $z_{\rm tot}(t)$ beating frequencies, we perform the two-component frequency fit after the initial decay. We find as main frequencies $\nu_2^{\rm tot} \simeq 14.85$ Hz (with a contribution of 66%) and $\nu_{\rm J}^{\rm tot} \simeq 11.52$ with comparable damping rates; $\gamma_2^{\rm tot} \simeq 1.18$ and $\gamma_{\rm J} \simeq 1.26$ respectively. Firstly, we note that the total imbalance dominant component has the same value as the thermal imbalance, whose spectrum is shown in Fig. 6.32 for the same barrier height and temperature, while the second component derives from the condensate motion. These results confirms the picture that in the presence of a large thermal cloud and for T such that $k_BT > V_0$ the thermal dynamics strongly effect the total imbalance which shows even beating between the thermal and condensate contributions.

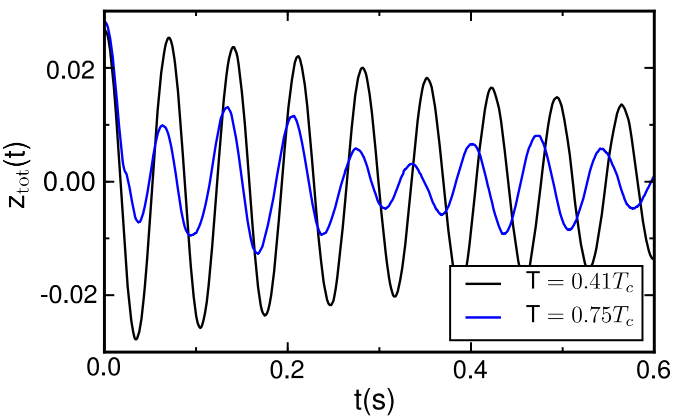

Figure 6.33: The time evolution of the total imbalance for T $= 0.41T_c$ and T $= 0.75T_c$ for the same $z_{\rm tot}(t = 0)$. The barrier height is kept fixed at $V_0 = 104\hbar\omega_x$ and fixed total number $N_{\rm tot} = 106000$.

Fixed $N_{\rm tot} = 50400$

In this section, we fix the total number at a smaller value $N_{\rm tot} = 50400$, chosen in order to match the condensate number used in the previous sections where $N_{\rm BEC}$ was instead fixed. We show here the comparision between $T = 0$ and $T = 0.81T_c$ results. The linear potential gradient and the barrier height are kept fixed. The time evolution of the condensate and thermal imbalance are shown in Fig. 6.34(a) while the DFT spectrum of the thermal imbalance is shown in (b).

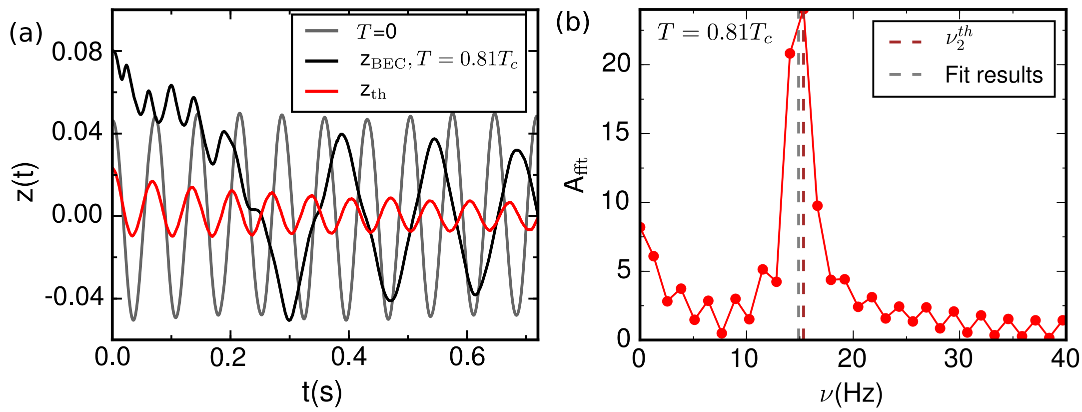

Figure 6.34: (a) The time evolution of the condensate imbalance for $T = 0$ and for $T = 0.81T_c$ for the same barrier shift ϵ and for the same barrier height $V_0 = 104\hbar\omega_x$. In the subplot is shown also the time evolution of the thermal population imbalance. (b) The DFT spectrum of the thermal imbalance time evolution $T = 0.81T_c$, for the case of $z^0_{\rm BEC} = 0.06$. The vertical dashed line indicate the main component frequency value found by two-component frequency fit in excellent agreement with the position of the main peak of DFT. The total number is kept fixed $N_{\rm tot} = 50400$.

The condensate imbalance shows different profiles at $T = 0$ and at $T = 0.81T_c$. While at $T = 0$ the condensate imbalance (the condensate fraction is 100%) exhibits Joesphson-like oscillations with single-dominant frequency; at finite T instead the condensate imbalance shows the typical behaviour of a decaying MQST regime followed by anharmonic high-amplitude oscillations around zero-mean value. The thermal cloud oscillates mainly with a single-component and its value, shown in the DFT spectrum (Fig. 6.27 (b)) and in good agreement with the two-component frequency fit, is almost 15Hz consistent with all the analysis on the thermal imbalance done so far.

6.7 Collisional limit

So far we have shown the results in the collisionless limit of the ZNG model. In this section we show the effect of collisions considering both C_{12} and C_{22} collisional integrals for all the three regimes we studied previously; Josephson 'plasma' oscillations, vortex-induced dissipative and MQST regime. Even though we are not going to give a detailed description of the effect of the collisions, we are going to show the main effects of the collisions on the condensate and total imbalance dynamics.

In the collisional limit, even though the total number is conserved (within few percent in our simulations), the condensate number ($N_{\rm BEC}(t) = N_L^{\rm BEC}(t) + N_R^{\rm BEC}(t)$) instead changes in time due to the particle exchange between the condensate and thermal clouds (as shown in Appendix B). This is taken into account in the C_{12} collisional integral in the Quantum Boltzmann equation Eq. (2.100) and is related to the source term $-iR$ in the generalized GPE equation Eq. (2.92). As a consequence also the thermal cloud particle number changes in time ($N_{\rm th}(t) = N_L^{\rm th}(t) + N_R^{\rm th}(t)$). The condensate and thermal cloud imbalance are defined as in Eq. (6.10) but now the $N_{\rm BEC}(t)$ and $N_{\rm th}(t)$ are time-dependent.

Fig. 6.35 shows the condensate and thermal cloud time evolution for a single run and for $T = 0.22T_c$ in the (a) Josephson 'plasma' regime, in (b) vortex-induced dissipative regime and (c) in the MQST regime both in the collisional and collisionless limit for comparison. At this low T, the effect of collisions on the condensate imbalance in the Josephson and dissipative regime is almost negligible while they significantly influence the $z_{\rm BEC}(t)$ in the MQST regime causing it to decay earlier in time. We note that the MQST regime is very unstable in the presence of the thermal cloud and its decay time can change from run to run even in the collisionless limit (as we showed previously). However at $T = 0.22T_c$ the $z_{\rm BEC}$(t) of all the five runs in the collisionless limit did not decay within 0.72s so Fig. 6.35 (c) shows that the collisions can decrease the decay time (it will be shown in more details later). The thermal cloud imbalance in the Josephson and dissipative regime (with a clearer evidence in the second case) oscillates around a non-zero mean value in the collisionless limit, while the collisions between the thermal particles (C_{22}) and between the condensate and thermal particles (C_{12}) shift the thermal population imbalance mean value to around zero value. Referring back to the study in the collisionless limit, at such low temperature the thermal particles cross the barrier via tunneling. The results in Fig. 6.35 suggest that collisions, in particular the particle exchange between the thermal and condensate clouds, induces the thermal particles to cross the barrier faster. In the MQST regime instead, the initial condensate and thus thermal imbalance is too small that the noise to signal ratio is high, so the thermal cloud imbalance oscillations are barely visible.

Next we consider an intermediate temperature $T = 70{\rm nK} = 0.5{\rm T_c}$, which is equal to

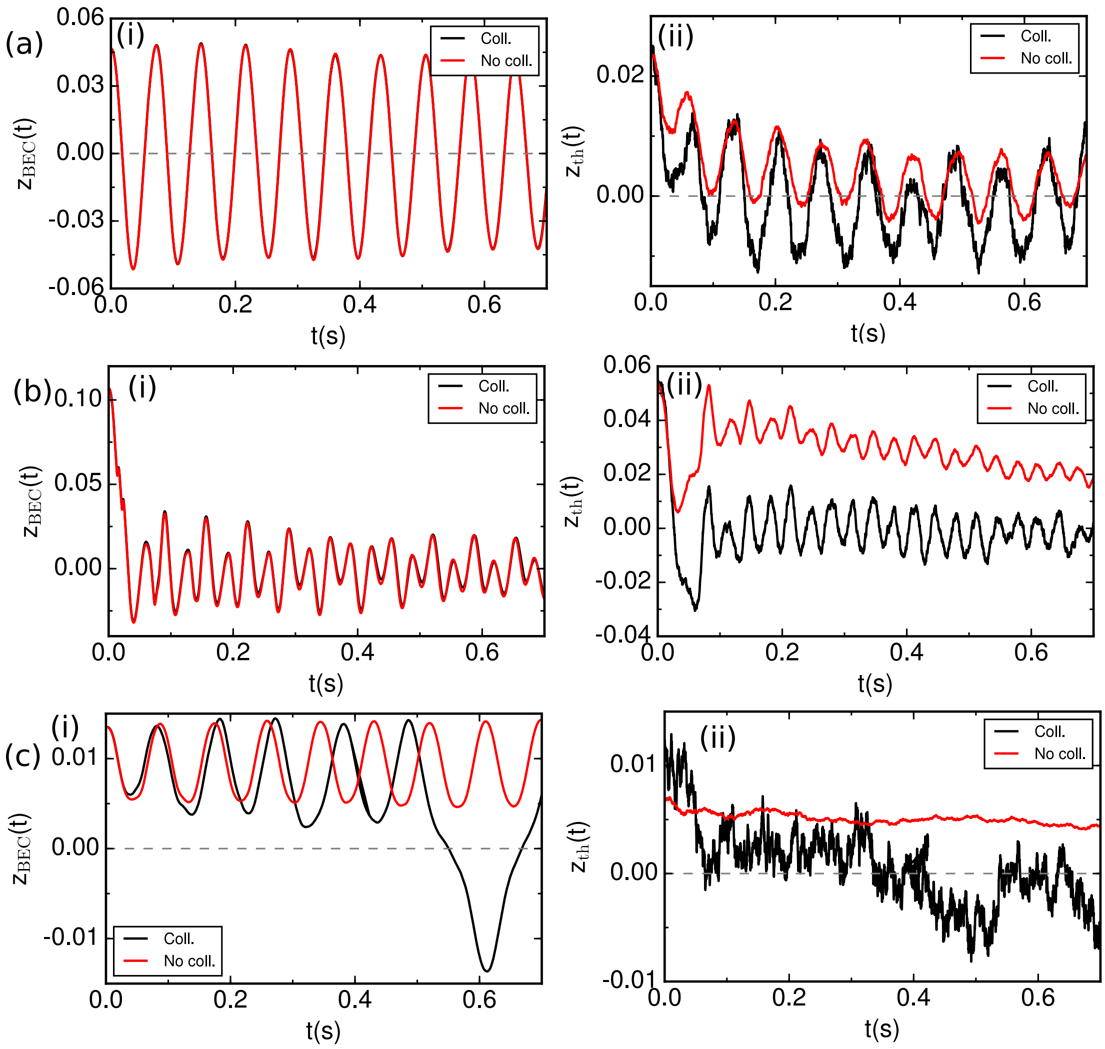

Figure 6.35: The condensate (i) and thermal population imbalance time evolution (ii) in the Josephson 'plasma' regime (a), in the vortex-induced dissipative regime (b) and in the MQST regime (c) at $T = 0.22T_c$. The data in (a)-(b) are both for $V_0 = 104\hbar\omega_x$, but $z^0_{\mathrm{BEC}} < z_{cr}$ in (a) while $z^0_{\mathrm{BEC}} > z_{cr}$ in (b). The data in (c) are for $V_0 = 210\hbar\omega_x$ and $z^0_{\mathrm{BEC}} = z_{\mathrm{cr}}$. In all cases $N_{\mathrm{BEC}}(t = 0) \approx 50400$.

the temperature associated to the barrier height value $V_0 = 104\hbar\omega_x$, i.e. $k_B T = V_0$, chosen for the study of Josephson and vortex-induced dissipative regime. We note that in the study of the MQST regime, the selected barrier height value $V_0 = 210\hbar\omega_x$ corresponds to a temperature $T_{\mathrm{eff}} = V_0/k_B \simeq 140nK$, i.e. double the value $T = 70$nK chosen for the plots Fig. 6.36. The respective plots of the $z_{\mathrm{BEC}}(t)$ and $z_{\mathrm{th}}(t)$ in all the three regimes are shown in Fig. 6.36. At this temperature the $z_{\mathrm{BEC}}(t)$ profiles in the Josephson (Fig. 6.36(a)) and dissipative regime (Fig. 6.36(b)) reveals that the collisions damps further the imbalance oscillations amplitude, interestingly with a larger effect in the dissipative regime (as will

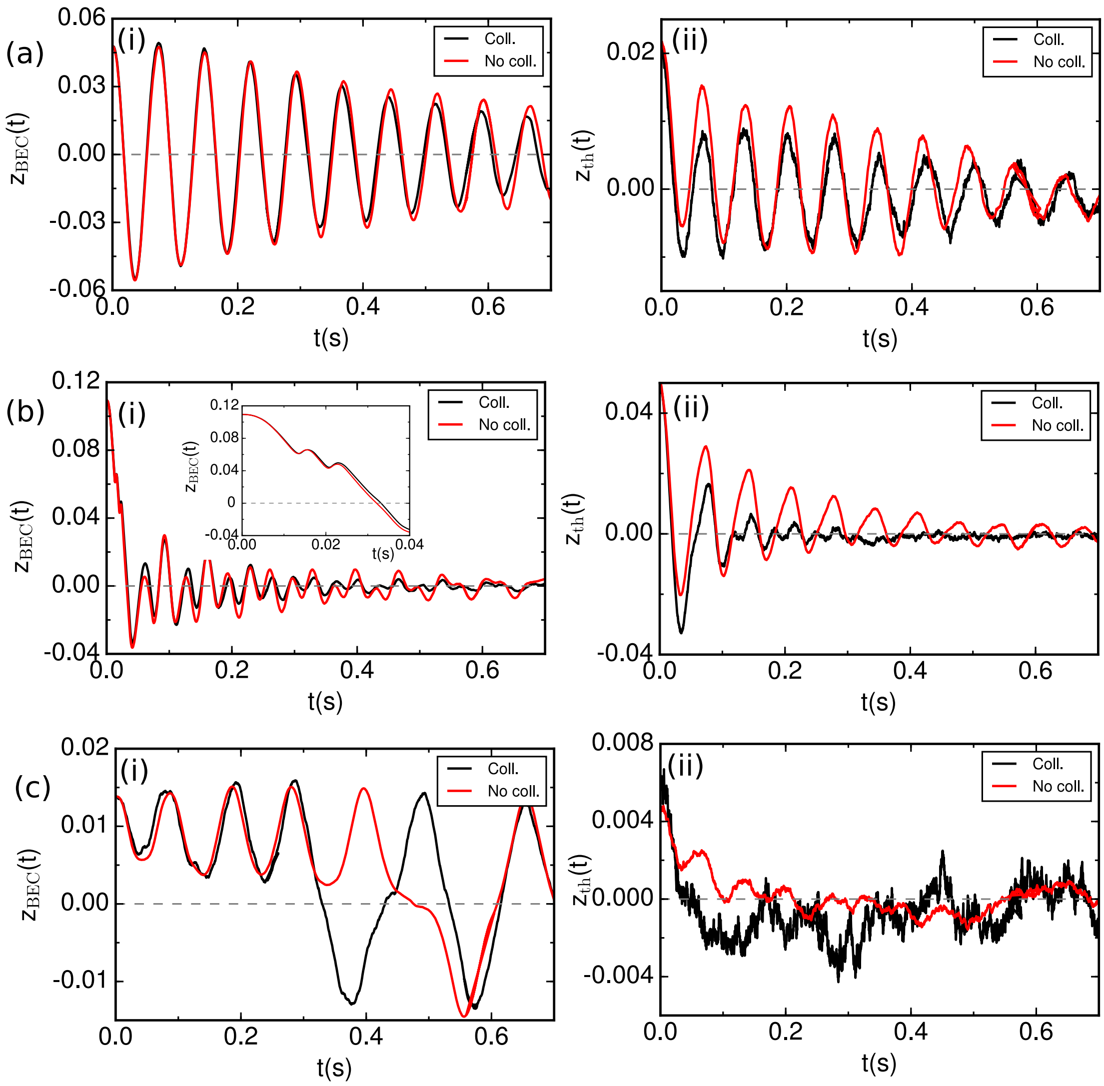

Figure 6.36: The condensate (i) and thermal population imbalance time evolution (ii) in the Josephson 'plasma' regime (a), in the vortex-induced dissipative regime (b) and in the MQST regime (c) at $T = 0.5T_c$. The data in (a)-(b) are both for $V_0 = 104\hbar\omega_x$, but $z_0^{\mathrm{BEC}} < z_{cr}$ in (a) while $z_0^{\mathrm{BEC}} > z_{cr}$ in (b). The data in (c) are for $V_0 = 210\hbar\omega_x$ and $z_0^{\mathrm{BEC}} = z_{cr}$. In all cases $N_{\mathrm{BEC}} \simeq 50400$ is fixed.

be described later). The collisions damps more, with respect to $T = 0.22T_c$, also the $z_{\mathrm{th}}(t)$ amplitude in time; being so totally damped at $t = 0.4$s in the dissipative regime (Fig. 6.36 (b)-(ii)). Fig. 6.36(b)-(i) shows a zoomed-in of $z_{\mathrm{BEC}}(t)$ profile at early time evolution, showing that the collisions have practically no effect at the start time of the 'dips', i.e. at the VR generation time (or better the time the VR enters the local TF surface, as described in Chapt. 3 and Chapt. 5 for $V_0/\mu \simeq 1$) and slightly affects the decay time (i.e. the time when $z_{\mathrm{BEC}} = 0$). At this higher T in the MQST regime, the condensate imbalance decay time and profile differs from run to run and these differences are even more pronounced in the collisional limit. Thus the results in Fig. 6.36(c) is just an example of different possible cases.

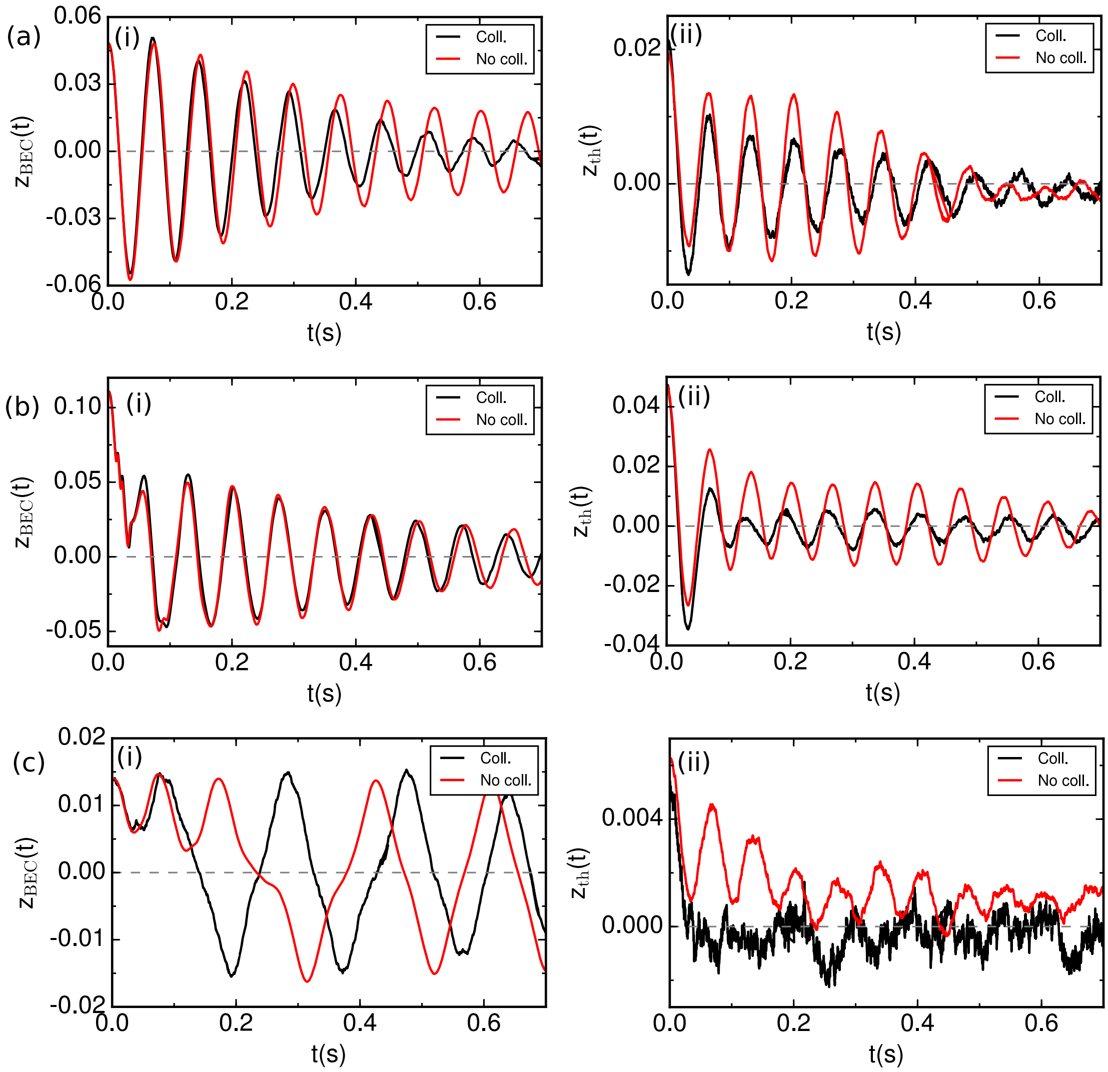

Figure 6.37: The condensate (i) and thermal population imbalance time evolution (ii) in the Josephson 'plasma' regime (a), in the vortex-induced dissipative regime (b) and in the MQST regime (c) at $T = 0.58T_c$. The data in (a)-(b) are both for $V_0 = 104\hbar\omega_x$, but $z^0_{\rm BEC} < z_{cr}$ in (a) while $z^0_{\rm BEC} > z_{cr}$ in (b). The data in (c) are for $V_0 = 210\hbar\omega_x$ and $z^0_{\rm BEC} = z_{cr}$. In all cases $N_{\rm BEC} \simeq 50400$ is fixed.

The next temperature we show is $T = 0.58T_c$, with the profiles of $z_{\rm BEC}(t)$ and $z_{\rm th}(t)$ shown in Fig. 6.37. In the Josephson 'plasma' regime (Fig. 6.37(a)) the collisions introduce even more damping of the amplitude of $z_{\rm BEC}(t)$ and $z_{\rm th}(t)$ with respect to the collisionless case. Interestingly, the collisions have small effects in the $z_{\rm BEC}(t)$ in the dissipative regime (Fig. 6.37(b)-(i)) while strongly influencing the $z_{th}(t)$ (Fig. 6.37(b)-(ii)). In the MQST regime, is shown just as an example of possible profiles $z_{\rm BEC}(t)$ and $z_{\rm th}(t)$, but it can change significantly from run to run.

6.7.1 The effect of collisions on the main oscillation frequencies

At one of the temperature explored, $T = 74\mathrm{nK} = 0.52\mathrm{T_c}$, in the dissipative regime and in the collisional limit we find an interesting behaviour: our results are usually obtained from a total of five different runs [2] for each T explored and for $T = 74nK$ we find that in two of the runs the $z_{\mathrm{BEC}}(t)$ shows a profile as in Fig. 6.38(a) while in the other three runs the $z_{\mathrm{BEC}}(t)$ profile is different with a typical example shown in Fig. 6.38(b). The $z_{\mathrm{BEC}}(t)$ in (a), in both collisionless and collisional limit, oscillates mainly with the frequency ν_1^{BEC} while in (b) the $z_{\mathrm{BEC}}(t)$, in the collisional limit, oscillates mainly with the ν_J^{BEC}. The last profile reminds us the one in Fig. 6.36(b)-(i) found at a higher temperature $T = 88\mathrm{nK} = 0.58T_c$. It seems that at high enough T, the collisions can even invert the role of the dominant frequency.

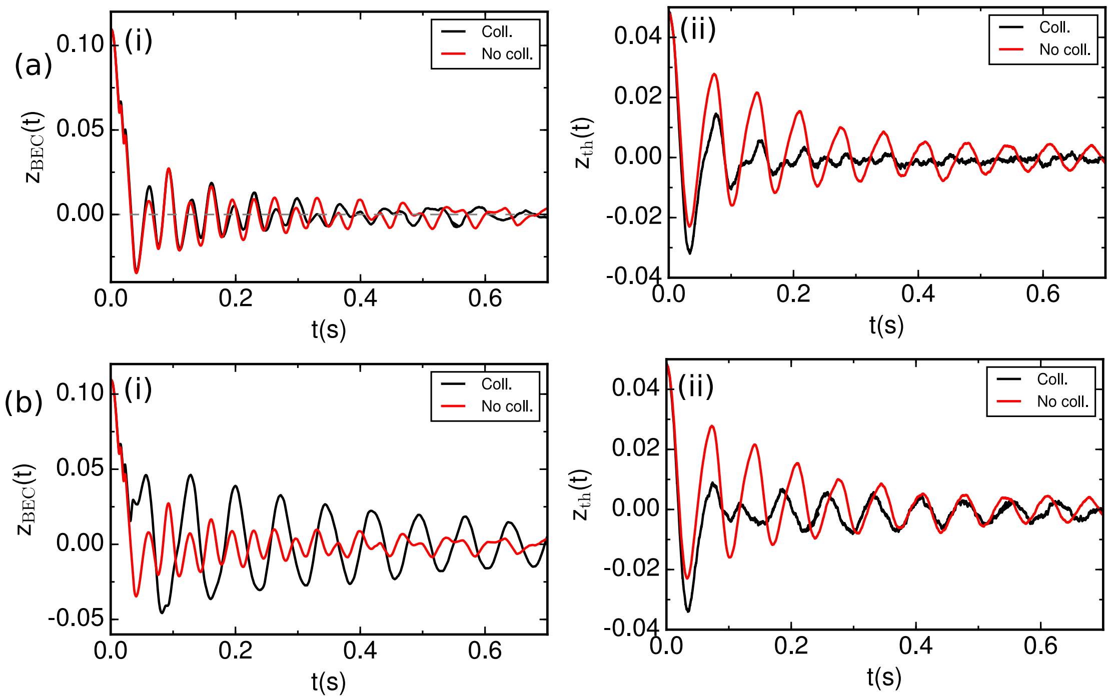

Figure 6.38: The condensate (i) and thermal imbalance (ii) time evolution for two different runs in the collisional limit at $T = 74nK$=$0.52T_c$. The data are for $V_0 = 104\hbar\omega_x$, $N_{\mathrm{BEC}}(t = 0) \simeq 50400$ and $z^0_{\mathrm{BEC}} > z_{cr}$ (vortex-induced dissipative regime).

We then perform a two-component frequency fit (for simplicity) of $z_{\mathrm{BEC}}(t)$ at different T and we show the results of each-component relative amplitude in Fig. 6.39 alongside with the corresponding two-component frequency fit results in the collisionless limit (we show

[2] in the collisional limit

only two-component frequency fit results in the collisionless limit for consistency with the collisional limit analysis). The results are for a single simulation run everywhere except $T = 0.52T_c$ which shows the results from two different runs of Fig. 6.29. We observe that, as it happens in the collisionless limit, for $T < 0.58T_c$ the $\nu_1^{\rm BEC}$ is the dominant frequency while for $T \geq 0.58T_c$ the $\nu_J^{\rm BEC}$ becomes the dominant one. Moreover in Fig. 6.39 are shown the results from the two different runs shown in Fig. 6.38 indicated with purple symbols (for the data in Fig. 6.38 (a)) and orange symbols (for the data in Fig. 6.38 (b)). From this analysis we confirm that at the two different runs the role of the dominant frequency is played by $\nu_1^{\rm BEC}$ in Fig. 6.38 (a) and by $\nu_J^{\rm BEC}$ in Fig. 6.38 (b).

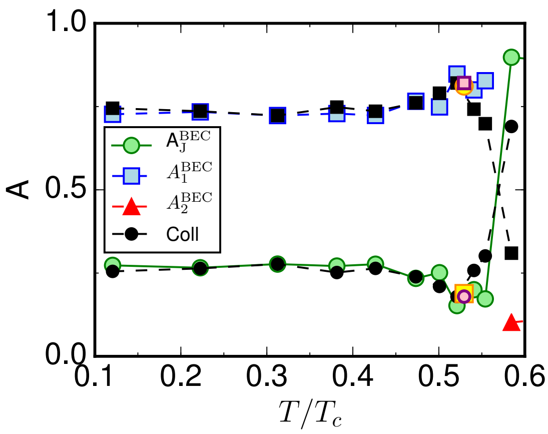

Figure 6.39: The relative amplitude of each component found from two-component frequency fit of $z_{\rm BEC}(t)$ at different temperatures both in the collisionless and collisional limit. The black symbols are in the collisional limit where the black squares indicate the relative amplitude of $\nu_1^{\rm BEC}$ and the black circles indicate the relative amplitude of $\nu_J^{\rm BEC}$. The purple and orange points are the data from two different runs at $T = 0.52T_c$. The parameters are $V_0 = 104\hbar\omega_x$, $N_{\rm BEC}(t = 0) \simeq 50400$ and $z^0_{\rm BEC} > z_{cr}$ (vortex-induced dissipative regime).

Finally, for the Josephson and dissipative regime, we fit the $z_{\rm BEC}(t)$ and $z_{\rm tot}(t)$ at each of the five runs with two-component frequency fit and take their mean value as best estimate of our results with the errorbars given by the maximum deviation. Fig. 6.40 shows the results for the dominant frequency in (a) the Josephson 'plasma' $\nu_J^{\rm BEC}$ and $\nu_J^{\rm tot}$ and (b) dissipative regime for $\nu_1^{\rm BEC}$ and $\nu_1^{\rm tot}$. Firstly, we observe that the inclusion of collisions affects differently the dominant frequency in the Josephson and dissipative regime both for the condensate and total imbalance. In fact, in the former case collisions soften the effect of the decrease of $\nu_J^{\rm BEC}$ and $\nu_J^{\rm tot}$ value with temperature. For $T < 0.5T_c$ the damping rate in the collisional limit has similar value to the collisionless limit but when the thermal cloud starts having more of an effect and exhibiting its own motion, i.e. for $T \gtrsim 0.5T_c = V_0/k_B$, the damping rate $\gamma_J^{\rm BEC}$ and $\gamma_J^{\rm tot}$ becomes larger in the collisional limit. In the dissipative regime instead, the collisions makes the $\nu_1^{\rm BEC}$ (i) and $\nu_1^{\rm tot}$ (ii) achieving smaller values with respect to the collisionless limit (for the same T/T_c) but with a profile similar to the collisionless limit. Moreover, the damping rates $\gamma_1^{\rm BEC}$ and $\gamma_1^{\rm tot}$ are larger in the collisional limit almost the entire range of T. Interestingly, $\nu_1^{\rm BEC}$ and $\nu_1^{\rm tot}$ in the dissipative regime are damped faster with respect to the dominant frequency $\nu_J^{\rm BEC}$ and $\nu_J^{\rm tot}$ in the Josephson regime. The reason for that could be that, if the frequency $\nu_1^{\rm BEC(tot)}$ originates from the coupling between the condensate and noncondensate states through tunneling, in the presence of the thermal cloud and in particular, when including the full coupling between the thermal and condensate clouds, (i.e. both the mean-field potential and the collisional integrals) could cause the sound waves amplitude decaying faster.

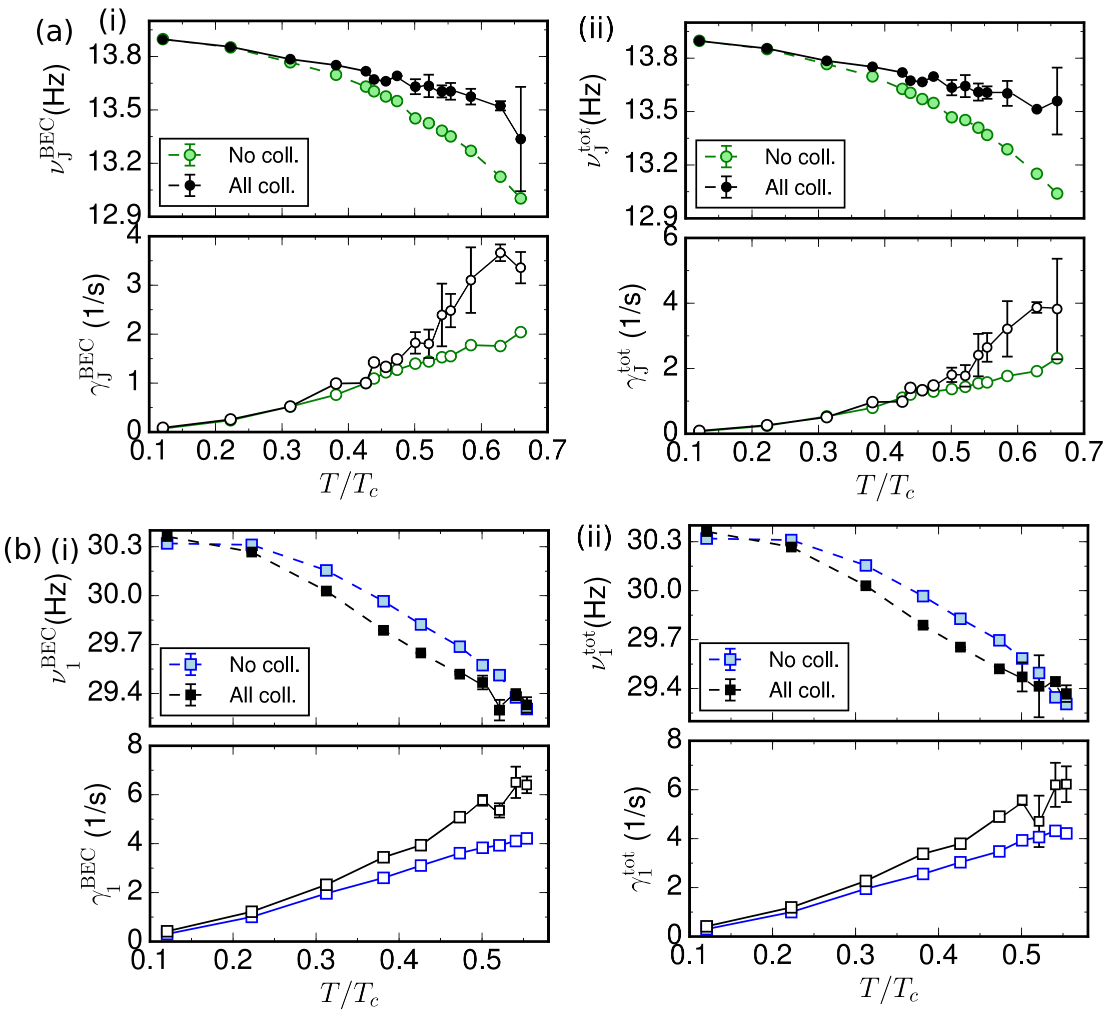

Figure 6.40: The dominant frequency profile as a function of the temperature and the corresponding damping rates in the Josephson (a) and dissipative regime (b) in both the collisionless and collisional limit. The data are for $V_0 = 104\hbar\omega_x$, $N_{\rm BEC}(t=0) \simeq 50400$ and $z^0_{\rm BEC} > z_{cr}$ (vortex-induced dissipative regime). In (a) the mean value for the highest two temperatures is extracted from two runs while the rest of the numerical data are the results from five runs.

The only analysis we perform for the MQST regime (due to the sensitivity of MQST on the presence of thermal cloud) is the study of the effect of collisions on the decay time of MQST with the results from the five different runs shown in Fig. 6.41. We observe that the effect of the collisions is to slightly reduce the MQST decay time.

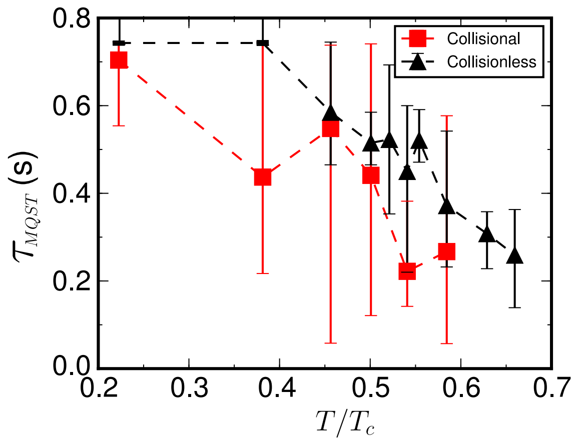

Figure 6.41: The profile of the mean decay time of the condensate imbalance in the collisionless and collisional limit as a function of the temperature. The data are for $V_0 = 210\hbar\omega_x$ and $N_{\rm BEC}(t = 0) \simeq 50400$.

6.8 The vortex ring dissipative dynamics at finite T

The vortex rings are characterized by a core where the condensate density goes to zero and its size is defined by the condensate healing length ξ. The VR core at finite T is filled by the thermal cloud, i.e. it acts like a local 'trapping' potential for the thermal particles. This picture becomes clearer by looking at the transverse (a) condensate and (b) thermal cloud density as reported in the Fig. 6.42. The thermal cloud is concentrated at the almost-circular vortex core where the condensate density has a local minimum and it also surrounds the condensate by being additionally concentrated at the edges of the condensate.

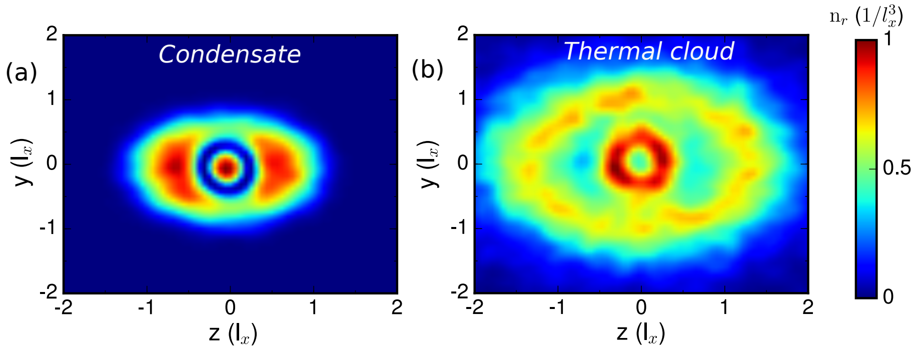

Figure 6.42: Density profile along the trasverse $y-z$ plane at the position $x = x_{\text{VR}}$ of the condensate (a) and thermal cloud (b) at $t = 17.4$ms time evolution (b) where a VR is present for $V_0 = 67.2\hbar\omega_x = 0.6\mu(T=0)$, $z^0_{\text{BEC}} = 0.19$ and $T = 0.53T_c$. The density in each plot is rescaled to the maximum density.

6.8.1 Thermal cloud induced phase slippage

In Chapt. 4 we showed that at $T = 0.3T_c$ the thermal cloud has practically no effect on the condensate velocity and vortex ring nucleation. Here we consider higher temperatures. The barrier height chosen is $V_0 = 67.2\hbar\omega_x = 0.6\mu(T=0)$ and $z^0_{\text{BEC}} = 0.19$. In this section we kept fixed the condensate number to $N_{\text{BEC}} \simeq 6\times10^4$ as in Chapt. 4 and differently from the value $N_{\text{BEC}} = 50400$ chosen in the rest of this chapter. The chosen barrier height value in this section corresponds to an effective temperature $T_{eff} = V_0/k_B \simeq 45$nK. In order to show the effect of the thermal cloud on the VR generation we study the profile of the condensate density-weighted x axis velocity defined as in Eq. (3.25):

$$\langle v_x \rangle = \frac{\int v_x \cdot |\psi(x=0,y,z)|^2 dydz}{\int |\psi(x=0,y,z)|^2 dydz} \,, \tag{6.16}$$

where $|\psi(x = 0, y, z)|^2$ is the condensate density along x axis and the integrations take into account the condensate transverse extention at $x = 0$. The time evolution of $-\langle v_x \rangle$ at different temperatures is shown in Fig. 6.43. As we described in Chapt. 3 and as it is evident in Fig. 6.43, the condensate velocity increases initially in time, due to the presence of an initial chemical potential gradient across the barrier, until it achieves a local maximum value which exceeds a critical velocity and a VR is generated. The VR generation causes the condensate phase to slip by around 2π (phase-slippage mechanism) and the condensate density-weighted velocity to jump almost abruptly to a smaller value by a quantized quantity $\mathit{\Delta} \langle v_x \rangle$. Interestingly, at $T = 0$, the condensate velocity $-\langle v_x \rangle$ shows two local maxima but only the first one exceeds the critical velocity for VR generation and thus only one VR is generated at $z_0 = 0.19$, i.e. $z_{\rm cr} = 0.19$. In fact, the $-\langle v_x \rangle$ shows only one abrupt jump in the correspondence of the vortex ring nucleation at $t \sim 15$ms. At a first approximation, the first $-\langle v_x \rangle$ peak gives an estimation of the threshold or critical velocity for VR generation. As T increases the $-\langle v_x \rangle$ profile, which shows more 'noise', achieves its maximum value earlier in time, which means that the VR is nucleated earlier in time at higher T. Moreover this maximum value is almost independent on the temperature.

Another interesting feature of the profile in Fig. 6.43 is the presence of the second local peak of $-\langle v_x \rangle$ whose value is close to the value of the threshold velocity (i.e. first peak value) but it is still not high enough to generate a vortex ring. As T increases and as the thermal particles energy approaches V_0, the value of the second peak increases. Then, at $T = 0.48T_c > T_{eff}$, the second peak exceeds the first peak value and the condensate velocity exhibits a second abrupt jump, thus a second VR is nucleated. As at slightly smaller temperature $T = 0.42T_c$, the second peak value is close to the $-\langle v_x \rangle$ first maximum but still no second VR is generated, we choose it instead as a threshold $-\langle v_x \rangle_{thr}$ or critical velocity such that for $-\langle v_x \rangle > v_c$ there is a second VR generated. Such value is indicated as a dashed horizontal grey line in Fig. 6.43. Note that this value is 15% different from the value we estimated for the critical velocity during the barrier removal process which was set by $\langle c \rangle = \sqrt{\mu/2M}$.

As the temperature goes from $T = 0.48T_c$ to $T = 0.59T_c$ the second local peak condensate velocity decreases its value, and also the velocity jump $\mathit{\Delta} \langle v_x \rangle$ decreases. Summarizing, an increasing thermal cloud fraction with T has three main effects: Firstly, for the first VR which is also present at $T = 0$, the thermal cloud causes the nucleation of such VR earlier in time. Secondly, as T increases, the larger thermal cloud enhances the second peak velocity value (which was near the $-\langle v_x \rangle_{thr}$ even at $T = 0$) and the thermal induced phase fluctuations could even cause the nucleation of a second VR. Contrary to this effect and for temperature even larger, in our case for $T > 0.48T_c$, the thermal cloud reduces the second maximum value of the condensate velocity. The thermal induced phase slippage has been studied in different geometries and dimensionality [54, 242, 243, 58, 56].

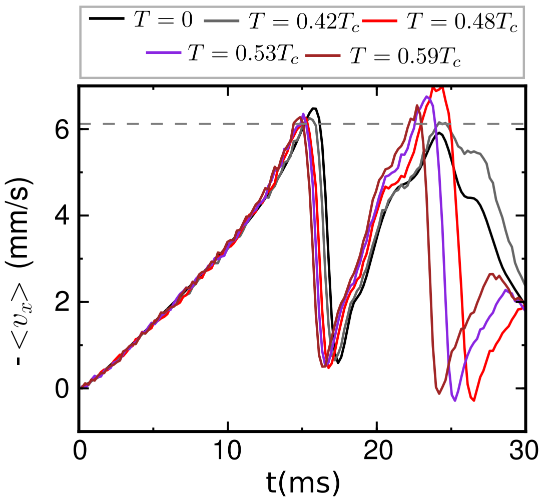

Figure 6.43: The time evolution of the density weighted condensate velocity along x-axes at different temperatures. The data are for $V_0 = 67.2\hbar\omega_x = 0.6\mu(T=0)$, for $N_{\rm BEC} \simeq 60000$ and for $z_0^{\rm BEC} = 0.19$. The vertical dashed line indicate the threshold value of $-\langle v_x \rangle_{thr}$ set by the second peak in the condensate velocity where there are no VR generated. For $-\langle v_x \rangle > -\langle v_x \rangle_{thr}$ there is a second VR generated.

Moreover we check that the second VR at $T = 0.48T_c$ is not related to the shift in the initial condensate imbalance induced by the thermal cloud as discussed in Sect. 6.4.7. In fact, Fig. 6.44(a) shows the short-time evolution of the condensate imbalance at $T = 0$ and $T = 0.48T_c$ for the same (within 10^{-4}) initial condensate imbalance. We find that the second 'dip' is not present in the population imbalance profile at $T = 0$ which means that its origin is connected to the presence of the thermal cloud. Fig.6.44(b) shows the relative phase along the x axis (for $y = z = 0$) at some of the temperatures explored previously. At $T = 0$ there is only one 'dip' in the $z_{\rm BEC}(t)$ profile and the relative phase shows only one jump. At $T = 0.48T_c$ a second 'dip' appears in the $z_{\rm BEC}(t)$ and the relative phase shows a second jump, thus a second VR is generated. This phenomena can be explained by the fact that the thermal cloud causes phase fluctuations which induces phase slippage and a second VR is generated. As also observed from Fig. 6.44(b) the phase-slippage happens earlier in time at higher T, confirming the results found from the condensate velocity profile.

6.8.2 The vortex ring thermal-induced dissipative dynamics

The thermal excitations are scattered by the vortex [244] and in this process there is a momentum transfer between the thermal excitations and the vortex. This momentum transfer per unit time defines a friction force which is responsible for the drifting of the vortex off-center; this is expected to be larger at higher temperature. Based on this

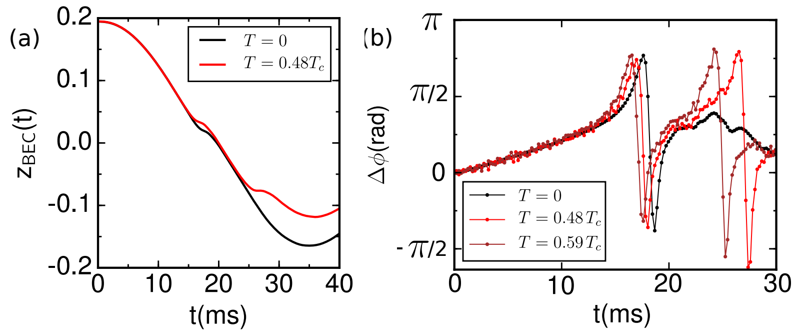

Figure 6.44: (a) The short-time evolution of the condensate population imbalance at $T = 0$ and at $T = 0.48T_c$ for the same initial condensate imbalance. (b) The temporal profile of the relative phase along x axis calculated for $y = z = 0$ and at different temperatures. The data are for $V_0 = 67.2\hbar\omega_x = 0.6\mu(T = 0)$, for $N_{\rm BEC} \simeq 60000$ and for $z^0_{\rm BEC} = 0.19$.

argument, we extract the vortex ring center in the transverse $y - z$ plane defined as $r_0(t) = \sqrt{y_0^2(t) + z_0^2(t)}$, where y_0 and z_0 are the vortex center along y and z axis.

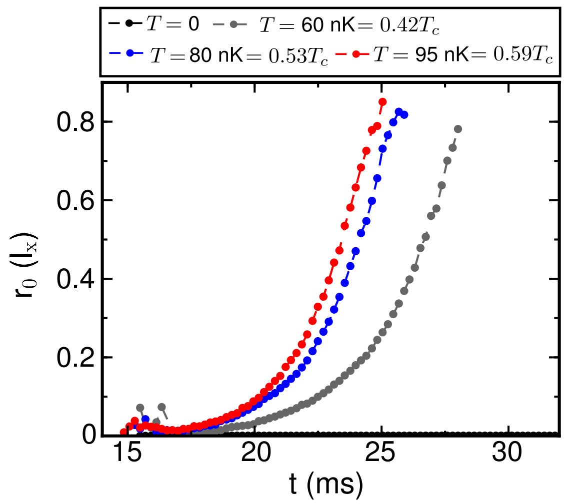

Figure 6.45: The first vortex ring time evolution of the center in the radial plane at different temparature for $V_0 = 67.2\hbar\omega_x = 0.6\mu(T = 0)$, for $N_{\rm BEC} \simeq 60000$ and for $z_0^{\rm BEC} = 0.19$.

This study is performed at different temperatures with Fig. 6.45 showing the time evolution of $r_0(t)$ for the first VR generated at each explored temperature. At $T = 0$ the vortex ring center remains at zero during all the VR evolution. At finite T instead, the vortex ring center increases from an initial value near zero and this increase is exponential as also found by [113, 112, 115] of the form $r_0(t) = ae^{\gamma t}$, where γ gives the rate of the VR center increase. As expected, at higher T the vortex goes off-center faster and thus γ becomes larger. By fitting the numerical data in the time interval $[16, 24]$ ms we find that the value of γ changes by $\Delta\gamma \simeq 0.06(1/\text{ms})$ between the lowest $T = 60\text{nK} = 0.42\text{T}_\text{c}$ and the highest temperature $T = 95\text{nK} = 0.59\text{T}_\text{c}$ explored. As the VR approaches the edges of the condensate, the effect of the vortex images becomes important as the distance between the vortex and its image decreases. This makes the VR go off-center faster during the last part of its evolution after 24 ms. When the vortex ring then reaches the condensate edges, it breaks in one long single line (or in other words, the vortex reconnects with its image). While the VR goes off-center its elliptic profile shows also an inclination induced by the thermal cloud.

For each T, the VR mean radius is extracted with its time evolution given in Fig. 6.46. This plot does not take into account the vortex core finite size. In our analysis, whose results are shown in this plot, we start the VR tracking at the moment the VR enters the condensate transverse extension at $x = 0$.

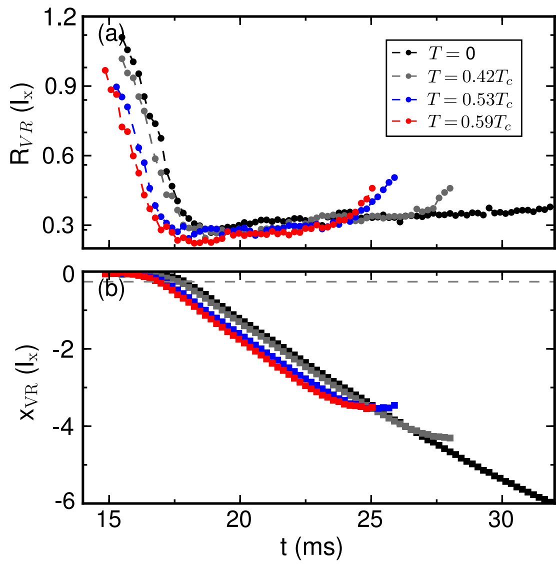

Figure 6.46: The time evolution of the first vortex ring radius at different temperatures. The data are for $V_0 = 67.2\hbar\omega_x$, for $N_{\rm BEC} \simeq 60000$ and for $z^0_{\rm BEC} = 0.19$.

We observe that at higher T the VR initial radius is smaller. Further insight is given by looking at the transverse condensate density at $T = 0$ and at $T = 0.59T_c$ for $x = 0$ shown in Fig. 6.47. We observe that at finite T the condensate transverse extension is smaller, due to surrounding thermal cloud (not shown in this plot), and it presents some fluctuations. These fluctuations could facilitate the VR entrance inside the TF surface, which in fact occurs earlier in time at higher T, and the VR initial radius is smaller.

Except for $T = 0$, in all other case the VR dynamics is shown until the VR breaks in one-single vortex line. An example of the VR dynamics at finite T is shown in Fig. 6.48 for $T = 95$nK, consistent with the description given in Chapt. 4, the VR goes off-center in time until breaks in one long single vortex when it reaches the condensate edges in (d). In (b) we observe that the VR core is thinner in the part of the VR which is more distant from the edge, i.e. where the condensate density is larger, and it becomes thicker at the

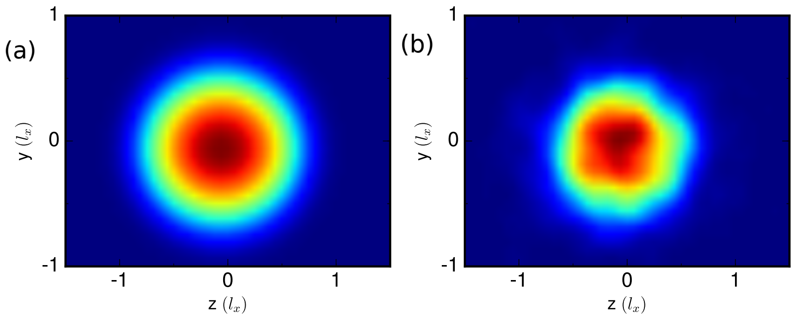

Figure 6.47: The transverse condensate density for $x = 0$ at $T = 0$ (a) and $T = 95$nK (b) at 14.9 ms. The data are for $V_0 = 67.2\hbar\omega_x$, for $N_{\rm BEC} \simeq 60000$ and for $z^0_{\rm BEC} = 0.19$.

other extreme. The results shown in this section are from a single run but we expect the direction the VR goes offcenter to be different from run to run even though the underlying physics is the same. Another thing to note is that our VR is elliptic when it is generated and thus it shows Kelvin-wave excitations (as described in Chapt. 3 and Chapt. 4) which further dissipates the VR motions.

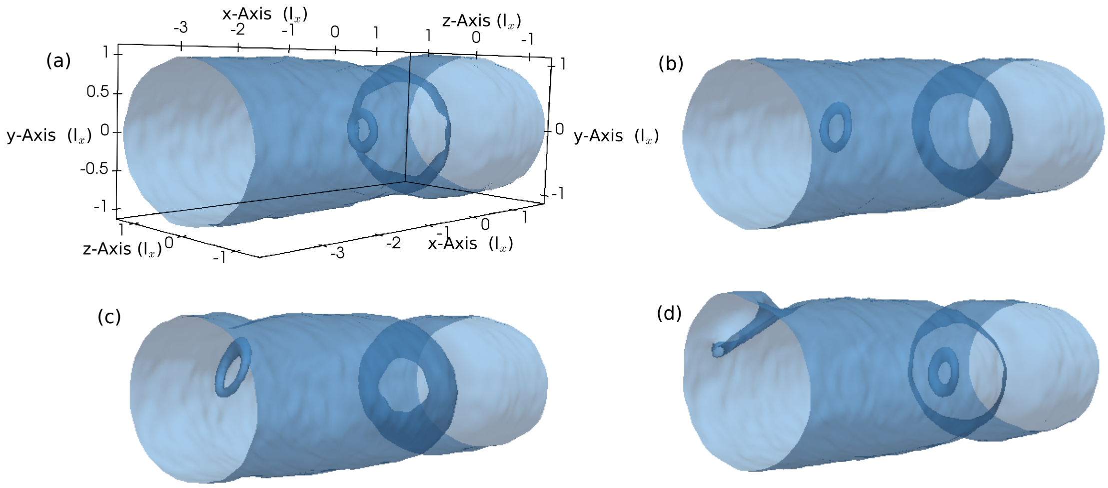

Figure 6.48: The 3D isocontour density plot at 15% of maximum density at different time evolution (a) $t = 18$ms, (b) $t = 21.2$ms, (c) $t = 22.9$ms and (d) $t = 24.8$ms for $T = 0.59T_c$, for $V_0 = 67.2\hbar\omega_x = 0.6\mu(T = 0)$, $N_{\rm BEC} \simeq 60000$ and for $z^0_{\rm BEC} = 0.19$.

6.8.3 The effect of collisions

For one of the temperatures explored $T = 0.42T_c$ we show in Fig. 6.49 also the effect of the collisions between condensate-thermal and between thermal-thermal particles.

The collisions introduce more friction between the vortex and thermal excitations increasing the rate γ of the vortex ring center and according to the reference [112, 115] the main contribution comes from the exchange collisions term C_{12}. Furthermore, collisions

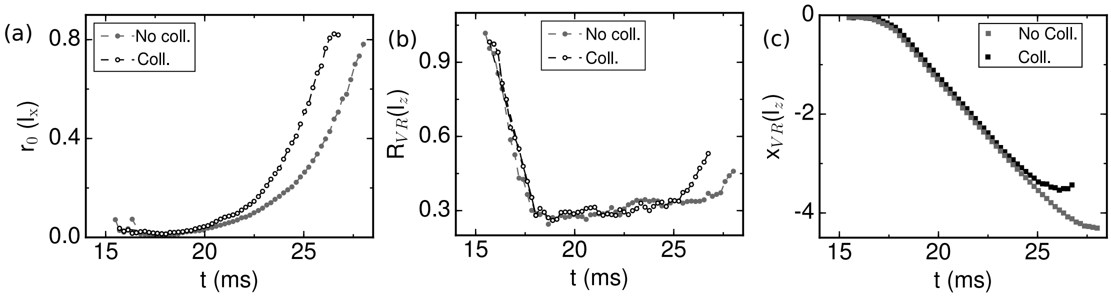

Figure 6.49: The time evolution of the first vortex ring (a) center in the radial plane, (b) mean radius and x axis position (x_{VR}) at $T = 60\text{nK} = 0.42\text{T}_\text{c}$ in the collsional and collisionless limit. The data are for $V_0 = 67.2\hbar\omega_x$, for $N_{\text{BEC}} \simeq 60000$ and for $z^0_{\text{BEC}} = 0.19$.

have no significative effect on the VR mean radius and position x_{VR} at short time evolution while they strongly effects the VR dynamics during the end of its lifetime (at $t \sim 25$ms); the collisions causes the VR radius to increase faster and then VR slows its motion and it can even reverses its direction (visible in Fig. 6.49(c)) while going off-center.

6.9 Conclusions and future work

6.9.1 Conclusions

In this chapter, we analyzed the role of thermal dissipation in the three main dynamical regimes found in an elongated three-dimensional Josephson junction: the Josephson 'plasma' regime, the vortex-induced dissipative and MQST or pure self-trapped regime. To model our system at finite T we used ZNG model, a self-consistent theory, which incorporates a dynamical thermal cloud and its back action on the condensate. We started by studying the dynamical evolution of the condensate/thermal/total population imbalance across the Josephson and dissipative regimes, and analyze their dominant contributions and corresponding frequencies of oscillations. In particular, in the vortex-induced dissipative regime the analysis was perfomed after the initial decay, i.e. after the vortex rings generation. Such study was performed firstly in the collisionless limit. The range of temperature probed by us was $[0.1, 0.7]T_c$, and we initially kept fixed condensate number $N_{\text{BEC}} \simeq 50400$ fixing so the condensate axial extension. The chosen barrier height was $V_0 = 104\hbar\omega_x \simeq \mu(T = 0)$, for which the Josephson 'plasma' and vortex-induced dissipative regimes were found for $z_0 < z_{\text{cr}} = 0.08$ and $z_0 > z_{\text{cr}}$ respectively.

We identified two distinct dynamical regimes, namely a low temperature regime ($k_BT < V_0$) in which the small thermal cloud is driven by the condensate, and a high temperature regime ($k_BT \gtrsim V_0$) in which the thermal cloud has enough energy to overcome the barrier, and thus begins to drive the condensate. The dominant frequencies identified are the Josephson plasma frequency ν_J , its second order contributions ν_1, and a characteristic frequency of the thermal cloud ν_2 which is close to the underlying harmonic trap frequency. These frequencies are found to be relevant in both the Josephson plasma and the dissipative regimes. The associated temperature to the barrier height value is $T_{\text{eff}} = V_0/k_B = 70\text{nK} = 0.5\text{T}_\text{c}$.

In particular, for the condensate imbalance, we showed that at low temperatures $k_BT < V_0$, the frequencies $\nu_J^{\text{BEC}} \approx 14\text{Hz}$ and $\nu_1^{\text{BEC}} \approx 30\text{Hz}$ are the dominant ones. As the temperature increases towards T_{eff}, i.e. as the thermal fraction increases, the thermal particles have sufficient kinetic energy to exhibit their own motion at a frequency $\nu_2^{th} \approx 15\text{Hz}$. Thus, the thermal cloud back action to the condensate motion affects this latter spectrum with the appearance of a frequency $\nu_2^{\text{BEC}} \approx 15\text{Hz}$ for temperatures such that $k_BT \gtrsim V_0$.

However, we found an important distinction between the Josephson and vortex-induced dissipative regime: although the dominant frequencies are the same, their relative contributions and phases of oscillations are not. Specifically, in the low temperature limit, in the Josephson regime the ν_J^{BEC} is the dominant frequency at more than 97%, while in the dissipative regime its contribution becomes less than 30% with the ν_1^{BEC} being the dominant frequency at more than 70% of relative contribution. Moreover even the relative phase between the two components is different in two regimes: in the Josephson 'plasma' regime the ν_1^{BEC} has a relative phase of π with respect to ν_J^{BEC}, while in the dissipative regime the relative phase is around $\pi/2$. In the Josephson regime, based on these findings on the relative phase between the components and on the fact that $\nu_1^{\text{BEC}} \approx 2\nu_J^{\text{BEC}}$, we attributed the origin of ν_1^{BEC} to the second-order non dissipative term in the current-phase relation coming from considering the tunneling process between condensate-noncondensate states across the junction as described in [65]. In the vortex-induced dissipative regime, given the dominant role played by the generated vortex rings and associated sound waves, a second-order dissipative term instead becomes important which, as shown in [65], has a relative phase of $\pi/2$ with respect to ν_J^{BEC}. Even though the last observation requires further future investigation, we think it is the most probable scenario.

In the intermediate regime ($k_BT \sim V_0$), all the three components ν_J^{BEC}, ν_1^{BEC} and ν_2^{BEC} are present in the condensate spectrum. We then characterized further the temperature dependence of the oscillation frequencies values and corresponding damping rates. Interestingly the dominant frequency in both regimes shows similar profile as a function of the temperature; it decreases its value with the temperature while the corresponding damping rate increases. The main difference is that the dominant frequency in the vortex-induced dissipative regime (ν_1^{BEC}) suffers more damping with respect to the dominant frequency ν_J^{BEC} in the Josephson regime. Therefore the ν_1^{BEC} in the dissipative regime is already damped at $T = 0.58T_c$ and the condensate oscillates mainly with ν_J^{BEC} frequency. These results seem to suggest that at high enough temperature the thermal cloud attenuates the sound wave's amplitude helping the condensate to oscillate around zero value mainly with the temperature-shifted Josephson frequency. In the Josephson regime, the dominant frequency $\nu_J^{\rm BEC}$ persists along the entire range of T explored having a contribution of more than 85% at the highest probed temperature $T = 0.66T_c$.

In particular, we showed that, in the dissipative regime, a drastic change happens in the $\nu_1^{\rm BEC}$ relative contribution: its contribution jumps from around 60% to 'disappearing' from the condensate spectrum at $T = 0.58T_c$. At this temperature another 'dip' appears in the initial fast decay of the $z_{\rm BEC}(t)$, i.e. another VR is generated. We showed that the reason for that is the following: when comparing different temperature, we fixed at the same value the linear tilted barrier shift $-\epsilon x$, which creates an initial condensate imbalance. As T increases, for the same ϵ, the initial condensate imbalance increases slightly and at $T = 0.58T_c$ this small shift is sufficient for inducing the generation of another VR. We checked that if instead of fixing ϵ, we fix the initial condensate imbalance to be the same at $T = 0$ and at $T = 0.58T_c$, the same number of VRs is generated. Moreover at $T = 0$ for this slightly larger z_0 the population imbalance oscillates in time with different frequencies where the $\nu_1^{\rm BEC}$ is not the dominant frequency, in contrast to the slightly smaller z_0 case of our analysis. These considerations alongside the effect of a large thermal cloud explain the drastic change in the relative amplitude of $\nu_1^{\rm BEC}$ at $T = 0.58T_c$.

Next we analyzed the thermal cloud population imbalance profiles. We showed that, one of the main oscillation frequencies of the thermal imbalance is a component ν_2^{th} which approaches the axial trap frequency $\nu_x = 15$Hz as the temperature increases. In fact, as the thermal particles kinetic energy exceeds the barrier height value, the increasing thermal component executes its own oscillations over the barrier, at a distinct frequency to that of condensate oscillations. Another interesting feature of the thermal imbalance spectrum along the entire range of temperatures is that it presents a second component which has a value close to the dominant condensate imbalance frequency, due to the mean-field coupling between condensate and thermal cloud.

We then analyzed the total population imbalance time evolution. We showed the the same three frequencies emerges also for the total imbalance appearing in the same temperature ranges: $\nu_J^{\rm tot}$, $\nu_1^{\rm tot}$ and $\nu_2^{\rm tot}$, where the first two are dominant for $k_BT < V_0$ while $\nu_J^{\rm tot}$ and $\nu_2^{\rm tot}$ become the main frequencies for $k_BT > V_0$. However, there is a critical difference between the condensate and total imbalance temporal profiels in the Josephson regime: the increase in temperature leads to an increase in the number of particles in the thermal cloud and as such, the relative contribution of $\nu_J^{\rm tot}$ decreases rapidly as the total population becomes more dependent on the increasing thermal contribution. In fact, at $T/T_c \sim 0.66$ the Josephson contribution is only 65% of the total amplitude and the total population difference exhibit some beating between $\nu_J^{\rm tot}$ and $\nu_2^{\rm tot}$ components (whose values are close to each other). Even in the dissipative regime, for $T \geq 0.58T_c$, the contributions of the two main components become comparable and the total imbalance presents beating.

Further to our analysis we investigated the effect of the thermal cloud in the MQST regime, where the barrier height was kept fixed at $V_0 = 210\hbar\omega_x \simeq 2\mu(T = 0)$. We showed that the MQST regime is highly unstable in the presence of the thermal cloud and its decay time can differ from run to run even in the collisionless limit. However, by extracting the mean decay time from five runs we showed that on average the MQST decay time becomes smaller at larger T.

We then considered the case of fixed total particle number, and we showed that having different condensate numbers at different T can make the condensate or total population imbalance to be in a different dynamical regime for the same value of the barrier height because V_0/μ is different.

We then added the effect of collisional integrals by including both the condensate-thermal and thermal-thermal collisions with the first one giving rise to particle exchange between the condensate and thermal cloud. We showed that at very low T (for example $T = 0.22T_c$) the collisions have no effect on the condensate imbalance but their presence strongly affects the thermal cloud imbalance. At such low temperature, the thermal dynamics across the barrier occurs via incoherent tunneling. Consequently, and in the collisionless limit, the thermal cloud remains 'trapped' in the right well for relatively long time. Interestingly, the inclusion of collisions helps the thermal particles to cross the barrier and the thermal imbalance temporal mean value becomes close to zero. Next, we showed the effect of collisions on the dominant frequency of the condensate and total imbalance in the Josephson and dissipative regime, with collisions found to add an extra damping conribution to the dominant frequency. Moreover, the ν_J^{BEC} and ν_J^{tot} in the Josephson regime decrease at a slower rate in the collisional limit while the ν_1^{BEC} and ν_1^{tot} decreeases slightly faster in the collisional limit. For the MQST regime we showed that the inclusions of collisions make the MQST decay faster with respect to collisionless limit.

We then showed the role of the thermal cloud on the VR nucleation and dynamics for a smaller barrier height $V_0 = 67\hbar\omega_x = 0.6\mu(T = 0)$, to which is associated an effective temperature of $T_{eff} = V_0/k_B \simeq 45$nK. The initial condensate imbalance was chosen such that only one VR is generated at $T = 0$ once the condensate maximum velocity exceeds a threshold value. Firstly, we found that the presence of the thermal induced phase fluctuations and transverse density fluctuations causes the generation of the VR earlier in time. Moreover, at $T = 0$, we showed that the condensate velocity has a second local maximum whose value is close to the threshold velocity for VR generation. Interestingly, as T increases, and thus the thermal fraction increases, the larger thermal cloud enhances the second peak value until it exceeds the threshold velocity and a second VR is generated. The thermally induced VR generation occurs at $T = 70\mathrm{nK} = 0.48\mathrm{T_c} > \mathrm{T_{eff}}$. Further increasing the temperature, leads to a reduction of the second peak velocity value. Thus, for smaller barrier height value V_0 and for temperature larger than V_0/k_B, the thermally induced VR could be generated. Finally, we showed that in the presence of the thermal cloud the VR 'drifts' off-center, due to the scattering of thermal excitations by the vortex [244]. Once the VR aproaches the condensate edges it breaks into one long vortex line. The rate at which the VR goes off-center increases with temperature, consistent with the results in [112, 115]. Thus the VR lifetime decreases with increasing temperature.

6.9.2 Future works

The origin of second order component at $T = 0$

Even at $T = 0$, for $N = 50400$ and for $V_0/\mu \simeq 1$ in the Josephson and dissipative regime we found a second component ν_1 with a frequency near 30Hz that has a contribution of 3% in the Josephson regime while becomes the dominant frequency in the dissipative regime. This second component is $\simeq 2.15\nu_J$ but it is also twice the x axis trap frequency. In this chapter, we attributed the origin of this second component to the presence of second-order term in the current-phase relation that oscillates with twice the Josephson frequency. In order to investigate further the origin of this component, if it comes from trapping potential, intra-well excitations or if it is relative to the tunneling physics, we studied the DFT spectrum of the population imbalance time evolution at different barrier heights and different initial imbalance. From the paper of Zapata *et al.* [60] the Josephson 'plasma' frequency is expected to be a fraction of the x axis trap frequency and it is expected to become smaller as the barrier height increases. Thus, if the second component ν_1 is related with ν_J then it will become smaller too. In this section our study is done at $T = 0$ and for a particle number $N = 6 \times 10^4$ as we have more statistics with respect to the $N = 5.04 \times 10^4$ case. Moreover, the addition of the linear tilted potential in our double-well trap in order to create an initial imbalance leads also to a non-zero value of the condensate center of mass COM along the x axis. After removing the linear potential, the condensate dynamics starts and collective modes could even be excited [2, 245, 246, 34] depending on the initial value of the axial COM. Such low energy collective modes frequencies could be calculated by solving the linearized Bogoliubov-de Gennes equations and it would be subject of further studies [247] but here we estimate the $m = 0$ collective excitation frequency by solving the equation (86) of the paper of Dalfovo *et al.* [34]. Such equation, for the low energy mode, gives a frequency of 23.7Hz for our trap frequencies that is different from the frequency 30Hz we found in our analysis. Another possibility can be that the 30 Hz frequency originates from the fact that our trapping potential is not purely quadratic but it has an anharmonic term due to the presence of the Gaussian barrier [245, 248]. If this is the case, than this term is expected to be larger for higher barrier heights but we will show that it does not happen for ν_1.

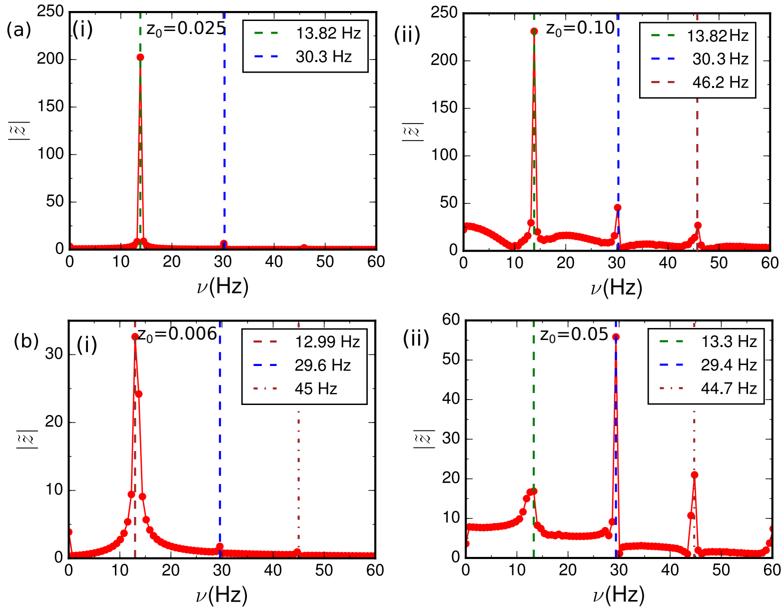

Figure 6.50: The Discrete Fourier Transform spectrum of the population imbalance for $V_0/\mu = 1$ (a) and $V_0/\mu = 1.17$ for $z_0 < z_{cr}$ (i) and for $z_0 > z_{cr}$ (ii). The data are for particle number $N = 60000$. The DFT resolution is around 0.7Hz.

L. J. LeBlanc *et al.* in Ref. [48] found that the hydrodynamic modes arising from the coupling between the x axis and transverse directions, due to the nonlinear interaction term and due the transversal axial asymmetry, vanish for barrier height around the chemical potential. According to this study, for $V_0/\mu \geq 1$ the Josephson frequency is the dominant frequency. Thus, the hydrodynamic modes should be negligible for our case $V_0/\mu \simeq 1$. In fact, we also consider here a barrier height $V_0/\mu \gtrsim 1$ in order to avoid having the contribution from hydrodynamic modes.

Fig. 6.50 shows the DFT spectrum of the population imbalance for $V_0/\mu = 1$ (a) and $V_0/\mu = 1.17$ (b) for $z_0 < z_{cr}$ (i) and for $z_0 > z_{cr}$ (ii). Interestingly, in both (a) and (b) in the Josephson 'plasma' (i) and in the dissipative regime (ii) we find the same components (within the DFT finite resolution). If in the Josephson regime [(a)-(b),(i)] the contribution of the second component ν_1 is around 3%, in the dissipative regime the second component contribution increases but it can still be less important than the Josephson frequency (at around 14Hz) as happens in (a)-(ii) or it can even become more important than the ν_J as occurs for $V_0/\mu = 1.17$ (b)-(ii). In the plots a third component is present at around 44Hz which it is three times the ν_x but it is also 3.3 times the ν_J. However we focus our attention on the first two components. Based on these two plots, if the origin of this frequency was from intra-well excitations then we would expect it to have more importance for larger z_0 and smaller V_0 as in (a)-(ii) but in our case the opposite happens. As the ν_1

frequency is also present in the DFT spectrum in the Josephson regime, another possible explanation (which we considered as the most probable reason) is that the ν_1 comes from the second-order term in the tunneling Hamiltonian [65] which has a frequency twice ν_J. If it is the case, then ν_J and ν_1 are expecting to become smaller as the barrier height increases. Moreover, we note that we are looking at the $z(t)$ and not at the current-phase relation and a better future analysis could be to study the current-phase relation instead.

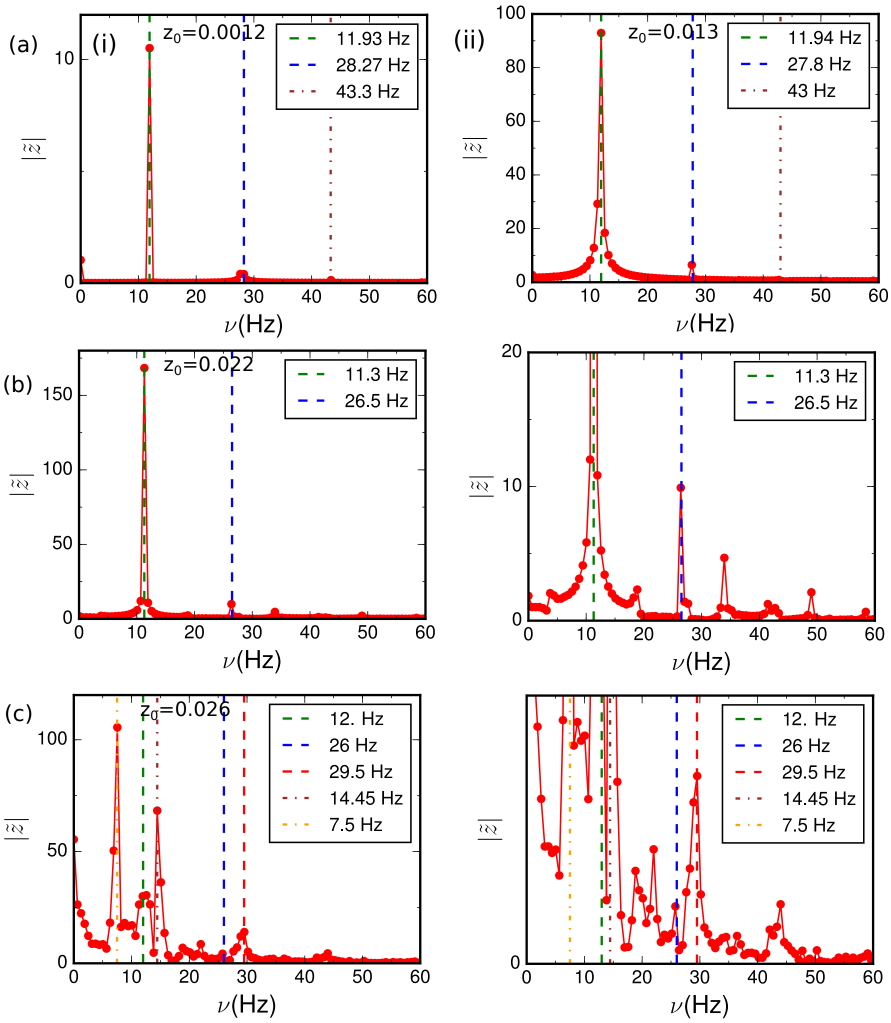

Figure 6.51: The Discrete Fourier Transform spectrum of the population imbalance for $V_0/\mu = 1.4$ and different z_0 from Josephson to the crossover regime. In (b)-(c) in the right is shown a zoomed-in of the plots on the left. The data are for particle number $N = 60000$. The DFT resolution is around 0.63 Hz.

We then investigate a higher barrier height $V_0/\mu = 1.4$ with results at different z_0 shown in Fig. 6.51. For this barrier height for $z_0 = z_{cr} = 0.026$, the system enters the crossover regime as shown in the Chapt. 5. For $z_0 < z_{cr}$, the $\nu_J \simeq 12$Hz and $\nu_1 \simeq 26$Hz have smaller values with respect to the values in the Josephson 'plasma' regime shown in Fig. 6.50 but the ratio $\nu_1/\nu_J \simeq 2.3$. Interestingly, at $z_0 = 0.026$ many frequencies are present: in addition to the onse at 12Hz and 26Hz, there are two other frequencies, one at 14.45Hz and another one at 29.5Hz which are near the x axis trap frequency $\nu_x = 15$Hz and twice the x axis frequency. Thus at this barrier height, it is clear that at $z_0 < z_{cr}$ the frequency 11.3-12 Hz and the second component at 26-28 Hz comes from the tunneling Hamiltonian and they are distinct from the x axis trap frequency and multiple of trap frequencies found for $z_0 = z_{cr}$.

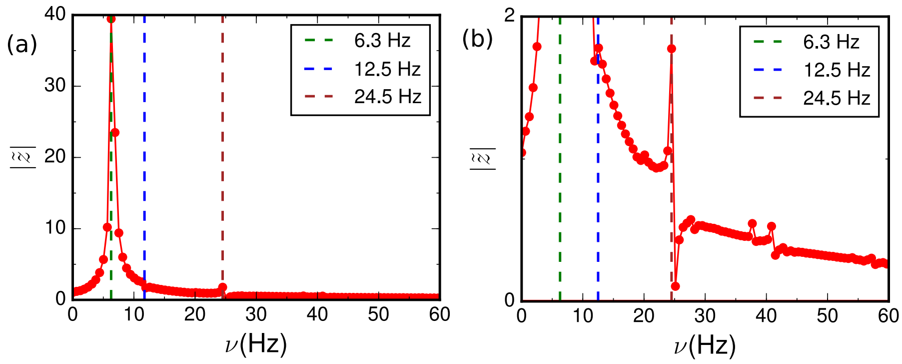

Figure 6.52: (a)The Discrete Fourier Transform spectrum of the population imbalance for $V_0/\mu \simeq 2$ and for two different values of x-axes frequency and its zoomed-in plot (b). The initial imbalance $z_0 < z_{cr}$ being $z_0 \simeq 0.006$. The data are for particle number $N = 60000$. The DFT resolution is around 0.63 Hz.

We increase further the barrier height and the last value explored is $V_0/\mu = 2$. Fig. 6.52 shows the DFT spectrum of $z(t)$ and a zoomed-in plot in (b). Even though it is not so well resolved, the second component is at exactly twice the $\nu_J \simeq 6.3$Hz. The study presented here seems to suggest that second and/or third component can originate from higher order term in the tunneling Hamiltonian and their value becomes closer to twice and three times the Josephson frequency as the barrier height increases.

Moreover, we think that in the Josephson regime, the frequency $\nu_1 \approx 2\nu_J$ is associated to the non-dissipative second-order term in the current-phase relation 'sin$(2\Delta\phi)$', while in the vortex-induced dissipative regime, where VRs and sound waves are generated, such frequency comes from the second-order dissipative term 'cos$(2\Delta\phi)$' in the current-phase relation. We showed that the second-order term in the dissipative regime, in some cases could have a contribution even larger than ν_J and in some other cases it is less important than ν_J. An interesting future study could be the analysis of the relation between the number of vortex rings generated and barrier height value with the relative contribution of ν_1.

The effect of the thermal cloud on the sound waves

We have shown that the thermal cloud drifts the vortex ring off-axis due to the scattering of the thermal excitations from the vortex. Moreover the VR lifetime is usually smaller at finite T with respect to $T = 0$ if we look at the first VR generated. If instead there are many VRs generated, the situation can change. Fig. 6.53 shows the time evolution of the x axis position of the VRs generated at $T = 0$ and $T = 50$nK for $V_0/\mu(T = 0) = 0.8$ and $z_0 = 0.25$. This is one of the cases studied in details in Chapt. 3 and Chapt. 4 where at $T = 0$ (blue circles) there are seven VRs generated while in the case of $T = 50$nK (red circles) there are 8 VRs with the last shrinking at $x = 0$. We checked here that this difference between the number of VRs generated is due to the slight shift in initial condensate imbalance induced by the thermal cloud populating the barrier and the edges of the condensate. Surprisingly the 3rd, 5th and 6th VR at $T = 50$nK have a longer lifetime with respect to $T = 0$. There are two possible reasons for this; one explanation can be the fact that the presence of the thermal cloud can attenuate the sound waves amplitude and thus affecting the vortex ring dynamics and the second one is related with the small change of $z^0_{\rm BEC}$ making $z^0_{\rm BEC}$ at $T = 50$nK slightly larger. As future works it would be interesting to study the effect of the thermal cloud on sound waves and how it influences the VR lifetime. Moreover, in order to rule out or not the second explanation it must be studied at $T = 0$ the case for z_0 the same as the finite temperature $z^0_{\rm BEC}$.

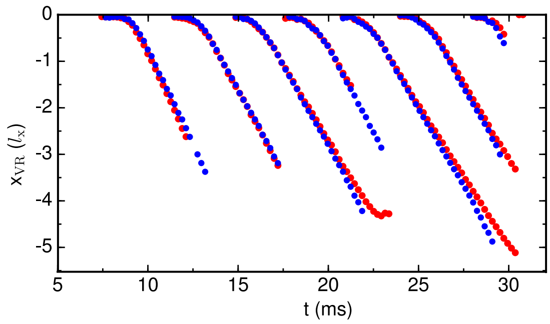

Figure 6.53: The time evolution of the position of the generated VR at $T = 0$ (blue circles) and $T = 50$nK (red circles), for $V_0 = 90\hbar\omega_x = 0.8\mu(T = 0)$ and for $N_{\rm BEC} \simeq 60000$.

Part V

Summary of conclusions

Chapter 7

Summary of conclusions

In this chapter we briefly describe the main findings from the study presented in this thesis. A more detailed description is provided in the end of each chapter together with the possible future works.

Chapt. 3: Modeling the LENS experiment: From dissipationless to the dissipative regime

Motivated by a recent experiment with ^{6}Li at LENS (Florence) [49, 20], in this chapter we firstly characterized the dynamical regimes emerging in an elongated three-dimensional atomic Josephson junction. We modelled this experiment in the limit of BEC of molecules of lithium and the results presented here were at $T = 0$, produced by using the GPE equation for a molecular BEC. Our Josephson junction consisted of two molecular BECs coupled through a Gaussian barrier with a $1/e^2$ width set at $w \simeq 2\mu$m $\simeq 4\xi$ and with variable barrier height V_0 in the range $[0.6, 1.22]\mu$ (experimental values). The superfluid dynamics across the barrier was induced by an initial population imbalance between the two-wells z_0, which induces an initial acceleration of the superfluid across the barrier.

Firstly, we showed that, depending on the value of z_0, the superfluid maximum velocity at the barrier position could be smaller or exceed a critical velocity for topological defect generation, which was shown to be set locally by the speed of sound. In the former case, found for $z_0 < z_{cr}$, the system enters the well-known Josephson 'plasma' regime [59–61] characterized by coherent oscillations of both the population imbalance and the relative phase between the two wells around a zero mean value at a characteristic 'plasma' frequency. In the latter case, found for $z_0 \geq z_{cr}$, vortex rings are generated at the barrier position and the superfluid flow becomes resistive. The VR emission causes the relative phase to jump by around 2π everytime a VR is generated (phase-slippage mechanism) and thus the superfluid velocity jumps by a quantized quantity. The system enters so the dissipative regime, in which was shown that the population imbalance decay initially fast in time and then oscillates around a zero mean value with different frequencies. We then tracked the generated vortex ring motion finding that the VR, nucleated outside the local Thomas-Fermi radius (as a 'ghost' vortex), initially shrinks its radius by entering the condensate, thus becoming a hydrodynamical vortex ring. Moreover, we showed that the vortex ring swirling velocity induces a reduction of the superfluid potential flow which can even invert its sign, that we termed the backflow. Due to the remaining chemical potential difference $\Delta\mu(t)$, the superfluid velocity increases again until it exceeds again the critical velocity and another VR is nucleated with a rate given by the phase-slippage rate $\Delta\mu/h$.

Further to this analysis we showed that, for the range of parameters explored in this chapter, the well-known two-mode model is out of its validity range. This model takes into account first-order processes in the tunneling Hamiltonian. Beyond the two-mode model, Ref. [65] showed that second-order term considering tunneling from condensate to non-condensate states could be important and we showed that such terms have a non-negligible contribution in the current-phase relation for our probed values of barrier heights $V_0 \sim \mu$. We then extracted the critical parameters delimiting dissipationless and dissipative transport, such as the critical initial imbalance and the maximum Josephson current, for each barrier heights, from the GPE simulations. We then showed that the critical current is well-predicted by the model described in Ref. [65, 159].

We further investigated the origin of dissipation by showing that the dissipation of Josephson oscillations originates from two irreversible effects: incompressible kinetic energy transfer from the superfluid flow to the swirling one of the nucleated vortex rings and phonon emission during VR early stage dynamics. Next, we directly connected microscopic features of early-stage vortex ring dynamics with macroscopic observables, such as population imbalance and superfluid current. In particular, we showed that every time a VR enters the local Thomas-Fermi surface it causes a local 'dip' in the otherwise monotonic decay of $z(t)$: each such local minimum corresponds to the generation of a VR. The number of vortex rings, i.e. the number of 'dips' in $z(t)$, which can be generated in the junction depends on how far the initial imbalance is from its critical value.

Depending on the value of the barrier height, the vortex ring could leave the barrier and propagate further into the left reservoir. We then followed the first vortex ring subsequent dynamics in the left condensate and we studied the dependence of the VR dynamics on the initial population imbalance at fixed $V_0/\mu = 0.8$. In particular, we showed that the VR velocity descreases with increasing z_0 and its incompressible kinetic energy increases instead. It was shown that for these cases, the VR, after propagating for a while in the left reservoir, shrinks further its size, 'disappearing' and giving rise to rarefaction pulses. Furthermore, the dependence of the amount of dissipation on z_0 was investigated, finding that the fraction of the total kinetic energy (until the nucleation of the first VR) that is dissipated in sound or transferred to the first VR, increases as z_0 gets larger.

Chapt. 4: Comparison with an ultracold atom experiment (^{6}Li experiment in Florence)

In this chapter we compared our numerical simulation results of Chapt. 3 with the experimental results from the LENS experiment in Florence [20] in the limit of BEC of lithium molecules. In particular, our prediction of the critical imbalance and critical superfluid current across the barrier, defining the transition to the dissipative regime was found to be in very good agreement with the experimental data. Furthermore, we showed that the maximum current delimiting the two regimes can also be calculated in a simpler way by the product of the population imbalance oscillation frequency ω_J (found for $z_0 < z_{cr}$), of the critical imbalance z_{cr} and of half the condensate number $N_{BEC}/2$. This finding is of significant importance for experiments as the ω_J and z_{cr} can be easily extracted. We also showed that the $z(t)$ profiles achieved numerically excellently reproduce the experimental data. As the experiment was done at low, but finite temperature, we also consider the presence of a small thermal cloud, by describing our system via the Zaremba-Nikuni-Griffin (ZNG) kinetic model, where a generalized GPE equation, describing the condensate evolution, is solved self-consistently with a Quantum Boltzmann equation (QBE) describing the thermal cloud dynamics [28, 26, 27]. In this chapter we performed the studies in the collisionless limit. Specifically, we selected $T \simeq (0.3 - 0.4)T_c$ in our numerical simulations, consistent with the estimated experimental value from the condensate fraction. Even at finite T the comparison was very good with the experimental data and, for such low temperatures, the thermal cloud has no significant effect on the critical parameters and the population imbalance time evolution as long as we kept fixed the condensate number when comparing the $T = 0$ and finite T results (which are thus done at variable total particle number).

Next, we implemented in our simulations the protocol of barrier removal used in the experiment before observing the vortices in time of flight (TOF) image. We showed that the barrier removal is an efficient tool for producing longer living vortices with larger propagation radius, and thus making it easier to be observed experimentally, although less VRs are generated. In fact, while the barrier height value decreases, the density at the barrier position increases. Consequently, the density-weighted superfluid maximum velocity achieves smaller values until it becomes smaller than a threshold, which we found is equal to the mean speed of sound $\langle c \rangle = \sqrt{\mu/2M}$. Finally, the role of the thermal cloud on the VR motion was considered. We showed that the thermal cloud causes the vortex ring to go off-center until it breaks into one long single vortex line when approaches the condensate boundaries asymmetrically, consistent with the experimental observation of single off-center vortices.

Chapt. 5: Full phase-diagram for a three-dimensional Josephson junction

In this chapter, we characterized the full phase diagram of a three-dimensional Josephson Junction where three main dynamical regimes were found: Josephson plasma, self-trapping, and dissipative. In particular, for $z_0 = z_{cr}(V_0)$, the pure self-trapping or Macroscopic Quantum Self-Trapping regime was found, as predicted by Smerzi et al. [59]. In such regime, the population imbalance features regular symmetric oscillations about a non-zero value, and it is characterized by an increasing relative phase in time. Furthermore, we showed that increasing the initial population imbalance much beyond z_{cr} leads to more complicated self-trapped states with oscillations at multiple frequencies.

Specifically, we showed that for elongated traps, such as the ones studied in Ref. [49, 20] and described in Chapt. 3 and Chapt. 4 of this thesis, where only the transition from the Josephson plasma regime to the dissipative one was observed, the self-trapping regime can in fact also be observed for higher and/or wider barriers. As a counterpart, our result indicated that for isotropic traps in which only the transition from the Josephson plasma to the self-trapped regime has been seen (such as in Ref. [42]), the dissipative regime can also be observed by lowering the barrier height (to values slightly below, but still a sizable fraction of, μ). For both geometries we found a smooth, and rather irregular, crossover between dissipative and self-trapped regimes. Thus, our work presented in this chapter suggested that for any geometry we can find all three dynamical regimes, and that such regimes should be experimentally observable within a single experimental set-up by careful control of the barrier height or width.

Our results in this chapter also clarified what distinguishes between the dissipative and macroscopic quantum self-trapping regimes, not just in terms of $z(t)$ and $\phi(t)$, but also in terms of vortex ring dynamics. As V_0/μ increases, the vortex rings go from a regime in which they can propagate (leaving the barrier region), to a regime where they shrink within the barrier. Whether the vortex ring leaves or not the barrier is defined by the value of incompressible kinetic energy that is present in the system. We showed that in the crossover between the self-trapped and dissipative regimes, the main difference comes from sound waves: specifically, in the self-trapped regime (for z_0 values slightly larger than z_{cr}) there are practically no sound waves, while in the dissipative regime such sound waves propagate and make the condensate dissipate.

Chapt. 6: Bose-Einstein condensates at finite temperature in an atomic Josephson-junction

In this chapter, we showed, for the elongated Josephson junction, the role of thermal dissipation on the three main dynamical regimes found at $T = 0$ in Chapt. 3 and Chapt. 5: Josephson 'plasma', vortex-induced dissipative and pure self-trapped or MQST regimes. In order to model the finite temperature Bose gas we used the Zaremba-Nikuni-Griffin model where a generalized GPE describing the condensate evolution is solved self-consistently with a Quantum Boltzmann equation (QBE) describing the thermal cloud dynamics. Firstly, we performed our studies in the collisionless limit, where the collisions between condensate-thermal particles (resulting in particle-exchange between the two subsystems) and the collisions within the thermal cloud are not included. Many ultracold atom experiments are in the collisionless limit due to their low density and the ZNG collisionless limit has given results in quantitative agreement with experimental observation [153, 105, 96–98, 134, 156, 154, 155]. However, a complete description of the system would require the inclusion of collisions, which was also studied in this chapter even though to less extent with respect to the collisionless limit.

We mainly considered the case of fixed condensate number when comparing different temperatures, i.e. variable total particle number and thus variable critical temperature $T_c(N)$. Firstly, we studied the dynamical evolution of the condensate/thermal/total population imbalance across the Josephson and dissipative regimes, where for the latter the analysis of oscillations was performed after the initial decay, i.e. after the VRs generation. In particular, we showed the temperature dependence of the dominant frequency values, their damping rates, relative contribution and each component's initial phase. The range of temperature probed by us was $[0.1, 0.7]T_c$, and we initially kept fixed condensate number $N_{BEC} \simeq 50400$, thereby fixing the condensate axial extension. The chosen barrier height was $V_0 = 104\hbar\omega_x \simeq \mu(T = 0)$, for which the Josephson 'plasma' and vortex-induced dissipative regimes were found for $z_0 < z_{\rm cr} = 0.08$ and $z_0 > z_{\rm cr}$ respectively. The associated temperature to the barrier height value is $T_{\rm eff} = V_0/k_B = 70\rm{nK} = 0.5T_c$.

We identified two distinct dynamical regimes, namely a low temperature regime ($k_BT < V_0$) in which the small thermal cloud is driven by the condensate, and a high temperature regime ($k_BT \gtrsim V_0$) in which the thermal cloud has enough energy to overcome the barrier, and thus begins to drive the condensate. The dominant frequencies identified are the Josephson plasma frequency ν_J , its second order contributions ν_1, and a characteristic frequency of the thermal cloud ν_2 which is close to the underlying harmonic trap frequency. These frequencies are found to be relevant in both the Josephson plasma and the dissipative regimes. In particular, for the condensate and total imbalance, we showed that at low temperatures $k_BT < V_0$, the frequencies $\nu_J^{\rm BEC(tot)} \approx 14\rm{Hz}$ and $\nu_1^{\rm BEC(tot)} \approx 30\rm{Hz}$ are the dominant ones. As the temperature increases towards $T_{\rm eff}$, i.e. as the thermal fraction increases, the thermal particles have sufficient kinetic energy to exhibit their own motion at a frequency $\nu_2^{th} \approx 15\rm{Hz}$. Thus, the thermal cloud back action to the condensate motion affects this latter spectrum with the appearance of a frequency $\nu_2^{\rm BEC(tot)} \approx 15\rm{Hz}$ for temperatures such that $k_BT \gtrsim V_0$. Moreover, the thermal cloud damps the component $\nu_1^{\rm BEC(tot)}$ and in the limit of high temperature the main components become $\nu_J^{\rm BEC(tot)}$ and

$\nu_2^{\rm BEC(tot)}$.

However, an important distinction between the Josephson and vortex-induced dissipative regime was found: although the dominant frequencies are the same, their relative contributions and phases of oscillations are not. Specifically, in the low temperature limit, in the Josephson regime the $\nu_J^{\rm BEC}$ is the dominant frequency, while in the dissipative regime its contribution is smaller than $\nu_1^{\rm BEC}$, with the latter being the dominant frequency of relative contribution. Moreover even the relative phase between the two components was found to be different in two regimes: in the Josephson 'plasma' regime the $\nu_1^{\rm BEC}$ has a relative phase of π with respect to $\nu_J^{\rm BEC}$, while in the dissipative regime the relative phase is around $\pi/2$. Based on the last considerations and on the fact that $\nu_1^{BEC} \approx 2\nu_J^{BEC}$, we attributed the origin of ν_1^{BEC} in the Josephson regime to second-order non-dissipative term in the current-phase relation. On the other hand, in the vortex-induced dissipative regime, given the dominant role played by the generated vortex rings and associated sound waves, a second-order dissipative term should become important which, as shown in [65], has a relative phase of $\pi/2$ with respect to $\nu_J^{\rm BEC}$.

Further to our analysis we investigated the effect of the thermal cloud in the MQST regime, where the barrier height was kept fixed at $V_0 = 210\hbar\omega_x \simeq 2\mu(T=0)$. We found that the MQST regime is highly unstable in the presence of the thermal cloud and its decay time can differ from run to run even in the collisionless limit. However, by extracting the mean decay time from five numerical runs we showed that on average the MQST decay time becomes smaller at larger T. We then considered the case of fixed total particle number, and we showed that having different condensate numbers at different T can cause the condensate or the total population imbalance to be in a different dynamical regime for the same value of the barrier height because V_0/μ and the axial condensate extension are different.

We then added the effect of collisional integrals by including both the condensate-thermal and thermal-thermal collisions. We showed that at very low T (for example $T = 0.22T_c$) the collisions have no effect on the condensate imbalance but their presence strongly affects the thermal cloud imbalance, favouring the thermal particles incoherently tunneling across the barrier. Next, we showed the effect of collisions on the dominant frequency of the condensate and total imbalance in the Josephson and dissipative regime, with collisions found to add an extra damping contribution to the dominant frequency. For the MQST regime we showed that the inclusion of collisions makes the MQST decay faster with respect to collisionless limit.

We then showed the role of the thermal cloud on the VR nucleation and dynamics for a smaller barrier height $V_0 = 67\hbar\omega_x = 0.6\mu(T=0)$, with an effective temperature of $T_{eff} = V_0/k_B \simeq 45$nK. We found that the presence of the thermally induced phase fluctuations and transverse density fluctuations could cause the generation of the VR, present also at $T = 0$, earlier in time. Moreover, as temperature increases and the thermal particles mean kinetic energy exceeds the barrier height, a thermally-induced VR emission occurs. In particular, it was found to occur at $T = 70$ nK$= 0.48T_c > T_{\text{eff}}$ for such relatively low barrier height.

Appendix A

The vortex ring dynamics in the spherical trap.

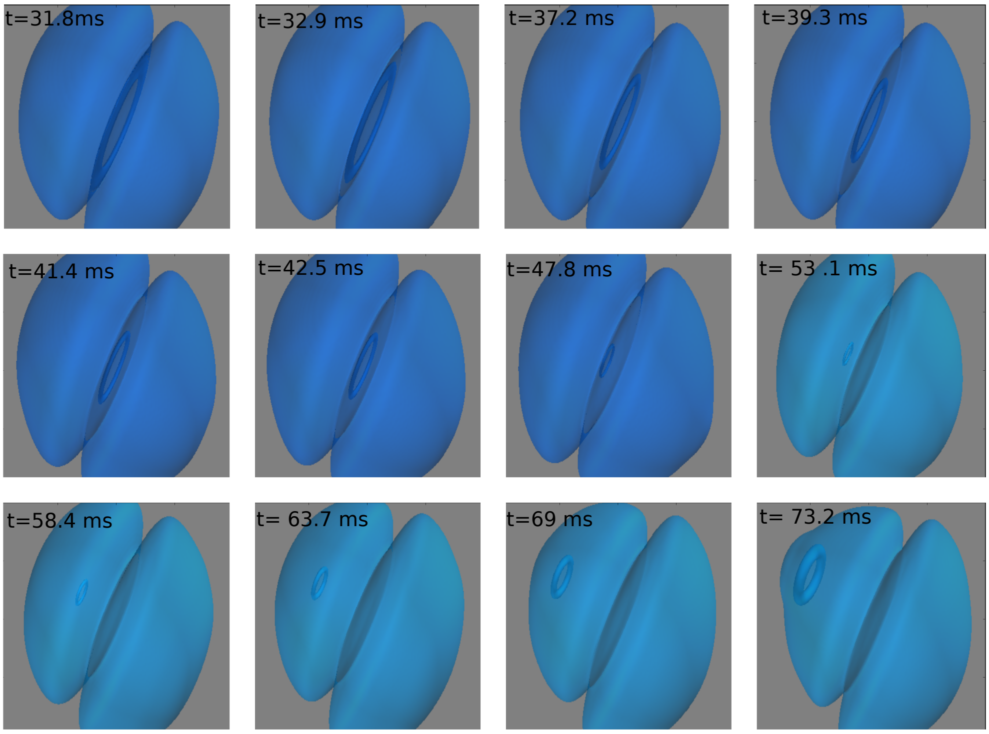

Figure A.1: Three dimensional isocontour surface density for $V_0 = 0.8\mu$, $w/\xi = 4$ and for the isotropic trap $\nu_x = \nu_y = \nu_z = 15$Hz at different times. The isocontour is shown at different values of the maximum density in order to better visualize the VR.

In Chapt. 5 we showed that the dissipative regime could be found even for an isotropic or a spherical trap. In such regimes, as for the elongated trap, vortex rings are generated and could even propagate in the left reservoir depending on the value of the barrier height, i.e. on the value of the incompressible kinetic energy. As for the elongated trap, the VR is nucleated outside the local TF surface and then shrinks initially its radius while entering the transverse condensate extension. Fig. A.1 shows some examples of three dimensional isocontour surface at different times during the VR dynamics. Once the VR is inside the condensate, it shrinks further its radius in order to conserve its kinetic energy while density is increasing, remaining so initially within the barrier. When it achieves a certain radius it enters in the left side of the BEC and propagates. While going towards the edge of the condensate it increases it radius (for $t \geq$63.7 ms) and after that reverses its motion. In this isotropic case, when the VR radius becomes comparable to the transverse TF radius, the VR does not break into two vortex lines but it instead becomes larger than the condensate size moving so at the surface without breaking as shown in Fig. A.2.

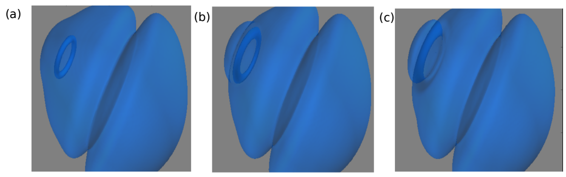

Figure A.2: Three dimensional isocontour surface density for $V_0 = 0.8\mu$, $w/\xi = 4$ and for the isotropic trap $\nu_x = \nu_y = \nu_z = 15$Hz. The plots are shown at (a) $t = 76$ms, (b) $t = 79$ms and (c) $t = 81$ms.

Appendix B

Finite temperature analysis

In this section, we show some results from the analysis of the condensate and thermal population imbalance oscillations both in the Josephson and vortex-induced dissipative regime, in relation to the results presented in Chapt. 6.

Fitting the condensate imbalance

In Sect. 6.4.2 we showed the results obtained by fitting the condensate imbalance time evolution in the vortex-induced dissipative regime after the initial decay and in the time interval $[0.05, 0.72]$s. In the limit of low ($k_B T < V_0$) and relatively high temperatures ($k_B T > V_0$), the numerical data were fitted by using a two-component frequency fit by using the function $F(t)$ defined in Eq. (6.12) as

$$\begin{aligned} F(t) = &\ a_J \cos(2\pi\nu_J t + \phi_J) \exp(-\gamma_J t) \\ &+ a_i \cos(2\pi\nu_i t + \phi_i) \exp(-\gamma_i t). \end{aligned} \tag{B.1}$$

In the intermediate range of temperatures such that $k_B T \sim V_0$, we perform a three-component frequency fit by using $G(t)$ (defined in Eq. (6.15) as

$$\begin{aligned} G(t) = &\ a_J \cdot \cos(2\pi\nu_J t + \phi_J) \cdot \exp(-\gamma_J t) \\ &+ a_1 \cdot \cos(2\pi\nu_1 t + \phi_1) \cdot \exp(-\gamma_1 t) + \\ &+ a_2 \cdot \cos(2\pi\nu_2 t + \phi_2) \cdot \exp(-\gamma_2 t). \end{aligned} \tag{B.2}$$

Specifically, the intermediate regime corresponds to the range $0.45T_c < T < 0.56T_c$. In order to avoid the problem of having the highest damped components with a large relative contribution, we set two of the three damping rates in Eq. (6.15) to be the same. In particular, we chosed two cases: $\gamma_{\mathrm{J}}^{\mathrm{BEC}} = \gamma_2^{\mathrm{BEC}}$ and $\gamma_1^{\mathrm{BEC}} = \gamma_2^{\mathrm{BEC}}$ and the data shown in Sect. 6.4.2 are obtained from the mean value between the two fits.

Here instead, we show a comparison between the fit and the condensate imbalance, with the results shown in Fig. B.1 for three different temperatures: in the limit of (a) low temperature $T = 0.22T_c$, hight temperature (b) $T = 0.66T_c$ and in the intermediate regime $T = 0.54T_c$. In the first two cases a two-component frequency fit is performed while in the last case a three-component frequency fit is performed where the damping $\gamma_1^{\mathrm{BEC}} = \gamma_2^{\mathrm{BEC}}$. We find that the numerical data and the fit are in very good agreement.

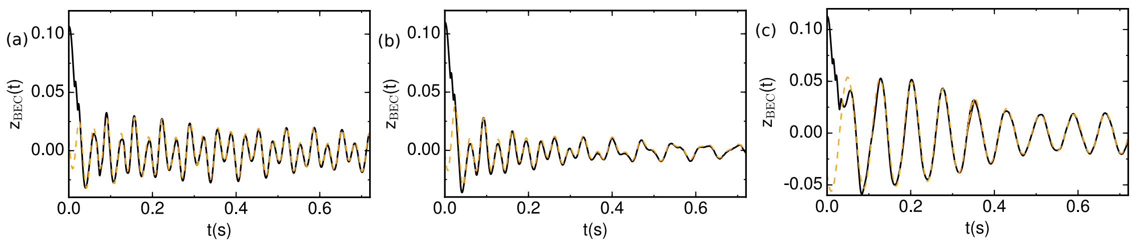

Figure B.1: The population imbalance time evolution at (a) $T = 28\mathrm{nK} = 0.22\mathrm{T_c}$, (b) $T = 78\mathrm{nK} = 0.54\mathrm{T_c}$ and (c) $T = 110\mathrm{nK} = 0.66\mathrm{T_c}$ and the corresponding fits (orange profiles). In (a)-(c) the numerical data are fitted by a two-component frequency, while in (b) a three-component fit is performed. In the latter we set $\gamma_1^{\mathrm{BEC}} = \gamma_2^{\mathrm{BEC}}$. The numerical data are for $V_0 = 104\hbar\omega_x$ and condensate initial imbalance $z_{\mathrm{BEC}}^0 > z_{\mathrm{cr}}$.

The frequency at 45Hz

As discussed in Chapt. 6, at low temperatures there is a third component in the spectrum of the condensate imbalance with a frequency around 45Hz, which we term here as ν_3^{BEC}. This component has a negligible contribution of less than 1% in the Josephson regime and contribution of around 10% in the dissipative regime at $T = 0$. Here we show the results for the dissipative regime. The contribution of ν_3^{BEC} decreases as the temperature increases. An example of Discrete Fourier Transform spectrum for the condensate imbalance revealing the presence of ν_3^{BEC} is shown in Fig. B.3 at $T = 40\mathrm{nK}$. We note that ν_3^{BEC} amplitude is much smaller than ν_J^{BEC}. Such results are in good agreement with the three-component frequency fit, in which the main component values are indicated by the vertical dashed lines. The dependence of ν_3^{BEC} and its corresponding damping rate on the temperature is shown in Fig. B.3. The highest temperature in such plot corresponds to $T = 0.44T_c$. While ν_3^{BEC} value decreases with increasing T, its damping rate increases fast and at $T = 40\mathrm{nK} = 0.31T_c$ its value is much larger than the damping rates γ_1^{BEC} and γ_2^{BEC}, which are shown in Sect. 6.4.2.

Collisional limit

Until now, in this chapter we considered the collisionless limit. Here instead we show some results in the case where all the collisional integral are included. In particular, in Fig. B.4 we show how the condensate and thermal cloud particle number changes in time

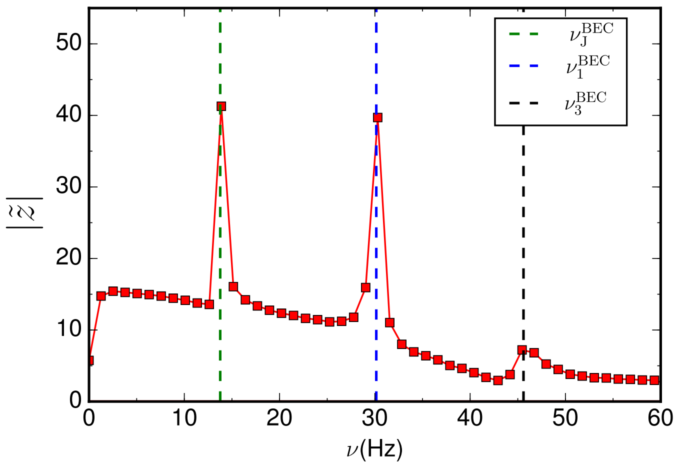

Figure B.2: The Discrete Fourier Transform spectrum for the condensate imbalance revealing the presence of a frequency at around 45Hz. The vertical dashed lines indicate the values of the frequencies from the three-component frequency fit. The numerical data are for $V_0 = 104\hbar\omega_x$ and condensate initial imbalance $z^0_{\rm BEC} > z_{\rm cr}$.

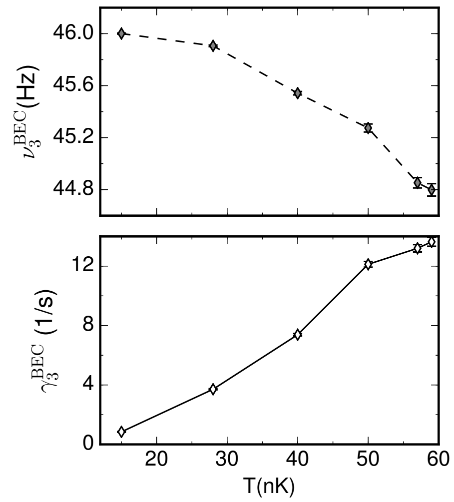

Figure B.3: The temperature dependence of $\nu_3^{\rm BEC}$ and its corresponding damping rate as found from the the three-component frequency fit. The numerical data are for $V_0 = 104\hbar\omega_x$ and condensate initial imbalance $z^0_{\rm BEC} > z_{\rm cr}$.

for the case of $T = 88$nK$= 0.58T_c$. Interestingly, the condensate particle number increases in time. This is a consequence of particle-exchange between the condensate and thermal clouds, which is taken into account by the term C_{12} in the Quantum Boltzmann equation and by the source term $-iR$, related to C_{12}, in the generalized GPE equation. We note that $N_{\rm BEC}$ and $N_{\rm th}$ refers to the sum of the particle number in the left and right well. At this temperature, the total particle number is conserved in time (for at least 0.72) within 5%. Thus, the thermal particle number decreases in time.

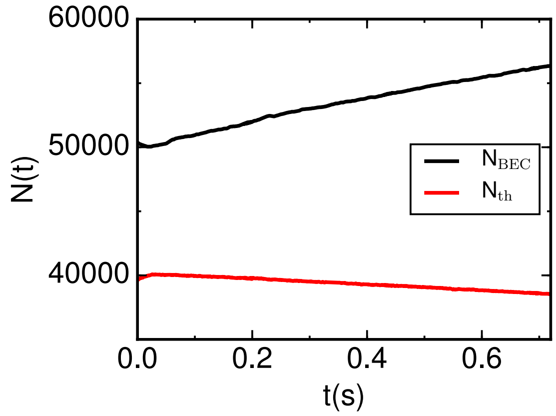

Figure B.4: The time evolution of the condensate and thermal cloud particle number at $T = 88$nK$= 0.58T_c$ and in the collisional limit. The numerical data are for $V_0 = 104\hbar\omega_x$ and condensate initial imbalance $z^0_{\mathrm{BEC}} < z_{\mathrm{cr}}$.

Bibliography

[1] C. Pethick and H. Smith, *Bose-Einstein Condensation in Dilute Gases (2nd ed.).* (Cambridge University Press, 2008).

[2] L. Pitaevskii and S. Stringari, *Bose-Einstein Condensation and Superfluidity* (Oxford University Press, 2016).

[3] Bose, Zeitschrift fr Physik **178** (1924).

[4] A. Einstein, Sitzungsberichte der Preussischen Akademie der Wissenschaften, Physikalisch-mathematische Klasse p. 261267 (1924).

[5] M. H. Anderson, J. R. Ensher, M. R. Matthews, C. E. Wieman, and E. A. Cornell, Science **269**, 198 (1995), ISSN 0036-8075, URL `https://science.sciencemag.org/content/269/5221/198`.

[6] K. B. Davis, M. O. Mewes, M. R. Andrews, N. J. van Druten, D. S. Durfee, D. M. Kurn, and W. Ketterle, Phys. Rev. Lett. **75**, 3969 (1995), URL `https://link.aps.org/doi/10.1103/PhysRevLett.75.3969`.

[7] C. C. Bradley, C. A. Sackett, J. J. Tollett, and R. G. Hulet, Phys. Rev. Lett. **75**, 1687 (1995), URL `https://link.aps.org/doi/10.1103/PhysRevLett.75.1687`.

[8] J. F. Allen and A. D. Misener, Nature **141**, 75 (1938), ISSN 1476-4687, URL `https://doi.org/10.1038/141075a0`.

[9] P. Kapitza, Nature **141**, 74 (1938), ISSN 1476-4687, URL `https://doi.org/10.1038/141074a0`.

[10] F. London, Phys. Rev. **54**, 947 (1938), URL `https://link.aps.org/doi/10.1103/PhysRev.54.947`.

[11] L. Landau, Phys. Rev. **60**, 356 (1941), URL `https://link.aps.org/doi/10.1103/PhysRev.60.356`.

[12] P. W. Anderson, Rev. Mod. Phys. **38**, 298 (1966), URL https://link.aps.org/doi/10.1103/RevModPhys.38.298.

[13] R. Feynman, **1**, 17 (1955), ISSN 0079-6417, URL http://www.sciencedirect.com/science/article/pii/S0079641708600773.

[14] O. Avenel and E. Varoquaux, Phys. Rev. Lett. **55**, 2704 (1985), URL https://link.aps.org/doi/10.1103/PhysRevLett.55.2704.

[15] Y. Sato and R. E. Packard, Rep. Prog. Phys. **75**, 016401 (2011), URL https://doi.org/10.1088%2F0034-4885%2F75%2F1%2F016401.

[16] S. Moulder, S. Beattie, R. P. Smith, N. Tammuz, and Z. Hadzibabic, Phys. Rev. A **86**, 013629 (2012), URL https://link.aps.org/doi/10.1103/PhysRevA.86.013629.

[17] D. McKay, M. White, M. Pasienski, and B. DeMarco, Nature **453**, 76 (2008), ISSN 1476-4687, URL https://doi.org/10.1038/nature06920.

[18] K. C. Wright, R. B. Blakestad, C. J. Lobb, W. D. Phillips, and G. K. Campbell, Phys. Rev. Lett. **110**, 025302 (2013), URL https://link.aps.org/doi/10.1103/PhysRevLett.110.025302.

[19] L. Tanzi, S. Scaffidi Abbate, F. Cataldini, L. Gori, E. Lucioni, M. Inguscio, G. Modugno, and C. D'Errico, Scientific Reports **6**, 25965 (2016), ISSN 2045-2322, URL https://doi.org/10.1038/srep25965.

[20] A. Burchianti, F. Scazza, A. Amico, G. Valtolina, J. A. Seman, C. Fort, M. Zaccanti, M. Inguscio, and G. Roati, Phys. Rev. Lett. **120**, 025302 (2018), URL https://link.aps.org/doi/10.1103/PhysRevLett.120.025302.

[21] F. Jendrzejewski, S. Eckel, N. Murray, C. Lanier, M. Edwards, C. J. Lobb, and G. K. Campbell, Phys. Rev. Lett. **113**, 045305 (2014), URL https://link.aps.org/doi/10.1103/PhysRevLett.113.045305.

[22] S. Eckel, J. G. Lee, F. Jendrzejewski, C. J. Lobb, G. K. Campbell, and W. T. Hill, Phys. Rev. A **93**, 063619 (2016), URL https://link.aps.org/doi/10.1103/PhysRevA.93.063619.

[23] G. Gauthier, S. S. Szigeti, M. T. Reeves, M. Baker, T. A. Bell, H. Rubinsztein-Dunlop, M. J. Davis, and T. W. Neely, Phys. Rev. Lett. **123**, 260402 (2019), URL https://link.aps.org/doi/10.1103/PhysRevLett.123.260402.

[24] J. Polo, R. Dubessy, P. Pedri, H. Perrin, and A. Minguzzi, Phys. Rev. Lett. **123**, 195301 (2019), URL https://link.aps.org/doi/10.1103/PhysRevLett.123.195301.

[25] C. J. Foot, *Atomic physics*, Oxford master series in atomic, optical, and laser physics (Oxford University Press, Oxford, 2007), URL https://cds.cern.ch/record/1080846.

[26] T. Nikuni, E. Zaremba, and A. Griffin, Phys. Rev. Lett. **83**, 10 (1999), URL https://link.aps.org/doi/10.1103/PhysRevLett.83.10.

[27] E. Zaremba, T. Nikuni, and A. Griffin, Journal of Low Temperature Physics **116**, 277 (1999), ISSN 1573-7357, URL https://doi.org/10.1023/A:1021846002995.

[28] A. Griffin, T. Nikuni, and E. Zaremba, *Bose-Condensed Gases at Finite Temperatures* (Cambridge University Press, 2009).

[29] L. V. P. R. de Broglie, Annals Phys. **2** (1925).

[30] W. Pauli, Zeitschrift fr Physik **31** (1925), ISSN 0044-3328.

[31] A. Leggett, ed., *Quantum Liquids Bose condensation and Cooper pairing in condensed-matter systems* (Oxford University Press, 2006).

[32] C. C. Bradley, C. A. Sackett, J. J. Tollett, and R. G. Hulet, Phys. Rev. Lett. **79**, 1170 (1997), URL https://link.aps.org/doi/10.1103/PhysRevLett.79.1170.

[33] N. N. Bogoliubov, J. Phys. (USSR) **11** (1947).

[34] F. Dalfovo, S. Giorgini, L. P. Pitaevskii, and S. Stringari, Rev. Mod. Phys. **71**, 463 (1999), URL https://link.aps.org/doi/10.1103/RevModPhys.71.463.

[35] R. Lopes, C. Eigen, N. Navon, D. Clément, R. P. Smith, and Z. Hadzibabic, Phys. Rev. Lett. **119**, 190404 (2017), URL https://link.aps.org/doi/10.1103/PhysRevLett.119.190404.

[36] O. Penrose and L. Onsager, Phys. Rev. **104**, 576 (1956), URL https://link.aps.org/doi/10.1103/PhysRev.104.576.

[37] B. D. Josephson, Phys. Lett. **1**, 251 (1962), ISSN 0031-9163, URL http://www.sciencedirect.com/science/article/pii/0031916362913690.

[38] P. W. Anderson and J. M. Rowell, Phys. Rev. Lett. **10**, 230 (1963), URL https://link.aps.org/doi/10.1103/PhysRevLett.10.230.

[39] E. Hoskinson, Y. Sato, I. Hahn, and R. E. Packard, Nat. Phys. **2**, 23 (2006), URL `https://doi.org/10.1038/nphys19`.

[40] Y. Sato, E. Hoskinson, and R. Packard, in *Fundamentals and Frontiers of the Josephson Effect*, edited by F. Tafuri (Springer, Cham, 2019), vol. 286.

[41] F. S. Cataliotti, S. Burger, C. Fort, P. Maddaloni, F. Minardi, A. Trombettoni, A. Smerzi, and M. Inguscio, Science **293**, 843 (2001), ISSN 0036-8075, URL `https://science.sciencemag.org/content/293/5531/843`.

[42] M. Albiez, R. Gati, J. Fölling, S. Hunsmann, M. Cristiani, and M. K. Oberthaler, Phys. Rev. Lett. **95**, 010402 (2005), URL `https://link.aps.org/doi/10.1103/PhysRevLett.95.010402`.

[43] T. Anker, M. Albiez, R. Gati, S. Hunsmann, B. Eiermann, A. Trombettoni, and M. K. Oberthaler, Phys. Rev. Lett. **94**, 020403 (2005), URL `https://link.aps.org/doi/10.1103/PhysRevLett.94.020403`.

[44] T. Schumm, S. Hofferberth, L. M. Andersson, S. Wildermuth, S. Groth, I. Bar-Joseph, J. Schmiedmayer, and P. Krüger, Nature Physics **1**, 57 (2005), ISSN 1745-2481, URL `https://doi.org/10.1038/nphys125`.

[45] Y. Shin, M. Saba, T. A. Pasquini, W. Ketterle, D. E. Pritchard, and A. E. Leanhardt, Phys. Rev. Lett. **92**, 050405 (2004), URL `https://link.aps.org/doi/10.1103/PhysRevLett.92.050405`.

[46] S. Levy, E. Lahoud, I. Shomroni, and J. Steinhauer, Nat. Phys. **449**, 579 (2007), URL `https://doi.org/10.1038/nature06186`.

[47] G. Spagnolli, G. Semeghini, L. Masi, G. Ferioli, A. Trenkwalder, S. Coop, M. Landini, L. Pezzè, G. Modugno, M. Inguscio, et al., Phys. Rev. Lett. **118**, 230403 (2017), URL `https://link.aps.org/doi/10.1103/PhysRevLett.118.230403`.

[48] L. J. LeBlanc, A. B. Bardon, J. McKeever, M. H. T. Extavour, D. Jervis, J. H. Thywissen, F. Piazza, and A. Smerzi, Phys. Rev. Lett. **106**, 025302 (2011), URL `https://link.aps.org/doi/10.1103/PhysRevLett.106.025302`.

[49] G. Valtolina, A. Burchianti, A. Amico, E. Neri, K. Xhani, J. A. Seman, A. Trombettoni, A. Smerzi, M. Zaccanti, M. Inguscio, et al., Science **350**, 1505 (2015), ISSN 0036-8075, URL `https://science.sciencemag.org/content/350/6267/1505`.

[50] W. J. Kwon, G. Del Pace, R. Panza, M. Inguscio, W. Zwerger, M. Zaccanti, F. Scazza, and G. Roati, Science **369**, 84 (2020), ISSN 0036-8075, URL `https://science.sciencemag.org/content/369/6499/84`.

[51] N. Luick, L. Sobirey, M. Bohlen, V. P. Singh, L. Mathey, T. Lompe, and H. Moritz, Science **369**, 89 (2020), ISSN 0036-8075, URL https://science.sciencemag.org/content/369/6499/89.

[52] K. G. Lagoudakis, B. Pietka, M. Wouters, R. André, and B. Deveaud-Plédran, Phys. Rev. Lett. **105**, 120403 (2010), URL https://link.aps.org/doi/10.1103/PhysRevLett.105.120403.

[53] A. F. Adiyatullin, M. D. Anderson, H. Flayac, M. T. Portella-Oberli, F. Jabeen, C. Ouellet-Plamondon, G. C. Sallen, and B. Deveaud, Nature Communications **8**, 1329 (2017), ISSN 2041-1723, URL https://doi.org/10.1038/s41467-017-01331-8.

[54] A. C. Mathey, C. W. Clark, and L. Mathey, Phys. Rev. A **90**, 023604 (2014), URL https://link.aps.org/doi/10.1103/PhysRevA.90.023604.

[55] K. Snizhko, K. Isaieva, Y. Kuriatnikov, Y. Bidasyuk, S. Vilchinskii, and A. Yakimenko, Physical Review A **94** (2016).

[56] C. D'Errico, S. S. Abbate, and G. Modugno, Philos. Trans. Royal Soc. A **375**, 20160425 (2017), URL https://royalsocietypublishing.org/doi/10.1098/rsta.2016.0425.

[57] J. Polo, V. Ahufinger, F. W. J. Hekking, and A. Minguzzi, Phys. Rev. Lett. **121**, 090404 (2018), URL https://link.aps.org/doi/10.1103/PhysRevLett.121.090404.

[58] J. Polo, R. Dubessy, P. Pedri, H. Perrin, and A. Minguzzi, Phys. Rev. Lett. **123**, 195301 (2019), URL https://link.aps.org/doi/10.1103/PhysRevLett.123.195301.

[59] A. Smerzi, S. Fantoni, S. Giovanazzi, and S. R. Shenoy, Phys. Rev. Lett. **79**, 4950 (1997), URL https://link.aps.org/doi/10.1103/PhysRevLett.79.4950.

[60] I. Zapata, F. Sols, and A. J. Leggett, Phys. Rev. A **57**, R28 (1998), URL https://link.aps.org/doi/10.1103/PhysRevA.57.R28.

[61] S. Raghavan, A. Smerzi, S. Fantoni, and S. R. Shenoy, Phys. Rev. A **59**, 620 (1999), URL https://link.aps.org/doi/10.1103/PhysRevA.59.620.

[62] R. Franzosi, V. Penna, and R. Zecchina, International Journal of Modern Physics B **14**, 943 (2000), URL https://doi.org/10.1142/S0217979200001011.

[63] Y. M. Bidasyuk, M. Weyrauch, M. Momme, and O. O. Prikhodko, Journal of Physics B: Atomic, Molecular and Optical Physics **51**, 205301 (2018), URL https://doi.org/10.1088%2F1361-6455%2Faae022.

[64] R. Gati, B. Hemmerling, J. Fölling, M. Albiez, and M. K. Oberthaler, Phys. Rev. Lett. **96**, 130404 (2006), URL https://link.aps.org/doi/10.1103/PhysRevLett.96.130404.

[65] F. Meier and W. Zwerger, Phys. Rev. A **64**, 033610 (2001), URL https://link.aps.org/doi/10.1103/PhysRevA.64.033610.

[66] A. Trombettoni and A. Smerzi, Phys. Rev. Lett. **86**, 2353 (2001), URL https://link.aps.org/doi/10.1103/PhysRevLett.86.2353.

[67] D. S. Hall, M. R. Matthews, C. E. Wieman, and E. A. Cornell, Phys. Rev. Lett. **81**, 1543 (1998), URL https://link.aps.org/doi/10.1103/PhysRevLett.81.1543.

[68] J. Williams, R. Walser, J. Cooper, E. Cornell, and M. Holland, Phys. Rev. A **59**, R31 (1999), URL https://link.aps.org/doi/10.1103/PhysRevA.59.R31.

[69] A. Smerzi, A. Trombettoni, T. Lopez-Arias, C. Fort, P. Maddaloni, F. Minardi, and M. Inguscio, The European Physical Journal B - Condensed Matter and Complex Systems **31**, 457 (2003), ISSN 1434-6036, URL https://doi.org/10.1140/epjb/e2003-00055-1.

[70] C. Gross, T. Zibold, E. Nicklas, J. Estève, and M. K. Oberthaler, Nature **464**, 1165 (2010), ISSN 1476-4687, URL https://doi.org/10.1038/nature08919.

[71] M. F. Riedel, P. Böhi, Y. Li, T. W. Hänsch, A. Sinatra, and P. Treutlein, Nature **464**, 1170 (2010), ISSN 1476-4687, URL https://doi.org/10.1038/nature08988.

[72] W. Ketterle and M. Zwierlein, Rivista del Nuovo Cimento **31**, 247 (2008), URL https://www.sif.it/riviste/sif/ncr/econtents/2008/031/05-06/article/0.

[73] M. Tinkham, *Introduction to Superconductivity* (McGraw-Hill, New York, 1996), 2nd ed.

[74] M. Edwards, Nature Physics **9**, 68 (2013), ISSN 1745-2481, URL https://doi.org/10.1038/nphys2546.

[75] C. Ryu, P. W. Blackburn, A. A. Blinova, and M. G. Boshier, Phys. Rev. Lett. **111**, 205301 (2013), URL https://link.aps.org/doi/10.1103/PhysRevLett.111.205301.

[76] C. Ryu, E. C. Samson, and M. G. Boshier, Nat. Comms. **11**, 3338 (2020), URL `https://www.nature.com/articles/s41467-020-17185-6`.

[77] S. Eckel, F. Jendrzejewski, A. Kumar, C. J. Lobb, and G. K. Campbell, Phys. Rev. X **4**, 031052 (2014), URL `https://link.aps.org/doi/10.1103/PhysRevX.4.031052`.

[78] L. Amico, G. Birkl, M. Boshier, and L.-C. Kwek, New Journal of Physics **19**, 020201 (2017), URL `https://doi.org/10.1088%2F1367-2630%2Faa5a6d`.

[79] J. G. Lee, B. J. McIlvain, C. J. Lobb, and W. T. Hill III, Scientific Reports **3**, 1034 (2013), ISSN 2045-2322, URL `https://doi.org/10.1038/srep01034`.

[80] A. Barone and G. Paterno, *Physics and Applications of the Josephson Effect* (John Wiley, New York, 1982).

[81] D. E. McCumber, Journal of Applied Physics **39**, 3113 (1968), URL `https://doi.org/10.1063/1.1656743`.

[82] W. C. Stewart, Applied Physics Letters **12**, 277 (1968), `https://doi.org/10.1063/1.1651991`, URL `https://doi.org/10.1063/1.1651991`.

[83] Abad, M., Guilleumas, M., Mayol, R., Piazza, F., Jezek, D. M., and Smerzi, A., EPL **109**, 40005 (2015), URL `https://doi.org/10.1209/0295-5075/109/40005`.

[84] S. Levy, E. Lahoud, I. Shomroni, and J. Steinhauer, Nature **449**, 579 (2007), ISSN 1476-4687, URL `https://doi.org/10.1038/nature06186`.

[85] E. Varoquaux, G. G. Ihas, O. Avenel, and R. Aarts, Journal of Low Temperature Physics **89**, 207 (1992), ISSN 1573-7357, URL `https://doi.org/10.1007/BF00692593`.

[86] O. Avenel, G. Ihas, and E. Varoquaux, Journal of Low Temperature Physics **93**, 1031 (1993).

[87] E. Varoquaux and O. Avenel, Physica B: Condensed Matter **197**, 306 (1994), ISSN 0921-4526, URL `http://www.sciencedirect.com/science/article/pii/0921452694902275`.

[88] E. Varoquaux, O. Avenel, and M. Meisel, Canadian Journal of Physics **65**, 1377 (2011).

[89] F. Piazza, L. A. Collins, and A. Smerzi, Phys. Rev. A **81**, 033613 (2010), URL `https://link.aps.org/doi/10.1103/PhysRevA.81.033613`.

[90] K. Xhani, E. Neri, L. Galantucci, F. Scazza, A. Burchianti, K.-L. Lee, C. F. Barenghi, A. Trombettoni, M. Inguscio, M. Zaccanti, et al., Phys. Rev. Lett. **124**, 045301 (2020), URL `https://link.aps.org/doi/10.1103/PhysRevLett.124.045301`.

[91] D. S. Jin, M. R. Matthews, J. R. Ensher, C. E. Wieman, and E. A. Cornell, Phys. Rev. Lett. **78**, 764 (1997), URL `https://link.aps.org/doi/10.1103/PhysRevLett.78.764`.

[92] D. M. Stamper-Kurn, H.-J. Miesner, S. Inouye, M. R. Andrews, and W. Ketterle, Phys. Rev. Lett. **81**, 500 (1998), URL `https://link.aps.org/doi/10.1103/PhysRevLett.81.500`.

[93] O. Maragò, G. Hechenblaikner, E. Hodby, and C. Foot, Phys. Rev. Lett. **86**, 3938 (2001), URL `https://link.aps.org/doi/10.1103/PhysRevLett.86.3938`.

[94] F. Chevy, V. Bretin, P. Rosenbusch, K. W. Madison, and J. Dalibard, Phys. Rev. Lett. **88**, 250402 (2002), URL `https://link.aps.org/doi/10.1103/PhysRevLett.88.250402`.

[95] F. Ferlaino, P. Maddaloni, S. Burger, F. S. Cataliotti, C. Fort, M. Modugno, and M. Inguscio, Phys. Rev. A **66**, 011604 (2002), URL `https://link.aps.org/doi/10.1103/PhysRevA.66.011604`.

[96] S. Burger, K. Bongs, S. Dettmer, W. Ertmer, K. Sengstock, A. Sanpera, G. V. Shlyapnikov, and M. Lewenstein, Phys. Rev. Lett. **83**, 5198 (1999), URL `https://link.aps.org/doi/10.1103/PhysRevLett.83.5198`.

[97] P. Rosenbusch, V. Bretin, and J. Dalibard, Phys. Rev. Lett. **89**, 200403 (2002), URL `https://link.aps.org/doi/10.1103/PhysRevLett.89.200403`.

[98] J. R. Abo-Shaeer, C. Raman, and W. Ketterle, Phys. Rev. Lett. **88**, 070409 (2002), URL `https://link.aps.org/doi/10.1103/PhysRevLett.88.070409`.

[99] G. Moon, W. J. Kwon, H. Lee, and Y.-i. Shin, Phys. Rev. A **92**, 051601 (2015), URL `https://link.aps.org/doi/10.1103/PhysRevA.92.051601`.

[100] D. A. W. Hutchinson, E. Zaremba, and A. Griffin, Phys. Rev. Lett. **78**, 1842 (1997), URL `https://link.aps.org/doi/10.1103/PhysRevLett.78.1842`.

[101] M. Olshanii, arXiv e-prints arXiv:cond-mat/9807412 (1998), `9807412`.

[102] V. B. Shenoy and T.-L. Ho, Phys. Rev. Lett. **80**, 3895 (1998), URL `https://link.aps.org/doi/10.1103/PhysRevLett.80.3895`.

[103] H. T. C. Stoof and M. J. Bijlsma, Journal of Low Temperature Physics **124**, 431 (2001), ISSN 1573-7357, URL `https://doi.org/10.1023/A:1017519118408`.

[104] U. Al Khawaja and H. T. C. Stoof, Phys. Rev. A **62**, 053602 (2000), URL `https://link.aps.org/doi/10.1103/PhysRevA.62.053602`.

[105] B. Jackson and E. Zaremba, Phys. Rev. Lett. **87**, 100404 (2001), URL `https://link.aps.org/doi/10.1103/PhysRevLett.87.100404`.

[106] B. Jackson and E. Zaremba, Phys. Rev. Lett. **89**, 150402 (2002), URL `https://link.aps.org/doi/10.1103/PhysRevLett.89.150402`.

[107] S. A. Morgan, M. Rusch, D. A. W. Hutchinson, and K. Burnett, Phys. Rev. Lett. **91**, 250403 (2003), URL `https://link.aps.org/doi/10.1103/PhysRevLett.91.250403`.

[108] S. A. Morgan, Phys. Rev. A **72**, 043609 (2005), URL `https://link.aps.org/doi/10.1103/PhysRevA.72.043609`.

[109] E. Arahata and T. Nikuni, Phys. Rev. A **77**, 033610 (2008), URL `https://link.aps.org/doi/10.1103/PhysRevA.77.033610`.

[110] B. Jackson, N. P. Proukakis, and C. F. Barenghi, Phys. Rev. A **75**, 051601 (2007), URL `https://link.aps.org/doi/10.1103/PhysRevA.75.051601`.

[111] B. Jackson, C. F. Barenghi, and N. P. Proukakis, Journal of Low Temperature Physics **148**, 387 (2007).

[112] B. Jackson, N. P. Proukakis, C. F. Barenghi, and E. Zaremba, Phys. Rev. A **79**, 053615 (2009), URL `https://link.aps.org/doi/10.1103/PhysRevA.79.053615`.

[113] S. J. Rooney, A. S. Bradley, and P. B. Blakie, Phys. Rev. A **81**, 023630 (2010), URL `https://link.aps.org/doi/10.1103/PhysRevA.81.023630`.

[114] S. P. Cockburn, H. E. Nistazakis, T. P. Horikis, P. G. Kevrekidis, N. P. Proukakis, and D. J. Frantzeskakis, Phys. Rev. Lett. **104**, 174101 (2010), URL `https://link.aps.org/doi/10.1103/PhysRevLett.104.174101`.

[115] A. J. Allen, E. Zaremba, C. F. Barenghi, and N. P. Proukakis, Phys. Rev. A **87**, 013630 (2013), URL `https://link.aps.org/doi/10.1103/PhysRevA.87.013630`.

[116] A. J. Allen, S. Zuccher, M. Caliari, N. P. Proukakis, N. G. Parker, and C. F. Barenghi, Phys. Rev. A **90**, 013601 (2014), URL `https://link.aps.org/doi/10.1103/PhysRevA.90.013601`.

[117] S. J. Rooney, A. J. Allen, U. Zülicke, N. P. Proukakis, and A. S. Bradley, Phys. Rev. A **93**, 063603 (2016), URL `https://link.aps.org/doi/10.1103/PhysRevA.93.063603`.

[118] C. N. Weiler, T. W. Neely, D. R. Scherer, A. S. Bradley, M. J. Davis, and B. P. Anderson, Nature **455**, 948 (2008), ISSN 1476-4687, URL `https://doi.org/10.1038/nature07334`.

[119] G. Lamporesi, S. Donadello, S. Serafini, F. Dalfovo, and G. Ferrari, Nature Physics **9**, 656 (2013), ISSN 1745-2481, URL `https://doi.org/10.1038/nphys2734`.

[120] S. Donadello, S. Serafini, M. Tylutki, L. P. Pitaevskii, F. Dalfovo, G. Lamporesi, and G. Ferrari, Phys. Rev. Lett. **113**, 065302 (2014), URL `https://link.aps.org/doi/10.1103/PhysRevLett.113.065302`.

[121] L. Corman, L. Chomaz, T. Bienaimé, R. Desbuquois, C. Weitenberg, S. Nascimbène, J. Dalibard, and J. Beugnon, Phys. Rev. Lett. **113**, 135302 (2014), URL `https://link.aps.org/doi/10.1103/PhysRevLett.113.135302`.

[122] L. Chomaz, L. Corman, T. Bienaimé, R. Desbuquois, C. Weitenberg, S. Nascimbène, J. Beugnon, and J. Dalibard, Nature Communications **6**, 6162 (2015), ISSN 2041-1723, URL `https://doi.org/10.1038/ncomms7162`.

[123] N. Navon, A. L. Gaunt, R. P. Smith, and Z. Hadzibabic, Science **347**, 167 (2015), ISSN 0036-8075, URL `https://science.sciencemag.org/content/347/6218/167`.

[124] I.-K. Liu, R. Pattinson, T. Billam, S. Gardiner, S. Cornish, T.-M. Huang, W.-W. Lin, S.-C. Gou, N. Parker, and N. Proukakis, Physical Review A **93** (2016).

[125] J. Stenger, D. M. Stamper-Kurn, M. R. Andrews, A. P. Chikkatur, S. Inouye, H.-J. Miesner, and W. Ketterle, Journal of Low Temperature Physics **113**, 167 (1998), ISSN 1573-7357, URL `https://doi.org/10.1023/A:1022565725910`.

[126] C. W. Gardiner, M. D. Lee, R. J. Ballagh, M. J. Davis, and P. Zoller, Phys. Rev. Lett. **81**, 5266 (1998), URL `https://link.aps.org/doi/10.1103/PhysRevLett.81.5266`.

[127] M. J. Davis, C. W. Gardiner, and R. J. Ballagh, Phys. Rev. A **62**, 063608 (2000), URL `https://link.aps.org/doi/10.1103/PhysRevA.62.063608`.

[128] M. J. Bijlsma, E. Zaremba, and H. T. C. Stoof, Phys. Rev. A **62**, 063609 (2000), URL `https://link.aps.org/doi/10.1103/PhysRevA.62.063609`.

[129] B. Svistunov, Physics Letters A **287**, 169 (2001), ISSN 0375-9601, URL http://www.sciencedirect.com/science/article/pii/S037596010100439X.

[130] D. M. Harber, J. M. McGuirk, J. M. Obrecht, and E. A. Cornell, Journal of Low Temperature Physics **133**, 229 (2003), ISSN 1573-7357, URL https://doi.org/10.1023/A:1026084606385.

[131] N. P. Proukakis, J. Schmiedmayer, and H. T. C. Stoof, Phys. Rev. A **73**, 053603 (2006), URL https://link.aps.org/doi/10.1103/PhysRevA.73.053603.

[132] M. Gring, M. Kuhnert, T. Langen, T. Kitagawa, B. Rauer, M. Schreitl, I. Mazets, D. A. Smith, E. Demler, and J. Schmiedmayer, Science **337**, 1318 (2012), ISSN 0036-8075, URL https://science.sciencemag.org/content/337/6100/1318.

[133] S. M. A. Handel, T. Wiles, S. Hopkins, and S. Cornish, Rev Sci Instrum. **83(1)**, 013105 (2012), URL https://link.aps.org/doi/10.1063/1.3676161.

[134] J. Märkle, A. J. Allen, P. Federsel, B. Jetter, A. Günther, J. Fortágh, N. P. Proukakis, and T. E. Judd, Phys. Rev. A **90**, 023614 (2014), URL https://link.aps.org/doi/10.1103/PhysRevA.90.023614.

[135] N. P. Proukakis and B. Jackson, Journal of Physics B: Atomic, Molecular and Optical Physics **41**, 203002 (2008), URL https://doi.org/10.1088%2F0953-4075%2F41%2F20%2F203002.

[136] T. R. Kirkpatrick and J. R. Dorfman, Phys. Rev. A **28**, 2576 (1983), URL https://link.aps.org/doi/10.1103/PhysRevA.28.2576.

[137] T. R. Kirkpatrick and J. R. Dorfman, Journal of Low Temperature Physics **58** (1985), URL https://doi.org/10.1007/BF00681133.

[138] T. R. Kirkpatrick and J. R. Dorfman, Journal of Low Temperature Physics **58**, 301 (1985), ISSN 1573-7357, URL https://doi.org/10.1007/BF00681309.

[139] N. Proukakis, S. Gardiner, M. Davis, and M. Szymaska, eds., *Quantum Gases: Finite Temperature and Non-Equilibrium Dynamics* (Imperial College Press, London, United Kingdom, 2013), URL https://doi.org/10.1142/p817.

[140] N. G. Berloff, M. Brachet, and N. P. Proukakis, Proceedings of the National Academy of Sciences **111**, 4675 (2014), ISSN 0027-8424, URL https://www.pnas.org/content/111/Supplement_1/4675.

[141] M. Brewczyk, M. Gajda, and K. Rzażewski, Journal of Physics B: Atomic, Molecular and Optical Physics **40**, R1 (2007), URL https://doi.org/10.1088%2F0953-4075%2F40%2F2%2Fr01.

[142] P. Blakie, A. Bradley, M. Davis, R. Ballagh, and C. Gardiner, Advances in Physics **57**, 363 (2008), https://doi.org/10.1080/00018730802564254, URL https://doi.org/10.1080/00018730802564254.

[143] S. J. Rooney, P. B. Blakie, and A. S. Bradley, Phys. Rev. A **86**, 053634 (2012), URL https://link.aps.org/doi/10.1103/PhysRevA.86.053634.

[144] S. P. Cockburn and N. P. Proukakis, Laser Physics **19**, 558 (2009), ISSN 1555-6611, URL https://doi.org/10.1134/S1054660X09040057.

[145] H. T. C. Stoof, Phys. Rev. Lett. **78**, 768 (1997), URL https://link.aps.org/doi/10.1103/PhysRevLett.78.768.

[146] H. T. C. Stoof and M. J. Bijlsma, Journal of Low Temperature Physics **124**, 431 (2001), ISSN 1573-7357, URL https://doi.org/10.1023/A:1017519118408.

[147] R. Meppelink, S. B. Koller, J. M. Vogels, H. T. C. Stoof, and P. van der Straten, Phys. Rev. Lett. **103**, 265301 (2009), URL https://link.aps.org/doi/10.1103/PhysRevLett.103.265301.

[148] K. L. Lee and N. P. Proukakis, Journal of Physics B: Atomic, Molecular and Optical Physics **49**, 214003 (2016), URL https://doi.org/10.1088%2F0953-4075%2F49%2F21%2F214003.

[149] T. Nikuni and A. Griffin, Phys. Rev. A **63**, 033608 (2001), URL https://link.aps.org/doi/10.1103/PhysRevA.63.033608.

[150] T. Nikuni and A. Griffin, Phys. Rev. A **65**, 011601 (2001), URL https://link.aps.org/doi/10.1103/PhysRevA.65.011601.

[151] A. Griffin and E. Zaremba, Phys. Rev. A **56**, 4839 (1997), URL https://link.aps.org/doi/10.1103/PhysRevA.56.4839.

[152] E. Zaremba, A. Griffin, and T. Nikuni, Phys. Rev. A **57**, 4695 (1998), URL https://link.aps.org/doi/10.1103/PhysRevA.57.4695.

[153] J. E. Williams and A. Griffin, Phys. Rev. A **63**, 023612 (2001), URL https://link.aps.org/doi/10.1103/PhysRevA.63.023612.

[154] B. P. Anderson, P. C. Haljan, C. E. Wieman, and E. A. Cornell, Phys. Rev. Lett. **85**, 2857 (2000), URL https://link.aps.org/doi/10.1103/PhysRevLett.85.2857.

[155] D. V. Freilich, D. M. Bianchi, A. M. Kaufman, T. K. Langin, and D. S. Hall, Science **329**, 1182 (2010), ISSN 0036-8075, URL https://science.sciencemag.org/content/329/5996/1182.

[156] K. L. Lee, N. B. Jørgensen, I.-K. Liu, L. Wacker, J. J. Arlt, and N. P. Proukakis, Phys. Rev. A **94**, 013602 (2016), URL `https://link.aps.org/doi/10.1103/PhysRevA.94.013602`.

[157] M. J. Edmonds, K. L. Lee, and N. P. Proukakis, Phys. Rev. A **92**, 063607 (2015), URL `https://link.aps.org/doi/10.1103/PhysRevA.92.063607`.

[158] M. J. Edmonds, K. L. Lee, and N. P. Proukakis, Phys. Rev. A **91**, 011602 (2015), URL `https://link.aps.org/doi/10.1103/PhysRevA.91.011602`.

[159] M. Zaccanti and W. Zwerger, Phys. Rev. A **100**, 063601 (2019), URL `https://link.aps.org/doi/10.1103/PhysRevA.100.063601`.

[160] N. Bogolyubov, J. Phys. (USSR) **11**, 23 (1947).

[161] D. G. D.S. Petrov and G. Shlyapnikov, J. Phys. IV France pp. 5–44 (1962), ISSN 0031-9163.

[162] E. P. Gross, Journal of Mathematical Physics **4**, 195 (1963), URL `https://doi.org/10.1063/1.1703944`.

[163] E. P. Gross, Il Nuovo Cimento (1955-1965) **20**, 454 (1961), ISSN 1827-6121, URL `https://doi.org/10.1007/BF02731494`.

[164] L. P. Pitaevskii, Zh. Eksp. Teor. Fiz. **40** (1961).

[165] D. S. Petrov, C. Salomon, and G. V. Shlyapnikov, Phys. Rev. Lett. **93**, 090404 (2004), URL `https://link.aps.org/doi/10.1103/PhysRevLett.93.090404`.

[166] G. Baym and C. J. Pethick, Phys. Rev. Lett. **76**, 6 (1996), URL `https://link.aps.org/doi/10.1103/PhysRevLett.76.6`.

[167] L. Landau, J. Phys. USSR V **71** (1941).

[168] G. W. Rayfield and F. Reif, Phys. Rev. **136**, A1194 (1964), URL `https://link.aps.org/doi/10.1103/PhysRev.136.A1194`.

[169] T. Frisch, Y. Pomeau, and S. Rica, Phys. Rev. Lett. **69**, 1644 (1992), URL `https://link.aps.org/doi/10.1103/PhysRevLett.69.1644`.

[170] D. Amit and E. P. Gross, Phys. Rev. **145**, 130 (1966), URL `https://link.aps.org/doi/10.1103/PhysRev.145.130`.

[171] P. H. Roberts and J. Grant, Journal of Physics A: General Physics **4**, 55 (1971), URL `https://doi.org/10.1088%2F0305-4470%2F4%2F1%2F009`.

[172] C. F. Barenghi and R. J. Donnelly, Fluid Dynamics Research **41**, 051401 (2009), URL https://doi.org/10.1088%2F0169-5983%2F41%2F5%2F051401.

[173] K. W. Madison, F. Chevy, W. Wohlleben, and J. Dalibard, Phys. Rev. Lett. **84**, 806 (2000), URL https://link.aps.org/doi/10.1103/PhysRevLett.84.806.

[174] W. J. Kwon, J. H. Kim, S. W. Seo, and Y. Shin, Phys. Rev. Lett. **117**, 245301 (2016), URL https://link.aps.org/doi/10.1103/PhysRevLett.117.245301.

[175] R. Hänninen and A. W. Baggaley, Proc. Natl. Acad. Sci. USA **111**, 4667 (2014).

[176] H. C. Pocklington, Philos. Trans. R. Soc. London, Ser. A **186** (1895).

[177] D. W. Moore and P. G. Saffman, Proc. R. Soc. London, Ser. A **338** (1974).

[178] C. F. Barenghi, R. J. Donnelly, and W. F. Vinen, Phys. Fluids **28**, 498 (1985), URL https://doi.org/10.1063/1.865113.

[179] C. F. Barenghi, R. Hanninen, and M. Tsubota, Phys. Rev. E **74**, 046303 (2006), URL https://link.aps.org/doi/10.1103/PhysRevE.74.046303.

[180] L. Kiknadze and Y. Mamaladze, Journal of Low Temperature Physics **124** (2002), URL https://doi.org/10.1023/A:1013793001548.

[181] C. Chin, R. Grimm, P. Julienne, and E. Tiesinga, Rev. Mod. Phys. **82**, 1225 (2010), URL https://link.aps.org/doi/10.1103/RevModPhys.82.1225.

[182] P. Naidon and L. Pricoupenko, Phys. Rev. A **100**, 042710 (2019), URL https://link.aps.org/doi/10.1103/PhysRevA.100.042710.

[183] M. Bartenstein, A. Altmeyer, S. Riedl, R. Geursen, S. Jochim, C. Chin, J. H. Denschlag, R. Grimm, A. Simoni, E. Tiesinga, et al., Phys. Rev. Lett. **94**, 103201 (2005), URL https://link.aps.org/doi/10.1103/PhysRevLett.94.103201.

[184] L. Pricoupenko and Y. Castin, Phys. Rev. A **69**, 051601 (2004), URL https://link.aps.org/doi/10.1103/PhysRevA.69.051601.

[185] S. Giorgini, L. P. Pitaevskii, and S. Stringari, Rev. Mod. Phys. **80**, 1215 (2008), URL https://link.aps.org/doi/10.1103/RevModPhys.80.1215.

[186] M. Albert, T. Paul, N. Pavloff, and P. Leboeuf, Phys. Rev. Lett. **100**, 250405 (2008), URL https://link.aps.org/doi/10.1103/PhysRevLett.100.250405.

[187] A. Smerzi and A. Trombettoni, Phys. Rev. A **68**, 023613 (2003), URL https://link.aps.org/doi/10.1103/PhysRevA.68.023613.

[188] F. Piazza, Ph.D. thesis, Universita' degli Studi di Trento (2011).

[189] R. A. Ferrell, Phys. Rev. B **38**, 4984 (1988), URL https://link.aps.org/doi/10.1103/PhysRevB.38.4984.

[190] J. Binney, ed., *The Theory of critical phenomena: an introduction to the renormalization group* (Clarendon Press, 1992, 1992).

[191] A. Griffin, Phys. Rev. B **53**, 9341 (1996), URL https://link.aps.org/doi/10.1103/PhysRevB.53.9341.

[192] D. A. W. Hutchinson, K. Burnett, R. J. Dodd, S. A. Morgan, M. Rusch, E. Zaremba, N. P. Proukakis, M. Edwards, and C. W. Clark, Journal of Physics B: Atomic, Molecular and Optical Physics **33**, 3825 (2000), URL https://doi.org/10.1088%2F0953-4075%2F33%2F19%2F302.

[193] H. Shi and A. Griffin, Physics Reports **304**, 1 (1998), ISSN 0370-1573, URL http://www.sciencedirect.com/science/article/pii/S0370157398000155.

[194] M. Hillery, R. O'Connell, M. Scully, and E. Wigner, Physics Reports **106**, 121 (1984), ISSN 0370-1573, URL http://www.sciencedirect.com/science/article/pii/0370157384901601.

[195] N. P. Proukakis and B. Jackson, J. Phys. B: At. Mol. Opt. Phys. **41**, 203002 (2008), URL https://doi.org/10.1088%2F0953-4075%2F41%2F20%2F203002.

[196] M. Holland, J. Williams, and J. Cooper, Phys. Rev. A **55**, 3670 (1997), URL https://link.aps.org/doi/10.1103/PhysRevA.55.3670.

[197] T. Nikuni and J. E. Williams, Journal of Low Temperature Physics **133**, 323 (2003), ISSN 1573-7357, URL https://doi.org/10.1023/A:1026206724886.

[198] Y. Endo and T. Nikuni, Journal of Low Temperature Physics **163**, 92 (2011), ISSN 1573-7357, URL https://doi.org/10.1007/s10909-010-0340-y.

[199] B. Jackson and E. Zaremba, Phys. Rev. A **66**, 033606 (2002), URL https://link.aps.org/doi/10.1103/PhysRevA.66.033606.

[200] E. Arahata and T. Nikuni, Phys. Rev. A **87**, 033610 (2013), URL https://link.aps.org/doi/10.1103/PhysRevA.87.033610.

[201] B. Jackson and E. Zaremba, Phys. Rev. Lett. **88**, 180402 (2002), URL https://link.aps.org/doi/10.1103/PhysRevLett.88.180402.

[202] B. Jackson and E. Zaremba, Phys. Rev. Lett. **88**, 180402 (2002), URL https://link.aps.org/doi/10.1103/PhysRevLett.88.180402.

[203] A. J. Allen, Ph.D. thesis, Newcastle University (2012).

[204] B. G. A., *Molecular Gas Dynamics and the Direct Simulation of Gas Flows* (Oxford: Clarendon, 1994).

[205] B. G. A., *Molecular Gas Dynamics* (Oxford: Clarendon, 1976).

[206] A. C. J. Wade, D. Baillie, and P. B. Blakie, Phys. Rev. A **84**, 023612 (2011), URL https://link.aps.org/doi/10.1103/PhysRevA.84.023612.

[207] M. Gallis, J. Torczynski, D. Rader, and G. Bird, Journal of Computational Physics **228**, 4532 (2009), ISSN 0021-9991, URL http://www.sciencedirect.com/science/article/pii/S0021999109001429.

[208] J. Ruostekoski and D. F. Walls, Phys. Rev. A **58**, R50 (1998), URL https://link.aps.org/doi/10.1103/PhysRevA.58.R50.

[209] F. Piazza, L. A. Collins, and A. Smerzi, New J. Phys. **13**, 043008 (2011), URL https://doi.org/10.1088%2F1367-2630%2F13%2F4%2F043008.

[210] C. Rorai, J. Skipper, R. M. Kerr, and K. R. Sreenivasan, Journal of Fluid Mechanics **808**, 641667 (2016).

[211] A. Villois, G. Krstulovic, D. Proment, and H. Salman, J Phys A: Math. Theor. **49**, 415502 (2016), URL https://doi.org/10.1088%2F1751-8113%2F49%2F41%2F415502.

[212] W. Wang, R. N. Bisset, C. Ticknor, R. Carretero-González, D. J. Frantzeskakis, L. A. Collins, and P. G. Kevrekidis, Phys. Rev. A **95**, 043638 (2017), URL https://link.aps.org/doi/10.1103/PhysRevA.95.043638.

[213] A. Klein, I. L. Aleiner, and O. Agam, Annals of Physics **346**, 195 (2014), ISSN 0003-4916, URL http://www.sciencedirect.com/science/article/pii/S0003491614000992.

[214] L. Galantucci, A. W. Baggaley, N. G. Parker, and C. F. Barenghi, Proceedings of the National Academy of Sciences **116**, 12204 (2019), ISSN 0027-8424, URL https://www.pnas.org/content/116/25/12204.

[215] J. R. Anglin, Phys. Rev. A **65**, 063611 (2002), URL https://link.aps.org/doi/10.1103/PhysRevA.65.063611.

[216] P. Mason, N. G. Berloff, and A. L. Fetter, Physical Review A **74**, 043611 (2006).

[217] A. L. Fetter, Rev. Mod. Phys. **81**, 647 (2009), URL `https://link.aps.org/doi/10.1103/RevModPhys.81.647`.

[218] C. Nore, M. Abid, and M. E. Brachet, Phys. Rev. Lett. **78**, 3896 (1997), URL `https://link.aps.org/doi/10.1103/PhysRevLett.78.3896`.

[219] R. Numasato, M. Tsubota, and V. S. L'vov, Phys. Rev. A **81**, 063630 (2010), URL `https://link.aps.org/doi/10.1103/PhysRevA.81.063630`.

[220] T.-L. Horng, C.-h. Hsueh, S.-W. Su, Y.-M. Kao, and S.-C. Gou, Phys. Rev. A **80** (2009).

[221] A. Griffin, S. Nazarenko, and D. Proment, **53**, 175701 (2020), URL `https://doi.org/10.1088%2F1751-8121%2Fab7ad0`.

[222] E. Goldobin, D. Koelle, R. Kleiner, and A. Buzdin, Phys. Rev. B **76**, 224523 (2007), URL `https://link.aps.org/doi/10.1103/PhysRevB.76.224523`.

[223] A. J. Groszek, D. M. Paganin, K. Helmerson, and T. P. Simula, Phys. Rev. A **97**, 023617 (2018), URL `https://link.aps.org/doi/10.1103/PhysRevA.97.023617`.

[224] S. Donadello, S. Serafini, M. Tylutki, L. P. Pitaevskii, F. Dalfovo, G. Lamporesi, and G. Ferrari, Phys. Rev. Lett. **113**, 065302 (2014), URL `https://link.aps.org/doi/10.1103/PhysRevLett.113.065302`.

[225] T. W. Neely, E. C. Samson, A. S. Bradley, M. J. Davis, and B. P. Anderson, Phys. Rev. Lett. **104**, 160401 (2010), URL `https://link.aps.org/doi/10.1103/PhysRevLett.104.160401`.

[226] W. J. Kwon, S. W. Seo, and Y.-i. Shin, Phys. Rev. A **92**, 033613 (2015), URL `https://link.aps.org/doi/10.1103/PhysRevA.92.033613`.

[227] R. M. Caplan, J. D. Talley, R. Carretero-Gonzlez, and P. G. Kevrekidis, Physics of Fluids **26**, 097101 (2014), `https://doi.org/10.1063/1.4894745`, URL `https://doi.org/10.1063/1.4894745`.

[228] L. Galantucci, M. Sciacca, N. Parker, A. Baggaley, and C. F. Barenghi (2020), `2006.07196`.

[229] S. Serafini, L. Galantucci, E. Iseni, T. Bienaime, R. Bisset, C. Barenghi, F. Dalfovo, G. Lamporesi, and G. Ferrari, Phys Rev X **7**, 021031 (2017).

[230] M. D. Reichl and E. J. Mueller, Phys. Rev. A **88**, 053626 (2013), URL https://link.aps.org/doi/10.1103/PhysRevA.88.053626.

[231] P. Scherpelz, K. Padavić, A. Rançon, A. Glatz, I. S. Aranson, and K. Levin, Phys. Rev. Lett. **113**, 125301 (2014), URL https://link.aps.org/doi/10.1103/PhysRevLett.113.125301.

[232] A. M. Mateo and J. Brand, New J. Phys **17**, 125013 (2015), URL https://doi.org/10.1088%2F1367-2630%2F17%2F12%2F125013.

[233] A. Imamoḡlu, M. Lewenstein, and L. You, Phys. Rev. Lett. **78**, 2511 (1997), URL https://link.aps.org/doi/10.1103/PhysRevLett.78.2511.

[234] G. J. Milburn, J. Corney, E. M. Wright, and D. F. Walls, Phys. Rev. A **55**, 4318 (1997), URL https://link.aps.org/doi/10.1103/PhysRevA.55.4318.

[235] Y. M. Bidasyuk, O. O. Prikhodko, and M. Weyrauch, Phys. Rev. A **94**, 033603 (2016), URL https://link.aps.org/doi/10.1103/PhysRevA.94.033603.

[236] M. R. Momme, Y. M. Bidasyuk, and M. Weyrauch, Phys. Rev. A **100**, 033601 (2019), URL https://link.aps.org/doi/10.1103/PhysRevA.100.033601.

[237] K. Xhani, L. Galantucci, C. F. Barenghi, G. Roati, A. Trombettoni, and N. P. Proukakis, New Journal of Physics **22**, 123006 (2020), URL https://doi.org/10.1088/1367-2630/abc8e4.

[238] Y. M. Bidasyuk, O. O. Prikhodko, and M. Weyrauch, Phys. Rev. A **94**, 033603 (2016), URL https://link.aps.org/doi/10.1103/PhysRevA.94.033603.

[239] S. Martínez-Garaot, G. Pettini, and M. Modugno, Phys. Rev. A **98**, 043624 (2018), URL https://link.aps.org/doi/10.1103/PhysRevA.98.043624.

[240] M. Iskin and C. A. R. Sá de Melo, Phys. Rev. A **83**, 045602 (2011), URL https://link.aps.org/doi/10.1103/PhysRevA.83.045602.

[241] K. Xhani and N. P. Proukakis, in preparation (2021).

[242] M. Kunimi and I. Danshita, Phys. Rev. A **95**, 033637 (2017), URL https://link.aps.org/doi/10.1103/PhysRevA.95.033637.

[243] A. Kumar, S. Eckel, F. Jendrzejewski, and G. K. Campbell, Phys. Rev. A **95**, 021602 (2017), URL https://link.aps.org/doi/10.1103/PhysRevA.95.021602.

[244] P. O. Fedichev and G. V. Shlyapnikov, Phys. Rev. A **60**, R1779 (1999), URL https://link.aps.org/doi/10.1103/PhysRevA.60.R1779.

[245] H. J. H. Al-Jibbouri, Karbala International Journal of Modern Science **2**, 124 (2016), ISSN 2405-609X, URL `http://www.sciencedirect.com/science/article/pii/S2405609X16300409`.

[246] M. Fliesser, A. Csordás, P. Szépfalusy, and R. Graham, Phys. Rev. A **56**, R2533 (1997), URL `https://link.aps.org/doi/10.1103/PhysRevA.56.R2533`.

[247] Gary Liu, Private Communications.

[248] H. Ott, J. F. gh, and C. Zimmermann, Journal of Physics B: Atomic, Molecular and Optical Physics **36**, 2817 (2003), URL `https://doi.org/10.1088%2F0953-4075%2F36%2F13%2F311`.